PASSIVE THERMAL MANAGEMENT IN HIGH-POWER FIBER LASER SYSTEMS

BY

NANJIE YU

DISSERTATION

Submitted in partial fulfillment of the requirements
for the degree of Doctor of Philosophy in Electrical and Computer Engineering
in the Graduate College of the
University of Illinois Urbana-Champaign, 2022

Urbana, Illinois

Doctoral Committee:

Assistant Professor Peter D. Dragic, Chair
Professor Kent D. Choquette
Professor J. Gary Eden
Professor Lynford L. Goddard
Professor John Ballato, Clemson University

ABSTRACT

Parasitic and catastrophic thermal effects serve as the limiting factors for further power scaling in high-power fiber lasers. Among the different thermal energy generation processes, quantum defect (QD) heating ultimately serves as the dominant heat source in an optimized system. In a typical laser system, a positive QD gives net heating because the pump photon energy is higher than that of the signal. To reduce quantum defect heating, two approaches are investigated, both theoretically and experimentally. Since Yb-doped fiber lasers give the highest output power compared to any other fiber laser systems, the discussions herein mainly focus on Yb-doped fiber laser systems.

The first approach is to reduce the QD heating by bringing the signal wavelength closer to the pumping wavelength. This requires exploring new host glasses for Yb^{3+} including fluorosilicates and phosphosilicates, so that efficient optical gain at shorter wavelengths can be achieved. Both low-power (< 1W pump power) linear cavity lasers and high-power (20 W pump power) amplifiers are demonstrated when pumping at ~975 nm. The former exhibited nearly 70% slope efficiency at 985.7 nm while the latter had an 87.4 % slope efficiency with respect to absorbed pump power when operating at 1005 nm. Theoretical models based on rate equations were built and the experimental results agree well with the simulations. Calculations are also performed to explore improved fiber designs and the possibility of a double-end pumping scheme.

The second approach is to introduce a “cooling” mechanism so that the overall QD heating is reduced. To do so, a negative contribution to the QD is added via a second pumping wavelength positioned to the red side of the lasing wavelength (anti-Stokes pump). Since the

balancing of the thermal energy is introduced through excitation of the system at two wavelengths, such a system is named excitation-balanced fiber laser or amplifier. Demonstrated first is a laser operating in a pulsed regime. The experimental results indicate that anti-Stokes pumping can effectively contribute to stimulated emission in a solid, resulting in a form of self-cooling. An FDTD model is built to further understand and optimize the system. Next, modeling of a high-energy excitation-balanced pulse amplifier is performed. Results indicate that a heat-free mJ-level pulse amplifier is possible. The influences from several input parameters, such as pump power, pump pulse width, and repetition rate are also discussed in detail, providing valuable guidance for future design and experiments.

Last but not the least, since thermal energy can also be generated via nonradiative processes, a testing platform based on Brillouin scattering is proposed to quantify those sources of heating. The functionality of the platform is confirmed by testing a commercial Yb-doped fiber, and a few demonstrations of anti-Stokes fluorescence cooling are made in nanoparticle doped fiber. Such a flatform will be useful for optimizing glass quality.

Finally, a brief conclusion is provided, and several future works are proposed.

ACKNOWLEDGMENTS

I will begin by thanking my family members:

Thank you, mom and dad, for your unconditional support on me pursuing a Ph.D degree abroad, although it means we cannot see each other because of the travel restrictions between the United States and China in the past several years.

Thank you, mother and father-in-law, for treating me like your own child, and for always giving me suggestions so that I can become a better person.

Thank you, my fiancée and future wife, Mingye Xiong. Thank you for lighting up my life with you love. I am short of words at expressing how much I appreciate all the time that we have spent together. I promise to love you forever.

Next, I would like to thank my advisor, Prof. Peter Dragic. I entered the group four years ago, knowing little about optical fibers and even without good English profiency. Now, I will have my Ph.D. degree from one of the best ECE department in the United States. Thank you for all the instructions you have provided to me, thank you for giving me so many opportunities to perform and present research on so many areas, and finally, thank you for always being a good friend to me. You are the best advisor.

I would like to extend my thanks to all the committee members. Prof. Ballato, it was such a pleasure to work with you and your team during my Ph.D. study. All my work is closely related to the fibers fabricated from your group, and I always feel lucky that to a certain degree, I have two advisors. Prof. Eden, you know a lot about optics and photonics as a successful professor, but at the same time, you are always so humble and nice to me and everyone else. I am fortunate to work with you on several projects, and thank you for your insight and suggestions. Prof. Choquette, I took many classes from you in grad school, and they are all wonderful.

Although we work on different areas of photonics, you are the one who gave me a strong background knowledge which I used every day in my research. Thank you for teaching me how to be a better researcher. Prof. Goddard, I learned a lot from you during limited times of collaborations with you. You can always focus on details that may be ignored by others, and thank you for giving the same care to my thesis which resulted in a more complete work.

I wish to extend my thanks to all the collaborators. Maxime, Wade, Matt, Baris, Bailey, thank you for your assistance and support on fabricating fibers for me. Otherwise, this thesis would not even exist. Kavita, Andrey, Austin, Sehyun, I always learn something when discussing research with you, and I appreciate the opportunity to work with you during my Ph.D. study. Jenny Knall, Magnus, and Prof. Digonnet, thank you for including me as part of the team to accomplish the first ASF cooling in silica fiber. It was a memorable when we worked hard to beat the other team, and I'm glad we did it successfully.

Finally, I want to thank all the group members that I spend time with every day. Thank you for our daily discussion about research, for helping me to find things in the lab, although sometimes it turns out I hid them, for putting up with me listening to comedy in the lab, and finally for being a trustworthy teammate when we needed to collaborate.

TABLE OF CONTENTS

CHAPTER 1: Introduction to Thermal Problems in Fiber Lasers

Before talking about fiber lasers, it is necessary to first introduce some basics about optical fiber itself. Optical fiber is a transparent cylindrical dielectric waveguide that transmits light by the process of total internal reflection. A basic structure of optical fiber is shown in Fig. 1.1. The cladding is usually made from pure silica and the core is usually made from silica with certain dopants, which raises the refractive index so that the optical signal is largely confined in the core. A polymer buffer is usually coated outside the cladding layer to mechanically protect the fragile core and cladding. Standard sizes of cladding and buffer are 125 μm and 250 μm in diameter, and the core diameter usually varies from 5 μm to 10 μm in a single-mode fiber, and as large as 100 μm in a multi-mode fiber.

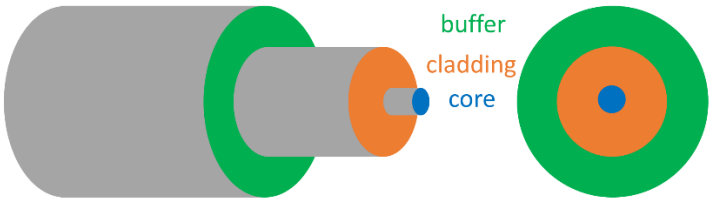

Fig. 1.1: Basic structure of optical fiber.

With its specific geometry and material, optical fiber has certain advantages considering laser application. First, since light is mostly confined in the small core, light output from fibers usually has a high beam quality (especially in single-mode fibers) and often possesses diffraction-limited beam quality. Second, fiber lasers have high brightness compared to other high-power laser sources, which is an important feature since many applications require very high power in a single transverse mode. Brightness is a measure of the power per unit area per

unit solid angle, or simplified for the case of fiber, power per unit area per unit of divergence, which is related to the fiber numerical aperture (NA). For example in material processing [1] a 10 kW diode laser with 20 transverse modes is not as useful as a 1 kW fiber laser with 1 transverse mode due to the reduced beam quality. Third, optical fibers have very low transmission loss in the near infrared. This property reduces cavity loss in a laser configuration and therefore reduces the threshold and increases the slope efficiency of the laser. Finally, optical fiber is a very long and thin cylinder with a very large surface-to-volume ratio, which allows for an exceptional capacity of heat dissipation when compared to rod type solid state lasers.

Fiber lasers were proposed soon after the first laser demonstration by Maiman [2]. From then, decades of research and development have led to the modern fiber laser, covering a wide range of wavelengths across several different dopants that can be added into the glass, such as Nd^{3+} [3], Er^{3+} [4], Yb^{3+} [5], Tm^{3+} [6], etc. Among all the dopants, Yb-doped fiber lasers have provided so far the highest optical power of up to 20 kW with single-mode output [7], and up to 500 kW with multi-mode output [7]. As a result of the advantages of optical fibers discussed above, fiber lasers have many advantages compared to other types of high-power lasers, including diffraction-limited beam quality (especially when the active fiber is single mode) [8], high brightness [9], low threshold and high slope efficiency, as well as exceptional capacity of heat dissipation [10]. A variety of applications can benefit from such high-power fiber lasers, including material processing [11], particle acceleration [12], gas remote sensing [13]–[15], lidars [16], and industrial manufacturing [17], and efforts are continuously progressing toward further power scaling.

However, power scaling can be limited by many problems including damage thresholds, available pump powers, thermal effects, and nonlinear effects [18]. Considering the first issue,

the damage threshold of fiber is usually not reached with current output power levels [19] but may become a problem in the future. The available pump powers are solvable not only by combining more laser diodes into the active fiber via fiber combiners, but also by the development of higher-brightness laser diodes. The availability of power scaling in fiber lasers, at least at this point, is limited mainly by thermal and nonlinear effects [17], [18], [20], [21]. The two dominant nonlinear effects are known as stimulated Brillouin scattering (SBS) and stimulated Raman scattering (SRS), which have turn-on thresholds that are inversely proportional to the light intensity inside the fiber core. Therefore, a natural solution to reduce such effects is to increase the core size of the fiber, while reducing the numerical aperture (NA), which yields what are known as large mode area (LMA) fibers. In LMA fibers, optical intensity is reduced by spreading the power over a larger effective area. Because this is conceptually straightforward, many LMA fibers were developed with reduced nonlinearities [22], [23]. However, with increased core diameters, LMA fiber designs usually yield few-mode instead of single-mode operation and as a result, parasitic thermal effects such as transverse mode instability (TMI) [21] can happen and deteriorate output beam quality. This topic is discussed in more detail later in this section. Moreover, fibers are usually surrounded by a polymer coating with limited tolerance to heat, which may also limit the maximum output power achievable by the fiber laser. Therefore, all the discussions above lead to a single problem: thermal management in fiber lasers.

Before discussing thermal management in fiber lasers, it is important to point out that Yb-doped fiber laser itself already has advantageous thermal characteristics. In fact, thermal management was not a concern at the early stage of development of fiber lasers [24], becoming significant only as power levels approached the kW regime. Two main reasons can explain this.

First, as discussed above, because of the thin and long cylinder geometry, optical fiber can allow for an exceptional capacity of heat dissipation. Second, unlike other dopants such as Er^{3+} and Nd^{3+}, which have numerous higher energy levels, Yb^{3+} is characterized by a two-level system and allows for very small quantum defect, whose definition is discussed in detail later in this section. The two-level system results from the fact that the electron configuration of Yb^{3+} is $[Xe]4f^{13,}$ which leaves only one unpaired spin in the 4f subshell. Therefore, the total spin angular momentum S is 1/2, and total orbital angular momentum is $L = |-3 \times 2 - 2 \times 2 - 1 \times 2 + 0 \times 2 + 1 \times 2 + 2 \times 2 + 3| = 3$. This corresponds to the ${}^2F_{7/2}$ ground level and only one other high energy level (${}^2F_{5/2}$) because total angular momentum J can only take values from $|L - S|$ to $L + S$. The two-level system allows in-band transitions which naturally gives a relatively small energy difference between the pump and signal photons. Additionally, the two-level diagram removes the possibility of up-conversion from the upper laser level to higher levels. This up-conversion is a result of the clustering effect [25], which happens when two active ions are in close proximity and transfer energy from one to another. This is an inevitable process because of the nature of optical fiber as an amorphous material (i.e. glass), which does not possess the property of a periodic distribution over space like a crystal. When clustering happens, active ions could be excited to energy levels higher than the upper laser levels and generate higher energy (shorter wavelength) photons corresponding to transitions directly to the ground state. These processes strongly degrade laser efficiency, especially in heavily doped active fibers, because the generated photons are not at desired wavelengths. However, because of the two-level configuration of Yb^{3+}, this up-conversion process is removed. As a result, higher laser efficiency could be achieved and more Yb^{3+} could be doped into the fiber, which are very important properties in high-power applications. It is necessary to point out that when optically pumping a

Yb-doped fiber within its absorption band, there is still the possibility that a green or blue color is observable. However, this is not because of the up-conversion discussed above, but instead a result of cooperative luminescence from ion pairs. Its origin is still not fully understood but its strength is relatively low in high-quality Yb-doped fibers, and usually is an indicator of the presence of ion pairs [26], [27].

Although the Yb-doped fiber laser possesses the favorable characteristics discussed above, its thermal management has become an increasingly important issue to consider as the output power climbed past the 1 kW region. There are many processes by which thermal energy can be generated when Yb-doped fiber lasers are operating. Firstly, during the fabrication process of optical fiber, in addition to the desirable dopants, impurity atoms could also be introduced due to the purity of the materials. These impurities may possess broad absorption bands while not radiatively emitting photons. As a result, the absorbed energy is transferred to phonons and eventually dissipates as thermal energy in the material. This process is known as nonradiative heating and is discussed in more detail in Chapter 5. It is necessary to point out that multi-phonon decay is also a possibility for nonradiative decay and results in heating. However, the lasing wavelength energy, for example, 10000 cm^{-1} @ 1000 nm, is much higher than the phonon energy in silica (1100 cm^{-1}), making the multi-phonon process very unlikely to happen [28]. Secondly, in fiber laser systems there are inevitable fusion splices between active and passive fibers. If the modes in the two fibers do not perfectly match, it will lead to imperfect splices, which will result in light coupling into the cladding and eventually into the polymer buffer. Since the buffer is usually a purely absorbing material, all the energy from the leakage light will be absorbed and eventually transferred into thermal energy. Thirdly, since the signal photon energy must be smaller than the pump photon energy to achieve optical gain, the signal

wavelength λ_s must also be greater than pump wavelength λ_p. This energy difference leads to a figure-of-merit by which to quantify the heat generation in the active fiber, which is known as the quantum defect (QD) as defined in Eq. 1.1

$$QD = 1 - \frac{\lambda_p}{\lambda_s} \tag{1.1}$$

As a clarification, high-power fiber lasers are not necessarily always lasers but may instead be amplifiers. Therefore, the signal wavelength is taken to be the lasing wavelength if the system acts like a laser, or the signal wavelength if the system acts like an amplifier. More discussion is provided in Chapter 3. In either case, the QD represents the percentage of pump power transferred to thermal energy in the condition of quantum limit. This means that for every photon used to pump the system, there will always be a photon emitted out at the signal wavelength. The only thermal energy generated in this process is the energy difference between these two photons.

Of the above three processes, fiber purity is related to the fiber fabrication process and cannot be changed after the fiber is fabricated. Luckily, decades of research on fiber fabrication have made impurity absorption small compared to quantum defect heating in most cases. However, as will be shown in Chapter 5, when QD is small enough, nonradiative heating can become a significant heat source and may significantly influence the fiber temperature. The minimization of nonradiative heating is a fabrication problem and will not be the main discussion in this document, however, methods to characterize nonradiative heating will be discussed in Chapter 5. Second, for the thermal energy generation originating from splicing, this can be largely suppressed by tapering so that the modes of the two fibers are better matched. Finally, since the pump photon energy is always greater than that of the signal photon (exception will be discussed in Chapter 4 for the excitation balanced laser), quantum defect heating cannot be fully

eliminated and is usually the dominant source of thermal energy generation in an optimized fiber laser system. The main purpose of this document, therefore, is to develop passive approaches to lowering the quantum defect heating in high-power fiber lasers, without introducing additional cooling mechanism to the fiber, such as fan-blowing or water cooling.

Next, it is necessary to introduce some of the problems that may arise as significant thermal energy is generated during fiber laser operation. These may be either parasitic [5], [21] or catastrophic [10], [18]. Catastrophic failure, which means permanent damage to the fiber, obviously sets the upper limit to heat power that could be introduced in the core of a certain length of active fiber. The maximum allowable thermal load could be calculated based on the material properties of core and cladding, such as the rupture modulus and melting temperature [29]. While the calculation in [29] only considers the core and cladding of the fiber, fibers are usually coated with a polymer buffer, which is the easiest way to mechanically protect the fiber. However, a polymer coating not only impedes heat flow in the fiber and exacerbates heating because of its low thermal conductivity, it also has a relatively low melting point and can even burn when the temperature is sufficiently high. Therefore, in real fiber laser systems it is usually the damage threshold of the buffer that limits the maximum heating needed to cause catastrophic failure. Another potential catastrophic failure comes from the thermal-lensing effect. Since both the core and cladding usually have a positive thermal-optic coefficient (dn/dT), which is the change of refractive index with temperature. When operating at high powers, transverse thermal gradients can cause a lensing effect that focuses the light. Eventually the intensity becomes so high that it exceeds the damage threshold of the glass.

Parasitic effects, on the other hand, will not cause any damage to the optical fiber itself. However, they introduce other problems that limit the performance of the fiber laser, which

further influence the related applications. The most significant of these effects is transverse mode instability (TMI). It is a phenomenon whereby the output mode pattern starts to rapidly oscillate between the fundamental and higher-order modes when the output power is over a certain critical threshold. Interestingly, TMI is a relatively new parasitic process, introduced through power scaling in the low nonlinearity, few-moded LMA fibers discussed above. Such fibers usually are made to act "effectively" single mode, usually by coiling the fiber (and sometimes through waveguide design) resulting in greater bending (or propagation) loss to the higher-order modes, but not their complete removal. Their presence can be very detrimental at high power. The reason for this stems from the interference pattern generated from the modes in the fiber as they propagate. Consider, for example, the presence of two modes, the fundamental LP_{01} and the LP_{11} modes. There will be spots in the fiber core where the two modes constructively interfere and result in a greater probability of stimulated emission and therefore more QD-related heating. There also will be regions where the two modes destructively interfere and therefore experience less heating. As a result, there will be "hot" and "cool" spots periodically arranged in the fiber. As a result of the positive dn/dT for the glass comprising the fiber, a dynamic index profile with a period equaling to the beat length between the two modes is generated, much like a long period fiber grating. As proved in [20], such an index distribution will lead to coherent energy transfer between modes and therefore a stochastic transverse mode instability. To further illustrate this, for an effectively single-mode fiber laser, before reaching the TMI threshold, the output beam usually is close to a diffraction limited profile. However, after the laser power reaches the TMI threshold, the output beam shape becomes random and this randomness will result in bad system performance if the application requires a highly stable, diffraction limited beam, such as industrial manufacturing or lidars. To conclude, it may seem that introducing single-mode fiber

as the active region offers a solution to this problem. However, since single-mode fiber usually has a much smaller core, and therefore the optical intensity inside the active fiber is very high, strong nonlinear effects such as SRS and SBS will be introduced, degrading laser performance. This ultimately leads to a set of trade-offs in the design of high-power systems.

After stating the thermal problems in high-power fiber lasers, it is meaningful to summarize the solutions to such problems in the literature, and identify the subsequent approaches of this thesis. The flowchart in Fig. 1.2 is created to help understand the following discussions. In general, there are two methods to perform better thermal management in high-power fiber lasers: One is to generate less thermal energy during laser operation, the other is to reduce the thermal-related effects when the heat is generated.

Generating less heat has two branches, as shown in Fig. 1.2, since thermal energy can be generated either radiatively, or non-radiatively. In the former, there are two kinds of approaches: reducing the QD or adding a cooling effect to balance the radiative heating. In the latter, it is of equal importance to minimize non-radiative heating via better fiber fabrication, and to quantify the strength of non-radiative heating once a fiber is fabricated. For the “Reduce QD” branch, it is achievable by bring the pump and signal wavelength close to each other. An energy diagram is provided to the top-left corner of Fig. 1.2 to illustrate QD heating. Details of this topic which are discussed in Chapters 2 and 3. For the “Add cooling effect” branch, one method is to take advantage of an effect known as anti-Stokes fluorescence (ASF) cooling to make a radiation-balanced fiber laser (RBFL). An energy diagram to the bottom-left corner of Fig. 1.2 shows the processes in RBFL. ASF cooling in silica optical fiber was first achieved in 2020 [30], and the first RBFL was developed year later in 2021 using a similar fiber as the gain medium [31]. However, such a system suffers from relatively high threshold and low slope efficiency, and

research is still underway to optimize the system. An alternative method to introduce cooling effect is via stimulated emission by a second pumping wavelength, which is longer than the lasing wavelength. The method is known as excitation-balanced fiber laser (EBFL), and details are provided in Chapter 4. An energy diagram to the bottom-right corner of Fig. 1.2 shows the processes in EBFL. For the "Optimize fiber fabrication" branch, it is purely a material and fabrication problem as the strength of non-radiative heating will not change after the fiber is fabricated. Efforts have been continuously made from the fiber fabrication point of view to reduce the impurity levels so that the fiber suffers less from non-radiative heating [32]–[35]. In the meantime, after a fiber is fabricated, it is also important to quantify the strength of non-radiative heating, which is the "Quantify" branch and will be the main topic in Chapter 5.

In addition to reducing the heat generation, the other big branch for better thermal management is to reduce thermal-related effect, in particular TMI. As introduced above, TMI is a result of index grating formed along the fiber during laser operation, and an intuitive solution is to avoid forming such index grating by reducing the dn/dT of the fiber. As different dopants will introduce a different impact on dn/dT of the core, many material studies have been performed to examine their effect on the dn/dT in silica optical fibers [36]–[41]. Alternatively, when the dn/dT of the fiber core is smaller than that of the cladding, the fiber will be closer to single-mode operation as the temperature increase, leading to a new idea named diminished modedness with increasing temperature (DIMWIT) fiber and efforts are being made to accomplish such a fiber. Finally, the fiber can also be made with a higher thermal conductivity so that the heat can be carried away more effectively. One example is the YAG-derived fibers [42].

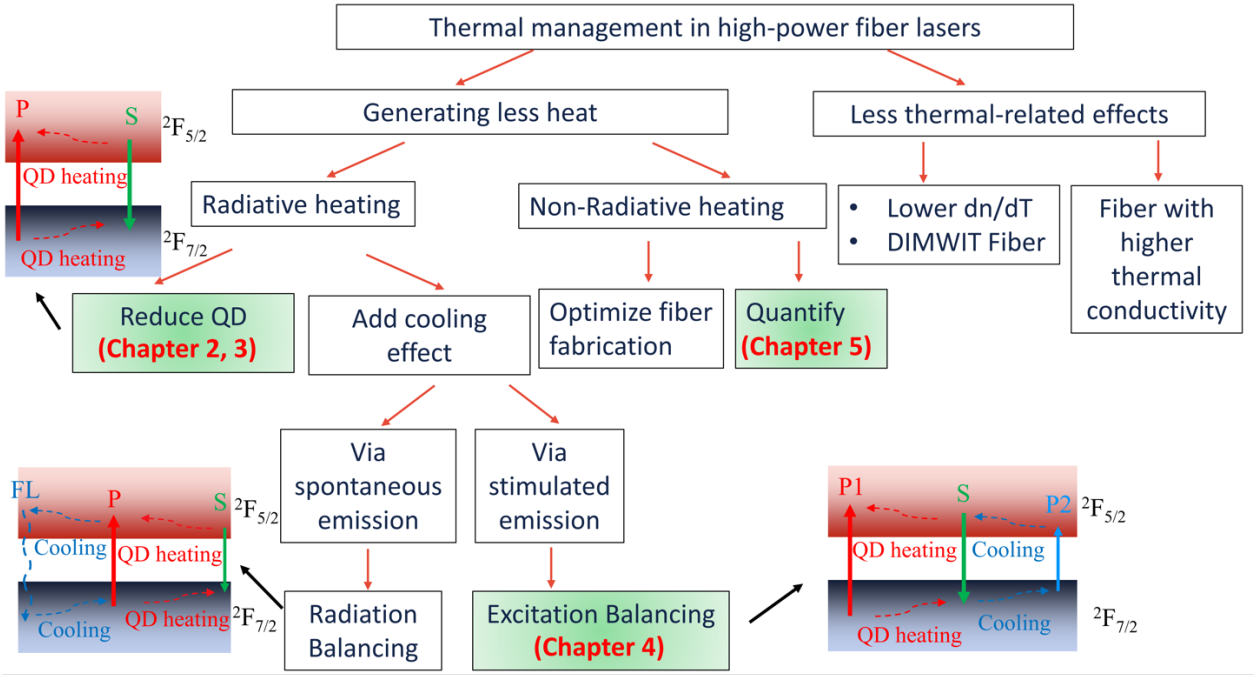

Fig. 1.2: Flowchart of the methods to improve thermal management in high-power fiber lasers. The approaches that are discussed in detail in this thesis are highlighted with the corresponding chapter numbers. The three energy diagrams represent a typical fiber laser (top-left corner), a radiation-balanced fiber laser (bottom-left corner), and excitation-balanced fiber laser (bottom-right cornor), respectively. "P" stands for pump ("P1" for pump 1 and "P2" for pump 2), "S" stands for signal, and "FL" stands for fluorescence. Cooling in the RBFL and EBFL results from the annihilation of phonons, which balances the creation of phonons.

The remainder of this document is organized as follows. Chapter 2 gives a short summary the low quantum defect fiber laser that was developed during the first two years of graduate school, which includes fiber design and characterization, experimental design, experimental results and discussion, and theoretical simulation. The system discussed in Chapter 2 serves as the base for Chapters 3 and 4. Specifically, Chapter 3 uses the laser in Chapter 2 as a seed laser in power scaling. Chapter 4 introduces an excitation-balanced approach to further reduce the quantum defect. Both chapters provide the experimental design, results, discussion, and theoretical modeling in detail. Chapter 5 discusses a measurement platform to quantify the nonradiative heating of Yb-doped fiber. However, as discussed earlier, it only serves as a

characterization platform, while attempts to reduce nonradiative heating is not within the scope of this document. Finally, Chapter 6 offers several important conclusions, and suggests future works to further optimize the systems.

CHAPTER 2: Low Quantum Defect Fiber Lasers

In this chapter, low-power (less than 1 W) and low-QD fiber lasers are discussed. First, approaches to reduce the QD in fiber lasers and reasonings behind choosing the method in this document are discussed. Then, a brief introduction of the special Yb-doped fiber is given, which is used as active medium in this chapter, as well as in Chapters 3 and 4. Then, experimental results of the low-power low-QD fiber lasers are presented, with theoretical simulations also provided to verify the experimental results.

As defined in Eq. 1.1, reducing the QD can either be achieved by increasing the pump wavelength, or by reducing the emission wavelength. The former approach is usually achieved by tandem pumping [43], which pumps the active fiber with longer wavelengths at later amplifier stages. For example, the 10 kW fiber laser commercially available at IPG photonics [7] was achieved by pumping the last-stage amplifier by fiber lasers at 1018 nm instead of laser diodes at 976 nm, which are among the most widely available pump laser diodes. However, it dramatically increases the complexity of the system since in addition to the power amplifier stage, which is discussed in detail in Chapter 3, 47 lasers (270 W @ 1018 nm) requires first making to serve as pumps to achieve a 10 kW fiber laser [44]. Another approach to reducing the QD without adding complexity to the system is to reduce the signal wavelength by selection of new host glasses such as phosphosilicates [45] and fluorosilicates [46], [47], while maintaining the 976 nm diode pumping. This approach offers a much simpler setup and opens potential for more affordable high-power lasers compared to the tandem-pumping approach. Therefore, we chose this simpler approach.

The reason to use new host glasses is that most commercial Yb-doped fibers are Yb-doped aluminosilicate fibers. In these host glasses, amplified spontaneous emission (ASE) near a local peak of the gain curve (~1030 nm, shown in Fig. 2.1 (a)) will introduce detrimental influences on laser performance, especially on the slope efficiency. On the other hand, research has shown that fibers (silica-based) co-doped with fluorine (F) or P_2O_5 renders a favorable characteristic of a blue-shift of the local peak originally at 1030 nm. This behavior is attributed to the nephelauxetic effect [48], where the ionicity of the active (Yb) ion in these fluorosilicate or phosphosilicate glasses modifies the spectroscopic properties of Yb^{3+} and results in a blue shift of the local peak mentioned above. Meanwhile, the general shape of the emission spectra is mostly preserved because the 4f subshell is not the outermost subshell in Yb^{3+} electron configuration. Instead, it is shielded by the 5s and 5p subshells and this shielding preserves 4f transitions, resulting in similar cross section line-shapes over a wide range of hosts. As a result, only very small perturbations can happen when Yb ions are in different hosts, resulting in small changees to the shape and amplitude, such as when the fiber is co-doped with F or P_2O_5.

Quantification of the emission cross section requires the measurement of fluorescence emission spectra and radiative lifetimes of the Yb dopant as indicated by the Füchtbauer-Ladenburg (F-L) formula

$$\sigma(\lambda) = \frac{1}{8\pi}\frac{\lambda^5}{\tau n^2 c}\frac{I(\lambda)}{\int I(\lambda)\lambda d\lambda} \tag{2.1}$$

where λ is the optical wavelength, τ is the fluorescence lifetime, n is the index of refraction, c is the speed of light in vacuum, $I(\lambda)$ is the emission spectral intensity for a given wavelength, and the integral corresponds to the total intensity of the emission bandwidth. To measure $I(\lambda)$, the test fiber is spliced to a fiber-coupled semiconductor laser, operating at 976 nm, as the excitation source. To collect the fluorescence signal, a multi-mode patch cable, connected to an optical

spectrum analyzer (OSA), was brought near the side of an arbitrary length of the test fiber using a precision positioning mount. The pump was operated continuous wave (CW) for the emission measurements. To measure the fluorescence lifetime τ, a short segment (< 1 mm) of fiber was end-pumped with the pump diode providing pulses. Reabsorption effects are negligible in such lengths of fiber. Then using Eq. 2.1, the emission cross section can be obtained. Normalized emission cross sections of the fluorosilicate fiber as well as the phosphosilicate fiber used in this document are shown in Fig. 2.1 (a) in comparison with a commercial aluminosilicate fiber. These fibers are the final results of significant efforts in fiber design, concentration optimization, as well as fabrication optimization. However, this is not the focus of this document and details of the fiber development can be found in [46] for fluorosilicate fiber, and [49] for phosphosilicate fiber. The most important information from the above research is that, because of the blue-shift, efficient lasing at short wavelength (~1000 nm) should be achievable without significant competition from ASE. The apparent shift comes from a more ionic (as opposed to covalent) bonding environment around the active ions (nephelauxetic effect) [50].

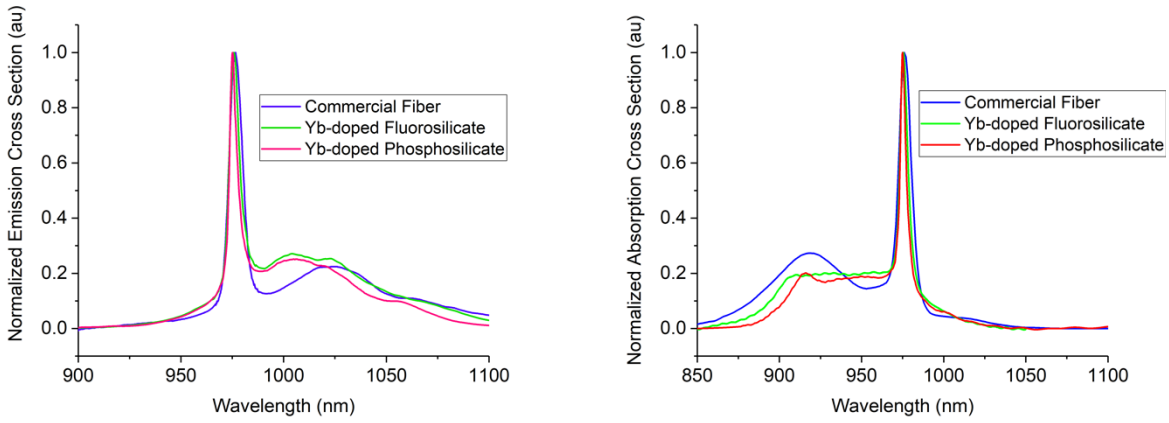

(a) (b)

Fig. 2.1: Normalized (a) emission cross section, and (b) absorption cross section for the commercial fiber, Yb-doped fluorosilicate, and Yb-doped Phosphosilicate. The absolute values are provided below.

In addition to the emission spectra, another important fiber parameter related to thermal management is dn/dT. Following the *Dong* formalism [21], the (nonlinear) coupling between modes is proportional to $\frac{(dn/dT)}{\rho \cdot c_p} \mathrm{QD} f(\Gamma_{ml}^{-1})$, where ρ is density, c_p is specific heat, and $f(\Gamma_{ml}^{-1})$ denotes a function of the damping factor, Γ_{ml}, which is proportional to the thermal diffusivity, D, given by $D = \kappa/\rho c_p$, where κ is the thermal conductivity. Obviously, the smaller the dn/dT of the fiber, the higher the TMI threshold attained. Luckily, when the fiber (silica) is co-doped with F or P_2O_5, the dn/dT will decrease compared to that of the silica, as shown in previous work in [46] for fluorosilicate fiber, and [51] for phosphosilicate fiber. Therefore, in combination with the lower QD, Yb-doped phosphosilicate and fluorosilicate are promising choices for high-power fiber lasers.

Furthermore, phosphosilicate and fluorosilicate fibers have other similar spectroscopic behaviors. The fluorescence lifetime of both fibers are longer than commercial Yb fibers (~800 μs) because P_2O_5 and F are known to promote a longer lifetime as discussed in previous works [46], [49]. Specifically, the lifetime for fluorosilicate and phosphosilicate fibers used here are determined to be 1.3 ms and 1.48 ms, respectively. Because of the difference in fluorescence lifetime, as indicated by Eq. 2.1, the peak values of the emission cross sections (zero-phonon line near 975 nm) are different in these fibers. Specifically, commercial fibers have a value of 2.5 pm^2, fluorosilicate has a value of 1.75 pm^2, and phosphosilicate has a value of 1.73 pm^2. To quantify the Yb absorption cross sections ($\sigma_a(\lambda)$), a broadband white-light source was coupled into a known length of test fiber that has been spliced between two passive fibers. The spectra were then measured before and after passing through the test fiber and Beer's law was applied to acquire the absorption spectrum ($\alpha(\lambda)$, in units of m^{-1}). Then, $\sigma_a(\lambda)$ can be determined by $\alpha(\lambda)/\Gamma\rho$. The peak absorption cross sections are the same as the corresponding peak emission

cross sections, while the normalized absorption cross sections for the commercial, fluorosilicate and phosphosilicate fibers are shown in Fig. 2.1 (b). From the figure, it can be observed that both the fluorosilicate and phosphosilicate fibers exhibit a similar region of wide and very flat bandwidth on the blue side of the zero-phonon line, which resembles fluoride and phosphate glasses[46], [49]. Finally, during the fiber fabrication, Al^{3+} is usually added to increase the Yb quenching concentration as discussed in [30]. While adding Al^{3+} to silica will increase the refractive index, potentially making the fiber multi-moded, co-doping of Al_2O_3 and P_2O_5 will form $AlPO_4$ in the drawing process, which has a lower refractive index than that of the silica [36] and therefore can be used to perform NA control.

After discussing the fiber behaviors, Yb-doped fluorosilicate fibers are used as the active medium to construct a simple Fabry-Perot (FP) cavity laser. A diagram of the experimental setup is shown in Fig. 2.2. Specifically, A commercial 976.6nm single-mode fiber-coupled diode laser was used as the pump. A matched pair of fiber Bragg gratings (FBGs) were used to construct the cavity. Specifically, FBG 1 and FBG 2 have 99.02 % and 38.34 % reflectivity at 985.7 nm, respectively. An isolator was placed between the pump and the cavity to avoid reflections from the cavity FBGs destabilizing the pumping wavelength. According to Eq. 1.1, the QD is calculated to be 0.92%. Finally at the output, a straight cleave is made and the output powers are characterized by a power meter while the output spectra are characterized by an optical spectrum analyzer (OSA).

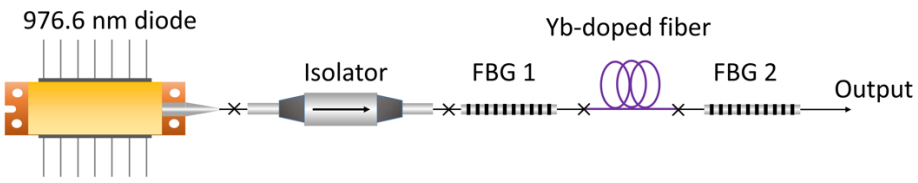

Fig. 2.2: Experimental setup for the Fabry-Perot (FP) cavity laser.

In order to optimize the lasing conditions and slope efficiencies, experiments started with a relatively long piece of Yb-doped fiber (around 20 cm), which then was shortened in roughly 1.5 cm increments to a final length of ~10 cm. For each increment, the output spectrum and the laser output power versus pump power was measured. Figure 2.3 (a) is a representative example of the spectral measurements for 976.6 nm pumping using five different active fiber lengths. Figure 2.3 (b) provides the slope efficiency measured for the different fiber lengths, and for completeness, figure 2.3 (c) shows an example lasing data (at the maximum slope efficiency) where the slope efficiency is subtracted, including a comparison to theoretical results. Note that the laser was quantified with more than five active fiber lengths, and Fig. 2.3 only selected the representative points for visual clarity. The model used for simulation is a well-established one [52] and the code for simulation is provided in the Appendix A.

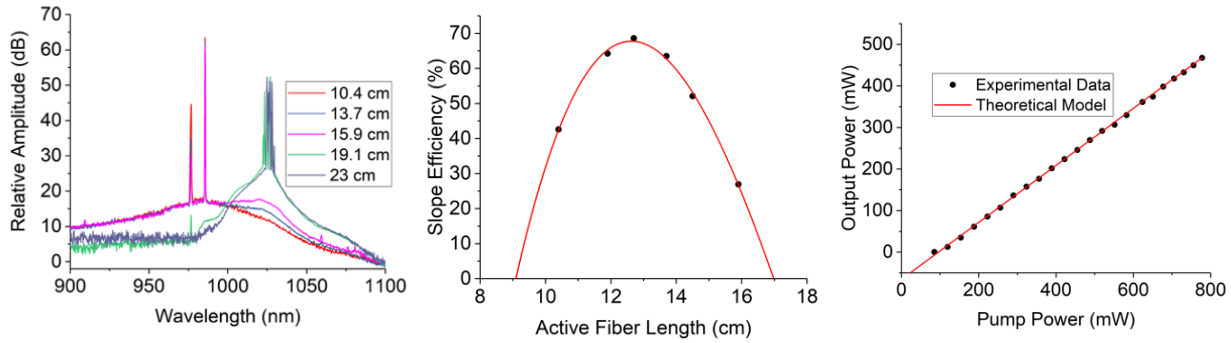

(a) (b) (c)

Fig. 2.3: (a) Example output spectra with different Yb-doped fiber lengths, (b) slope efficiency with different fiber lengths (the curve only serves as visual aid), (c) experimental and theoretical output power versus launched pump power at the near-optimized active fiber length.

Figure 2.3 shows that the spectra and slope efficiencies vary significantly with active fiber length. With a very short length (for example 10.4 cm), the pump power is not absorbed completely and much of it leaks from the cavity, therefore degrading lasing efficiency. When the fiber is longer than optimal, near-complete pump absorption occurs. However, the non-inverted

length of fiber imparts reabsorption to the signal wavelength, which leads to a greater likelihood of ASE, thereby also resulting in a degradation of the slope efficiency. With even longer fiber lengths, ASE ultimately dominates the lasing process and self-oscillation occurs near the ASE peak wavelength (~1022 nm).

It is obvious that greater pump absorption will increase the slope efficiency, while greater ASE will decrease the slope efficiency. Therefore, with decreasing length from ~20 cm, the slope efficiency is expected to increase at first as the ASE level is reduced, reach an optimal point, and then decline as incomplete pump absorption takes place. This is precisely the trend observed in Fig. 2.3 (b). The power data for the near-optimal fiber length (12.8 cm for 976.6 nm pumping) is shown in Fig. 2.3 (c). The corresponding slope efficiency is measured to be 68.7%.

The slope efficiency does not reach the theoretical quantum limit (1 - QD) mainly because of the splice losses between the Yb-doped fiber and the cavity FBGs (written into HI 1060 fiber) as well as background loss. Background loss (~ 1.36 dB/m) is mainly due to scattering and impurity absorption, which is something to be further optimized with the molten-core method. A detailed fabrication process of such a method is discussed in Chapter 3. While splice loss (~0.16 dB/splice) is influenced mainly by spatial mode competition within the cavity, with the observation that the output power may change significantly when bending or twisting the fiber. This, coupled with some variation of splice loss each time, leads to the data observed in Fig. 2.3 (b). Additionally, a reduction in the fiber numerical aperture should render improved splice quality. Modeling results indicate that further improvements to splice quality, optimization of FBG reflectivity and concomitant fiber length, and slope efficiencies approaching the quantum limit are feasible. However, low QD operation is of much more significance in any subsequent power-amplifier stages, as is the main topic in Chapter 3. Here, the main idea is to

show low QD operation in these fibers are feasible. The examples here are using fluorosilicate as the gain medium, while very similar results are obtained when using phosphosilicate.

As a summary, in this chapter, on the use of phosphosilicate and fluorosilicate Yb-doped fiber to reduce QD heating is discussed. Properties of the two candidate glasses are introduced, which will serve as the gain medium in the lasers and amplifiers in this chapter as well as in the following two chapters. A low-power low-QD fiber laser is constructed using the fluorosilicate as a demonstration, and slope efficiency close to 70% is achieved with careful optimization of the active fiber length. This laser will serve as a base for the further development in Chapter 3 and Chapter 4, as will show that the setup in Fig. 2.2 will be part of a larger overall experimental setup in both chapters.

CHAPTER 3: Power Scaling of Low Quantum Defect Fiber Lasers

In Chapter 2, a low-power low-QD fiber laser is demonstrated with nearly 70% slope efficiency, giving evidence that low-QD operation using Yb-doped fluorosilicate fiber is feasible. As discussed in the previous chapter, because Yb-doped phosphosilicates exhibit very similar spectroscopic characteristics, it is reasonable to predict that similar behaviors are expected if the Yb-doped phosphosilicate fiber is used in a setup similar to that demonstrated in Chapter 2. In this chapter, a master oscillator power amplifier (MOPA) is built to scale the power up while maintaining the low-QD operation. First, the reason to introduce a MOPA is discussed. Second, to enable MOPA operation, the concept of double-clad fiber is introduced and a typical MOPA setup using it is shown. Third, experimental results of a MOPA using double-clad Yb-doped fluorosilicate fiber are shown and reasons for the failure of this demonstration are discussed. Fourth, results on using double-clad Yb-doped phosphosilicate fibers are discussed, with modeling efforts presented along the way. Fifth, a commercial Yb-doped aluminosilicate fiber was used in the same setup as a comparison. Finally, the possibility of dual-end pumping was examined with simulation.

As discussed in Chapter 2, some of the high-power fiber "lasers" are instead a combination of one seed oscillator and multiple stages of amplifiers, known collectively as a MOPA. There are several reasons why a MOPA is preferable to a simple Fabry-Perot (FP) cavity laser. First, for a FP laser, depending on cavity design, there is the possibility that the intensity inside the cavity is much higher than that of the output, giving rise to an increasing possibility of nonlinear effect in the cavity. Second, the beam quality from the FP cavity laser will be much worse than that of the MOPA system because the latter could be seeded with a signal of

extremely high beam quality and slowly increase the power over several amplifier stages. The beam quality can be maintained with careful mode matching and launch conditions. In this document, therefore, a MOPA-based high-power fiber laser is pursued.

Generally speaking, three things are required for a MOPA to work. A low-power signal, a high-power pump, and an active medium allowing the energy to transfer from the pump to the signal. In our case, a low-power laser similar to the one in Chapter 2 will serve as the signal, one or a few high-power laser diodes will serve as the pumps, and the Yb-doped fluorosilicate or phosphosilicate will serve as the active medium. In a conventional fiber, most light is confined to the core, which possesses a higher refractive index. At the same time, it is also within the core that all the dopants (including Yb^{3+}) are found, which allows for light amplification to happen. The low power signal usually has a good beam quality and can be confined in the core. For the high-power laser diodes, however, because of the limited available brightness from them, it is very challenging to confine enough power within the small core of the fiber, so that it is hard to core-pump the system. Luckily, a design known as double-clad fiber was first proposed in 1974 [53] and was widely used in high-power lasers after its first demonstration in 1988 by E. Snitzer [3]. The main difference between a conventional fiber and a double-clad fiber is, instead of using a high-index polymer as the buffer material, as in conventional fibers, double-clad fiber possesses a low-index buffer so that the cladding of the fiber also works as a waveguide, enabling it to confine light. Figure 3.1 (a) shows the cross section of a double-clad fiber. By using this structure, the low brightness pump light can be confined in the waveguide formed by the cladding and the buffer, whereas the signal can still be confined in the core. Since the pump light also partially propagates in the core, where it can be absorbed by Yb^{3+}, after a certain length the pump power will be transferred to the signal power so that the signal is amplified as desired.

Such a process is illustrated in Fig. 3.1 (b). It should be noted that the cladding is highly multi-moded. Many of these do not have overlap with the fiber core and follow a helical trajectory in a region outside of the core. As a result, pump powers within these modes are wasted because they will never be absorbed by the Yb^{3+} ions in the core. To solve this problem, the cladding of a double-clad fiber is usually shaped, such as with a D-shape (in Fig. 3.1 (a)), a hexagonal shape, on octagonal shape, etc., so that most of the modes mentioned above can be eliminated because of the broken circular symmetry.

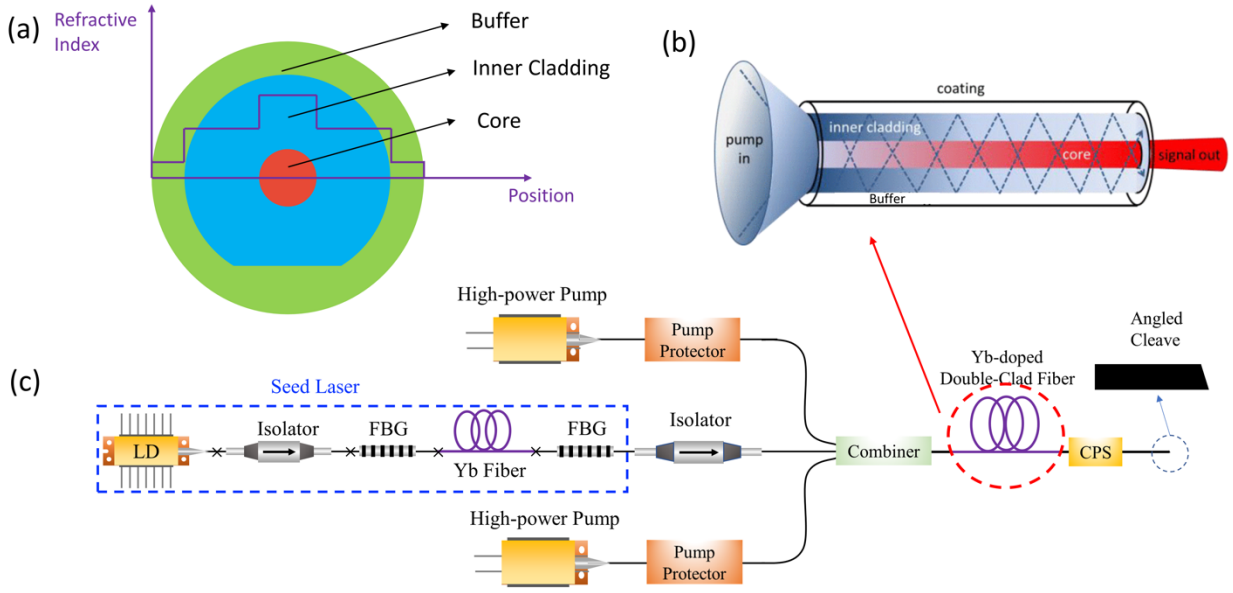

Fig. 3.1: (a) Cross section of a D-shaped double-clad fiber, (b) Illustration of the operation of pump and signal using double-clad fiber [54], (c) Experimental setup for the MOPA-based fiber laser. LD: laser diode, FBG: fiber Bragg grating, CPS: cladding power stripper. Each laser diode pump can provide up to 10 Watts of power.

Next, Fig. 3.1 (c) shows a MOPA-based setup built in the lab. The seed laser is exactly the same as described in Chapter 2 (Fig. 2.2), the only difference is that the laser wavelength varies by changing the FBGs in the setup, the reason of which is discussed later in this chapter. An isolator is placed after the seed laser for two purposes: First, to avoid any light entering into

the seed laser and destroy the components inside, and second, to avoid feedback from the components in the seed laser that contributes to self-lasing in the system. Two high-power laser diodes are used to pump the system, with a pump protector spliced afterward to filter out any possible light from the system that may enter the laser diode and affect its operation or even damage it. Next, pumps and signal light collectively go into the combiner, and are combined together into a passive double-clad fiber. It is necessary to point out that the fiber types in the combiner are selected to match the optical modes in its corresponding connecting fibers as well as possible. For example, the fiber connecting to the isolator is the same type (HI1060, Corning) as the fiber pigtail of the isolator. The fibers connecting the high-power pumps within the combiner are 105/125 multi-mode fibers, which is the same as the fiber pigtail of the pumps. The combiner output is a double-clad fibers, whose core and cladding sizes are selected to best match that of the Yb-doped double-clad fiber. After the Yb-doped double-clad fiber, a cladding power stripper (CPS) is added to strip the residual pump light. Finally, at the output, an angle cleave was made to avoid any feedback into the system.

Next, a double-clad fluorosilicate fiber was developed. Similar to the fluorosilicate fiber described in Chapter 2, the fiber was fabricated using the molten core method [55]. Specifically, a precursor material in the form of a powder mixture of YbF_3 (5%), SrF_2 (71.25%), and Al_2O_3 (23.75%) was inserted into a pure silica capillary. The tube is D-shaped previously so that the fiber fabricated from it will also be D-shaped. It can be observed that in addition to the Yb and F, Sr and Al are also introduced during the fabrication. The reason to introduce Sr is that SrF_2 is a convenient way to dope F in the core, and Al_2O_3 doping is used to assist with material miscibility when the core is molten and avoid phase separation (or in other words, alumina promotes glass

formation through inhibition of "clump" formation). Then this preform was heated to ~2000 °C, whereby the core precursor mixture becomes molten, and the pure silica cladding draws into fiber. As the fiber cools down, the core leads to a kinetically hindered glassy state in the resulting fiber. The drawn optical fiber possesses a core diameter of 20 μm, a cladding diameter of 125 μm, and a low-index coating diameter of 250 μm.

The entire process is the same as that used to develop the Yb-doped fluorosilicate fiber used in Chapter 2, with three key differences: (1) the shape of the tube (D-shape), (2) the core size of the fiber (20 μm here, whereas the fiber in Chapter 2 has a 9 μm core), and (3) the low-index coating. The reason to include the D-shape and low-index coating has already been discussed above. The reason to use a bigger core size is increased pump absorption. Pump absorption is proportional to an overlap between the pump field and the core, which approximately is the ratio of the core to cladding areas. As such, a bigger core is beneficial for more efficient pump absorption. Simulations results of two fiber, with the only difference to be core size, is discussed in detail later in this chapter. The fabricated fiber, unfortunately, was found to have several mechanical problems relating to its stability. Namely, due to the larger core/cladding ratio used in the double-clad fiber, cracks formed when a common cleave was applied to the fiber. This was found to be an insurmountable problem, occurring inevitably when the system is built, or the fiber is tested. The reason the cracks form originates from the large difference in thermal expansion between the core and the cladding. During the cool-down process in the fiber fabrication, tensions are formed between the core and cladding. Then, when the fiber is cleaved, the tensions are released, there is an equilibrium contraction of the core, and cracks are formed. An example image of the crack is shown in Fig. 3.2 (a), which might result in several problems, including damage to the fiber facet, unwanted back-reflection into the system,

and deterioration of the output beam quality. Meanwhile, the D-shaped cladding can be clearly observed in Fig. 3.2 (a).

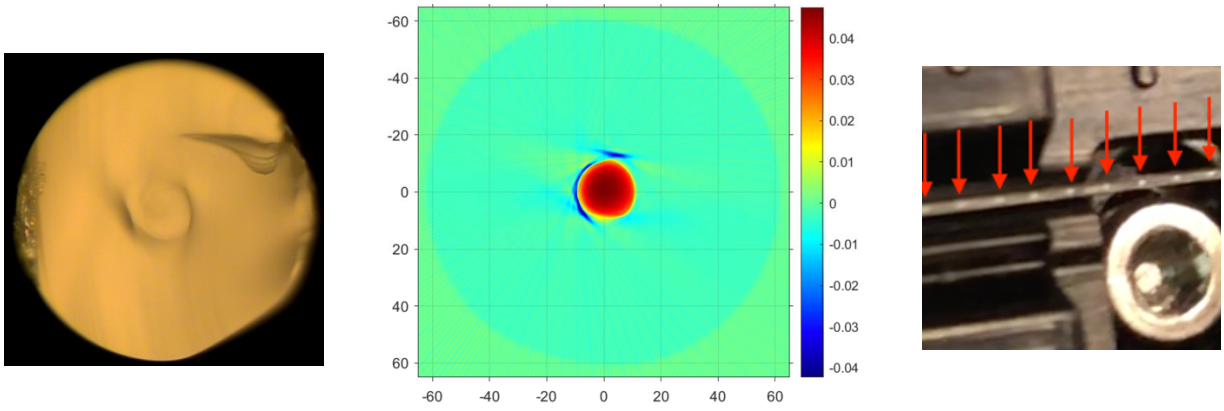

(a) (b) (c)

Fig. 3.2: (a) An image of the Yb-doped double-clad fiber end, (b) Refractive Index Profile of the Yb-doped double-clad fiber end, (c) Spiral cracks in fiber.

Another method to observe the crack is by measuring the refractive index profile (RIP) of the fiber. The RIP was measured using a form of spatially resolved Fourier Transform spectroscopy [56] as a service (Interfiber Analysis, Sharon, MA). The result is shown in Fig. 3.2 (b). Note that the forming of the cracks is random and therefore are different for every cleave that is made. Since the Fig. 3.2 (a) and Fig. 3.2 (b) are two separate measurements, there is no relation between the results in these two figures. However, cracks are formed every time that a cleave is made. As can be observed in Fig. 3.2 (b), the fiber possesses a core of ~20 μm and cracks are found near the boundary of the core and the cladding, resulting in a vast change of the refractive index. Since the crack is very close to the core, it will result in significant scattering loss, which is generally not desirable. Note that the shape and position of the cracks are consistent with contraction of the core.

Although cracks are formed after a mechanical cleave, this can still be avoided by polishing the fiber facet. However, another kind of crack can completely damage the fiber, which

is known as a spiral crack. Unlike the cracks discussed above that only impact the fiber facet, a spiral crack propagates along the fiber and leaves a trace of periodic defects along the fiber. The formation of spiral cracks can stem from many reasons, including non-uniform tensile and bending loads on the fiber, environmental effects such as humidity and temperature, or a sudden release of fiber interior pressure [57]. In our case, the most likely reason is that after one fiber cleave, the tension release is so strong that it causes the crack to propagate along the fiber. Unfortunately, it propagated the entire fiber spool and damaged all the available fiber from a single draw of ~30 meters. A real image of the spiral cracks is shown in Fig. 3.2 (c), from which the periodic structures can be clearly observed. In summary, because of the failure of the Yb-doped double-clad fluorosilicate fiber, low-QD operation from it has not yet been achieved and requires further development. A change in the fiber draw temperature is expected to improve fiber mechanical stability.

Next, Yb-doped double-clad phosphosilicate fibers are developed. Unlike the fluorosilicates, phosphosilicate fibers can be fabricated with the well-known modified chemical vapor deposition (MCVD) method, during which the core is doped more slowly compared to the molten core method and less stress is formed during the fabrication process. Under the same cleaving conditions, no cracks like those shown in Fig. 3.2 are observed, proving the high-quality of the fiber. However, because of the limited available glass tubes, the fabricated fiber has a relatively smaller core (~14 μm diameter) and the cladding is not shaped. This significantly influenced the pump absorption process as discussed earlier, however, it serves as a proof-of-concept fiber to demonstrate low-QD operation in Yb-doped phosphosilicate fibers. Further fiber design and optimization are discussed later in this chapter.

Using the same spatially resolved Fourier Transform spectroscopy method, the RIP of the fiber is measured as a service, and the result near the core is shown in Fig. 3.3. A typical dip in refractive index near the core center is observed, the reason of which is that P_2O_5 is volatile at high temperatures so that some volatizes from the inner surface during the preform consolidation process and leaves a low-index area near the core center. This dip is taken into consideration when the fiber modes are calculated. There are also some structures near the core-cladding edge; the reason for them is a deposition of a pure SiO_2 layer so that there is a pristine and pure surface on which to deposit the core material. It also ensures that the small portion of light propagating in the cladding is not affected by any contaminants or surface imperfections that may have been present in the substrate tube.

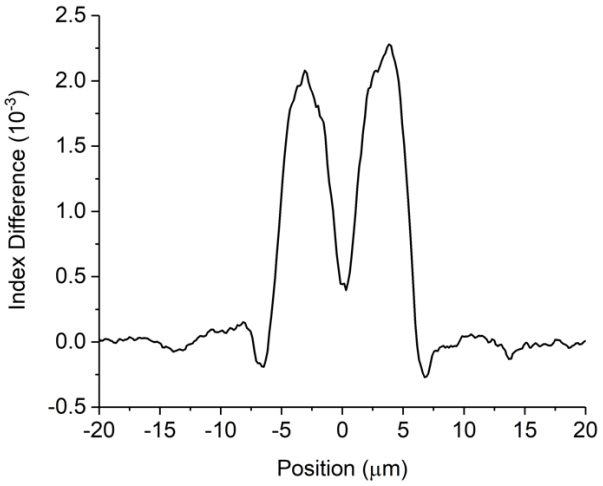

Fig. 3.3: Refractive index profile for the double-clad Yb-doped phosphosilicate fiber.

Next, a setup similar to that in in Fig. 3.1 is built with two differences. First, the cladding power stripper is not placed in the setup because it is important to quantify the pump leakage as the double-clad fiber is not yet shaped. Second, the Yb-doped double-clad fiber is not looped in a circle. Instead, it is looped in a kidney shape, which is helpful for pump absorption. As discussed in previous works [58], such coiling assists with mode scrambling in the cladding. However, as

will be shown later in this chapter, even under this method there is >50% pump leakage from the fiber, emphasizing the importance of cladding shaping. To start, an operating wavelength of 985.6 nm as in Chapter 2 was selected. However, after attempting to optimize the active fiber length and analyzing the results in a way similar to what was done in Chapter 2, it is found that there is no suitable fiber length to efficiently amplify the 985.6 nm signal. The main reason is that the fiber has a relatively small core so that the intensity of the ASE is higher and adds great competition with the signal gain. More discussion on the fiber geometry optimization is provided later in this chapter. An example spectrum with the 985.6 nm signal is provided in Fig. 3.4, which corresponds to an active fiber length of 2.85 m and a signal input power of 200 mW. From the figure, it can be observed that the power at the signal wavelength is much smaller compared to that in the ASE. Making the active fiber length longer or shorter from this point either leads to even stronger ASE or very small signal power. Therefore, longer signal wavelengths are investigated (994.5 nm and 1005 nm), which is enabled by simply changing the FBG pairs for the seed laser. With the same active fiber length (2.85 m) and the same signal input power (200 mW), the corresponding output spectra are also shown in Fig. 3.4. Obviously, a longer signal wavelength is beneficial for more efficient signal amplification. On the other hand, it also represents a higher QD, which is in opposition to the stated goals in this document. To balance the above two situations, a term ξ is defined as

$$\xi = \frac{\int_{\lambda_{s1}}^{\lambda_{s2}} I(\lambda)\, d\lambda}{\int_{\lambda_{ASE1}}^{\lambda_{ASE2}} I(\lambda)\, d\lambda - \int_{\lambda_{s1}}^{\lambda_{s2}} I(\lambda)\, d\lambda} \times \frac{1}{\mathrm{QD}} \tag{4.1}$$

in which $I(\lambda)$ is the emission spectrum in linear scale, λ_{s1} and λ_{s2} the lower and upper bound for signal wavelength and λ_{ASE1} and λ_{ASE2} is the lower and upper bound for ASE signal. The specific settings for λ_{s1}, λ_{s2}, λ_{ASE1} and λ_{ASE2} are summarized in Table 3.1, with the

corresponding ξ also calculated and summarized. The first term in ξ represents the ratio of signal power to the ASE power, and the second term represents the QD. Therefore, the bigger the value ξ is, the more desirable the system is. From the results, it can be concluded that a signal at 1005 nm is the best among the three cases and therefore will be further investigated in detail.

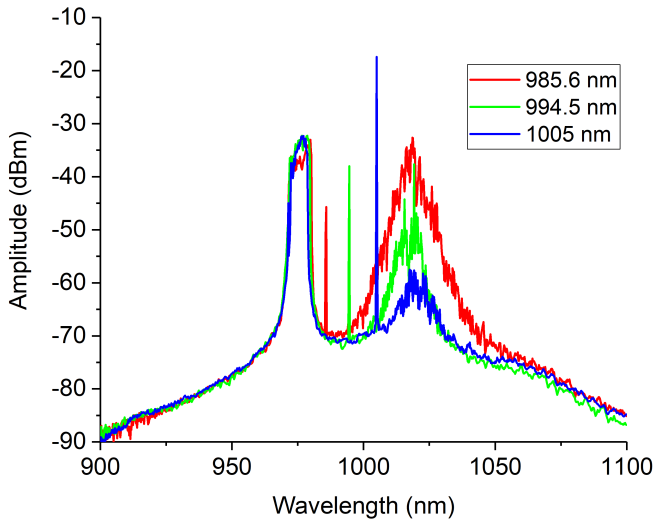

Fig. 3.4: Output spectra with signal wavelength of 985.6 nm, 994.5 nm, and 1005 nm. The active fiber length used to obtain the spectra is 2.85 m. The signal input power is 200 mW.

Table 3.1: Setting for the λ_{s1}, λ_{s2}, λ_{ASE1} and λ_{ASE2}, and the corresponding ξ under the three signal wavelength settings (~985 nm, ~995 nm, and ~1005 nm)

Signal wavelength	λ_{s1} (nm)	λ_{s2} (nm)	λ_{ASE1} (nm)	λ_{ASE2} (nm)	ξ
985.6 nm	985	986	985	1100	0.39
994.5 nm	994	995	985	1100	15.90
1005 nm	1004.5	1005.5	985	1100	8255.74

Next, a similar active fiber length optimization is required as in Chapter 2 because of the trade-off between pump absorption and ASE. To assist the process, a modified version of the model based on rates equations [52] is constructed. The main modification is that ASE is taken into consideration so that the model can resolve the competition between the signal amplification and ASE. In most of the previous modeling efforts considering ASE [59], [60], it is assumed that ASE is only at one single wavelength and the strength of it is simulated with the emission and

absorption cross sections at that single wavelength. However, this is not accurate because ASE has a broad spectrum and cross sections can vary significantly depending on the wavelength. Therefore, it is more accurate to break the ASE spectrum into "slices" and calculate the evolution of each slice independently. Similar to [52], the evolution of pump power, signal power, and power at each ASE slice (noted by i) with the fiber length L can be calculated by

$$P_P{}^{out} = P_P{}^{in} \times \Gamma_{shape} \times \exp\{-\alpha_P \mathrm{L} - \alpha_P{}^{bg}\mathrm{L} + \frac{P_P{}^{in} \times \Gamma_{shape} - P_P{}^{out} + P_S{}^{in} - P_S{}^{out} + \sum_i (P_A{}^{in^i} - P_A{}^{out^i})}{P_p{}^{sat}}\} \quad (4.2)$$

$$P_S{}^{out} = P_S{}^{in} \times \exp\{-\alpha_S \mathrm{L} - \alpha_S{}^{bg}\mathrm{L} + \frac{P_P{}^{in} \times \Gamma_{shape} - P_P{}^{out} + P_S{}^{in} - P_S{}^{out} + \sum_i (P_A{}^{in^i} - P_A{}^{out^i})}{P_s{}^{sat}}\} \quad (4.3)$$

$$P_A{}^{out^i} = P_A{}^{in^i} \times \exp\{-\alpha_A{}^{i}\mathrm{L} - \alpha_A{}^{bg^i}\mathrm{L} + \frac{P_P{}^{in} \times \Gamma_{shape} - P_P{}^{out} + P_S{}^{in} - P_S{}^{out} + \sum_i (P_A{}^{in^i} - P_A{}^{out^i})}{P_A{}^{sat^i}}\} \quad (4.4)$$

in which the subscript P stands for pump, subscript S stands for signal, and subscript A stands for ASE. P^{out} stands for the output power, P^{in} stands for the input power. Γ_{shape} is the pump absorption shaping factor, which equals to 1 if the outer cladding of the double-clad fiber is shaped, meaning that all the pump can be absorbed. In our case here, however, Γ_{shape} is not 1 and serves as a fitting parameter, α is the absorption coefficient and can be calculated by

$$\alpha = \rho \sigma_{ab} \Gamma \quad (4.5)$$

in which ρ is the Yb^{3+} doping concentration, σ_{ab} is the absorption cross section, and Γ is the overlap integral. For the pump, Γ can be estimated by the area of the core divided by the area of the cladding. For the signal and the ASE, on the other hand, Γ is calculated by

$$\Gamma = \frac{\int_0^{2\pi}\int_0^{r_{core}} rE^2 dr d\theta}{\int_0^{2\pi}\int_0^{\infty} rE^2 dr d\theta} \quad (4.6)$$

in which r_{core} is the core radius and E is the electric field mode in the fiber, which can be determined by an in-house mode solver. α^{bg} stands for the background loss of the fiber, which

can be considered to be negligibly small compared to α if the fiber is fabricated with MCVD. However, if the fiber is fabricated with the molten-core method, this number will become bigger and must be taken into consideration accordingly. Finally, P^{sat} represents the saturation power, which is calculated by

$$P^{sat} = \frac{A_{eff}}{\Gamma\tau(\sigma_{ab} + \sigma_{em})}\frac{hc}{\lambda} \tag{4.7}$$

in which A_{eff} is the mode effective area at the corresponding wavelength, τ is the upper state lifetime, σ_{em} is the emission cross section, h is the Plank's constant, c is the speed of light, and λ is the wavelength.

Obviously, Eqs. 4.2 - 4.4 are coupled equations and the analytical solution is ambiguous especially if the ASE is broken into more and more slices. Luckily, this can be overcome by modern software such as MATLAB. The number of slices for ASE is next to decide. On one hand, a finer step renders a more accurate simulation. On the other hand, a finer step also increases the number of coupled equations to be solved and therefore extends the simulation time. Currently, ASE is divided into 10 pieces and so that 12 coupled equations are required to be solved for one parameter input (${P_p}^{in}$, ${P_s}^{in}$, ${P_A}^{in}$, and L).

First, to determine the optimized fiber length, a simulation is run with a fixed ${P_p}^{in}$ = 16.85 W, ${P_s}^{in}$ = 0.2 W, and total ${P_A}^{in}$ = 3.73×10^{-5} W. The ratio between the 10 steps of ASE is determined by integration of the input spectra from the seed laser at each step. Then, L is looped and at each L, ${P_p}^{out}$, ${P_s}^{out}$, and the total ${P_A}^{out}$ is calculated and a summary is shown in Fig. 3.5.

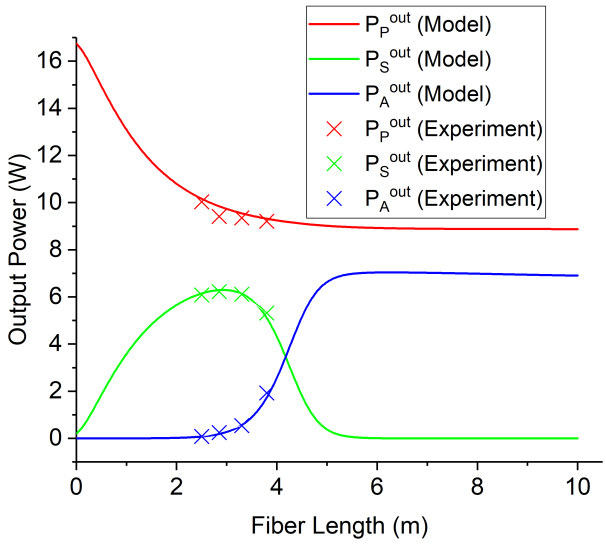

Fig. 3.5: Simulated and experimental output powers with P_p^{in} =16.85 W, P_s^{in} = 0.2 W, and total P_A^{in} = 3.73×10^{-5} W at varying active fiber lengths. The four lengths used in the experiment are 2.5 m, 2.85 m, 3.3 m, and 3.8 m.

Figure 3.5 shows that with 16.75 W of pump input, roughly half of the power leaks out. The main reason is that the cladding is not shaped so there are some high-order modes that do not have an overlap with the fiber core. The kidney shape helps to increase the absorption, but still cannot make Γ_{shape} equal to one. For the signal power, as expected, it first increases with the fiber length since more pump power is absorbed and the signal can be more greatly amplified. The maximum is reached when the fiber length equals 2.92 m. Beyond this point, ASE becomes increasingly stronger and eventually takes over the signal amplification. Experimentally, four different fiber lengths are used near the optimized length, and the corresponding output powers are measured and shown as the crosses in Fig. 3.5. The experimental results match the model well. At these four fiber lengths, the corresponding output spectra under the same parameter settings in the simulation are collected and shown in Fig. 3.6. From the figure as well as the simulation results, it can be observed that the active fiber length is critical and only several tens of centimeters may change the system from efficiently amplifying to excessive ASE.

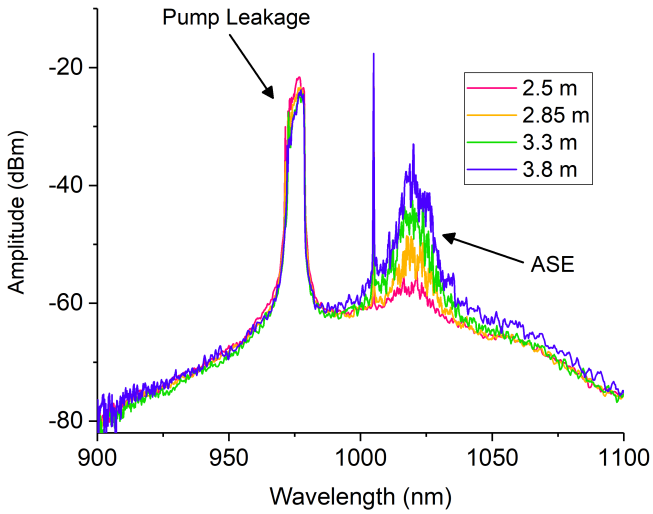

Fig. 3.6: Output spectra with different active fiber lengths with P_p^{in} = 16.85 W, P_s^{in} =0.2 W, and total P_A^{in} = 3.73×10^{-5} W.

Finally, a simulation was run using a fix length of active fiber (2.85 m) and with appropriate looping so that the pump power versus output powers can be simulated. The results are shown in Fig. 3.7 (a), with the experimental results under the same settings also presented. Figure 3.7 (a) shows that the model fits well with the experimental results. However, the linear fit is not perfect since the experimental result itself is not linear. The main reason for this is the shift of the pump wavelength as the operating current is changed. This is not the case for the low power laser diode used in Chapter 2 because its wavelength is stabilized by a FBG written into its fiber pigtail. Here, for the high-power laser diode, no wavelength-stabilization is performed and because the temperature of the laser diode will increase with increasing output power, the wavelength will gradually shift towards the red side. An example of the pump output spectrum is shown in Fig. 3.7 (b). At the maximum power (16.75 W), the output wavelength is 976 nm. However, with lower powers, the pump wavelength is shorter than 976 nm and therefore pumping where the Yb^{3+} has different emission and absorption cross sections. In the simulation,

however, it is assumed that the pump wavelength is locked at 976 nm, which results in the difference between the simulation and experimental results as observed in Fig. 3.7.

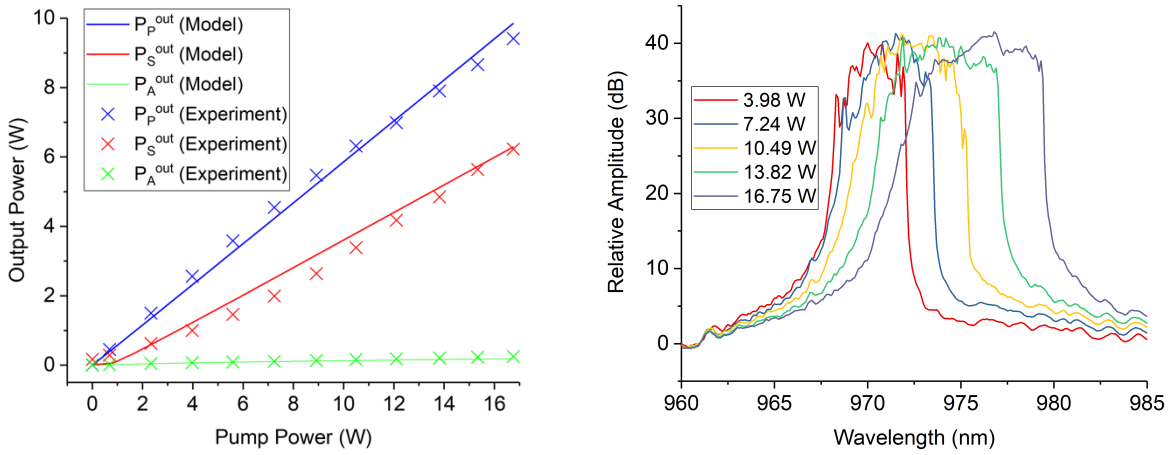

(a) (b)

Fig. 3.7: (a) Pump leak-out power ($P_p{}^{out}$), signal output power ($P_s{}^{out}$), and total ASE output ($P_A{}^{out}$) versus pump power with 2.85 m of active fiber length, (b) Pump spectra at five different power settings.

Finally, using the experimental data shown in Fig. 3.7 (a), signal output power vs absorbed pump power can be obtained and is shown in Fig. 3.8. A linear fit is performed and indicates a slope efficiency of 87.4%. This gives evidence that efficient amplification is feasible if more efficient pump absorption can be achieved in the fiber.

Up to this point, many experimental and simulation evidence is provided to show that low-QD operation using double-clad phosphosilicate fiber is feasible. However, the fiber used in previous discussions may not be optimized in terms of core size and cladding shape. Therefore, it is necessary to discuss the fiber geometry optimization. While it is not realistic to fabricate fibers with a lot of geometries and find an optimized one, since the previous model shows great

agreement with the experimental results, a simulation on different fiber geometries can be performed to assist the fiber design process. Details are provided next.

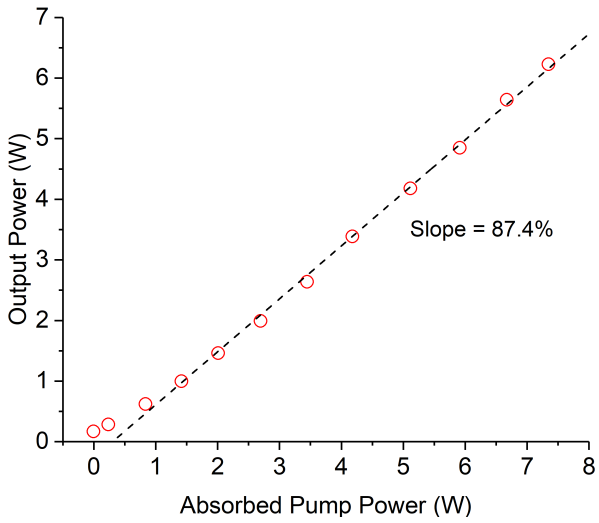

Fig. 3.8: Output power versus absorbed pump power with 2.85 m of active fiber.

First, simulations are performed with the same fiber geometry as above, but with a shaped cladding so that Γ_{shape} is 95% instead of 47 %. The reason that Γ_{shape} is not 100% is that even with a shaped cladding, those higher-order modes that do not have an overlap with the fiber core are not fully eliminated and 95% is a typical number for commercial double-clad Yb-doped fibers. Under this condition, and a maximum pump power of 20 W, the simulated pump, signal, and ASE power are shown in Fig. 3.9 (a). From the results, it can be observed that compared to Fig. 3.5, a higher percentage of the pump power is absorbed as a result of the bigger Γ_{shape}. However, at the optimized fiber length, only ~10 W of signal power is achieved as a result of the strong competition from the ASE. Specifically, at 1.6 m, a maximum of 9.83 W of signal power is achieved but at the same time, 2.33 W of ASE also presents. Beyond this fiber length, signal power decreases and ASE keeps growing.

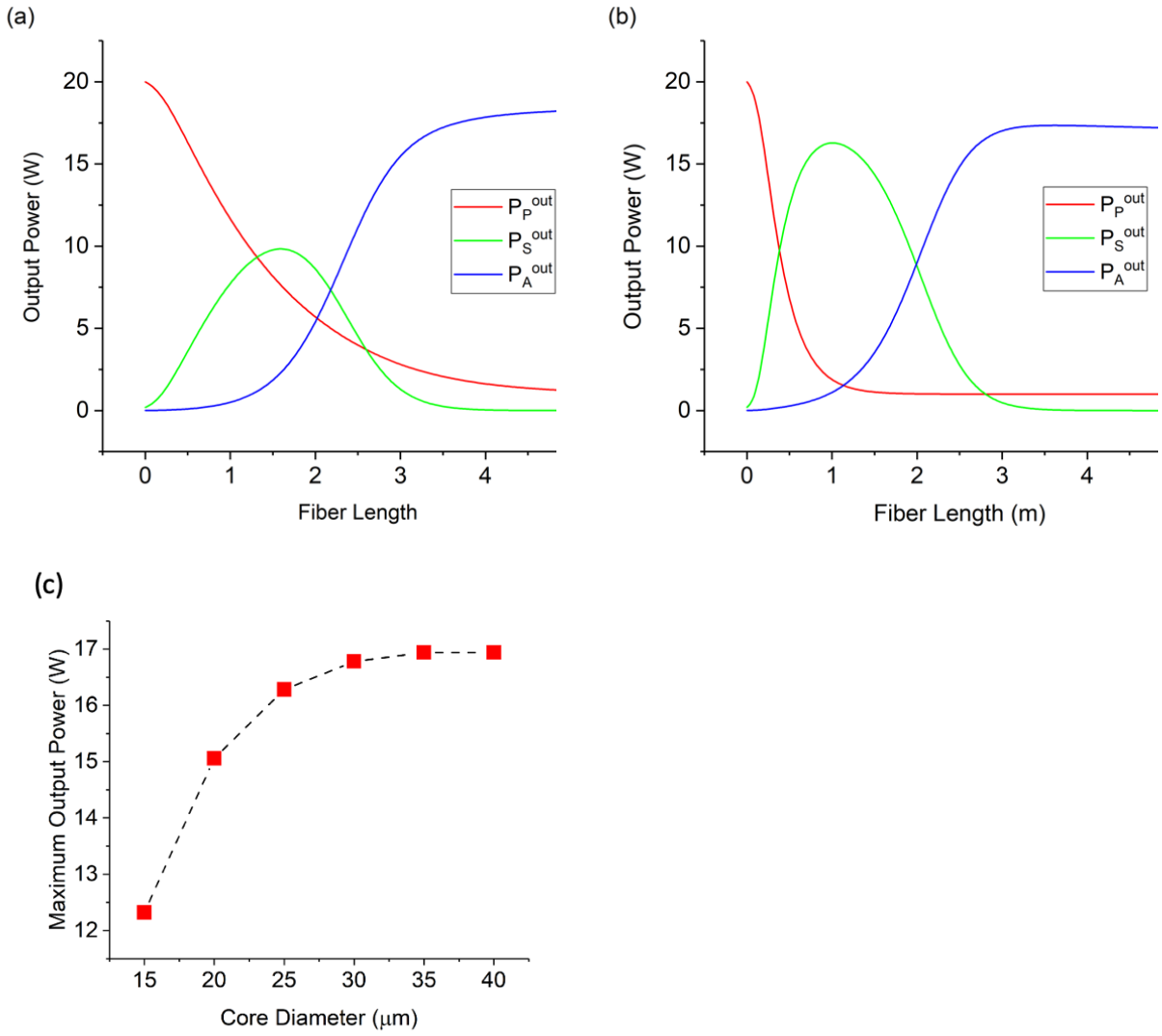

Fig. 3.9: Simulated output powers with P_p^{in} = 20 W, P_s^{in} =0.2 W, and total P_A^{in} = 3.73×10^{-5} W at varying active fiber lengths with (a) original fiber design with a Γ_{shape} of 95% and, (b) 25 μm core fiber design with a Γ_{shape} of 95%, (c) Maximum Output Power versus core diameter.

Next, a fiber with all the parameters remaining the same, except for a 25 μm core, is simulated. Similarly, with a maximum pump power of 20 W, the simulated pump, signal, and ASE power are shown in Fig. 3.9 (b). Comparing the results to that in Fig. 3.9 (a), the pump absorption is much quicker as a result of the bigger core-cladding ratio. As a result, a shorter optimized length of ~1 m is achieved with a maximum signal power of 16.28 W, which is greater than the situation with a smaller core. In terms of ASE, it still gives great competition with the

signal and it is again important the select the proper Yb-doped fiber length. But at the optimized fiber length, the ASE is less than 1 W, which is negligible compared to the signal power. Similar simulations with other core sizes are also performed, and the maximum output power is summarized as a function of core diameter in Fig. 3.9 (c). From the results, it is obvious that a bigger core is helpful for achieving greater output power, with reasons already discussed above. On the other hand, the trade-off is that a bigger core naturally introduces more high-order modes in the core (if NA is the same) so that the fiber is no longer single-mode, adding additional efforts to control the system output beam profile. As can be observed in Fig. 3.9 (c), the trend is asymptotic, and the output power does not increase significantly when the core is beyond 25 μm. At the same time, 25 μm core is the typical size of LMA fiber and single-mode operation should be possible. Therefore, a 25 μm core Yb-doepd double-clad phosphosilicate fiber becomes the designed fiber for the next round of fiber fabrication.

However, fabrication such as fiber has certain difficulties, which made the development process slower than expected. The main difficulty is the control of fiber core index. As discussed above, to support single-mode operation, the fiber index difference needs to be carefully controlled. However, during the fabrication process of the phosphosilicate fiber used here, Al, P, and Yb needs to be doped and all of them increase the refractive index when making the fiber preforms. Then, when the fibers are drawn, Al_2O_3 and P_2O_5 further reacts to form $AlPO_4$, which is known to decrease the refractive index [36]. However, what is still unclear is how much of the Al_2O_3 and P_2O_5 will react to form $AlPO_4$ and this subject itself is a pure material engineer study and may need tens of fiber preforms and fiber fabrication, which is beyond the point of this thesis. The influence on the Yb-doped phosphosilicate fiber is, within the four preforms made so far, none of the index difference is ideal for the single-mode operation and the index difference

results are not consistent between preforms when changing the Al doping concentration. However, with the above simulation, once the fabrication problem is solved, using such fiber for low-QD operation should be feasible.

Although development of fibers with the above optimized fiber geometry is not finished, a double-clad Yb-doped aluminosilicate optical fiber is commercially available and therefore used to show the importance of developing new phosphosilicate or fluorosilicate fiber to support low-QD operation. For the commercial optical fiber, it is a Yb-doped aluminosilicate optical fiber and exhibits the same emission and absorption spectroscopy in Fig. 2.1. The core diameter is 20 μm, the fiber NA is 0.08, the lifetime is measured to be 800 μs, the Yb^{3+} concentration is $8 \times 10^{25}/m^3$. First, putting these parameters into the amplifier code and a similar simulation with a maximum pump power of 20 W was performed and the simulated pump, signal, and ASE power are shown in Fig. 3.10. From the results, because of the relatively small emission cross section at the signal wavelength (1005 nm), the competition from ASE is severe and, as a result, only a maximum signal power of 7 W is achieved at a fiber length of 0.56 m, while at the same time 4.37 W of ASE power is present. Beyond this fiber length ASE quickly dominates and signal dies out. Next, the commercial fiber is placed in the experimental setup with the fiber length close to the optimized length (0.56 m). The results are also shown in Fig. 3.10, and again shows great agreement with the simulation results, further proving the feasibility of the model. However, comparing the data to that of the phosphosilicate fiber with a 14 μm core (Fig. 3.9 (a)), although the commercial fiber has a more ideal fiber geometry, it still gives less output power then the 14 μm core phosphosilicate fiber. This directly shows that due to the favorable spectroscopic properties in phosphosilicate glasses, it offers greater potential to achieve low-QD

operation and the development of phosphosilicate fiber is necessary, despite the great difficulty to fabricate such fibers.

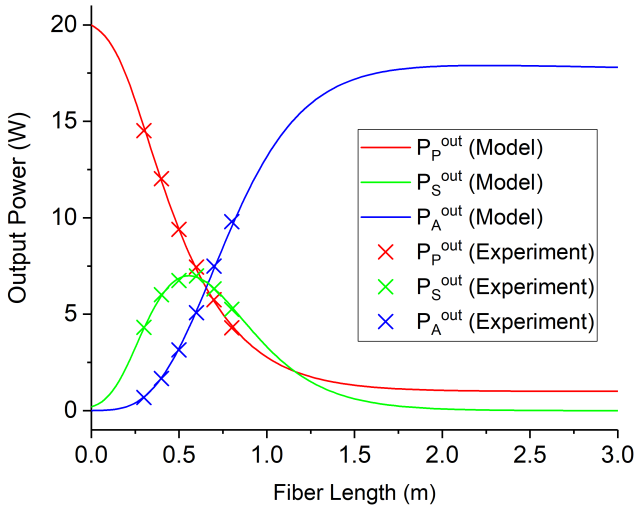

Fig. 3.10: Simulated and experimental output powers with P_p^{in} = 20 W, P_s^{in} = 0.2 W, and total P_A^{in} = 3.73×10^{-5} W at varying active fiber lengths. The lengths used in the experiment are 0.3 m, 0.4 m, 0.5 m, 0.6 m, 0.7 m and 0.8 m.

Finally, an investigation of double-end pumping is performed numerically. Double-end pumping is not a new idea and has its application in many types of lasers such as crystal-based lasers [61], semiconductor lasers [62], gas lasers [63], and fiber lasers [64]. There are many reasons behind choosing a double-end pumping configuration over a single-end pumping configuration, which will be discussed in detail below with the simulation results.

A typical double-end pumped fiber laser is shown in Fig. 3.11. The seed laser serves as the signal and its specific setup is not shown here in detail. It can be a laser like the one described in Chapter 2, or any types of lasers that are coupled into a fiber. The seed laser is connected to one end of the combiner via a isolator, and similar as before the fiber type will be matched. Two or more pumps can be used at the seed laser side and also go to the combiner via pump protectors. On the other side, pumps and pump protectors can be arranged in a similar way

and combined by a combiner, whereas one end of the combiner serves as the system output and a CPS and angled cleave are set the same as before to block residual pump in the cladding and avoid back reflection, respectively.

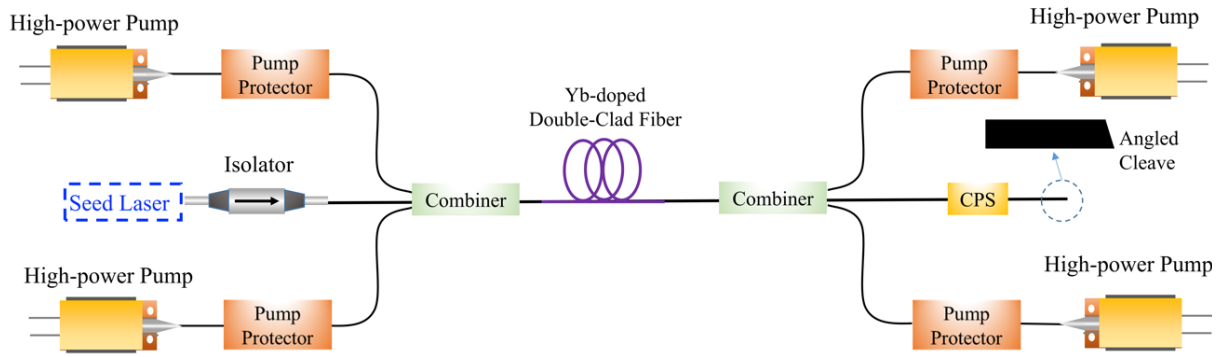

Fig. 3.11: Experimental setup for the double-end pumping MOPA-based fiber laser. LD: laser diode, FBG: fiber Bragg grating, CPS: cladding power stripper.

Previously, a 25 μm core phosphosilicate fiber is simulated and the results are shown in Fig. 3.9 (b). Using the same fiber as gain medium, the code is modified to simulate the double-end pumping configuration. Specifically, unlike the single-end case, a fiber length L needs to be determined first so that the initial condition for both pumps are set. Then, Eqs. 4.2 - 4.4 are modified to take both pumps into consideration and are used to simulate the inputs and outputs of both pumps, the signal, and the ASE within a fiber length L. Using these results as the initial condition, the power for both pumps, the signal, and the ASE at any location within length L can be calculated using the same equation sets. Following described procedures, double-end pumping with different fiber lengths are simulated, 10 W of pump power is assumed at each end, and the active fiber is the 25 μm core phosphosilicate fiber used above. The results are summarized in Fig. 3.12.

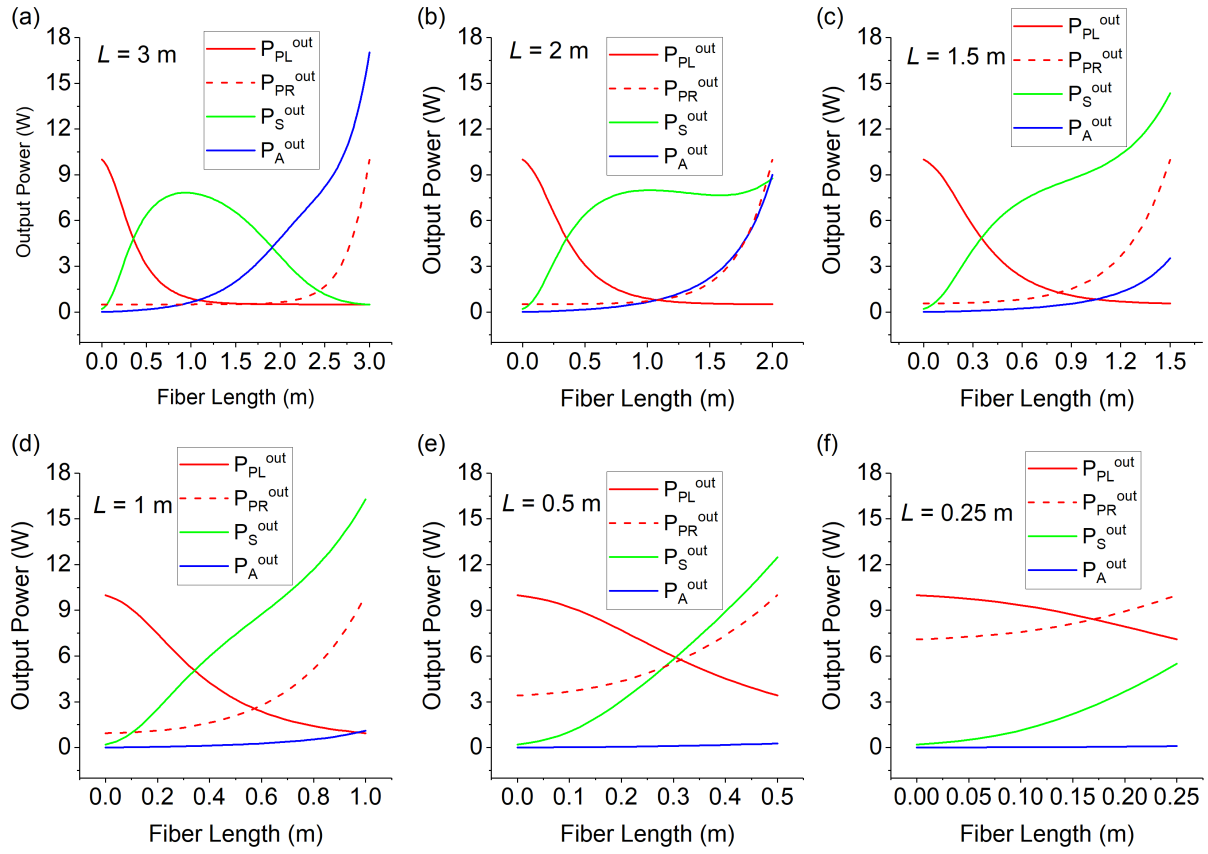

Fig. 3.12: Simulation results for the power evolution for pump from the left side (P_{PL}) and right side (P_{PR}), the signal, and the ASE with active fiber length of (a) 3 m, (b) 2 m, (c) 1.5 m, (d) 1 m, (e) 0.5 m, and (f) 0.25 m.

In Fig. 3.12 (a), with increasing fiber length the signal shows a similar trend as before with an optimized fiber length. However, the maximum achievable signal power is much less compared to the single-end pumping case shown in Fig. 3.9 (b). The reason is that when the maximum signal power is achieved, pump power from the other end (right end) has already been mostly absorbed and contribute to ASE so that very little pump power is available for the signal amplification. Therefore, a shorter fiber length should be used. As shown in Figs. 3.12 (b)-(d), with decreasing fiber lengths , a higher signal power and lower ASE power is achieved, making the system more efficient. For the optimized case in Fig. 3.12 (d) with 1 m of active fiber, pump power from both ends are mostly absorbed within the fiber length and contributes to signal

amplification, with only relatively small ASE present. If the fiber length continues to decrease, however, the signal power starts to decrease because of the incomplete pump absorption and therefore is also not preferable. For the six cases simulated in Fig. 3.12, by plotting the signal power evolution together with the signal result in Fig. 3.9 (b), a summary can be found in Fig. 3.13.

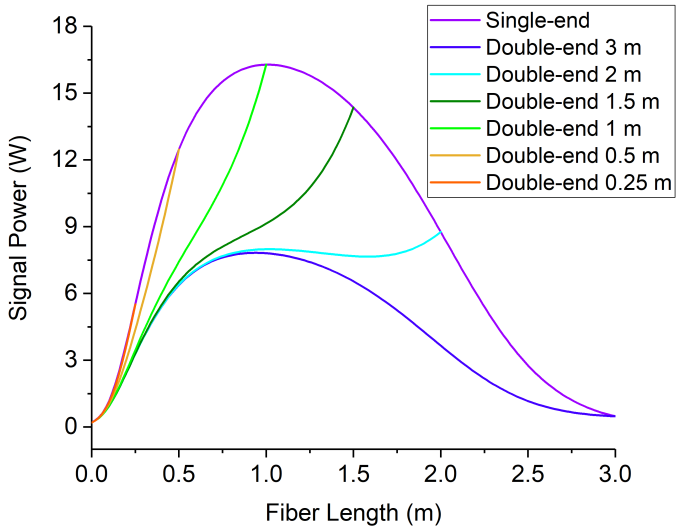

Fig. 3.13: Comparison of power evolution with single-end and double-end pumping.

From Fig. 3.13, it can be seen that in terms of the achievable signal power with a certain active fiber length, there is no difference between single-end or double-end pumping. However, some of the advantages of double-end pumping can be clearly seen from Fig. 3.13. First, to achieve the same signal power within the same fiber length, for example 16.28 W with 1 m of fiber, the signal power quickly increases with fiber length then slows down in the single-end pumping case, whereas in the double-end pumping case the signal grows slower but remains a similar increasing speed, making the final output power is the same at 1 m of fiber. However, the

nonlinear phase shift accumulated within the 1 m of the fiber is different between the two cases. The nonlinear phase shift (φ) is defined as

$$\varphi = \gamma PL \tag{4.7}$$

in which γ is the nonlinear coefficient of the fiber and is a constant, and P is the optical power. For the single-end case, since the signal power is greater than that of the double-side case at every position in between the 1 m of fiber, it will accumulate more nonlinear phase shift so that it is more likely to have self-phase modulation, which will influence the system behavior as a high-power laser.

Second, from the standpoint of thermal energy generation, because of the different is signal power evolution between the two cases, more thermal energy is more uniformly generated for the double-end case. Specifically, in the single-end case, the signal power increases quicker at the beginning of the power, generating more thermal energy as a result of QD heating. When the signal power increase slows down at later fiber, less thermal energy is generated. This will cause an nonuniform temperature distribution along the fiber the make the beginning part of the fiber more likely to suffer from thermal-related effects.

Finally, the number of ports in a combiner and the power in one laser diode unit are both limited, setting an upper limit for the maximum pump power that can be coupled into the active fiber. By using the double-end pumping method, this maximum pump power is doubled and will help to generate more signal power.

In summary, in this chapter Yb-doped double-clad fluorosilicate and phosphosilicate fibers are used as active medium within an amplifier setup. The Yb-doped fluorosilicate failed because of cracks and spiral cracks that formed after a cleave. The Yb-doped phosphosilicate fiber gave primary results that match well with a theoretical model incorporating the layer-ASE simulation. For the phosphosilicate fiber, further fiber optimization is performed numerically and

compared to a similar-geometry commercial aluminosilicate fiber. Finally, double-end pumping is implemented numerically, and the advantages are discussed.

CHAPTER 4: Excitation-Balanced Fiber Lasers and Pulse Amplifiers

In this chapter, a new approach is introduced by introducing pumping at wavelengths both to the blue and red sides of the lasing wavelength. According to Eq. 1.1, these two pumps will contribute to positive and negative QD, which collectively can be partially balanced giving a lower effective QD. It can also be understood that by adding another pump, which contributes a negative QD to the systems described in Chapters 2 and 3, the QD in the systems can be further reduced. Systems working under this pumping condition are named as excitation-balanced fiber lasers or amplifiers. In this chapter, both lasers and pulse amplifiers are investigated.

Before discussing excitation-balancing, another approach to thermal management in high power lasers was introduced by Bowman in late 1990s [65], which may also be applied to fibers lasers, giving rise to what are known as radiation-balanced fiber lasers (RBFL). Anti-Stokes fluorescence (ASF) cooling is integrated into these lasers to balance QD heating. Specifically, the ASF process can be understood as follows: when optically excited in the proper wavelength range, certain materials emit fluorescence with a mean energy that exceeds the pump-photon energy, resulting in net extraction of phonon energy from the material and, therefore, cooling [30]. In 2020, demonstrations of ASF cooling in several Yb-doped silica fibers were successful [30], [66], [67] for the first time, leading to the very first demonstration of radiation balanced silica-fiber amplifiers [68] and lasers [31] in 2021. Despite the success of such systems, there is one main drawback for such systems. As defined above, the cooling process depends on generating fluorescence, which is in the form of spontaneous emission instead of stimulated emission. Therefore, the fiber laser system needs to be designed to generate abundant spontaneous emission, which is not only a challenging task since fiber lasers usually operate very

efficiently when deeply saturated, but also is deleterious to the system threshold and overall efficiency. For example, in [47], nearly 2 W of pump power are required to achieve 350 mW of output, and the threshold is ~ 1.1 W. In comparison, for the low-QD laser described in Chapter 2, the threshold is ~50 mW and less than 600 mW of pump is required to achieve the same output power.

To overcome the aforementioned drawback, considering the fact that the shape of the emission spectrum remains invariant with pumping wavelength, a tantalizing question emerges: "Can anti-Stokes pumping (ASP) contribute to stimulated emission?" Obviously, lasing at a wavelength shorter than the pump would be impossible because gain cannot be achieved. Instead, the pumping wavelength is always less than the lasing wavelength (or Stokes pumping, SP). However, if the SP wavelength is retained, and a second, ASP wavelength is introduced, thermal energy could be removed by laser emission rather than fluorescence. In that case, QD heating could be partly mitigated while preserving efficiency by eliminating the need for spontaneous emission, which is the main idea behind this chapter. Obviously, if SP and ASP wavelengths are injected in a Yb-doped fiber simultaneously, SP will serve as the pump to amplify ASP like an amplifier described in Chapter 3. Therefore, SP and ASP must be mostly or completely separated in time, requiring that the pumps be operated in a pulsed regime and leading the system to a pulsed laser or amplifier.

Figure 4.1 (a) gives a schematic of the experimental setup to enable such regime. The Stokes pump (red dashed box) is a commercial, single-mode, grating-stabilized laser diode (LD) operating at λ_{SP} = 976.6 nm. It is driven by a pulsed current source and is followed by an optical isolator. The anti-Stokes pump (blue dashed box) is a linear-cavity CW fiber laser, similar to the one in Chapter 2, with an output wavelength of λ_{ASP} = 989.6 nm. It is pulse-modulated by an

external acousto-optic modulator (AOM), with an associated radio frequency (RF) driver providing power to the AOM. Note that, relative to the pulse widths used in the experiments, the various rise times in the system are negligible. A multi-channel digital delay/pulse generator controls the relative temporal behaviors of the two pumps, whose outputs are combined through a 50/50 coupler. One coupler output feeds directly into the laser cavity (green dashed box), while the other serves as a check point for the pumps' power and waveforms. The laser cavity is comprised of the FBGs at 985.6 nm described in Chapter 2, thus setting the laser wavelength, λ_L. As discussed in Chapter 2, ~12.8-cm of Yb-doped fluorosilicate fiber gives the near-optimized slope efficiency. Therefore, here, a 12.3-cm Yb-doped fluorosilicate fiber is used as the active medium, which, although not exactly the same, is close to the near-optimized fiber length. Fig. 4.1 (b) shows a simplified schematic of the multi-wavelength pumping process within the two manifolds of Yb^{3+}. Due to the amorphous nature of silica glass, precise identification of the Stark lines is challenging. Therefore, Fig. 4.1 (b) serves only as a simple aid in visualizing the photon and phonon processes. Specifically, absorption at λ_{SP} and emission at λ_L generates phonons and results in heating, whereas absorption at λ_{ASP} and emission at λ_L results in the annihilation of phonons and a form of cooling.

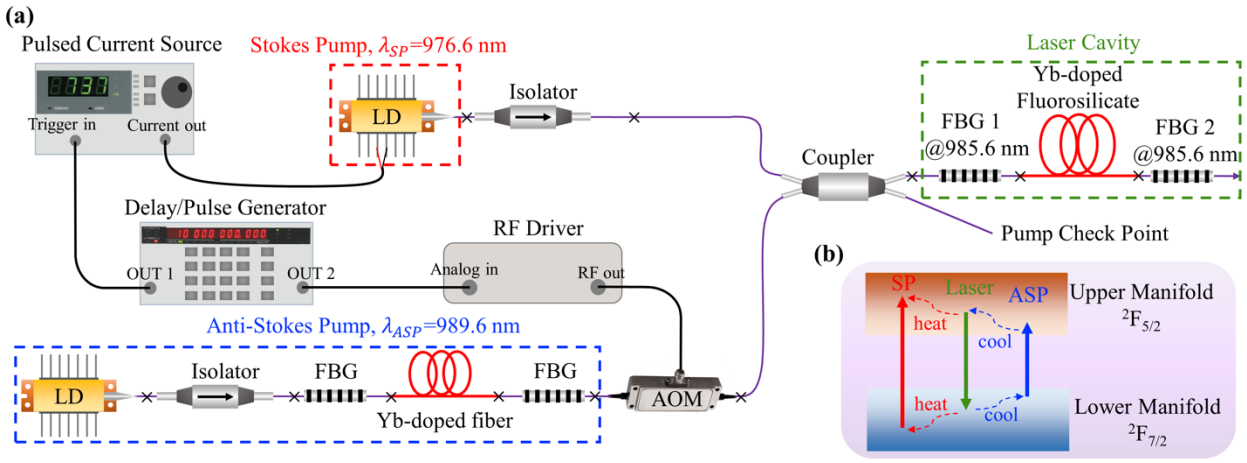

Fig. 4.1 (a) Schematic of the experimental setup. LD: laser diode, RF: radio frequency, FBG: fiber Bragg grating, AOM: Acousto-optic modulator. The symbol "×" represents a fusion splice between fibers, (b) representation of the Yb^{3+} energy level diagram.

To perform the pulsed regime as discussed above, the delay generator is set to produce t_{pulse} = 1 ms rectangular pulses with a variable repetition rate (f_{rep}) at OUT 2, driving ASP. OUT 1 produces the same signal delayed by Δt in time, driving SP. To aid in the discussion that follows, the parameters employed in the experiments are summarized in Table 4.1. The pump powers from SP (P_{SP}) and ASP (P_{ASP}) are adjustable and kept the same in all cases, and knowing f_{rep} and pulse width, the corresponding average power ($\bar{P}_{SP}$ and $\bar{P}_{ASP}$) can be calculated. Table 4.1 provides the maximum available pump powers. Note that f_{rep} was set to values equal to integer multiples of 100 Hz with the exception of the 499.95 Hz setting, which results from an instrument limitation in the delay generator.

Table 4.1: Parameters and Values Employed

Parameters	t_{pulse} (ms)	f_{rep} (Hz)	Δt (ms)	${P_{SP}}^{max}$ (mW)	${P_{ASP}}^{max}$ (mW)
Values	1	100, 200, 300, 400, 499.95	0.2, 0.4, 0.6, 0.8, 1	192.38	29.47

Next, the threshold of the system is analyzed. When the ASP is off, the laser is simply pulse-pumped and will reach threshold given sufficient power from SP and time. After turning on ASP, if it does indeed contribute energy toward lasing, then the energy required from SP to reach threshold should decrease with increasing P_{ASP}. To examine this, a first photodiode is placed at the pump check point and signal from the output is collimated through a bandpass filter and collected by another photodiode. The transmission profile of the bandpass filter is given in Fig. 4.2 (a). Both photodiode signals are subsequently displayed on an oscilloscope. Since three wavelengths (λ_{SP}, λ_{ASP}, and λ_L) can coexist at the output, with an example spectrum provided in Fig. 4.2 (b), the filter's purpose is to pass only λ_L while rejecting any pump leakage.

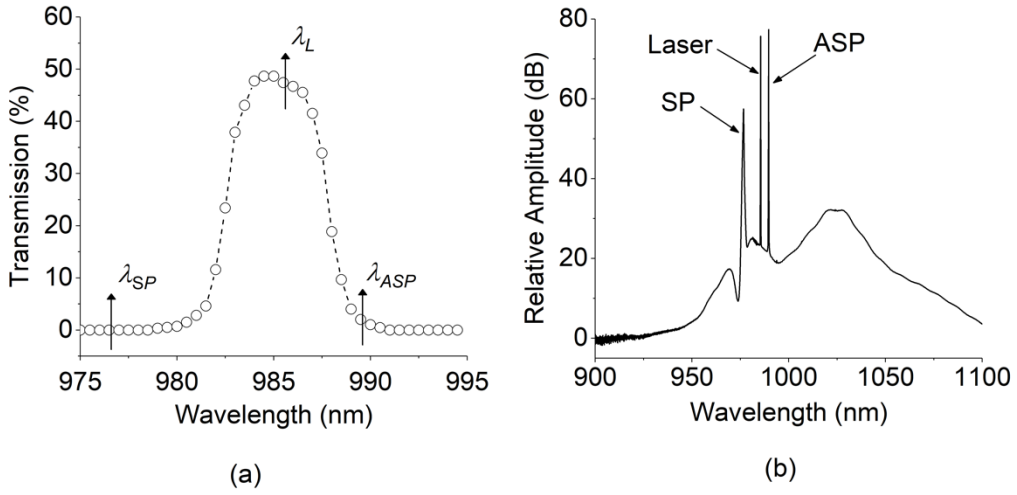

Fig. 4.2: (a) Transmission profile of the bandpass filter, (b) An example output spectrum.

Example oscilloscope traces are shown in Fig. 4.3, corresponding to f_{rep} = 400 Hz, Δt = 0.8 ms, P_{SP} = 192.38 mW, and varying P_{ASP}. Figure 4.3 (a) gives the trace of the two pumps, and Fig. 4.3 (b) gives the trace of the output. As can be observed from Fig. 4.3 (a), ASP arrives first, and for the first 0.8 ms it is unaccompanied by SP. As would be expected, threshold cannot be achieved during this time (see Fig. 4.3 (b)) for the reasons discussed above. For the next 0.2 ms, the two pumps coexist, after which ASP is off and SP brings the upper state population to lasing

threshold. As can clearly be seen, the time to lasing threshold decreases as P_{ASP} is increased. This clearly verifies the role of ASP in populating the upper state prior to the arrival of SP. When the threshold condition is reached, typical relaxation oscillations (RO) associated with pulse pumping are first observed as the system gradually approaches steady state.

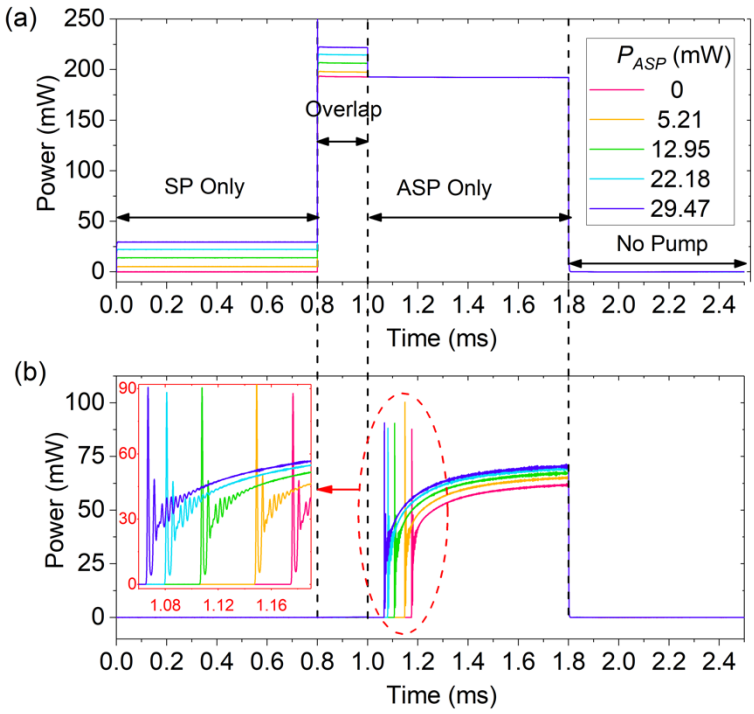

Fig. 4.3: (a) An example temporal trace of the pumps, (b) an example temporal trance of the outputs.

Next, P_{SP} required to reach threshold ($P_{SP}{}^{th}$) is measured for a wide range of parameter settings (f_{rep}, Δt and P_{ASP}). $P_{SP}{}^{th}$ is defined to be at the very first appearance of a RO peak. The $P_{SP}{}^{th}$ in all the cases are summarized in Fig. 4.4. Several trends can be observed in the results. First, $P_{SP}{}^{th}$ decreases with increasing f_{rep}. With a smaller f_{rep}, there is a wider gap of time between pump pulses, allowing more decay of the remaining excited ions through spontaneous emission. Second, the threshold generally decreases with increasing P_{ASP}. This is expected for the reasons outlined above. Third, for a fixed P_{ASP}, $P_{SP}{}^{th}$ first decreases, reaches a minimum,

and begins to increase with increasing Δt. This trend can be explained as stemming from a competition between several processes. First, when the pulses are fully (Δt = 0 ms) or mostly overlapping, the system reduces to the CW case, where gain on ASP has deleterious effects. When the pulses overlap for a relatively short time, insufficient excitation builds up from SP before ASP is turned off such that ASP never experiences any gain. At the same time, the effective total pumping pulse width decreases, which reduces the loss of excitation to spontaneous emission, thereby lowering the threshold. As the pulses become more non-overlapping, some early excitation from P_{ASP} will have been lost to spontaneous emission before the entrance of P_{SP}. This requires additional P_{SP} to make up for those lost photons.

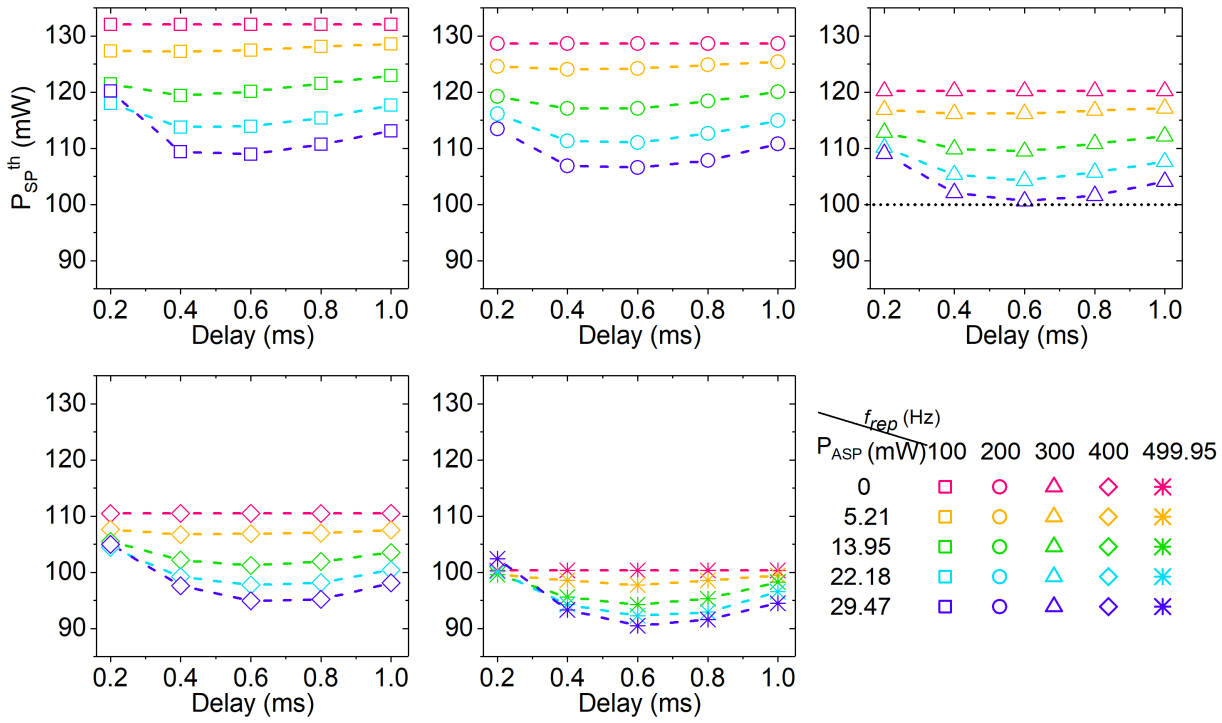

Fig. 4.4: threshold pump powers from SP under different setting of f_{rep}, Δt, and P_{ASP}.

To validate the observed influence of Δt on lasing threshold, a finite difference time domain (FDTD) simulation is constructed. The main reason to include FDTD is that the upper

state population (N_1(z,t)), as well as pump powers ($P_{SP}(z,t)$, $P_{ASP}(z,t)$), are all functions of time and position. From the theory of fiber laser rate equations [52], before lasing threshold is reached, N_1(z,t) can be expressed as

$$\frac{\partial N_1(\mathrm{z,t})}{\partial t} = -\frac{N_1(\mathrm{z,t})}{\tau} + \left\{\frac{P_{SP}(z,t){\sigma_{SP}}^a \lambda_{SP}}{A_{eff}hc}[\rho - N_1(\mathrm{z,t})] - \frac{P_{SP}(z,t){\sigma_{SP}}^e \lambda_{SP}}{A_{eff}hc}N_1(\mathrm{z,t})\right\} + \left\{\frac{P_{ASP}(z,t){\sigma_{ASP}}^a \lambda_{ASP}}{A_{eff}hc}[\rho - N_1(\mathrm{z,t})] - \frac{P_{ASP}(z,t){\sigma_{ASP}}^e \lambda_{SP}}{A_{eff}hc}N_1(\mathrm{z,t})\right\} \quad (4.1)$$

in which τ is the upper state lifetime, ${\sigma_{SP/ASP}}^e$ and ${\sigma_{SP/ASP}}^a$ are the emission and absorption cross sections at the corresponding pump wavelengths, A_{eff} is the effective mode area, h is Planck's constant, and c is the speed of light. To simplify the expression, $\beta_{SP/ASP}$ and $\gamma_{SP/ASP}$ are defined as follows

$$\beta_{SP/ASP} = \frac{\lambda_{SP/ASP}({\sigma_{SP/ASP}}^a + {\sigma_{SP/ASP}}^e)}{A_{eff}hc} \quad (4.2)$$

$$\gamma_{SP/ASP} = \frac{\lambda_{SP/ASP}{\sigma_{SP/ASP}}^a \rho}{A_{eff}hc} \quad (4.3)$$

Then, time t is discretized into small steps of Δt and the forward differencing formula is applied to estimate $\frac{\partial N_1(\mathrm{z,t})}{\partial t}$. After simplification, Eq. 4.1 becomes

$$N_1(\mathrm{z,t+\Delta t}) = N_1(\mathrm{z,t}) + \Delta t\{-\frac{N_1(\mathrm{z,t})}{\tau} + [-\beta_{SP}P_{SP}(z,t)N_1(\mathrm{z,t}) + \gamma_{SP}P_{SP}(z,t)] + [-\beta_{ASP}P_{ASP}(z,t)N_1(\mathrm{z,t}) + \gamma_{ASP}P_{ASP}(z,t)]\} \quad (4.4)$$

For the evolution of pump powers, the governing equation is

$$\frac{\partial P_{SP/ASP}(\mathrm{z,t})}{\partial t} = P_{SP/ASP}(\mathrm{z,t})\Gamma\{N_1(\mathrm{z,t})\sigma_{SP/ASP}{}^{e} - [\rho - N_1(\mathrm{z,t})]\sigma_{SP/ASP}{}^{a}\} \quad (4.5)$$

Next, distance z is discretized into small steps of Δz and the forward differencing formula is employed to estimate $\frac{\partial P_{SP/ASP}(\mathrm{z,t})}{\partial t}$. As a result, Eq. 4.5 is finally simplified to

$$P_{SP/ASP}(\mathrm{z}+\Delta\mathrm{z},\mathrm{t}) = P_{SP/ASP}(\mathrm{z,t})\exp\left[\Gamma\Delta\mathrm{z}\{N_1(\mathrm{z,t})\sigma_{SP/ASP}{}^{e} - [\rho - N_1(\mathrm{z,t})]\sigma_{SP/ASP}{}^{a}\}\right] \quad (4.6)$$

The initial conditions $P_{SP/ASP}(\mathrm{z,t})$ at z=0 are determined by the specific temporal settings of the two pumps. The boundary conditions for $N_1(\mathrm{z,t})$, that N_1 will return to the same value after each period, are set by f_{rep}. An assumption was made that the pulse propagation time through the fiber is infinitesimal when compared with the rate at which the upper state is populated, which is valid when considering an active fiber length of 12.3 cm. Now, with these conditions, as well as Eq. 4.4 and Eq. 4.6, $N_1(\mathrm{z,t})$, $P_{SP}(\mathrm{z,t})$, and $P_{ASP}(\mathrm{z,t})$ for the entire time period and fiber length can be solved, from which the roundtrip gain G_R (in unit of dB) can be calculated by

$$G_R(t) = 2 \times \sum_{z} \frac{10}{\ln(10)}\Gamma\{N_1(\mathrm{z,t})\sigma_L{}^{e} - [\rho - N_1(\mathrm{z,t})]\sigma_L{}^{a}\}dz \quad (4.6)$$

in which $\sigma_L{}^{e}$ and $\sigma_L{}^{a}$ are the emission and absorption cross section at the lasing wavelength.

Next, an example simulation is presented for fixed pump input powers P_{SP} = 100 mW, P_{ASP} = 29.47 mW, and f_{rep} = 300 Hz with varying Δt. Note that, as indicated by the black dashed line in Fig. 4.4, the selected P_{SP} is below threshold for all values of Δt when P_{ASP} = 29.47 mW (purple triangles). Given these conditions, the simulated results of, $N_1(\mathrm{z,t})$, $P_{SP}(\mathrm{z,t})$, $P_{ASP}(\mathrm{z,t})$, as well as $P_{SP}(\mathrm{z,t}) + P_{ASP}(\mathrm{z,t})$ are shown in Fig. 4.5, Fig. 4.6, Fig. 4.7, and Fig. 4.8, respectively.

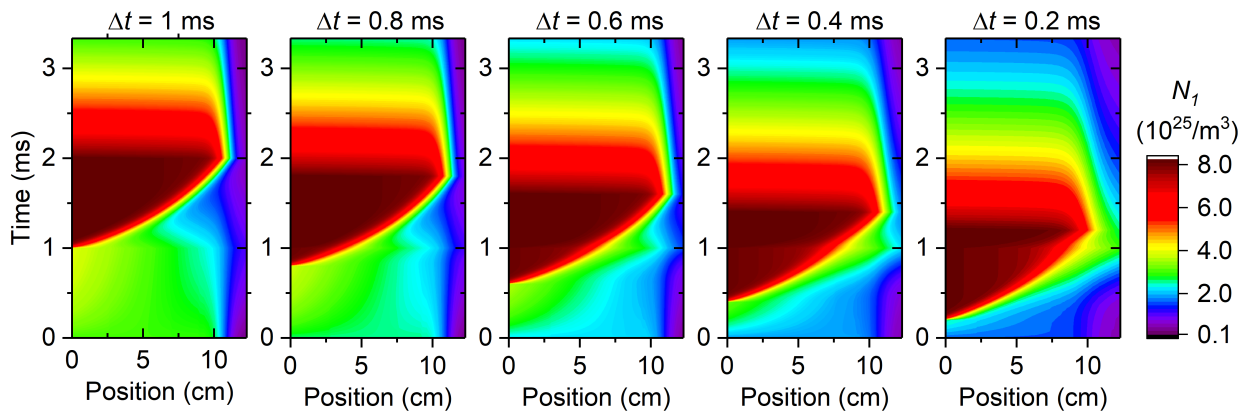

Fig. 4.5: Simulation results of $N_1(z, t)$ under settings of P_{SP} = 100 mW, P_{ASP} = 29.47 mW, and f_{rep} = 300 Hz with various Δt.

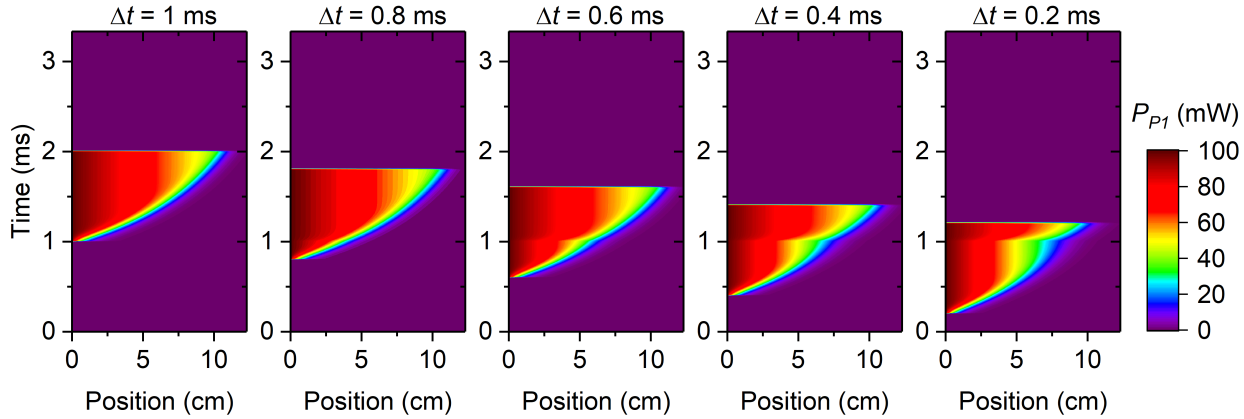

Fig. 4.6: Simulation results of $P_{SP}(z, t)$ under settings of P_{SP} = 100 mW, P_{ASP} = 29.47 mW, and f_{rep} = 300 Hz with various Δt.

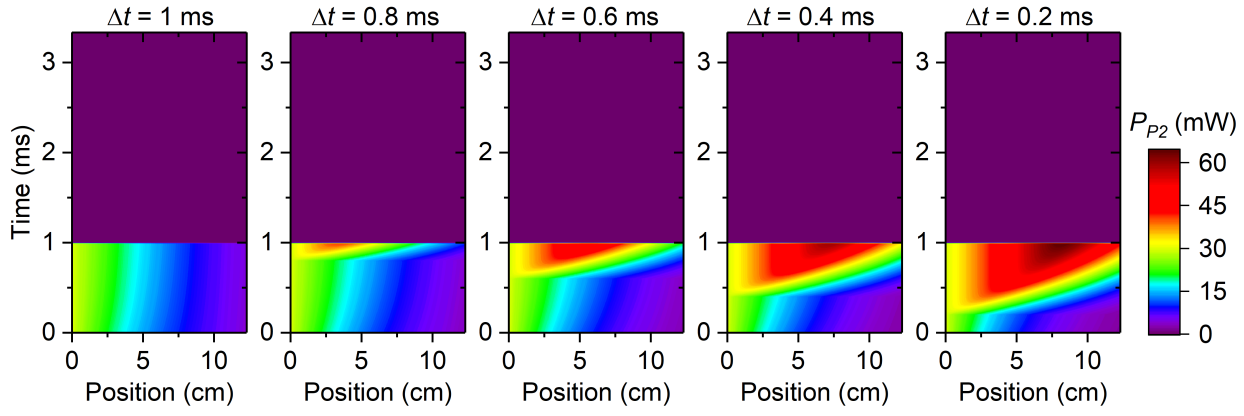

Fig. 4.7: Simulation results of $P_{ASP}(z, t)$ under settings of P_{SP} = 100 mW, P_{ASP} = 29.47 mW, and f_{rep} = 300 Hz with various Δt.

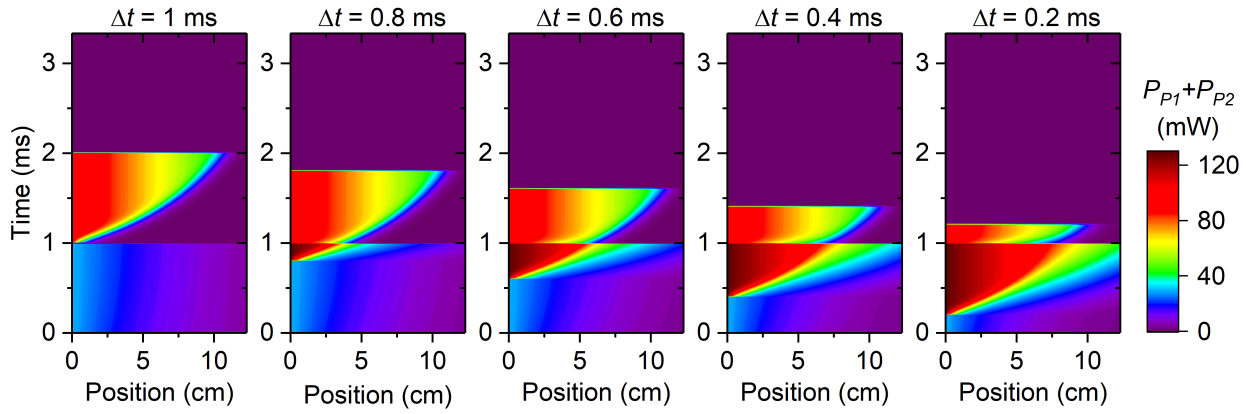

Fig. 4.8: Simulation results of $P_{SP}(z,t) + P_{ASP}(z,t)$ under settings of P_{SP} = 100 mW, P_{ASP} = 29.47 mW, and f_{rep} = 300 Hz with various Δt.

Several observations can be made from the simulation results: (1) in Fig. 4.5, it is obvious that after SP is off, N_1 decays exponentially with lifetime τ, which is empirically determined to be 1.3 ms as described in the Chapter 2. (2) From Figs. 4.6 and 4.7, it can be observed that the pumps are not uniformly absorbed along the fiber length. This is expected for a fiber with relatively high Yb^{3+} concentration like the one used here. (3) The power truncates almost instantaneously, for example at t = 1 ms in Fig. 4.6, at the time when the pumps are turned off. (4) Because higher pump powers are available at the start of the fiber, greater N_1 is observed at the beginning of the fiber, resulting in greater population inversion and therefore higher local gain.

Next, the roundtrip gain versus time then is calculated with the results shown in Fig. 4.9 (a) for five different Δt values. From the figure, it can be seen that, early in time ASP begins populating the upper state, but $G_R > 0\ dB$ cannot be reached since $\lambda_{ASP} < \lambda_L$. The maximum G_R, noted as ${G_R}^{max}$, occurs at 1+Δt ms, i.e., the point where both pumps are turned off, and the higher this value becomes, the closer the system is to threshold. Beyond 1+Δt ms, G_R decays in accordance with the upper state lifetime. It can further be observed that with decreasing Δt from 1 ms, ${G_R}^{max}$ first increases, reaches a maximum, then decreases (arrows in Fig. 4.9 (a)), in

agreement with the threshold trend discussed previously. In other words, gain is maximized where Δt is approximately 0.6 ~ 0.8 ms and, outside of this range, more power is required to reach threshold, fully consistent with experimental observations.

Finally, the same model is applied to 125 unique parameter settings at the experimentally determined thresholds (5 f_{rep} values × 5 P_{ASP} values × 5 Δt values) and used to find the corresponding ${G_R}^{max}$ values, which, in principle, should represent the threshold gain, G_{th}, of the system. From laser theory, G_{th} should equal the roundtrip loss, α, which is determined by

$$\alpha = -10 \times log_{10}(R_1 R_2) + 4\delta_s + 2L\alpha_b \tag{4.7}$$

in which R_1, R_2 are the reflectivities of the two FBGs.. δ_s is the splice loss between the active fiber and passive fiber hosting the FBG, and α_b is the background loss of the fiber. Plugging in the numbers, α is determined to be 5.522 dB. Then, a histogram of 125 G_{th} deduced from the measurements via the model is provided in Fig. 4.9 (b). A corresponding Gaussian fitting is performed, whereby the mean and the standard deviation are found to be 5.547 dB and 0.026 dB, respectively, in excellent agreement with α. This degree of self-consistency imparts high confidence in both the simulation and experimental results.

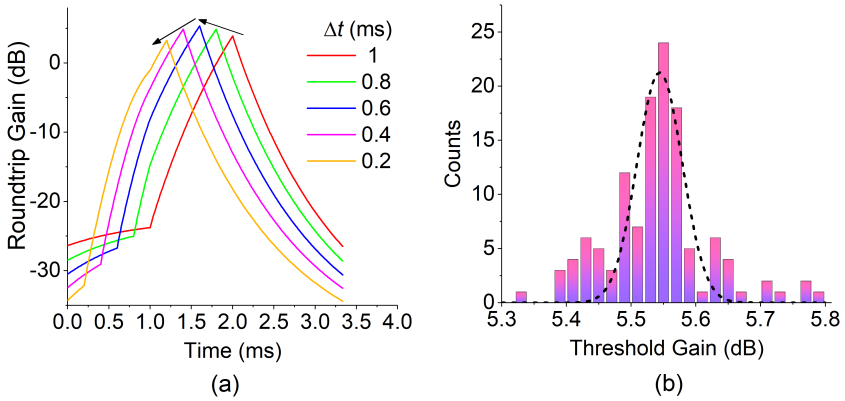

Fig. 4.9: (a) Simulation of roundtrip gain under settings of P_{SP} = 100 mW, P_{ASP} = 29.47 mW, and f_{rep} = 300 Hz with various Δt, (b) Histogram of the 125 simulated threshold gains under different settings of f_{rep}, Δt, and P_{ASP}.

Next, power measurements are presented and analyzed. As discussed above, three wavelengths can coexist at the output and their respective powers must be distinguished. This can be done by measuring the corresponding output spectra and integrating the corresponding wavelength range for each wavelength. Using this method, an example power measurement is provided in Fig. 4.10, corresponding to Δt = 1 ms and f_{rep} = 400 Hz. Note that the pump and output powers in Fig. 4.10 are all average powers. From Fig. 4.10 (a), most of $\bar{P}_{SP}$ is absorbed and leakage is negligible. For the given operating conditions, there is some increase in $\bar{P}_{ASP}$ leakage with increasing $\bar{P}_{SP}$, but this becomes clamped, as expected once threshold is reached. Two types of linear fits to the laser output power, $\bar{P}_{out}{}^{L}$ are performed, as shown in Fig. 4.10 (b); using the sum of pump powers on the abscissa, the ordinate values are linearly fitted where (1) $\bar{P}_{ASP}$ is fixed with varying $\bar{P}_{SP}$ (solid lines with slope η), and (2) $\bar{P}_{SP}$ is fixed with varying $\bar{P}_{ASP}$ (dashed line with slope η', for visual clarity only one η' fitting is shown). First, η beneficially increases with increasing $\bar{P}_{ASP}$. Meanwhile, η' is positive-valued, indicating that the fiber absorbs power at λ_{ASP} that contributes to $\bar{P}_{out}{}^{L}$ Since $\lambda_{ASP} < \lambda_L$, energy conservation requires that phonons must have been extracted from the fiber via stimulated emission. This is direct evidence that anti-Stokes pumping contributes to stimulated emission, which is a new type of cooling effect that partly balances the QD heating introduced by the Stokes pump.

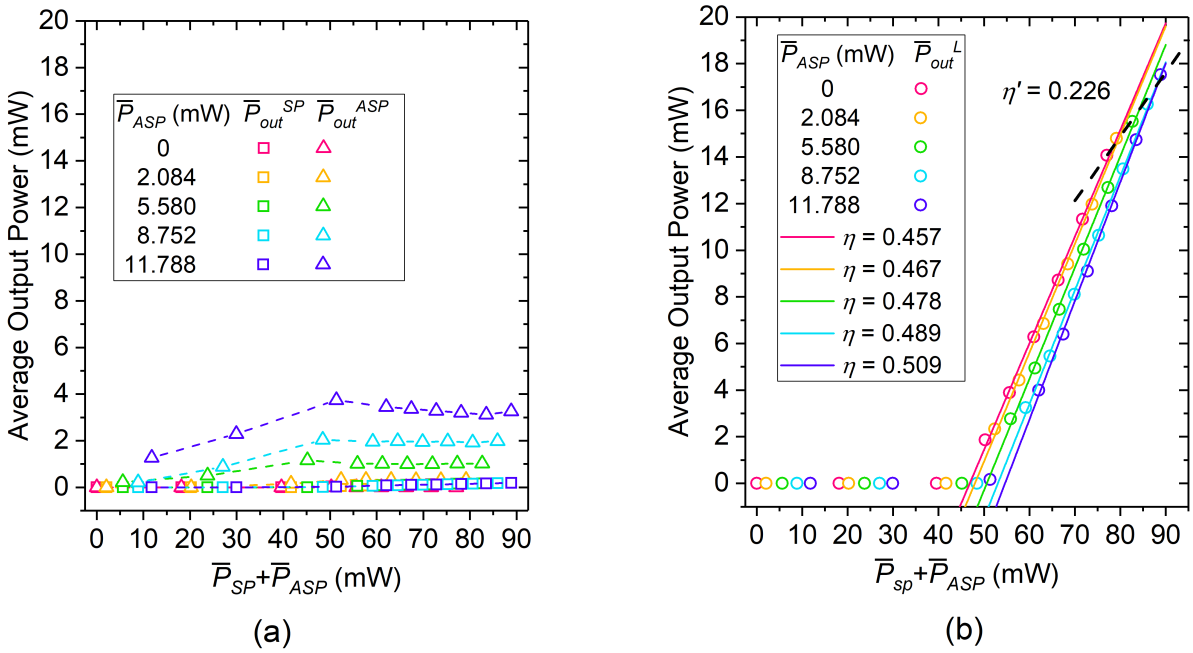

Fig. 4.10: Under the setting of Δt = 1 ms and f_{rep} = 400 Hz (a) average leakage SP and ASP power as a function of total average pump power, (b) average laser output power as a function of total average pump power. Two kinds of linear fit are provided, noted as η and η'.

This cooling effect is distinct from ASF cooling, wherein the pumping wavelength must be longer than the average spontaneous emission wavelength of the fiber. Instead, here λ_{ASP} can be selected to be any wavelength longer than the lasing wavelength, such as the example discussed above. As discussed above, ASF cooling requires the production of significant spontaneous emission, which usually is very weak in a deeply saturated amplifier or laser. Therefore, realizing a high power RBFL represents a challenging prospect. On the other hand, with the proposed multi-wavelength, excitation-balanced pumping scheme, thermal energy is carried away by the laser signal, garnering a significant improvement to the overall system efficiency relative to RBFLs. One drawback, however, is that the system must be operated in a pulsed region instead of CW.

To further quantify the effect of ASP on QD, and effective quantum defect (EQD) is defined as

$$EQD = QD_{SP} \times \frac{\bar{P}_{abs}{}^{SP}}{\bar{P}_{abs}{}^{SP} + \bar{P}_{abs}{}^{ASP}} + QD_{ASP} \times \frac{\bar{P}_{abs}{}^{ASP}}{\bar{P}_{abs}{}^{SP} + \bar{P}_{abs}{}^{ASP}} \tag{4.8}$$

where $QD_{SP} = 1 - \lambda_{SP}/\lambda_L$, $QD_{ASP} = 1 - \lambda_{ASP}/\lambda_L$, and $\bar{P}_{abs}{}^{SP}$ and $\bar{P}_{abs}{}^{ASP}$ are the absorbed pump powers for SP ans ASP, respectively, which are determined by taking the difference $\bar{P}_{abs}{}^{SP/ASP} = \bar{P}_{SP/ASP} - \bar{P}_{out}{}^{SP/ASP}$. The calculated EQDs with various pump power combinations are subsequently summarized in Fig. 4.11. The dashed line represents the value of QD_{SP}, and as can be seen, the EQD decreases with increasing $\bar{P}_{ASP}$, in line with the aforementioned cooling effect introduced by ASP. As expected, with increasing $\bar{P}_{SP}$ the EQD asymptotically approaches QD_{SP}. Similar analyses on the power data for all parameter settings were performed and the results for η, η', and EQD are summarized in Fig. 4.12.

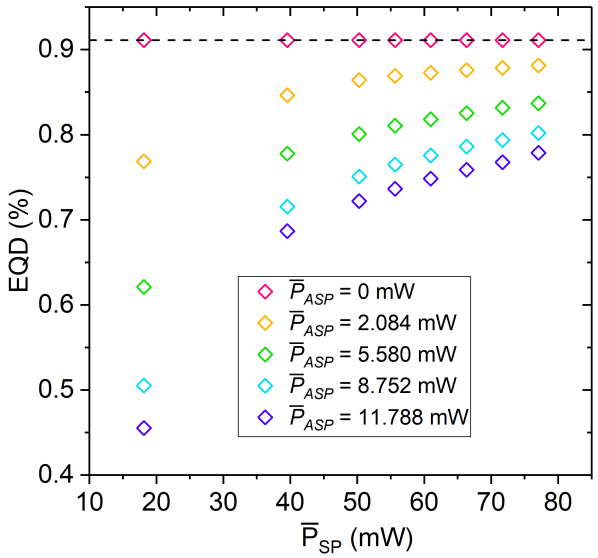

Fig. 4.11: Under the setting of Δt = 1 ms and f_{rep} = 400, the EQD at different pump powers.

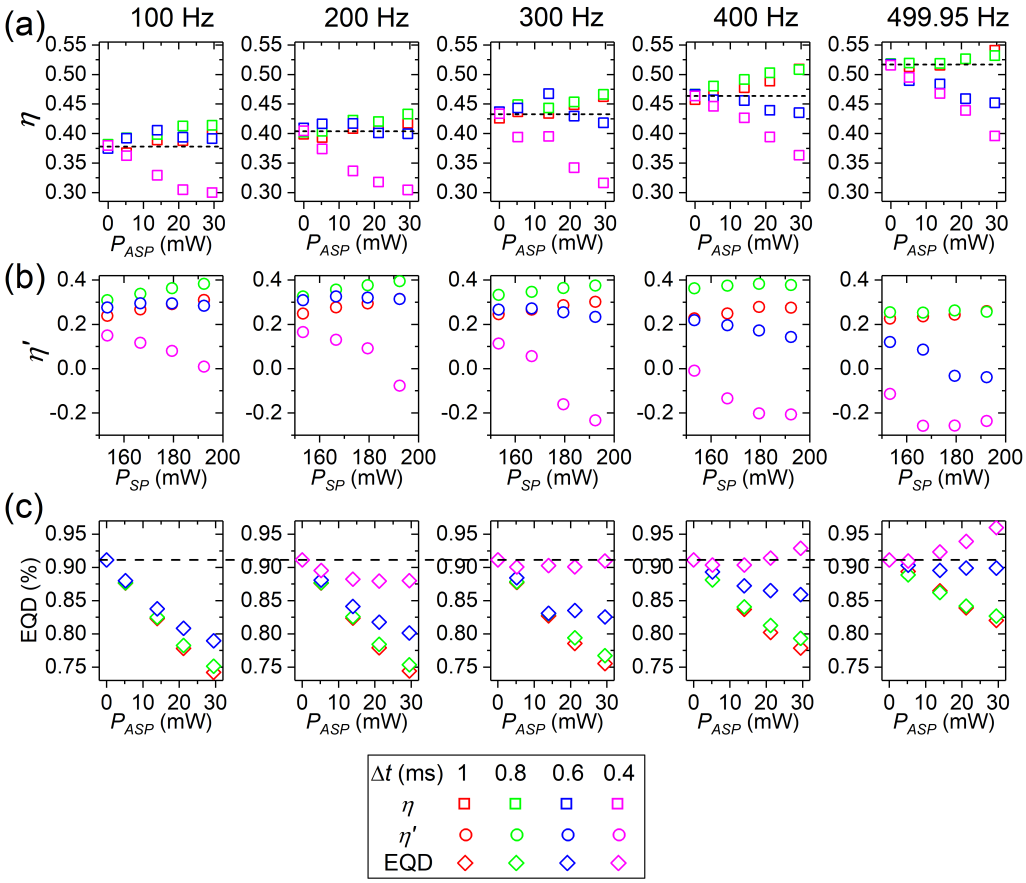

Fig. 4.12: Under the different parameter stated, the quantified (a) η, (b) η', (c) EQD.

Since η, η' and EQD all differs with different parameter setting, a dimensionless figure-of-merit (FOM) is proposed in order to compare these operating conditions:

$$FOM = \frac{\eta(1+\eta')}{EQD \times \frac{{P_{SP}}^{th}}{{P_{CW}}^{th}}} \tag{4.9}$$

in which η and ${P_{SP}}^{th}$ are the corresponding values using ${P_{ASP}}^{max}$, and η' and EQD are the corresponding values using ${P_{SP}}^{max}$. ${P_{CW}}^{th}$ is the threshold power when only SP is provided under CW operation, which is basically the laser demonstrated in Chapter 2. Its value is 70 mW. Using Eq. 4.9, the FOM in all the cases are summarized in Fig. 4.13. From the figure, it can be observed that when Δt = 0.8 ms and f_{rep} = 400 Hz, the FOM gives the greatest value of 72.27. As a

comparison, for the laser demonstrated in Chapter 2, after plugging in the corresponding η and EQD, considering η' to be 0, and seeing that the threshold term becomes unity, the FOM is calculated to be 69.25. Obviously, in the best case (Δt = 0.8 ms and f_{rep} = 400 Hz), the corresponding FOM surpasses that of the CW laser in Chapter 2, which while small, directly shows the potential of multi-wavelength pumping. It unequivocally demonstrates that an efficient laser may be constructed with reduced EQD for improved thermal management. It is important to point out that the results presented here are limited due to the limited available power from ASP. To further cement this assertion, referring back to Fig. 4.10 (b), where one can see that η increases roughly linearly with increasing $\bar{P}_{ASP}$. Furthermore, although the lasing threshold increases with an increased $\bar{P}_{ASP}$, the power curves appear to be converging to an intersect, beyond which the multi-wavelength pumped system with the highest $\bar{P}_{ASP}$ will have the largest optical-to-optical conversion efficiency.

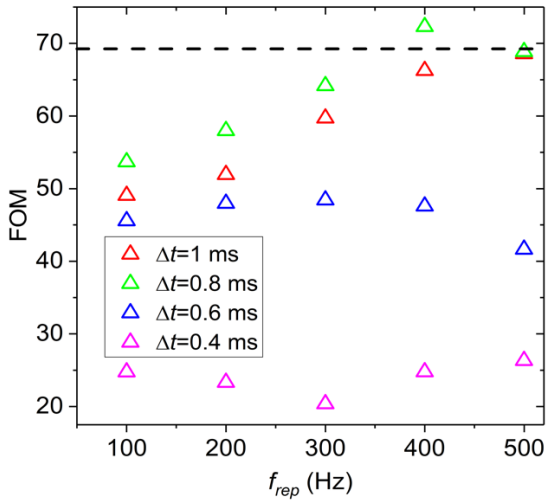

Fig. 4.13: Under the different parameter stated, the quantified FOM.

Up to this point, the idea of excitation-balancing has been demonstrated experimentally and theoretically. However, the power level in the previous experiments is relatively low and it is

more meaningful to discuss the power scaling possibility. Limited by the available high-power equipment, the discussion below is based on the FDTD simulations. However, since in previous discussions the FDTD code gives confidence on its results, the simulations below should also be meaningful and provide instructions for future design of excitation-balanced fiber lasers and amplifiers.

In the above experiments and simulations, core-pumping was applied at relatively low energy levels. Realistically, however, to scale the pulse energy (and commensurate average power) to mJ level, cladding pumping should be considered. In the meantime, the pulse width in previous setup is on the ms scale, which is relatively long in most pulse laser applications. Here, ns scale pulse width is assumed so that it suits more application needs. Figure 4.14 (a) provides a schematic of the proposed experimental setup. The active medium is a double-clad Yb-doped fiber. The SP and ASP, with operating wavelengths of λ_{SP} and λ_{ASP}, respectively, are coupled into the inner cladding of the active fiber via a combiner. The signal, with an operating wavelength of λ_{SIG}, is coupled into the core of the active fiber via the same combiner. Then, the active fiber is spliced to a cladding mode stripper (CMS) to remove the unabsorbed pump energies. Finally, there is an output end cap to reduce the light intensity at the air-glass interface. The two pumps and the signal are all pulsed, and the timing between them is precisely controlled in a way that is illustrated in Fig. 4.14 (b). Specifically, it is assumed that the rise times related to the timing control of both pumps are short compared to the pulse width so that the pump pulses are rectangularly shaped. The signal pulse, however, is taken to be Gaussian instead of rectangular. The ASP pulse first arrives with a peak power of P_{ASP} and a duration of t_{ASP}. This is followed by the SP pulse which has a peak power of P_{SP} and duration of t_{SP}. The signal pulse enters lastly with a peak power of P_{SIG} and a full width half maximum (FWHM) of t_{SIG}. The time between the end of the SP pulse

and the peak of the signal pulse is dt_1, and the time between the end of the SP pulse and the peak of the signal pulse is dt_2. Finally, following the signal pulse, no input is provided until the arrival of the next ASP pulse, the timing of which is set by the system repetition rate f_{rep}. The aforementioned parameters all serve as inputs to the simulations and their effects on laser behavior are discussed in detail.

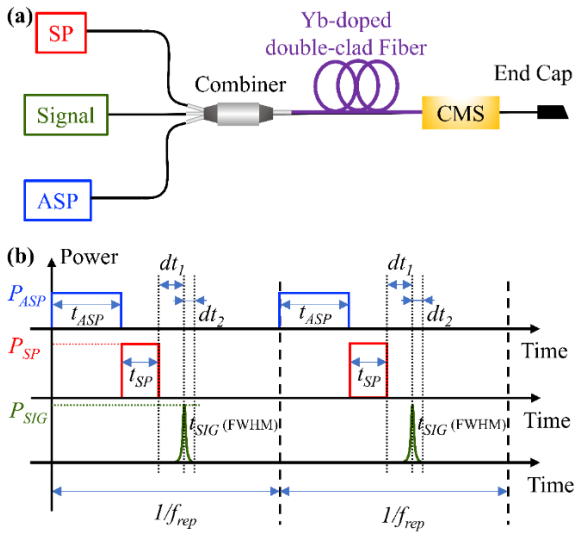

Fig. 4.14: (a) Proposed experimental setup, (b) Time settings for ASP, SP, and signal input (not to scale). The ASP pulse is rectangularly shaped with a pulse width of t_{ASP} and arrives at t = 0. Right after the ASP pulse ends, the rectangularly shaped SP pulse arrives with a pulse width of t_{SP}. Then, the Gaussian shaped signal pulse enters with a FWHM of t_{SIG}. The time between the end of the SP pulse and the peak of the signal pulse is dt_1, and the time between the end of the SP pulse and the peak of the signal pulse is dt_2. The system runs at a rep rate of f_{rep}.

Similar to the excitation-balanced fiber laser, the pump and signal power evolution are all functions of time and position (along the fiber). Therefore, to fully simulate the problem, a FDTD model is invoked. The FDTD model here is based on what has been discussed above, but with some modification to take the signal into account. To simply the expressions below, the first ASP pulse is assumed to arrive at $t = 0$, and a subscript i is defined to be

$$i \Rightarrow \begin{cases} ASP & nf_{rep}^{-1} \le t < nf_{rep}^{-1} + t_{ASP} \\ SP & nf_{rep}^{-1} + t_{ASP} \le t < nf_{rep}^{-1} + t_{ASP} + t_{SP} \\ SIG & f_{rep}^{-1} + t_{ASP} + t_{SP} \le t < nf_{rep}^{-1} + t_{ASP} + t_{SP} + dt_1 + dt_2 \end{cases} \quad n = 1,2,3,\cdots\cdots \tag{4.10}$$

which changes with time within a pumping cycle, and where n refers to the n^{th} pumping cycle. It is necessary to point out that ASE is neglected here mainly because the signal pulse width is much shorter compared to the pumping cycle. For example, in the examples below the pulse width is 10 ns, whereas the pumping cycle is 100 μs. To solve for the various powers, the upper state Yb^{3+} population ($N_1(z,t)$) is again an important intermediate parameter and can be calculated based on the rate equations

$$\frac{\partial N_1(z,t)}{\partial t} = -\frac{N_1(z,t)}{\tau} + \frac{I_i(z,t)\sigma_i^a \lambda_i}{hc}[\rho - N_1(z,t)] - \frac{I_i(z,t)\sigma_i^e \lambda_i}{hc} N_1(z,t) \tag{4.11}$$

in which τ is the upper state lifetime, σ_i^e and σ_i^a are the emission and absorption cross sections at the corresponding wavelengths λ_i, h is Planck's constant, c is the speed of light, and ϱ is the fiber Yb^{3+} concentration (m^{-3}). $I_i(z,t)$ is the light intensity and can be calculated as

$$I_i(z,t) = \begin{cases} \dfrac{P_{ASP}(z,t)}{\pi r_{clad}^2} & i \Rightarrow ASP \\ \dfrac{P_{SP}(z,t)}{\pi r_{clad}^2} & i \Rightarrow SP \\ \dfrac{P_{SIG}(z,t)}{A_{eff}} & i \Rightarrow SIG \end{cases} \tag{4.12}$$

where r_{clad} is the radius of the inner cladding of the active fiber, and A_{eff} is the effective mode area of the active fiber. Note that any slight perturbation due to the presence of a shaped cladding is neglected here. Then, time t is discretized into small steps of Δt and the forward differencing formula is applied to estimate $\dfrac{\partial N_1(z,t)}{\partial t}$. As a result, Eq. 4.11 becomes

$$\frac{N_1(z,t+\Delta t)-N_1(z,t)}{\Delta t}=-\frac{N_1(z,t)}{\tau}+\frac{I_i(z,t)\sigma_i^{\,a}\lambda_i}{hc}[\rho-N_1(z,t)]-\frac{I_i(z,t)\sigma_i^{\,e}\lambda_i}{hc}N_1(z,t) \qquad (4.13)$$

which can be further simplified to

$$N_1(z,t+\Delta t)=N_1(z,t)+\Delta t\left[-\frac{N_1(z,t)}{\tau}+\frac{I_i(z,t)\sigma_i^{\,a}\lambda_i}{hc}[\rho-N_1(z,t)]-\frac{I_i(z,t)\sigma_i^{\,e}\lambda_i}{hc}N_1(z,t)\right. \qquad (4.14)$$

For the evolution of pump powers, the governing equation is

$$\frac{\partial P_i(z,t)}{\partial z}=P_i(z,t)\times\left\{\Gamma_i\left\{N_1(z,t)\sigma_{Pi}^{\,e}-\left[\rho-N_1(z,t)\right]\sigma_{Pi}^{\,a}\right\}-\alpha\right\} \qquad (4.15)$$

in which α is the absorptive background loss in the fiber, and Γ_i is the overlap integral between the light and Yb^{3+} ions. Specifically, when $i \Rightarrow ASP$ or $i \Rightarrow SP$, $\Gamma_i = r_{core}^{\,2} / r_{clad}^{\,2}$, where r_{core} is the core radius. When $i \Rightarrow SIG$, Γ_i can be calculated based on the mode in the fiber. It is necessary to point out absorptive background loss is considered to be 100% thermal, meaning that all the absorbed optical energy because of α turns into thermal energy. Background scattering loss is neglected here. Next, distance z is discretized into small steps of Δz and the forward differencing formula is employed to estimate $\frac{\partial P_i(z,t)}{\partial z}$. As a result, Eq. 4.15 is finally simplified to

$$P_i(z+\Delta z,t)=P_i(z,t)\exp\left\{\Gamma_i\Delta z\left\{N_1(z,t)\sigma_{Pi}^{\,e}-\left[\rho-N_1(z,t)\right]\sigma_{Pi}^{\,a}\right\}-\alpha\Delta z\right\} \qquad (4.16)$$

It is necessary to point out that during the time where no input is provided, only spontaneous emission remains so that Eq. 4.13 reduces to $\partial N_1(z,t)/\partial t = -N_1(z,t)/\tau$, and there is no output power. The initial conditions for $P_i(z,t)$ at z = 0 are determined by the corresponding input settings. The boundary condition for $N_1(z,t)$ is $N_1(z,t)|_t = N_1(z,t)|_{t+1/f_{rep}}$, indicating that N_1 will return to the same value after each pump cycle. An assumption was made that the pulse propagation time through Δz is infinitesimal when compared with the rate at which the upper state is populated. This is implemented in the simulations below by setting a sufficiently small Δz. With these into

conditions, as well as Eq. 4.14 and Eq. 4.16, $P_i(z,t)$ and $N_1(z,t)$ for the entire time period and fiber length can be solved. In addition, at each step, the power difference introduced by α is recorded so that at the end of the simulation the total energy lost from background loss can be quantified.

Next, an example simulation is presented. First, the fiber geometry and optical parameters are required inputs to the model. In the example shown below, as well as in the next section, the fiber is assumed to have a core radius (r_{core}) of 15 μm and a cladding radius (r_{clad}) of 62.5 μm. The core is assumed to have a step-index refractive index profile with NA = 0.05, from which A_{eff} and Γ_{SIG} are calculated using an in-house mode solver [69]. The absorption and emission cross sections are adapted from the aluminosilicate fiber data found in [47]. It is necessary to point out that measuring the absorption cross section of the long-wavelength tail of the Yb^{3+} can be challenging. As a result, any errors in the cross-section values may necessarily impart errors on the analysis below. The Yb^{3+} concentration (ϱ) is assumed to be $2 \times 10^{26}/m^3$, the lifetime (τ) to be 850 μs, and the absorptive background loss to be 10 dB/km. For the present example, λ_{SP}, λ_{SIG}, and λ_{ASP} are selected to be 1010 nm, 1020 nm, and 1035 nm. Finally, the settings for P_{ASP}, P_{SP}, P_{SIG}, t_{ASP}, t_{SP}, t_{SIG}, dt_1 , and f_{rep} are summarized in Table 4.2.

Table 4.2: Parameters and Values Employed

Parameters	P_{ASP} (W)	P_{SP} (W)	P_{SIG} (W)	t_{ASP} (μs)	t_{SP} (μs)	t_{SIG} (ns)	dt_1 (ns)	f_{rep} (Hz)
Values	500	500	1000	40	20	10	30	10

With the above parameters as inputs, the various power [$P_{ASP}(z,t)$, $P_{SP}(z,t)$, and $P_{Sig}(z,t)$] and upper state concentration [$N_1(z,t)$] are all calculated. First, an optimized fiber length is determined from the standpoint of maximizing the output signal energy, E_{SIG}^{out}, which is calculated by integrating the signal output power $P_{SIG}(t)$ over time. For this specific case, the output signal

energy versus fiber length is shown in Fig. 4.15 (a), from which a maximum E_{SIG}^{out} is found to be 1.27 mJ at an optimized fiber length (L_{op}) of 3.21 m. With respect to the input pulse energy (E_{SIG}^{in}), the amplification is calculated to be 22.2 dB.

To better understand the reason for the existence of L_{op}, $N_1(z)$ at the time when the ASP pulse ends (t = 40 μs), the SP pulse ends (t = 60 μs), and the signal pulse ends (t = 60.06 μs) are each shown in Fig. 4.15 (b). As can be observed, after 40 μs of ASP excitation, $N_1(z)$ is almost uniform with only a small decrease along the maximum simulated fiber length (5 m). The decrease results from absorption, such that more pump power is available at the earlier parts of the fiber. Then, after 20 μs of ASP excitation, N_1 is increased. However, as a result of the higher absorption cross section at λ_{SP}, $N_1(z)$ is far less uniform along the 5 m of fiber. Finally, when the signal pulse arrives it quickly depletes N_1. It is necessary to point out that during the ASP and SP pumping time period (0 - 60 μs), the maximum achievable N_1 is relatively low compared to ρ. The reason lies in the transparency limit. Specifically, if one assumes an infinite power at wavelength λ_i, and taking Eq. 4.12 into the steady state while neglecting the spontaneous emission term, the maximum avaliable N_1 (i.e., the transparency limit, N_i^{tran}) is

$$N_i^{tran} = \frac{\rho \sigma_i^a}{(\sigma_i^a + \sigma_i^e)} \tag{4.17}$$

In present example, N_i^{tran} is calculated to be $1.08 \times 10^{25}/m^3$ and $3.17 \times 10^{25}/m^3$ for the ASP and SP, respectively. In Fig. 4.15 (b), these transparency levels are shown as dashed lines, and it is clearly simulated that N_1 never exceeds the transparency limit for either of the two pumps. Using the same equation, the signal transparency is calculated to be $2.09 \times 10^{25}/m^3$ and is shown as the green dashed line in Fig. 4.15 (b), which intersects the solid red curve ($N_1(z, t = 60$ μs)) at L_{op}.

Since the signal can only be amplified when N_1 is greater than the signal transparency population, gain becomes unavailable for $z > L_{op}$, and thus the signal will suffer from reabsorption and therefore the energy decreases. As such, the intersection of signal transparency level and the solid red curve represents a convenient way to obtain L_{op}.

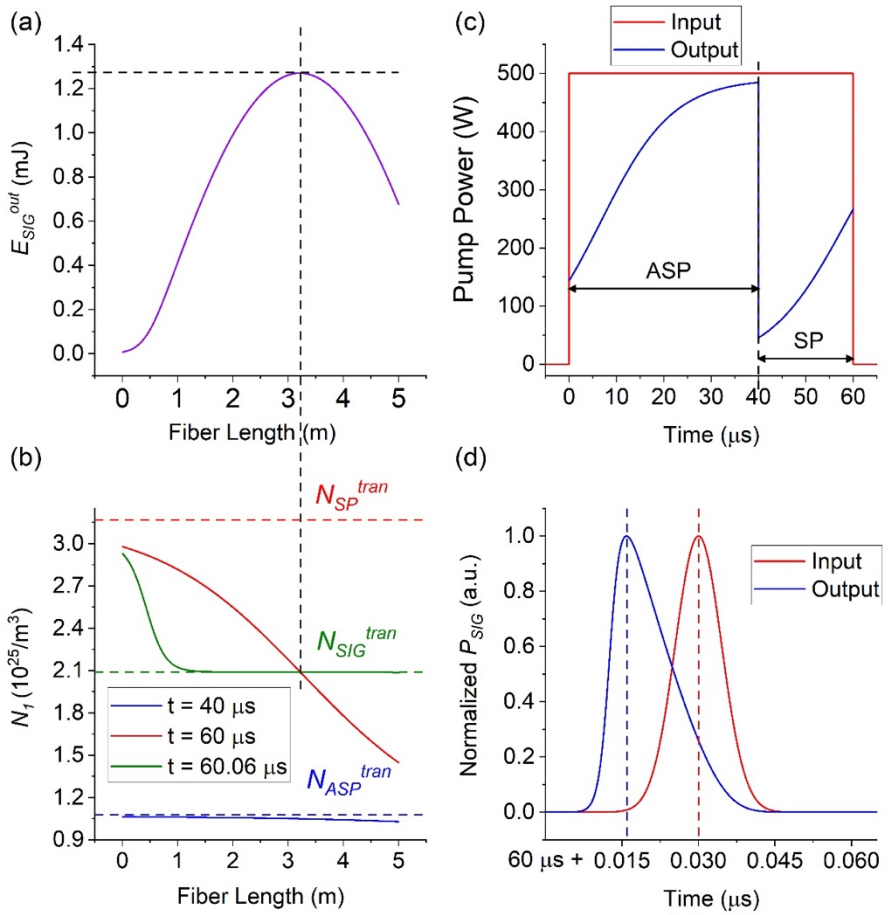

Fig. 4.15: For the example simulation, the calculated (a) output signal pulse energy versus fiber length, (b) upper state concentration, $N_1(z)$, at t = 40 μs, 60 μs, and 60.06 μs (solid lines) along with the transparency level at λ_{ASP}, λ_{SP}, and λ_{SIG} (dashed lines), (c) input and output ASP and SP power versus time, and (d) normalized input and output signal power versus time. Note that in (d), the abscissa origin is at $t = 60\ \mu$s, when the SP pulse ends in (b).

Next, the corresponding P_{ASP} (L_{op}, t) and P_{SP} (L_{op}, t) are shown in Fig. 4.15 (c). For comparison, the input P_{ASP} (0, t) and P_{SP} (0, t) are also shown. From Fig. 4.15 (c), both pumps exhibit energy leakage, while the corresponding total absorbed energy can be quantified by taking

the difference between the input (E_{ASP}^{in} or E_{SP}^{in}) and output energies. For the present example, the absorbed ASP (E_{ASP}^{ab}) and SP (E_{SP}^{ab}) energies are 4.90 mJ and 7.23 mJ, respectively, from which the optical-optical conversion efficiency ($\eta_{O\text{-}O}$) can be quantified to be

$$\eta_{O-O} = \frac{E_{SIG}^{out} - E_{SIG}^{in}}{E_{ASP}^{ab} + E_{SP}^{ab}} \approx 10.4\% \tag{4.18}$$

In terms of wall-plug efficiency (η_W), it can be calculated

$$\eta_W = \frac{E_{SIG}^{out} - E_{SIG}^{in}}{E_{ASP}^{in} + E_{SP}^{in}} \approx 4.21\% \tag{4.19}$$

Next, to investigate pulse shaping in the amplifier the normalized input and output signal pulses ($P_{SIG}(0, t)$, $P_{SIG}(L_{op}, t)$, respectively) are shown in Fig. 4.15 (d). It can be seen that the peak of the output pulse occurs earlier in time relative to that of the original pulse. This results from the rapid depletion of the upper state early in time, with the later parts of the pulse therefore experiencing less gain relative to the beginning of the pulse. The output peak appears at t_{peak} = 15.87 ns after the SP ends, whereas the input peak position is determined by dt_1, which is 30 ns in this example. The influence from different parameters on t_{peak} is discussed in more detail later in this chapter.

Finally, the thermal energy generated is quantified. Although it is true that thermal energy can be generated either during the process of spontaneous emission (as a result of the energy difference between the pump photons and the spontaneous emission photons), or when pump power is lost due to background absorption, the time scales corresponding to these process (τ, t_{SP}, t_{ASP}) are much longer compared to t_{SIG}. As a result, the most rapid temperature change is expected to happen during the process of pulse amplification, which is when thermal effects such as thermal lensing or TMI are most likely to happen. Therefore, only the thermal energy generated during the

pulse amplification process is calculated here. In that process, the signal quickly depletes any available population inversion resulting in stimulated emission. Meanwhile, there will also be some signal loss due to background absorption, which is considered to contribute 100% to thermal energy. Once absorbed, ASP and SP photons are both equally likely to contribute to stimulated emission. Therefore, the total thermal energy (E_t) produced from one signal pulse can be calculated by

$$E_t = N_{SIG} \times \frac{{E_{ASP}}^{ab}}{{E_{ASP}}^{ab} + {E_{SP}}^{ab}} \times hc\left(\frac{1}{\lambda_{ASP}} - \frac{1}{\lambda_{SIG}}\right) + N_{SIG} \times \frac{{E_{SP}}^{ab}}{{E_{ASP}}^{ab} + {E_{SP}}^{ab}} \times hc\left(\frac{1}{\lambda_{SP}} - \frac{1}{\lambda_{SIG}}\right) + E_\alpha \quad (4.20)$$

where E_α is the total background signal energy loss during this time period. N_{SIG} is the total number of generated signal photons and can be calculated using

$$N_{SIG} = \frac{({E_{SIG}}^{out} - {E_{SIG}}^{in})}{hc / \lambda_{SIG}} \quad (4.21)$$

The first term on the right-hand side of Eq. 4.20 gives the cooling from the ASP while the second term corresponds to heating from the SP. In the example here, E_t is calculated to be 0.06 μJ. Specifically, the thermal contribution from ASP (first term in Eq. 4.20), SP (second term in Eq. 4.20), and E_α are -7.39, 7.45, and 0.0015 μJ, respectively. From the results, it can be observed that ASP and SP contributes negative and positive thermal energy to the system, respectively, and E_α is negligible compared to the absolute thermal contribution from ASP and SP. The influence of input parameters on E_t is discussed in greater detail later in this chapter.

As a phased summary, discussed so far is the theory of the FDTD model and one example simulation has been provided. The analysis approach to the simulation results was described in the context of various calculated output parameters, including ${E_{SIG}}^{out}$, L_{op}, t_{peak}, $\eta_{\text{O-O}}$, η_{W}, E_t, etc. In the following discussion, the influence of several input parameters on amplifier performance is

discussed, which can serve as a guide for system optimization. For convenience, the parameters used here in this example will be referred as “test example” for the remaining of this chapter.

The influence from P_{ASP} is first investigated. Using the same input parameters as the test example, P_{ASP} is varied in the simulation. First, as was done above, $N_1(z)$ at the time when the ASP pulse ends (t = 40 μs) and the SP pulse ends (t = 60 μs) are shown in Fig. 4.16 (a) and 4.16 (b), respectively. Similar to the previous section, the corresponding N_{ASP}^{tran}, N_{SP}^{tran}, and N_{SIG}^{tran} are also shown. From Fig. 4.16 (a), it can be observed that with increasing P_{ASP}, more total Yb^{3+} ions are excited to the upper state. However, when P_{ASP} exceeds about 500 W, the N_1 distribution remains almost uniform along the fiber length of interest (5 m) because of the transparency limit. In other words, almost all the Yb^{3+} ions in 5 m of the fiber are excited to N_{ASP}^{tran} so that further increases in P_{ASP}, beyond about 500 W, will not change $N_1(z)$ significantly, while pump leakage increases substantially. This will later be referred to as “ASP saturation”. As a result of the “head start” introduced by the increasing P_{ASP}, more Yb^{3+} ions are excited to the upper state at t = 60 μs (see Fig. 4.16 (b)). However, as a result of ASP saturation, $N_1(z)$ remains almost unchanged as P_{ASP} is increased beyond about 500 W. As discussed in the previous section, the corresponding fiber length at the intersection of N_{SIG}^{tran} and $N_1(t$ = 60 μs, $z)$ gives the L_{op} for the amplifier. Utilizing this approach, as can be observed in Fig. 4.16 (b), L_{op} increases with increasing P_{ASP}, and remains almost the same after ASP saturation. L_{op} is summarized in Fig. 4.16 (c).

Next, at their corresponding L_{op} values, E_{ASP}^{ab}, E_{SP}^{ab} and E_{SIG}^{out} are summarized in Fig. 4.16 (c) (right-side vertical axis). In the figure, it can be observed that as P_{ASP} increases, E_{ASP}^{ab}, E_{SP}^{ab} and E_{SIG}^{out} all follow a similar trend, that they first increase, then reach an asymptotic value. The asymptotes, as before, result from saturation. The reason is twofold. First, as discussed earlier, L_{op} follows a similar trend, which is beneficial for absorbing more pump energy and the transfer

those to signal amplification. Second, a greater P_{ASP} is beneficial to excite more Yb^{3+} ions within the same time and fiber length, therefore more signal output energy. With these two reasons combined, the E_{ASP}^{ab}, E_{SP}^{ab} and E_{SIG}^{out} follow the trend as observed in Fig. 4.16 (c).

Next, the $\eta_{O\text{-}O}$ and η_W are quantified as shown in Fig. 4.16 (d). As P_{ASP} increases, the efficiency first increases because of the increase in E_{SIG}^{out}, then drops because most of the additional pump energy just leaks out instead of being absorbed. A maximum $\eta_{O\text{-}O}$ of ~10.4% is observed at P_{ASP} = 500 W, and a maximum of η_W of 5.5% is observed at P_{ASP} = 200 W. Then, the total generated thermal energy E_t is quantified and summarized in Fig. 4.16 (e). Obviously, with increasing P_{ASP}, E_t decreases and at P_{ASP} = 800 W, to a negative value. This means that during the process of generating the ~1.3 mJ pulse, instead of generating thermal energy, energy are actually extracted from the fiber and the fiber cools. Finally, pulse shaping is investigated and summarized in Fig. 4.16 (f). Similar to previously, pulse shaping is always observed, with the peak of the output signal appearing earlier than that of the input signal pulse. It can be seen that t_{peak} first decreases with increasing P_{ASP}, then reaches an asymptotic value when P_{ASP} exceeds about 500 W. The reason is, as analyzed above, that the N_1, P_{ASP}, P_{SP}, and P_{SIG} distributions become nearly invariant after P_{ASP} exceeds 500 W.

Next, the influence from E_{SIG}^{in} is investigated. To do so, the same input parameters as the test example are used, with the only change to be P_{SIG}. In other words, the input pulse shapes all remain Gaussian with the same FWHM and dt_1 (see Fig. 4.14) values, while only the peak power varies and therefore the input pulse energy, E_{SIG}^{in}, changes correspondingly. Since the system runs at a low f_{rep} of 10 Hz, which corresponds to a 100 ms period (much longer than the fluorescence lifetime), there are almost no remaining excited Yb^{3+} ions when the ASP pulse arrives in the fiber at the beginning of a pumping cycle. As a result, N_1 at the time when the ASP pulse ends

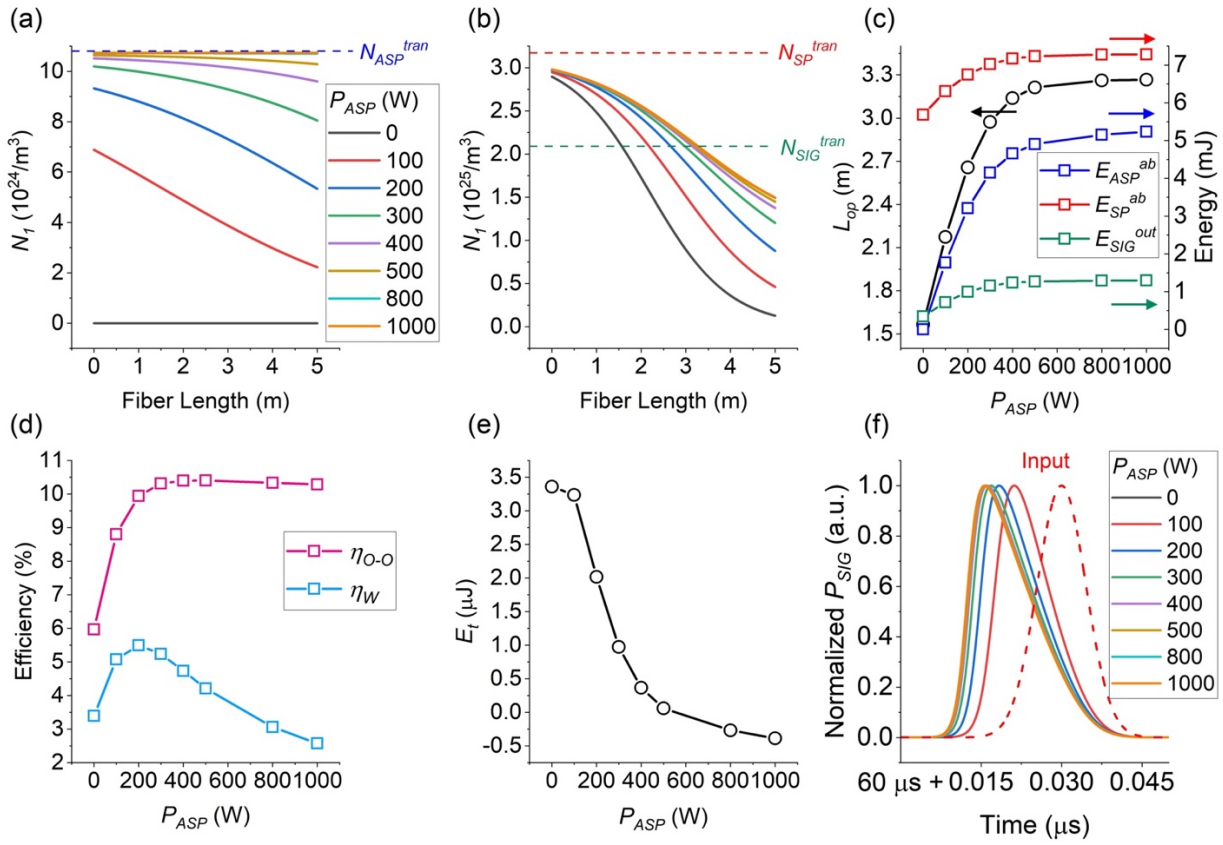

Fig. 4.16: With increasing P_{ASP}, the quantified (a) $N_1(z)$ at t = 40 μs, (b) $N_1(z)$ at t = 60 μs (the corresponding transparency levels are also shown), (c) optimized fiber length (L_{op}), absorbed ASP and SP energies (E_{ASP}^{ab}, E_{SP}^{ab}), and output signal energy (E_{SIG}^{out}), (d) the optical to optical efficiency ($\eta_{O\text{-}O}$) and wall-plug efficiency (η_W), (e) total generated thermal energy (E_t), and (f) the change of pulse shape.

(t = 40 μs) and when the SP pulse ends (t = 60 μs) are independent of E_{SIG}^{in}, therefore also making the E_{ASP}^{ab}, E_{SP}^{ab} independent of E_{SIG}^{in}. This is confirmed in the simulation and the results for $N_1(z)$ at t = 40 μs and t = 60 μs are shown in Fig. 4.17 (a). On the other hand, when the signal pulse ends (t = 60.06 μs), $N_1(z)$ is found to be strongly dependent upon E_{SIG}^{in}. These results are also shown in Fig. 4.17 (a). For the case where E_{SIG}^{in} = 0, $N_1(z)$ at t = 60 μs and 60.06 μs are almost identical (i.e., overlapping) since the only process to depopulate N_1 is spontaneous emission and over 60 ns little fluorescence can be produced. Then, with increasing E_{SIG}^{in} into the system, not only is N_1 depopulated faster, but also more population inversion is used to amplify the signal. As a result,

greater E_{SIG}^{out} is produced by the system, as can be seen in Fig. 4.17 (b). During the signal amplification process, however, this leads to increased QD heating and therefore E_t also increases with increasing E_{SIG}^{in}, as shown in Fig. 4.17 (b). It can also be observed that neither E_{SIG}^{out} nor E_t increases linearly with E_{SIG}^{in}. The main reason for this is the limited excited population that can be achieved at the pumping wavelengths. This eventually limits the maximum extractable pulse energy from a length of fiber.

The system efficiency is also investigated. As discussed above, the E_{ASP}^{ab}, E_{SP}^{ab}, E_{ASP}^{in} and E_{SP}^{in} are all independent of E_{SIG}^{in}, while E_{SIG}^{out} increases with increasing E_{SIG}^{in}. As a result, from Eqs. 4.18 and 4.19, it can be concluded that both the $\eta_{\text{O-O}}$ and η_{W} will increase with E_{SIG}^{in}, as is confirmed in Fig. 4.17 (c). Finally, pulse shaping results are summarized in Fig. 4.17 (d). Similar as before, pulse shaping is observed in all cases and the peaks of the output signal all appear earlier than that of the input signal pulse. t_{peak} can also be seen to reach an asymptotic value as E_{SIG}^{in} is increased.

Next, t_{ASP} becomes the variable while all the other input parameters remain the same as in the test example. As before, $N_1(z)$ at the times when the ASP and SP pulses end are shown in Fig. 4.18 (a) and 4.18 (b), respectively. As seen from Fig. 4.18 (a), with increasing t_{ASP}, more Yb^{3+} ions are excited into the upper state. However, $N_1(z)$ remains almost unchanged when t_{ASP} is increased to beyond 40 μs, again as a result of the transparency limit. Similar trends are observed in Fig. 4.18 (b). Next, L_{op} is quantified and is shown in Fig. 4.18 (c), again matching the results speculated from Fig. 4.18 (b) from the standpoint of the intersection of N_{SIG}^{tran} and $N_1(z)$ when SP pulse ends.

Then, in each case, the energies E_{ASP}^{ab}, E_{SP}^{ab} and E_{SIG}^{out} are calculated at their corresponding L_{op}, and the results are summarized in Fig. 4.18 (c) (right-hand vertical axis). As shown in the figure, as t_{ASP} increases, E_{ASP}^{ab}, E_{SP}^{ab} and E_{SIG}^{out} all follow a similar trend of a rapid

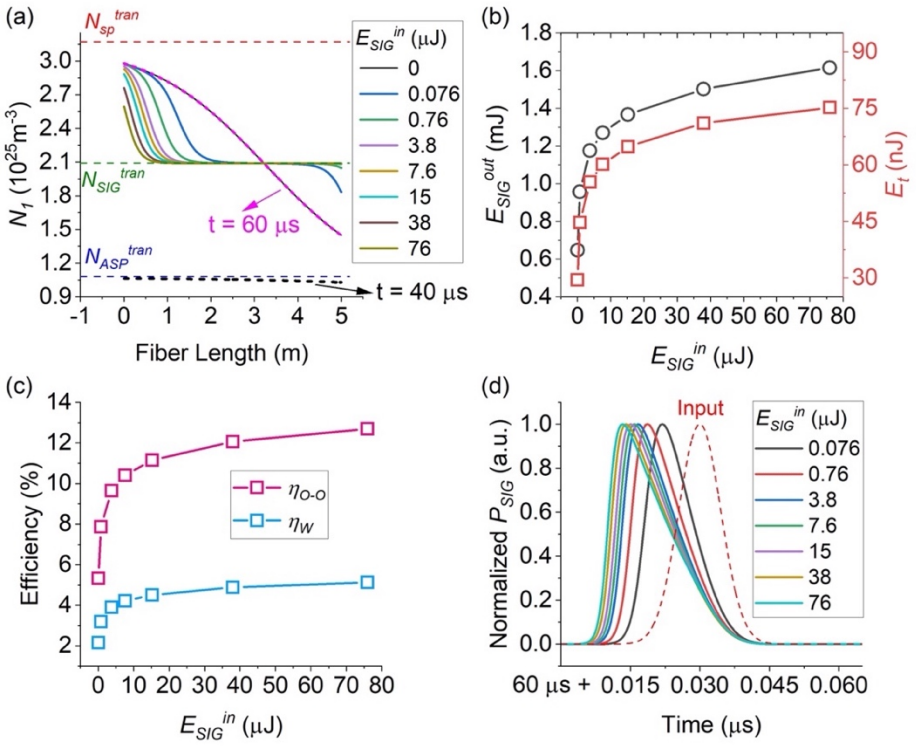

Fig. 4.17: With increasing E_{SIG}^{in}, the quantified (a) upper state population at t = 40 µs (black dashed line), t = 60 µs (pink dashed line), and t = 60.06 µs (solid lines), (the corresponding transparency levels for ASP, ASP, and signal are also shown), (b) output signal energy (E_{SIG}^{out}) and total generated thermal energy (E_t), (c) the optical to optical efficiency ($\eta_{O\text{-}O}$) and wall-plug efficiency (η_W), (d) evolution of the pulse shape.

increase at first then "saturating" beyond some value. The initial slope can be understood from two standpoints. First, L_{op} follows a similar trend, and a longer L_{op} is helpful to absorb more pump energy, which can subsequently be transferred to signal energy. Second, a longer t_{ASP} is beneficial in that it excites more Yb^{3+} ions for a fixed fiber length, and therefore more population is available for signal amplification. The saturation occurs because, regardless of t_{ASP} and fiber length, transparency at the signal wavelength can never be reached with the ASP alone. The net gain, therefore, is driven largely by E_{SP}^{in} which in this case is fixed.

Next, both the η_W and $\eta_{O\text{-}O}$ are calculated and are shown in Fig. 4.18 (d). Both efficiencies have maximum values, beyond which $\eta_{O\text{-}O}$ remains at a similar level while droppes because the additional pump energy just leaks out. A maximum $\eta_{O\text{-}O}$ of ~10.4% is observed at t_{ASP} = 30 μs, and a maximum of η_W of 5.5% is observed at t_{ASP} = 20 μs. Next, E_t is calculated for each case and shown in Fig. 4.18 (e). When t_{ASP} increases, E_t decreases monotonically and when t_{ASP} = 50 μs and above, E_t becomes negative. Again, this indicates that instead of generating heat during the signal amplification process, the fiber actually cools, elinimating any thermal-related problems. Finally, the evolution of the pulse shape is shown in Fig. 4.18 (f). Once again, t_{peak} first decreases, then reaches an asymptotic value as a result of ASP saturation.

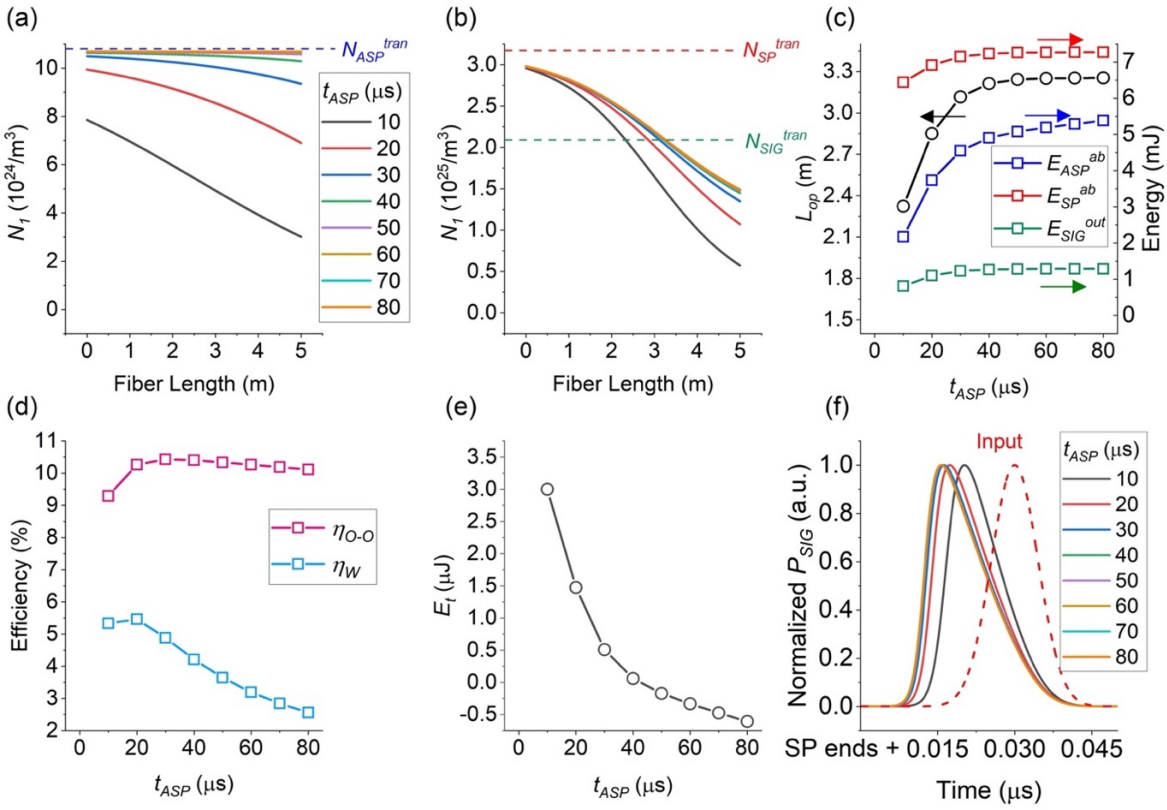

Fig. 4.18: With increasing t_{ASP}, the quantified (a) upper state population when the ASP pulse ends, (b) upper state population when the SP pulse ends (the corresponding transparency levels are also shown), (c) optimized fiber length (L_{op}), absorbed ASP and SP energy (E_{ASP}^{ab}, E_{SP}^{ab}), and output signal energy (E_{SIG}^{out}), (d) the optical to optical efficiency ($\eta_{O\text{-}O}$) and wall-plug efficiency (η_W), (e) total generated thermal energy (E_t), and (f) evolution of the pulse shape.

Next, the influence from dt_1 is investigated. Using the same input parameter as in the test example with varying dt_1, simulations are performed. Since the pump energies and timing are the same in all cases, and given the long period, the population inversion (and therefore also E_{ASP}^{ab} and E_{SP}^{ab}) when the signal arrives will be independent of dt_1. For the signal pulse, as long as dt_1 is much shorter than the fluorescence lifetime, which is usually the case in pulse amplifiers, the population inversion will remain at basically at the same level because the loss from spontaneous emission is negligible. Therefore, no matter when the pulse arrives, the amplification process will remain the same, leading to the same E_{SIG}^{out} and further to the same $\eta_{\text{O-O}}$, $\eta_{\text{W.}}$, and E_t, independent of dt_1 when it is much shorter than τ. This was confirmed via the simulations and the relevant values are summarized in Table 4.3.

Table 4.3: Output Parameters

Parameters	E_{ASP}^{ab} (mJ)	E_{SP}^{ab} (mJ)	E_{SIG}^{out} (mJ)	L_{op} (m)	$\eta_{O\text{-}O}$	η_W	E_t (μJ)
Values	4.9	7.59	1.27	3.213	10.4%	4.2%	0.06

From the pulse shaping standpoint, given the above arguments, the output pulse shape should also be independent of dt_1. This is shown in Fig. 4.19 (a). To provide a better view of the pulse shaping, the output pulses in all the cases have been translated in time to overlap at $t = 0$ s with the result shown in Fig. 4.19 (b). They are indistinguishable, further confirming the analysis above.

Up to this point, all the simulations run at $f_{rep} = 10$ Hz, which is typical of some commercial high-energy pulsed lasers. However, there are applications that require higher repetition rates and therefore this section explores this possibility. To do so, the same input parameters as before are

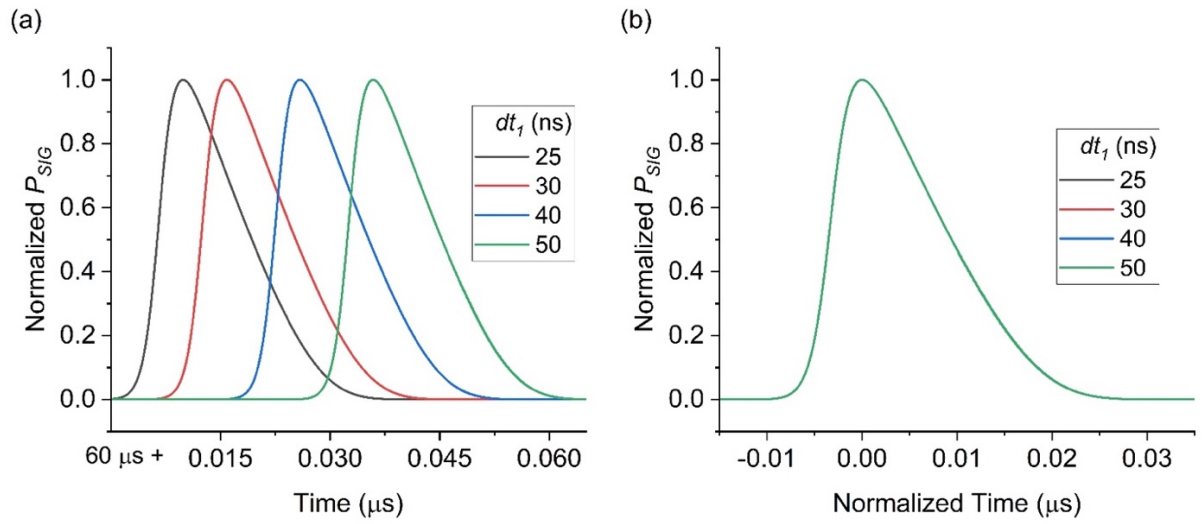

Fig. 4.19: With different dt_1, the simulated normalized output pulse versus (a) real time and, (b) normalized time.

once again employed, except with changes made only to f_{rep}. First, similar as before, $N_1(z)$ at the time when the ASP and SP pulses end are shown in Figs. 4.20 (a) and 4.20 (b), respectively. From the results, it can be seen that a higher repetition rate is only marginally beneficial in exciting more Yb^{3+} ions for both ASP and SP pumping. Since the intersection between N_{SIG}^{tran} and $N_1(t =$ 60 μs, z) is largely independent of f_{rep}, as shown in Fig. 4.20 (b), so is L_{op}.

Although $N_1(z)$ and L_{op} are largely independent of f_{rep}, the absorbed energy from the ASP varies a lot. To understand this, the output pump pulses at L_{op} for all cases are shown in Fig. 4.20 (c), with the input pump pulse also shown as a reference. From the figure, it can be observed that the output pump pulses differ considerably in the range 0-40 μs. More specifically, with increasing f_{rep}, an increasing abundance of pump leakage is observed. Furthermore, at 2 kHz and 5 kHz, the energy leaked is even larger than what is input. In other words, with increasing f_{rep}, the absorbed energy from the ASP decreases, and at a certain point there is no net absorption of the ASP, after which (or for further increasing f_{rep}) it is amplified.

The reason behind this is that when f_{rep} is small, there is sufficient time for the excited Yb^{3+} ions (from the previous period) to relax to the ground state. In this case, when the ASP pulse arrives, N_1 is very small so that the ASP pump can bring N_1 from essentially zero to N_{ASP}^{tran}. As f_{rep} increases, there is less time for the excited Yb^{3+} ions to relax so that when the ASP pulse arrives, some excited population remains. As a result, less ASP is absorbed in reaching N_{ASP}^{tran}. If f_{rep} is further increased, so that when the ASP pulse arrives N_1 is greater than N_{ASP}^{tran}, then instead of being absorbed, the ASP will be amplified. This explains the 2 kHz and 5 kHz situations in Fig. 4.20 (c). For the SP and signal pulses, since the N_1 distributions at 40 μs are all very similar among the different cases, the output SP powers and signal pulse shapes are also expected to largely independent of f_{rep}. This is shown in Figs. 4.20 (c) and (d), respectively. Similarly, the absorbed SP energy and output pulse energy are also expected to be independent of f_{rep}. This calculation is shown in Fig. 4.20 (e).

Next, the system efficiency is quantified. As discussed above, with increasing f_{rep} the output signal energy is essentially constant, so that η_W will also be similar for varying f_{rep}. For $\eta_{O\text{-}O}$, however, because the absorbed energy from the ASP gradually decreases to zero, even becoming negative as a result of ASP amplification (which is shown in Fig. 4.20 (e) for better visualization), $\eta_{O\text{-}O}$ will change correspondingly. Specifically, referring to Eq. 4.18, a decrease in E_{ASP}^{ab} will lead to a greater $\eta_{O\text{-}O}$ with the same signal power. However, as E_{ASP}^{ab} becomes negative, it does not make sense to put the negative value into Eq. 4.18 since only the SP contributes to signal amplification. Therefore, the equation should reduce to

$$\eta_{O-O}' = \frac{E_{SIG}^{out} - E_{SIG}^{in}}{E_{SP}^{ab}} \qquad (\text{if } E_{ASP}^{ab} < 0) \tag{4.22}$$

Using above analysis, the For $\eta_{O\text{-}O}$ and η_W are calculated as shown in Fig. 4.20 (f).

Finally, the total generated thermal energy E_t is calculated and is shown in Fig. 4.20 (f), indicating that E_t increases with f_{rep}. As analyzed above, less energy is absorbed from the ASP with increasing f_{rep} so that energy transfer from the ASP to signal also decreases. As a result, the ASP-related term in Eq. 4.20 (first term) contributes less to offsetting E_t, even turning positive due to QD heating during the amplification of the ASP, leading to a greater E_t, which is opposite to the desired direction.

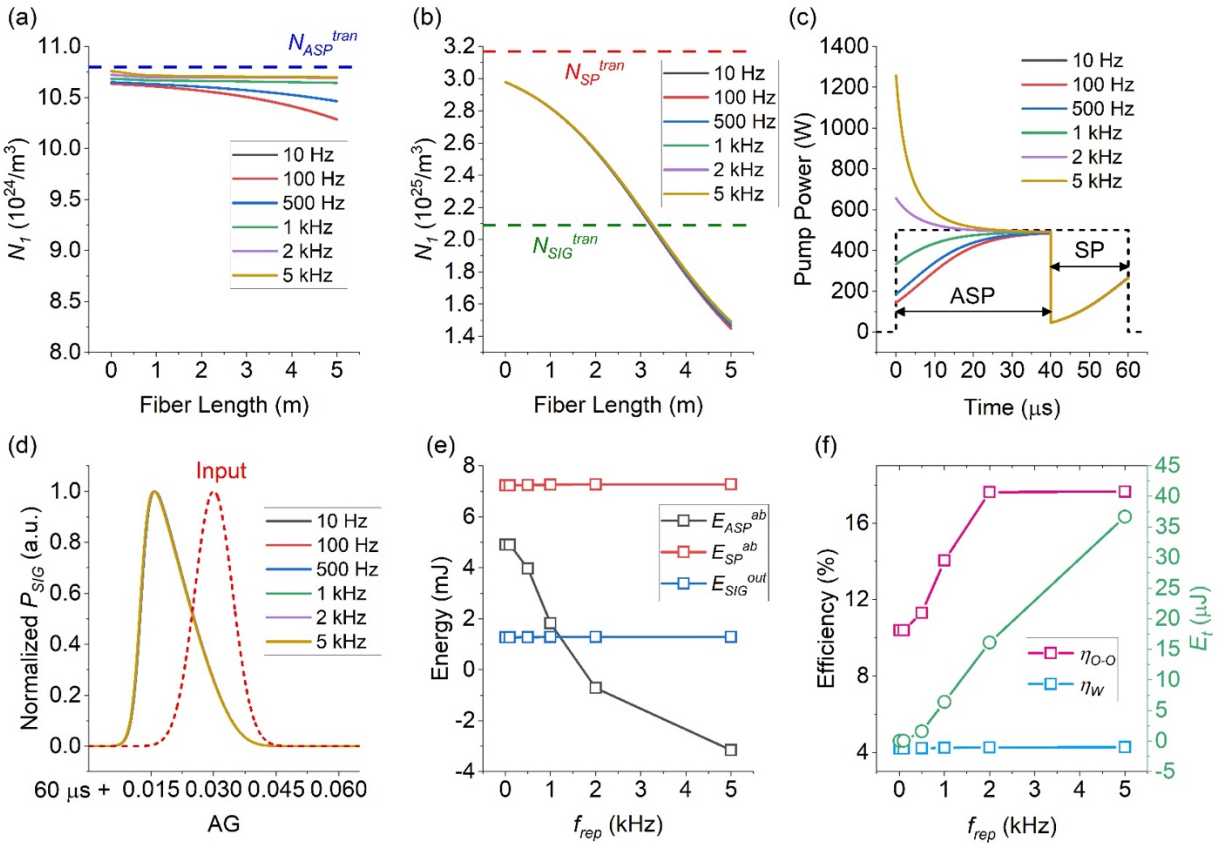

Fig. 4.20: With increasing f_{rep}, the quantified (a) upper state population when ASP pulse ends, (b) upper state population when SP pulse ends (the corresponding transparency levels are also shown), (c) leakage ASP and SP leakage powers shown with the pumping pulses, (d) evolution of the pulse shape, (e) absorbed SP and ASP powers (note a negative value for a pump means energy is extracted via gain) and signal output energy, and (f) the optical to optical efficiency ($\eta_{O\text{-}O}$), wall-plug efficiency (η_W), and total generated thermal energy (E_t).

Finally, all the three wavelengths (λ_{ASP}, λ_{SP}, and λ_{SIG}) can also be variables and influence the system behavior. Clearly, there are numerous possible wavelength combinations, and it is impossible to examine all of them here. Therefore, the discussions in this part are just some examples, whereas the wavelength selection experimentally relies on the availability of light sources and application requirements. In previous examples, λ_{ASP}, λ_{SP}, and λ_{SIG} are selected to be 1035 nm, 1010 nm, and 1020 nm, respectively. In this section, the wavelength differences between them are maintained and six other situations are examined as summarized in Table 4.4. In the results below, since λ_{ASP}, λ_{SP}, and λ_{SIG} are variables and it is hard to choose just one as the x-axis in the figures, "situation" is used as an arbitrary x-axis where the wavelength selection in such axis can be found in Table 4.4.

Table 4.4: Wavelength selections employed in this section

Situation	1	2	3	4	5	6	7
λ_{SP} (nm)	1010	1012.5	1015	1017.5	1020	1022.5	1025
Λ_{SIG} (nm)	1020	1022.5	1025	1027.5	1030	1032.5	1035
λ_{ASP} (nm)	1035	1037.5	1040	1042.5	1045	1047.5	1050

Then, simulations were performed using the same input parameters as in the test example and the results are summarized in Fig. 4.21. Figure 4.21 (a) gives the results for the absorbed energy from both pumps, as well as the output pulse energy, from which the system efficiency can be calculated and summarized in Fig. 4.21 (b). From the figures, at situation 5, a maximum output pulse energy, optical-optical efficiency, and wall-plug efficiency is observed, making this a more preferable wavelength combination to be used. For the optimized fiber length (L_{OP}), as the two pump wavelengths (λ_{ASP}, λ_{SP}) move to longer wavelengths, the absorption cross section decreases so that a longer fiber is required to absorb the pump energy, this is confirmed as shown in Fig. 4.21 (c) for L_{OP}. As a result of the longer fiber, more absorptive background loss occurs and more

thermal energy is generated, which is confirmed in Fig. 4.21 (c). For the output pulse shaping, the results are summarized in Fig. 4.21 (d). To give a clearer vision, the time difference between the time (t_{max}) when ASP pulse ends and when the peak of the output signal pulse happens are quantified and shown in Fig. 4.21 (d). From the results, it can be observed that it follows the opposite trend as the output signal energy. In other words, the higher the output signal energy is, the more severe pulse shaping occurs.

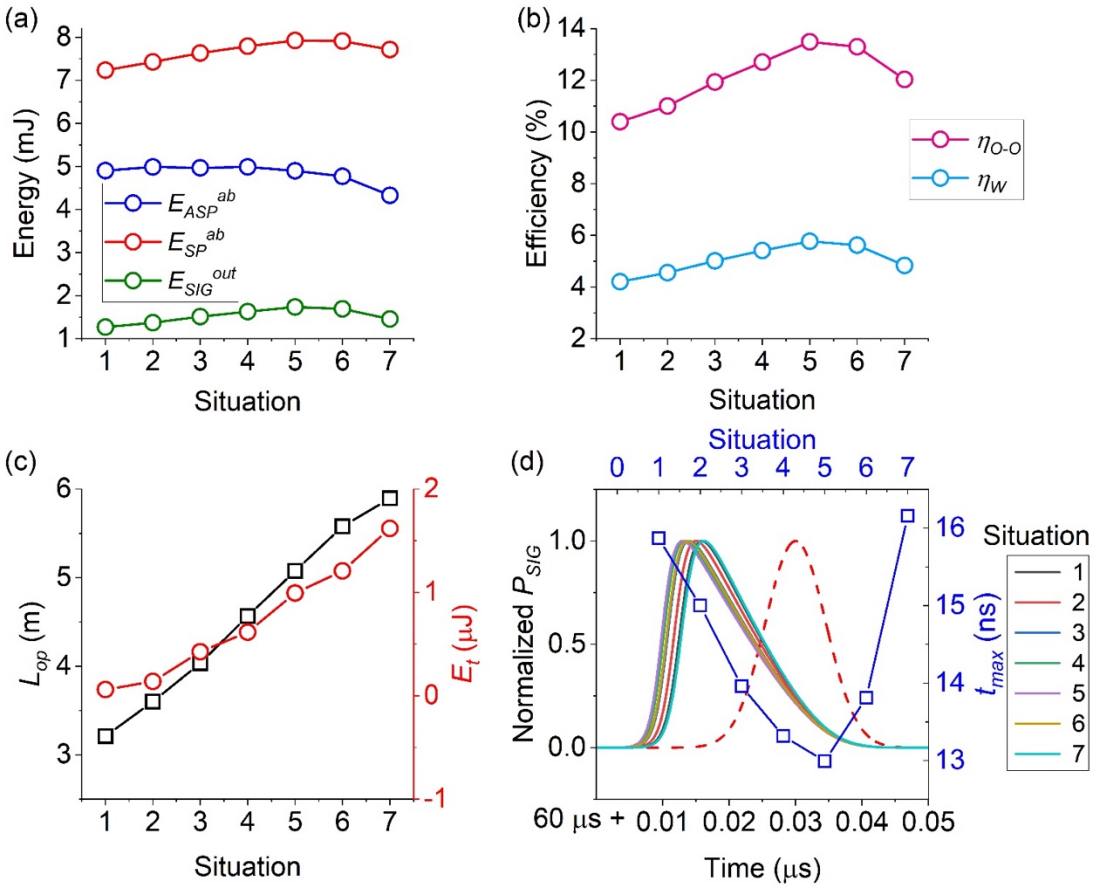

Fig. 4.21: With seven different wavelength settings (refer to Table 4.4), the quantified (a) absorbed ASP and SP energy (E_{ASP}^{ab}, E_{SP}^{ab}), and output signal energy (E_{SIG}^{out}), (b) the optical to optical efficiency (η_{O-O}) and wall-plug efficiency (η_W), (c) optimized fiber length (L_{OP}) and total generated thermal energy (E_t) and (d) the change of pulse shape and peak time (t_{max}).

In conclusion, in this chapter, the idea of excitation-balancing was first explored experimentally with the low-energy laser. Evidence were provided that ASP can contribute to

stimulated emission and as a result, the effective quantum defect decreases. Then a FDTD model was developed to help analyzing the system, which give simulation results agree well with the experimental results. Finally, to create a more useful design, further FDTD modeling of a high-energy excitation-balancing pulse amplifier was proposed and simulated, with the influence from ASP pump power, signal input power, ASP pump time, time delay between the pump and signal, repetition rate, and wavelength selections for λ_{ASP}, λ_{SP}, and λ_{SIG} are all discussed in detail. This will be helpful to provide guidance for the future experiment design. The selection of all the input parameters eventually depends on the applications and requirements, for example, if the main concern is thermal management, then a higher P_{ASP}, longer t_{ASP}, smaller f_{rep}, and shorter pumping wavelengths will be beneficial. If system efficiency is a second concern, which is usually in contradiction of better thermal management, then the input parameters can be further adjusted to balance these two requirements. The model can also be modified to simulate other solid-state systems, such as Er-doped fiber amplifiers or crystal-based lasers.

CHAPTER 5: Characterization of Quantum Conversion Efficiency

In Chapters 2 – 4, the focus was mostly on reducing the quantum defect heating in fiber lasers. However, as introduced in Chapter 1, there are also other sources of thermal energy generation. Non-radiative heating, in particular, may become non-negligible if the QD heating in a laser is very low using the methods introduced in Chapters 2-4. Therefore, it is meaningful to quantify the non-radiative heating in fibers. Unfortunately, there is a lack of research on such measurements. Therefore, the focus on this chapter is the development of a platform to quantify the nonradiative heating in fibers.

To better quantify the nonradiative heating, a related parameter known as quantum conversion efficiency (QCE) is a meaningful physical term to be quantified. The QCE is defined to be the fraction of pump photons that undergo a desired radiative process. Ideally, QCE should equal to 1 in the quantum limit, meaning that for every photon provided for pumping, there will always be a photon emitted as signal. However, nonradiative processes originating from impurities (such as transition metals, undesirable rare-earth ions, OH^-, etc.) or quenching [30], [66], [67] will make the QCE less than one. Obviously, this will adversely influence laser or amplifier efficiency because the pump photons that undergo nonradiative heating will not contribute to the optical output power. To evaluate the QCE of a fiber, one can first precisely measure the temperature change of the fiber when the pump light is injected. Then, the QCE of the fiber can be deduced from the temperature difference between the measurement and a model that considers a QCE of 100%. This method is discussed in more detail later in this chapter and is only valid when two requirements are met. First, those pump photons that undergo nonradiative processes contribute to thermal energy through fast phonon processes. This is

generally a valid assumption with Yb^{3+} as suggested by other references [30], [66], [67], [70]. Second, the fiber should have minimum conductive and convective thermal energy transfer to extrinsic materials, such as mechanical supports for the fiber, so that the temperature of the fiber itself is accurately measured. Fortunately, this is the same requirement as found in ASF cooling measurements and many methods can therefore be found in the literature that address this latter requirement [30], [66], [67], [71]–[75]. For example, mounts made of thin silica filaments, onto which samples are placed, are used in [72]–[75]. Physical contact between the test fiber and the sensor with extremely low absorbance is created with the aid of isopropanol [30], [66], [67]. As for temperature sensing, a variety of methods are used, including thermal cameras [72], [73], [75], temperature-dependent Yb^{3+} emission [74], and slow-light, ultra-high resolution FBGs [30], [66], [67], [71], each exhibiting great ability to quantify the temperature in the given configuration. In terms of advantages, some methods possess high temperature resolution (0.3 mK [71]) or fast response time (50 ms [73]), while others exhibit high dynamic range (>100 K [75]) or convenient all-fiber setup without free-space coupling components [30], [66], [67].

However, the configurations mentioned above all have their own drawbacks. First, where free-space components are used [72]–[75], there is additional time needed for alignment and careful control of any mechanical instability that may misalign the fiber (such as the air flow when pumping down a vacuum chamber) and introduce additional coupling loss to the system. Second, for those methods using thermal cameras [72], [73], [75], the sample dimensions are on the order of 10 millimeters, nearly 100 times greater than a standard 125 μm fiber. Therefore, it may be challenging for the thermal camera to image a much smaller fiber, unless a magnifying system is constructed [76], adding considerable cost and complexity to the measurement. Third, the dynamic range is relatively small in the methods described in other references [30], [66],

[67], [71], which is only 14 K. Although it can be increased with a more powerful laser source, a range of 100 K or more is more desirable, as this is a temperature change that can be reached in high-power lasers [77]. Therefore, a simple, all-fiber (no free space coupling) and wide-temperature range method with careful control of the conductive and convective thermal transfer is desired. Here, such a method, based on Brillouin scattering, is demonstrated.

Figure 5.1 gives a schematic of the proposed setup, which is a modified version of the heterodyne approach commonly used to characterize spontaneous Brillouin scattering [36], [78], [79]. A narrow-linewidth (85 kHz) laser signal at 1534 nm, amplified by an erbium-doped fiber amplifier (EDFA), is passed through a circulator and launched into Port 1 of a wavelength division multiplexer (WDM). This wavelength serves as the pump for the Brillouin scattering process ("Brillouin pump"). A second pump laser, which is used to excite the Yb^{3+} ion ("Yb pump"), is directly coupled into Port 2 of the WDM. Then the combined signal (Ports 1 + 2) is injected into the test fiber, which is placed on top of a silica aerogel tile inside an acrylic vacuum chamber. The thermal conductivity of the aerogel tile is as small as 0.023 W/mK so that conductive heat transfer is extremely low. Meanwhile, through the use of the vacuum chamber, both conductive and convective heat transfer via air are largely eliminated. In this way, the temperature change of the fiber is larger compared to performing the same experiment at ambient pressure, enhancing the accuracy in determining small temperature variations. To perform heterodyning with a minimum number of components, a simple straight-cleave was made at the end of the test fiber to provide the local oscillator (LO) signal. Then the LO signal together with the back-reflected Brillouin signal are collected from Port 3 of the circulator, through an optical filter (Bandpass @1534 $\pm$ 0.75 nm) and amplified by another EDFA. Finally, the beat signal

between the LO and Brillouin signal is detected by a fast PiN photodetector and displayed on an electrical spectrum analyzer.

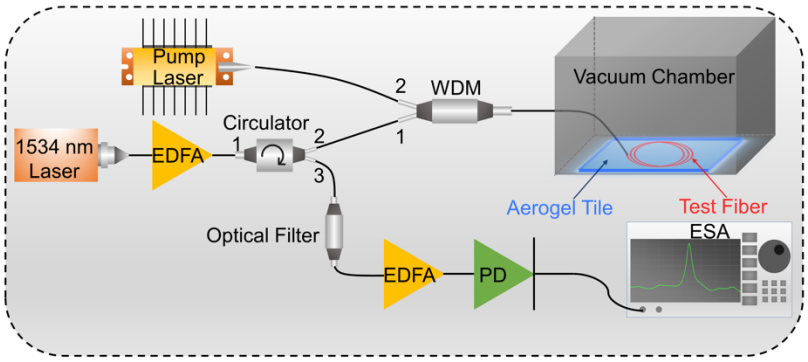

Fig. 5.1: Experimental Setup of the QCE quantification platform. EDFA: Erbium-doped fiber amplifier, WDM: wavelength division multiplexing, PD: photodiode, ESA: electrical spectrum analyzer.

The Brillouin frequency shift is known to be a function of temperature because the material acoustic velocity increases with increasing temperature in most silica glasses [50]. The approach here is to first measure the Brillouin spectrum at equilibrium temperatures as calibration, with no Yb pump power provided. More details on this are provided in the next section. Then, Yb pump laser power is varied, and any change in the temperature of the test fiber can be characterized through the frequency shift of the Brillouin signal. Since the measurement does not require any physical contact with the fiber (aside from the low-thermal-conductivity aerogel) and all the components are fiber-coupled, it forms a simple, all-fiber, and contactless platform for temperature characterization, which is tested and discussed below. As will be shown, since the system integrates the Brillouin spectrum of the whole fiber length, pumping is adjusted in order to create uniform inversion (in other words a uniform temperature distribution) throughout the length of test fiber. Finally, it is necessary to point out that the measurement

range of the setup is not limited, as long as calibration can first be done at such temperatures, enabling the possibility of high-temperature measurements if required.

Now a fiber is required to be tested by the system. Instead of using the Yb-doped fiber in Chapters 2-4, a commercial fiber (National Optics Institute (INO) is used to test the functionality of the system. The reason to use this specific fiber is it has a relatively small Yb^{3+} so that it only requires a low pump power (Yb pump) to create a uniform temperature distribution, adding convenience to this first demonstration experiment. Should fibers with higher Yb^{3+} concentrations, such as the one used in previous chapters be required to test, the system is still functional as long as enough pump power is provided to create a uniform temperature distribution. Before testing, several basic fiber parameters are tested. The RIP is measured using the method introduced in a previous chapter. The result near the core is shown in Fig. 5.2 (a), from which the core diameter is determined to be 4.7 μm. The Yb^{3+} concentration is given by the manufacture to be 3.27×10^{24} m^{-3}, the emission and absorption cross sections are quantified using with the same method discussed in Chapter 2. The final results of absorption and emission cross sections are shown in Fig. 5.2 (b). From the emission spectrum, the average emission wavelength is determined to be 1009.3 nm. The radiative lifetime is quantified to be 760 μs, which is a typical number for commercial Yb-doped fiber. The Brillouin signal temperature dependence is calibrated using the setup in Fig. 5.1. With the test fiber placed inside a heated water bath instead of the vacuum chamber, the Brillouin signal is measured as a function of temperature with no Yb pump power present. The result is shown in Fig. 5.2, indicating a linear Brillouin frequency temperature dependence of 1.075 MHz/°C. This value will be used to convert the measured frequency shift to corresponding temperature change in the following discussion.

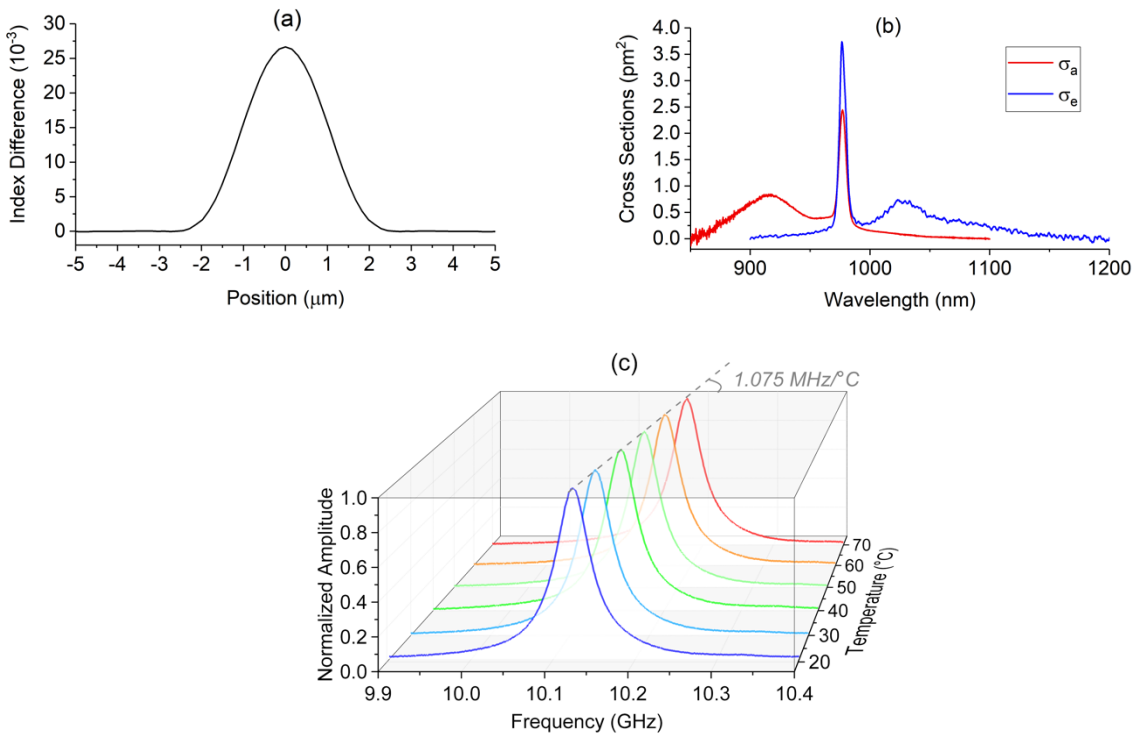

Fig. 5.2: The measurement results of (a) Refractive index profile, (b) absorption and emission cross section, (c) Brillouin signal from 20 °C to 70 °C.

Next, a 1.4 m sample of the test fiber is spliced into the system and placed on top of the aerogel tile inside the vacuum chamber. The fiber length is chosen to be long enough to provide sufficient Brillouin scattering for detection with high signal-to-noise ratio, but not so long so that less than 300 mW of pump power is needed to achieve a uniform temperature distribution. In our absorbed power per length characterization, there was significant pump leakage from the fiber, guaranteeing that pumping was in the saturated regime, which further gives rise to a uniform distribution of temperature. The buffer of the test fiber is stripped off mechanically with a standard fiber stripper to avoid absorptive heating in that layer. The Yb^{3+} pump laser is chosen to be a single-mode fiber-coupled laser diode with a wavelength (λ_p =976.5 nm) that is shorter than the average emission wavelength ($\bar{\lambda}$ = 1009.3 nm). As a result, phonons will be generated via Stokes processes when fluorescence is produced, and a temperature increase is therefore

expected. Then, after pumping down the vacuum chamber, Brillouin signals of the fiber are measured as a function of absorbed pump power (input power minus power leakage at the end) and relative frequency shifts are recorded. Using the Brillouin signal temperature dependence calibration from above, the temperature change of the fiber as function of the absorbed pump power can be determined and is shown as triangles in Fig. 5.3. (the rest of the data shown in this figure will be explained later few paragraphs)

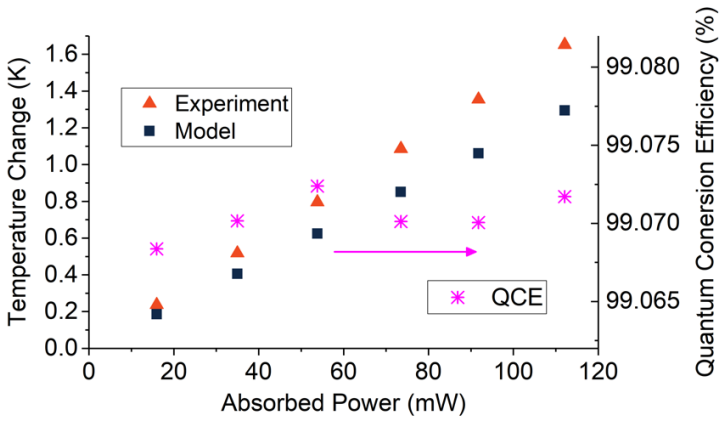

Fig. 5.3: Experimental (triangles) and modeling (squares) temperature change versus absorbed pump power and the corresponding QCEs (stars).

Next, a theoretical model is constructed to simulate the thermal distribution of the fiber considering a QCE of 1. The radial thermal distribution $T(r)$ is governed by thermal conduction equation [77]

$$\frac{1}{r}\frac{\partial}{\partial r}\left(r\frac{\partial T(r)}{\partial r}\right) = -\frac{Q}{k} \tag{5.1}$$

where r is the radial coordinate, Q the heat power density, and k the thermal conductivity. Here, the thermal conductivities of both the core and the cladding are assumed to be that of silica (1.38 W/mK [77]). Next, since the buffer is removed in the setup, only two regions (core and cladding) are considered in the model. Applying boundary conditions, the temperature distribution in the core $T_1(r)$ and cladding $T_2(r)$ can be determined to be [47]

$$T_1(r) = T_0 - \frac{Q_1 r^2}{4k_1} \tag{5.2}$$

$$T_2(r) = T_0 - \frac{Q_1 a^2}{4k_1} - \frac{Q_1 a^2}{2k_2} \ln\left(\frac{r}{r_{core}}\right) \tag{5.3}$$

where T_0 is the temperature at the core center and is expressed by

$$T_0 = T_c + \frac{Q_1 a^2}{2hr_{clad}} + \frac{Q_1 a^2}{4k_1} + \frac{Q_1 a^2}{2k_2} \ln\left(\frac{r_{clad}}{r_{core}}\right) \tag{5.4}$$

in which T_c is the coolant temperature and h the heat transfer coefficient. Considering QCE = 1, heat is only generated by the quantum defect of the system. Therefore, Q_1 is calculated by

$$Q_1 = \frac{P_{abs}}{L} \times QD \tag{5.5}$$

where P_{abs} represents the absorbed pump power, L represents the fiber length, and the QD is defined by $1 - \frac{\lambda_p}{\bar{\lambda}}$. Since the fiber is placed on an aerogel tile inside the vacuum chamber, only radiative heat transfer is considered with its coefficient calculated from [80]

$$h = \frac{\varepsilon \sigma_b ({T_2}^4(r_{clad}) - {T_c}^4)}{T_2(r_{clad}) - T_c} \tag{5.6}$$

where ε =0.85 is the emissivity and σ_b the Stephan-Boltzmann constant.

Using the model described above, the radial temperature distributions in the fiber at different absorbed pump powers are calculated, with an example shown in Fig. 5.4. In this specific case (112.1 mW absorbed pump power), the ambient temperature, T_c, is 298 K and the temperature at the core center is 1.352 K above T_c, whereas the temperature variation from the core center to the cladding edge is less than 1.2 mK. Therefore, the temperature variation can be neglected, and the temperature of the core center is taken to be the fiber temperature. As a matter of fact, it is from within the core that the Brillouin signal originates, making this a valid and appropriate simplification. Finally, the temperature change as a function of absorbed pump power is calculated and shown as the squares in Fig. 5.3.

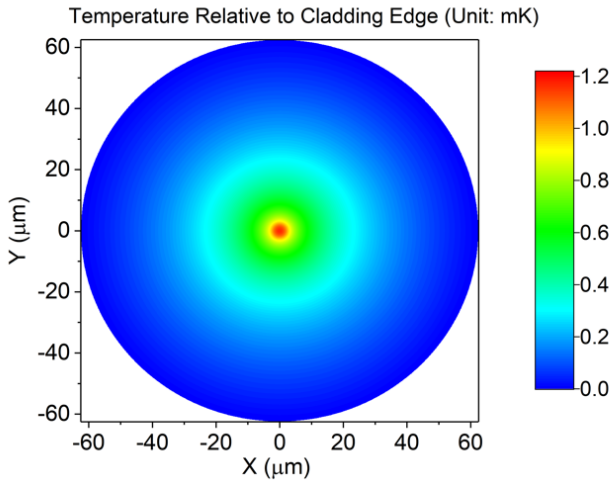

Fig. 5.4: Modeling results of 2D temperature distribution when the fiber absorbs 112.2 mW of pump power.

Obviously, a difference between the experimental result and the model is observed. This is due to the assumption of a 100% QCE, which is not necessarily the case in the fiber. As described above, the presence of nonradiative processes will generate additional thermal energy. Taking these nonradiative processes into consideration, the corrected heat power density becomes

$$Q_1' = \frac{P_{abs}}{L \times \pi {r_{core}}^2} \times QCE \times QD + \frac{P_{abs}}{L \times \pi {r_{core}}^2}(1 - QCE) \tag{5.7}$$

where the first term represents quantum defect heating that is reduced by the QCE factor, and the second term is heating due to nonradiative processes. Since the temperature increase has a linear relation with heat power density, as indicated by Eqs. 5.2 - 5.6, the experimentally measured (ΔT_e) and the modeled (ΔT_m) temperature changes have the relation of

$$\frac{\Delta T_e}{\Delta T_m} = \frac{Q_1'}{Q_1} = \frac{1 - QCE(1 - QD)}{QD} \tag{5.8}$$

in which the only unknown is the QCE. Therefore, the QCEs at the different absorbed pump powers can be determined and the results are shown in Fig. 5.3 (a) as stars. The average QCE is

determined to be 99.07%, with only small variations between measurements, indicating a high-quality fiber with very weak nonradiative processes and a power-independent QCE. This can be explained as follows. Given the low Yb^{3+} concentration in the fiber, no concentration quenching effects are expected [81]. As such, the nonradiative heating likely only comes from impurities, which is linearly proportional to pump power (or in other words, via unsaturable absorption). If the fiber does suffer from concentration quenching, the same measurement will possibly lead to a power-dependent QCE, giving insight into how quenching effects evolve with increasing pump power. However, this subject is not examined yet at this point.

To verify the QCE number obtained here, a linear laser similar to the one in Fig. 2.2 is constructed, the only difference is that the FBG2 is removed and the straight cleave at the end serves as the second reflector, which relies on the Fresnel reflection (~ 3.4%). Then, similar to Chapter 2, different active fiber lengths (5 m, 6 m, 7 m, 8 m) are used as the active medium and the corresponding slope efficiencies (η_e) are experimentally characterized. Next, the same theoretical model based on rate equations was used to simulate the pump powers versus output powers, from which the modeled slope efficiencies (η_m) are extracted. The only difference is that no terms related to the non-radiative processes are considered in the model, meaning that the model is under the assumption of a 100% QCE. For the four different active fiber lengths, η_e and η_m are summarized in Table 5.1. It can be observed that η_e is smaller than η_m in all the cases. The reason is the assumption of a 100% QCE in the fiber. In other words, the model assumes that for each pump photon that was absorbed by the test fiber, a corresponding signal photon was generated. However, the fact that nonradiative processes also take place in the fiber violates this assumption and decreases the slope efficiencies. To be more specific, only the QCE of the absorbed pump power contributes to the laser output power, while the proportion (1-QCE) of the

pump power ends up as heat. As such, at each data point the measured output power should be QCE multiplied by the modeled output power. Therefore, the value of η_e/η_m represents nothing more than the QCE of the fiber, which ranges from 98.58% to 99.13% in the four cases as summarized in Table 5.1.

Table 5.1: Comparison of the experimental (η_e) and modeled (η_m) slope efficiencies with different Yb-doped fiber lengths

	5 m	6 m	7 m	8 m
η_e	55.58 %	60.53 %	60.46 %	60.49 %
η_m	56.38 %	61.06 %	61.09 %	61.09 %
η_e/η_m	98.58 %	99.13 %	98.97 %	99.01 %

In comparison, the calculated QCE from the proposed method is around 99.07%, which lies in the range determined by the linear laser. Therefore, it can be concluded that the two methods substantiate the accuracy of the fiber QCE value. However, the QCEs determined from the linear laser have a greater intrinsic uncertainty than that determined from the proposed method. The reason is that the Brillouin setup is much more sensitive to variations in the QCE. For example, if the QCE of the fiber changes from 99% to 99.1%, the measured slope efficiency in the linear laser will also increase by ~0.1%, which can be hard to distinguish. On the other hand, for the same change in the QCE in the Brillouin setup, using Eq. 5.8 the $\Delta T_e/\Delta T_m$ value will increase by ~2.3%, or ~23 times greater than the change in the linear laser. Therefore, the proposed method is a more sensitive and accurate method.

It is necessary to discuss the origin of possible errors intrinsic to the proposed method. A first source of error is the temperature calibration of the Brillouin scattering signal. For instance, the temperature of the water bath may vary while acquiring the Brillouin spectra, adding uncertainty to the measurement of the peak frequency. Second, the theoretical model depends on

an accurate characterization of the average emission wavelength, which further relies on a clear emission spectrum. However, the measurement of emission spectrum depends on a strong side emission of the fiber, which can be challenging, introducing errors in the average emission wavelength. Third, fibers designed for high-power applications may have an intrinsically low Brillouin scattering strength [38], [42], [82], [83], rendering weak and potentially noisy spectra, making it hard to distinguish the shift of them. Last but not least, the thermal conductivity of the core is assumed to be that of silica in the model. However, this value can differ when dopants are incorporated in silica, thereby adding errors to the modeling result. The influence from it will also increase if the core size increases. In order to minimize the errors, a highly temperature-stable water bath or other temperature-controlled environment should be used during the calibration, sufficient averaging should be applied when measuring the emission and Brillouin spectra, and these have all been given careful attention during the demonstration in this chapter. As for the thermal conductivity of the core, additivity model [84] could be use estimate the number. In the fiber used in this chapter, however, modeling results indicate that even if the number is doubled, the temperature of the core will only decrease 0.1 mK, which is negligible, making the simulation in this chapter accurate.

After the analysis above, same testing platform was used to quantify several different fibers. The first two fibers are the fluorosilicate fiber used in Chapter 2, and the phosphosilicate fiber used in Chapter 3. For both fibers, the Yb^{3+} doping concentration is much higher compared to the commercial fiber used earlier in this chapter, making the absorption at 976 nm much higher. However, an assumption was made earlier that the pump is uniformly absorbed, which will not be the case for the fluorosilicate or the phosphosilicate fiber. To make the assumption still valid, pumping wavelength is moved to longer wavelengths (1030 nm and above) where the

absorption is much smaller compared to 976 nm. Meanwhile, as discussed in several works by Knall [30], [31], [66], anti-Stokes fluorescence (ASF) cooling may happen when pumping the fiber at such wavelengths. Therefore, the QCE as well as the possibility for the fiber to produce ASF cooling can be examined at the same time when pumping at longer wavelengths. For both fibers, the Brillouin frequency temperature dependence was first quantified using the water bath methods, and the results for fluorosilicate and phosphosilicate are shown in Fig. 5.5 (a) and 5.5 (b), respectively. From the results, the Brillouin frequency temperature dependence for fluorosilicate and phosphosilicate are determined to be 1.008 MHz/°C and 1.006 MHz/°C.

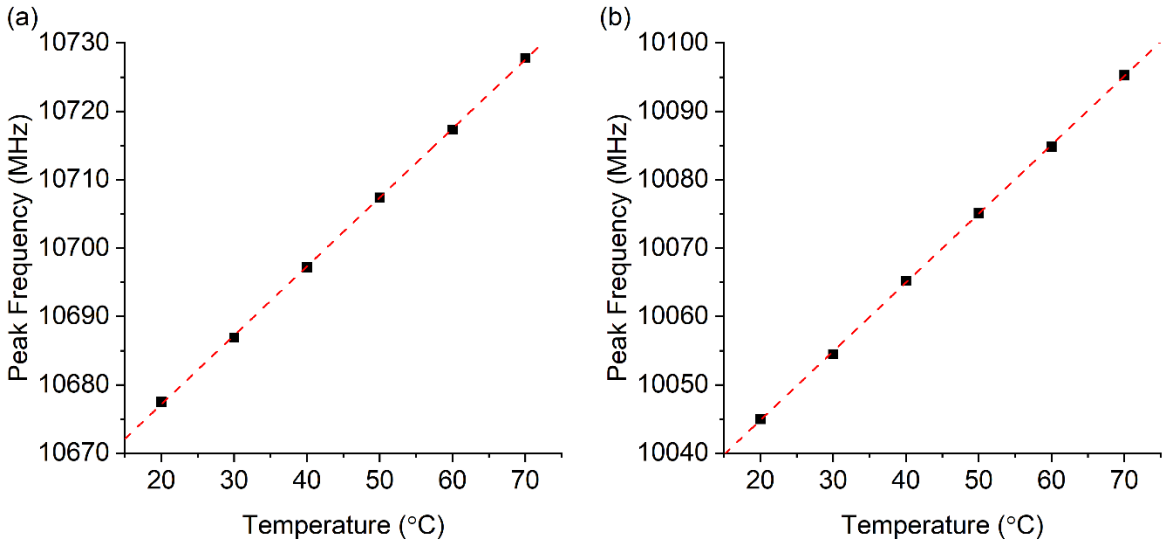

Fig. 5.5: Peak frequency of Brillouin signal as a function of temperature for the Yb-doped (a) fluorosilicate and, (b) phosphosilicate fiber. The dashed lines are linear fits to the data.

Then, Brillouin spectra were measured with 140 mW of pump power at 1030, 1035, and 1040 nm. As discussed above, the frequency will shift correspondingly if the fiber heats or cools. Using the analysis method introduced earlier in this chapter, the characterized temperature change (ΔT) and QCE for both fibers are summarized in Table 5.2. Example Brillouin spectra for both fibers are also provided in Fig. 5.6, which corresponds to the situation with and without the 1030 nm pump.

Table 5.2: Summary for the fluorosilicate and phosphosilicate fiber

	Fluorosilicate		Phosphosilicate	
λ_P (nm)	ΔT (K)	QCE	ΔT (K)	QCE
1030	2.93	94.25%	0.91	96.54%
1035	2.74	94.07%	0.61	96.83%
1040	2.07	94.48%	0.67	96.37%

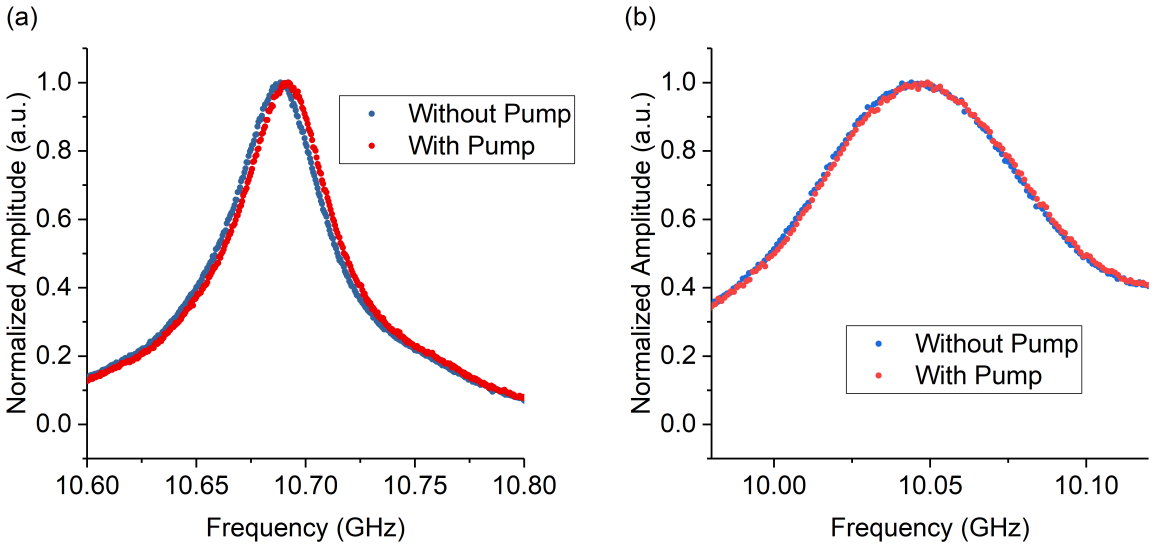

Fig. 5.6: Brillouin signal for (a) fluorosilicate fiber and, (b) phosphosilicate fiber with and without the 1030 nm pump.

From the results, both fibers heat when pumping at 1030, 1035, and 1040 nm, with more heating observed for the fluorosilicate fiber. The average QCE value for fluorosilicate and phosphosilicate fibers are 94.27% and 96.58%. The difference in QCE is mainly a result of different fabrication process. As discussed above, the fluorosilicate fiber was fabricated via a molten-core method, whereas the phosphosilicate fiber was fabricated via the common MCVD method. The molten-core method is more likely to introduce more impurities compared to MCVD, therefore making the QCE smaller. For the phosphosilicate fiber, although it is fabricated with MCVD method, it still has a relatively low QCE compared to the fiber discussed below with more careful fabrication processes. To examine the origin of this, a lifetime

measurement of the phosphosilicate fiber, using the procedures outlined in Chapter 2, is shown in Fig. 5.7. A triple-exponential fit is performed to the data and each of the individual exponential fits, as well as the overall fit are shown in Fig. 5.7 (a). Three exponential components with lifetimes of 0.126 ms, 0.823 ms, and 1.686 ms, respectively, are observed. The first fast component (0.126 ms lifetime) is a result of clustering in the fiber, which will lead to quenching and decrease the QCE. The second component (0.823 ms) has a lifetime close to that of the aluminosilicate, which indicates that although this is a phosphosilicate fiber, there may still some Yb^{3+} ions surrounded by Al_2O_3 so that it shows a Yb-doped aluminosilicate lifetime. More material study is needed to verify this indication. Finally, the third lifetime (1.686 ms) represents the true phosphosilicate lifetime. From the discussions above, the fact that fast components are observed give direct evidence of the existence of the non-radiative processes in the fiber, making the QCE smaller than 100%. For a better view of the fitting, the experimental data and the triple-exponential fit are shown in log scale in Fig. 5.7 (b).

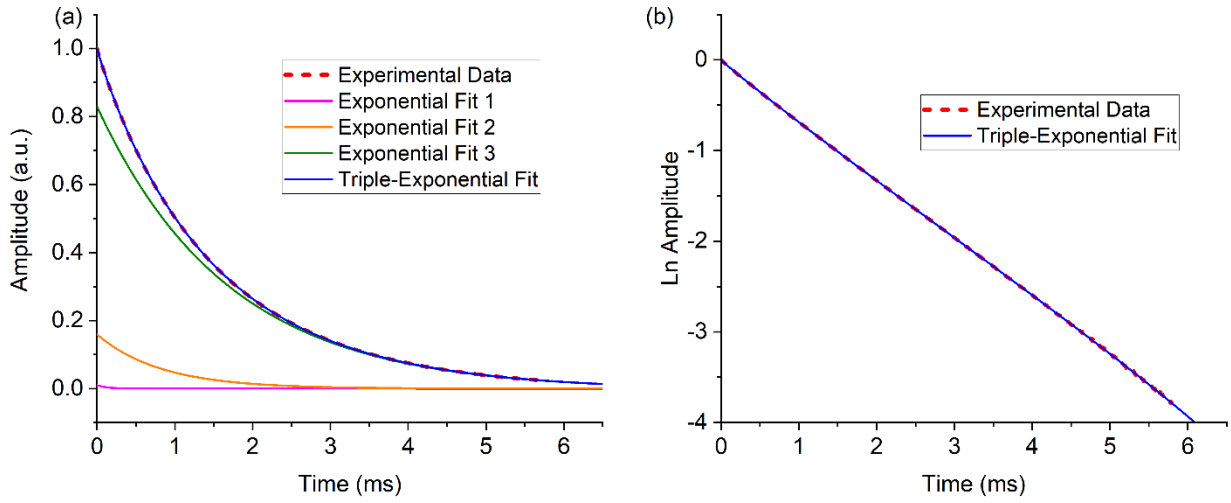

Fig. 5.7: Lifetime measurement of the Yb-doped phosphosilicate fiber in (a) linear scale and, (b) log scale. Triple-exponential fit (blue solid line) is performed to the experimental data (red dashed line), with lifetimes of 0.126 ms, 0.823 ms, and 1.686 ms, respectively.

Next, the testing platform was used to test three more Yb-doped fibers. In addition to Yb^{3+}, these fibers are doped with BaF_2, CaF_2, and SrF_2 nanoparticles, respectively. The reason behind nanoparticle doping is that the Yb^{3+} ions are surrounded by nanoparticles so that it is less likely for Yb^{3+} ions to form clusters, which is the main reason for quenching effect in Yb-doped fibers and may result in heating. The process can be understood that when a pump photon enters the fiber, instead of being absorbed by Yb^{3+} ions directly, the energy is instead passed around by Yb^{3+} ion clusters and eventually absorbed by an impurity and generating heat. The higher the Yb^{3+} concentration, the higher the possibility that quenching will happen. In fact, if the Yb^{3+} concentration becomes higher enough, the fiber may lose the ability to generate light and become a pure heater [85], [86]. By nanoparticle doping, the Yb^{3+} ions are more separated so that a higher QCE and less heat generation should be expected.

Following the same procedures as above, the Brillouin frequency temperature dependence was first quantified for all the three methods, and the results are shown in Fig. 5.8. From the results, the Brillouin frequency temperature dependence for BaF2 fiber, CaF2 fiber, and SrF2 fiber are determined to be 0.925 MHz/°C, 1.041 MHz/°C, and 1.021MHz/°C, respectively.

Then, Brillouin signal with and without 140 mW of pump power at 1030 nm, 1035 nm, and 1040 nm are measured for all the three fibers. Using the same analyzing procedure, the calculated temperature change and QCE are summarized in Table 5.3. From the results we can see that the BaF2 fiber has the lowest QCE with an average value of 97.23%, the heating is observed just as the fluorosilicate and Phosphosilicate fiber. However, for the CaF_2 fiber and SrF_2 fiber, the QCE has bigger values of 99.51% and 99.30%, respectively, and ASF cooling is observed. As a matter of fact, these are one of the first nanoparticle fibers that show ASF

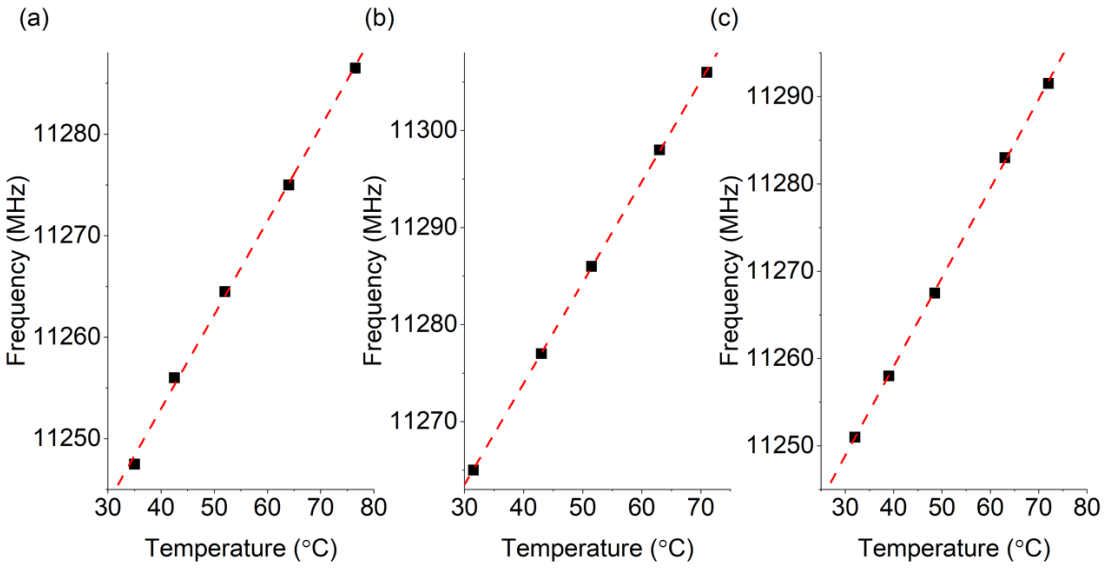

Fig. 5.8: Peak frequency of Brillouin signal as a function of temperature for the Yb-doped fiber with (a) BaF_2, (b) CaF_2 and, (c) SrF_2 nanoparticles. The dashed lines are linear fits to the data.

cooling, and such fibers will be useful in the development of radiation-balanced fiber lasers and amplifiers. One example measurement of the Brillouin spectra is shown in Fig. 5.9, which corresponds to the SrF_2 fiber with and without the 1030 nm pump. From Table 5.3, this represents the situation of the biggest temperature decrease.

Table 5.3: Summary for the three nanoparticle doped fibers

	BaF_2		CaF_2		SrF_2	
λ_P (nm)	ΔT (mK)	QCE	ΔT (mK)	QCE	ΔT (mK)	QCE
1030	495	97.12%	-702	99.50%	-784	99.46%
1035	204	97.10%	-534	99.45%	-512	99.15%
1040	0	97.48%	-32	99.57%	-323	99.27%

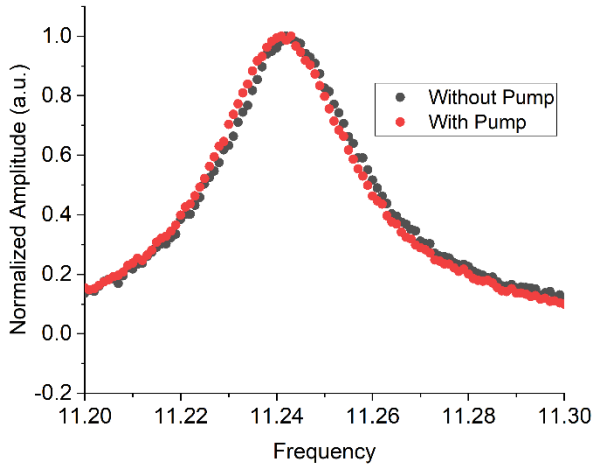

Fig. 5.9: Brillouin signal for SrF_2 fiber with and without the 1030 nm pump.

In summary, because non-radiative heating may also become a significant heat source, a testing platform to quantify the QCE was designed and tested in this chapter. The system functionality was first tested by a commercial Yb-doped fiber. A theoretical model based on thermal conduction equations was built to assist and analysis. To further prove the method, a linear-cavity-laser testing was performed and confirmed the QCE value. Next, the same testing platform was used to quantify the QCE of the fluorosilicate and phosphosilicate fiber used in previous chapters, and the calculated QCE are 94.27% and 96.58%, respectively. For these two fibers, under pumping wavelength of 1030 nm and above, heating was observed and the main reason is the non-radiative heating overpowers ASF cooling. To further explore the possibility of ASF cooling, three nanoparticle doped fibers are invested and two of them showed cooling. The platform in this chapter will be very useful for optimizing glass quality, quantifying ASF cooling, and as a temperature sensor.

CHAPTER 6: Conclusion and Future Work

In conclusion, discussed in this thesis were approaches to manage the thermal energy in high-power Yb-doped fiber lasers and amplifiers. The problem is first stated by introducing the processes of thermal energy generation in fiber lasers and the related thermal effects. Then a review is provided to outline the approaches to improve thermal management in fiber lasers, with several approaches highlighted to be discussed in detail in this thesis. In Chapter 2, a low-power low-QD fiber laser is developed to prove the concept of using Yb-doped fluorosilicate or phosphosilicate fibers as active media to achieve low-QD operation. For conventional Yb-doped fiber laser, QD can range from 5% – 8 %, whereas the laser discussed in this chapter has a QD of less than 1%. Next, in Chapter 3, power scaling efforts for both the fluorosilicate and the phosphosilicate fibers were discussed, and primary results are presented. For the fluorosilicate, the fiber suffers from cracks and spiral cracks that formed during the cleaving, which leaves a fabrication problem as future works to reduce the tension between the core and the cladding so that no cracks are formed. For the phosphosilicate, no cracking problems are observed, and experiments indicate an 87.4% slope efficiency with respect to the absorbed pump power. The signal wavelength was changed to 1005 nm to gain better efficiency, but the system still has a QD of 3%, which smaller than that of the conventional fiber laser (5% - 8%). A modified amplifier model was constructed to simulate the system, which gives results that agrees well with the experiments. To further optimized the fiber, the core-cladding ratio needs to be increased and the cladding needs to be shaped, which are not completed so far because of several difficulties in the fabrication. However, modeling results show that such a design will give promising results, leaving the fabrication of such a fiber an important future work. Finally, the possibility of

double-end pumping was investigated, and several advantages using such configuration were summarized, including lower nonlinear effect, more uniform thermal load, and possibility to incorporate more pump power.

Next, in Chapter 4, an excitation-balancing approach was proposed. The idea of excitation-balancing was first explored experimentally with a low-energy laser pumping at 976 nm (as SP) and 990 (as ASP). Evidence was given experimentally that the ASP can contribute to stimulated emission and therefore results in a corresponding cooling effect and decreases the effective QD. To better understand the process, a FDTD model was developed, and the simulation results agree well with the experimental results. Then, to explore the power scaling possibility to a high-energy pulse amplifier, further FDTD simulations of such a system were performed, with the influence from ASP pump power, signal input power, ASP pump time, time delay between the pump and signal, repetition rate, and wavelength selections for λ_{ASP}, λ_{SP}, and λ_{SIG} are all discussed in detail. The results show that such a system is possible to provide more than 1 mJ of pulse energy with zero or negative heat generation with proper design, which provide guidance for the future experiment design of such a system. In terms of QD, a zero or negative QD can be expected in such a system, which is considerably smaller than that of the conventional fiber laser (5% - 8%).

In Chapter 5, at the end, a method based on Brillouin scattering to quantify the non-radiative heating in Yb-doped fibers was proposed, with proof-of-concept testing results of a commercial Yb-doped fiber presented. Then, the same platform was used to test the fluorosilicate and phosphosilicate fibers used in Chapters 2-4, as well as three other nanoparticle doped fibers. It is shown that the QCE can be as low as ~ 94 % in a molten-core fabricated fiber, and as high as ~ 99.5 % in a carefully processed nanoparticle doped fibers. Results are also provided to show that a change of QCE from ~ 99.5 % to ~97 % can change the fiber from

cooling to heating (by the same amount), which emphasizes that the control of non-radiative processes is also of vital importance as reducing the QD heating, and the testing platform in this chapter will be helpful for the optimization of fiber quality in the future.

Although this will be the end for this thesis, it is never ending for the development for a better fiber laser system. In the author's point of view, the future for high-power fiber laser will have the following characteristics. First, the fiber will have a high quality with very low impurities, which will most likely be fabricated by the MCVD method. Second, the core materials are tuned to a point that it will allow efficient low-QD operation in the CW scenario, or excitation-balancing operation in the pulsed scenario, and at the same time, a low dn/dT value. Eventually, thermal effects will no longer be the limit for further power scaling, and it turns into the fundamental damage threshold of the silica that limits the further power scaling.

REFERENCES

[1] J. Ion, *Laser Processing of Engineering Materials: Principles, Procedure and Industrial Application*. Elsevier, 2005.

[2] T. H. MAIMAN, "Stimulated optical radiation in ruby," *Nature*, vol. 187, no. 4736, pp. 493–494, Aug. 1960.

[3] E. Snitzer, H. Po, F. Hakimi, R. Tumminelli, and B. C. McCollum, "Double clad, offset core Nd fiber laser," in *Optical Fiber Sensors*, 1988, p. PD5.

[4] L. Bigot, G. Le Cocq, and Y. Quiquempois, "Few-mode erbium-doped fiber amplifiers: A review," *J. Light. Technol.*, vol. 33, no. 3, pp. 588–596, 2015.

[5] C. Jauregui, J. Limpert, and A. Tünnermann, "High-power fibre lasers," *Nat. Photonics*, vol. 7, no. 11, pp. 861–867, 2013.

[6] A. Sincore, J. Bradford, J. Cook, L. Shah, and M. Richardson, "High average power thulium-doped silica fiber lasers: review of systems and concepts," *IEEE J. Sel. Top. Quantum Electron.*, vol. 24, no. 3, 2017.

[7] "IPG Photonics." https://www.ipgphotonics.com/en/products/lasers/high-power-cw-fiber-lasers.

[8] H. Zellmer *et al.*, "High-power cw neodymium-doped fiber laser operating at 92 W with high beam quality," *Opt. Lett.*, vol. 20, no. 6, p. 578, 2008.

[9] P. K. Cheo, L. Fellow, A. Liu, S. Member, and G. G. King, "A high-brightness laser beam from a phase-locked multicore Yb-doped fiber laser array," vol. 13, no. 5, pp. 439–441, 2001.

[10] M.-A. Lapointe, S. Chatigny, M. Piché, M. Cain-Skaff, and J.-N. Maran, "Thermal effects in high-power CW fiber lasers," *Fiber Lasers VI Technol. Syst. Appl.*, vol. 7195, no. February 2009, p. 71951U, 2009.

[11] W. M. Steen, "Laser material processing - An overview," *J. Opt. A Pure Appl. Opt.*, vol. 5, no. 4, 2003.

[12] A. Pukhov, Z. M. Sheng, and J. Meyer-ter-Vehn, "Particle acceleration in relativistic laser channels," *Phys. Plasmas*, vol. 6, no. 7, pp. 2847–2854, 1999.

[13] P. Werle, F. Slemr, K. Maurer, R. Kormann, R. Mücke, and B. Jänker, "Near- and mid-infrared laser-optical sensors for gas analysis," *Opt. Lasers Eng.*, vol. 37, no. 2–3, pp. 101–114, 2002.

[14] A. A. Kosterev and F. K. Tittel, "Chemical sensors based on quantum cascade lasers,"

IEEE J. Quantum Electron., vol. 38, no. 6, pp. 582–591, 2002.

[15] U. N. Singh *et al.*, "Twenty years of Tm:Ho:YLF and LuLiF laser development for global wind and carbon dioxide active remote sensing," *Opt. Mater. Express*, vol. 5, no. 4, p. 827, 2015.

[16] D. Engin, B. Mathason, and M. Storm, "Efficient, space-based, PM 100W thulium fiber laser for pumping Q-switched 2um Ho:YLF for global winds and carbon dioxide lidar," in *Lidar Remote Sensing for Environmental Monitoring 2017*, Aug. 2017, no. August 2017, p. 10.

[17] M. N. Zervas and C. A. Codemard, "High power fiber lasers: A review," *IEEE J. Sel. Top. Quantum Electron.*, vol. 20, no. 5, pp. 219–241, 2014.

[18] J. W. Dawson *et al.*, "Analysis of the scalability of diffraction-limited fiber lasers and amplifiers to high average power," *Opt. Express*, vol. 16, no. 17, p. 13240, 2008.

[19] M. N. Zervas, "High power ytterbium-doped fiber lasers - Fundamentals and applications," *Int. J. Mod. Phys. B*, vol. 28, no. 12, pp. 1–35, 2014.

[20] A. V. Smith and J. J. Smith, "Mode instability in high power fiber amplifiers," *Opt. Express*, vol. 19, no. 11, p. 10180, 2011.

[21] L. Dong, "Stimulated thermal Rayleigh scattering in optical fibers," *Opt. Express*, vol. 21, no. 3, p. 2642, 2013.

[22] F. Beier *et al.*, "Single mode 43 kW output power from a diode-pumped Yb-doped fiber amplifier," *Opt. Express*, vol. 25, no. 13, p. 14892, 2017.

[23] J. Zhang, V. Fromzel, and M. Dubinskii, "Resonantly cladding-pumped Yb-free Er-doped LMA fiber laser with record high power and efficiency," *Opt. Express*, vol. 19, no. 6, p. 5574, 2011.

[24] V. Dominic *et al.*, "110 W fiber laser," p. CPD11/1-CPD11/2, 2003.

[25] F. Auzel and P. Goldner, "Towards rare-earth clustering control in doped glasses," *Opt. Mater. (Amst).*, vol. 16, no. 1–2, pp. 93–103, 2001.

[26] A. V. Kir'yanov and Y. O. Barmenkov, "Cooperative luminescence and absorption in Ytterbium-doped silica fiber and the fiber nonlinear transmission coefficient at $\lambda = 980$ nm with a regard to the Ytterbium ion-pairs' effect: Reply," *Opt. Express*, vol. 14, no. 15, p. 6983, 2006.

[27] H. Gebavi *et al.*, "Temporal evolution and correlation between cooperative luminescence and photodarkening in ytterbium doped silica fibers," *Opt. Express*, vol. 19, no. 25, p. 25077, 2011.

[28] J. M. F. van Dijk and M. F. H. Schuurmans, “On the nonradiative and radiative decay rates and a modified exponential energy gap law for 4 f –4 f transitions in rare-earth ions,” *J. Chem. Phys.*, vol. 78, no. 9, pp. 5317–5323, May 1983.

[29] D. C. Brown and H. J. Hoffman, “Thermal, stress, and thermo-optic effects in high average power double-clad silica fiber lasers,” *IEEE J. Quantum Electron.*, vol. 37, no. 2, pp. 207–217, 2001.

[30] J. Knall *et al.*, “Laser cooling in a silica optical fiber at atmospheric pressure,” *Opt. Lett.*, vol. 45, no. 5, p. 1092, 2020.

[31] J. Knall *et al.*, “Radiation-balanced silica fiber laser,” *Optica*, vol. 8, no. 6, p. 830, Jun. 2021.

[32] V. Petit *et al.*, “ Improvement of Yb^{3+} doped optical fiber preforms by using MCVD method ,” *Solid State Lasers Amplifiers III*, vol. 6998, no. April 2008, p. 69980A, 2008.

[33] E. H. Sekiya, P. Barua, K. Saito, and A. J. Ikushima, “Fabrication of Yb-doped silica glass through the modification of MCVD process,” *J. Non. Cryst. Solids*, vol. 354, no. 42–44, pp. 4737–4742, 2008.

[34] A. J. Boyland *et al.*, “Optical fiber fabrication using novel gas-phase deposition technique,” *J. Light. Technol.*, vol. 29, no. 6, pp. 912–915, 2011.

[35] S. Unger *et al.*, “A highly efficient Yb-doped silica laser fiber prepared by gas phase doping technology,” *Laser Phys.*, vol. 24, no. 3, 2014.

[36] N. Yu, T. W. Hawkins, T. Bui, M. Cavillon, J. Ballato, and P. D. Dragic, “$AlPO_4$ in silica glass optical fibers: Deduction of additional material properties,” *IEEE Photonics J.*, vol. 11, no. 5, pp. 1–13, Oct. 2019.

[37] P. Dragic *et al.*, “Tailored glasses optimized for optical fiber-based photonic applications,” in *CLEO Pacific Rim Conference*, 2018, p. Th2E.2, [Online]. Available: https://www.osapublishing.org/abstract.cfm?uri=CLEOPR-2018-Th2E.2.

[38] M. Cavillon, P. D. Dragic, N. Yu, and J. Ballato, “A materials approach toward the mitigation of nonlinearities in glass optical fibers,” in *21st International Conference on Transparent Optical Networks (ICTON)*, 2019, p. We.D6.2.

[39] J. Ballato, T. W. Hawkins, N. Yu, and P. Dragic, “Novel materials for TMI mitigation,” in *Phtonics West*, 2021, pp. 11665–75.

[40] T. W. Hawkins, P. D. Dragic, N. Yu, A. Flores, M. Engholm, and J. Ballato, “Kilowatt power scaling of an intrinsically low Brillouin and thermo-optic Yb-doped silica fiber,” *J. Opt. Soc. Am. B*, vol. 38, no. 12, p. F38, Dec. 2021.

[41] G. Pan, N. Yu, B. Meehan, T. W. Hawkins, J. Ballato, and P. D. Dragic, "Thermo-optic coefficient of B_2O_3 and GeO_2 co-doped silica fibers," *Opt. Mater. Express*, vol. 10, no. 7, p. 1509, Jul. 2020.

[42] P. D. Dragic, M. Cavillon, A. Ballato, and J. Ballato, "A unified materials approach to mitigating optical nonlinearities in optical fiber. II. B. The optical fiber, material additivity and the nonlinear coefficients," *Int. J. Appl. Glas. Sci.*, vol. 9, no. 3, pp. 307–318, 2018.

[43] P. Zhou *et al.*, "High-power fiber lasers based on tandem pumping," *J. Opt. Soc. Am. B*, vol. 34, no. 3, p. A29, 2017.

[44] F. Kong *et al.*, "Efficient 240W single-mode 1018nm laser from an Ytterbium-doped 50/400μm all-solid photonic bandgap fiber," *Opt. Express*, vol. 26, no. 3, p. 3138, 2018.

[45] G. Gu, Z. Liu, F. Kong, H. Tam, R. K. Shori, and L. Dong, "Highly efficient ytterbium-doped phosphosilicate fiber lasers operating below 1020nm," *Opt. Express*, vol. 23, no. 14, p. 17693, 2015.

[46] M. Cavillon, C. Kucera, T. W. Hawkins, N. Yu, P. Dragic, and J. Ballato, "Ytterbium-doped multicomponent fluorosilicate optical fibers with intrinsically low optical nonlinearities," *Opt. Mater. Express*, vol. 8, no. 4, p. 744, Apr. 2018.

[47] N. Yu, M. Cavillon, C. Kucera, T. W. Hawkins, J. Ballato, and P. Dragic, "Less than 1% quantum defect fiber lasers via ytterbium-doped multicomponent fluorosilicate optical fiber," *Opt. Lett.*, vol. 43, no. 13, p. 3096, 2018.

[48] T. Som and B. Karmakar, "Nephelauxetic effect of low phonon antimony oxide glass in absorption and photoluminescence of rare-earth ions," *Spectrochim. Acta - Part A Mol. Biomol. Spectrosc.*, vol. 79, no. 5, pp. 1766–1782, 2011.

[49] T. Hawkins, "The materials science and engineering of advanced Yb-doped glasses and fibers for high-power lasers," *All Diss.*, no. May, 2020, [Online]. Available: https://tigerprints.clemson.edu/all_dissertations/2585.

[50] P. D. Dragic, M. Cavillon, and J. Ballato, "Materials for optical fiber lasers: A review," *Appl. Phys. Rev.*, vol. 5, no. 4, p. 041301, Dec. 2018.

[51] P. Dragic, M. Cavillon, and J. Ballato, "On the thermo-optic coefficient of P_2O_5 in SiO_2," *Opt. Mater. Express*, vol. 7, no. 10, p. 3654, Oct. 2017.

[52] G. Barnard, P. Myslinski, J. Chrostowski, and M. Kavehrad, "Analytical model for rare-earth-doped fiber amplifiers and lasers," *IEEE J. Quantum Electron.*, vol. 30, no. 8, pp. 1817–1830, 1994.

[53] R. Maurer, "Optical waveguide light source," 3,808,549, 1974.

[54] M. N. Zervas and C. A. Codemard, “High power fiber lasers: A review,” *IEEE J. Sel. Top. Quantum Electron.*, vol. 20, no. 5, 2014.

[55] J. Ballato and E. Snitzer, “Fabrication of fibers with high rare-earth concentrations for Faraday isolator applications,” *Appl. Opt.*, vol. 34, no. 30, pp. 6848–6854, 1995.

[56] A. D. Yablon, “Multi-wavelength optical fiber refractive index profiling by spatially resolved fourier transform spectroscopy,” *J. Light. Technol.*, vol. 28, no. 4, pp. 360–364, 2010.

[57] Y. Chen, Y. Cui, and W. Gong, “Crack propagation calculations for optical fibers under static bending and tensile loads using continuum damage mechanics,” *Sensors*, vol. 17, no. 11, p. 2633, Nov. 2017.

[58] M. Mikulla, “Tapered high-power, high-brightness diode lasers: design and performance,” in *High-Power Diode Lasers*, Berlin, Heidelberg: Springer Berlin Heidelberg, pp. 265–288.

[59] Y. Glick *et al.*, “Single-mode 230 W output power 1018 nm fiber laser and ASE competition suppression,” *J. Opt. Soc. Am. B*, vol. 33, no. 7, p. 1392, 2016.

[60] N. Yu *et al.*, “Low quantum defect fiber lasers via Yb-doped multicomponent fluorosilicate optical fiber,” in *CLEO*, 2018, p. STu3K.6, [Online]. Available: https://opg.optica.org/abstract.cfm?uri=CLEO_SI-2018-STu3K.6

[61] H. Ogilvy, M. Withford, P. Dekker, and J. Piper, “Efficient diode double-end-pumped Nd:YVO4 laser operating at 1342nm,” *Opt. Express*, vol. 11, no. 19, p. 2411, 2003.

[62] H. Kahle *et al.*, “Comparison of single-side and double-side pumping of membrane external-cavity surface-emitting lasers,” *Opt. Lett.*, vol. 44, no. 5, p. 1146, Mar. 2019.

[63] Y. Liu, B. Pan, J. Yang, Y. Wang, and M. Li, “Thermal effects in high-power double diode-end-pumped Cs vapor lasers,” *IEEE J. Quantum Electron.*, vol. 48, no. 4, pp. 485–489, Apr. 2012.

[64] D. Xue, Q. Lou, and J. Zhou, “Comparison of Yb-doped fiber laser with one-end and double-end pumping configuration,” *Opt. Laser Technol.*, vol. 39, no. 4, pp. 871–874, Jun. 2007.

[65] S. R. Bowman, “Lasers without internal heat generation,” *IEEE J. Quantum Electron.*, vol. 35, no. 1, pp. 115–122, 1999.

[66] J. Knall, M. Engholm, J. Ballato, P. Dragic, N. Yu, and M. Digonnet, “Experimental comparison of silica fibers for laser cooling,” *Opt. Lett.*, vol. 45, no. 14, pp. 4020–4023, 2020.

[67] J. M. Knall *et al.*, “Experimental observation of cooling in Yb-doped silica fibers,” *Photonics West*, no. March, pp. 11298–15, 2020.

[68] J. M. Knall, M. Engholm, T. Boilard, M. Bernier, and M. J. F. Digonnet, “A radiation-balanced silica fiber amplifier,” p. 7, Mar. 2021, [Online]. Available: http://arxiv.org/abs/2103.02698.

[69] S. Jagannathan *et al.*, “Random lasing from optical fibers with phase separated glass cores,” *Opt. Express*, vol. 28, no. 15, pp. 22049–22063, 2020.

[70] J. M. Knall *et al.*, “Experimental investigations of spectroscopy and anti-Stokes fluorescence cooling in Yb-doped silicate fibers,” in *Photonic Heat Engines: Science and Applications*, Mar. 2019, no. March 2019, p. 15.

[71] A. Arora, M. Esmaeelpour, M. Bernier, and M. J. F. Digonnet, “High-resolution slow-light fiber Bragg grating temperature sensor with phase-sensitive detection,” *Opt. Lett.*, vol. 43, no. 14, p. 3337, 2018.

[72] E. Mobini *et al.*, “Laser cooling of silica glass,” 2019, [Online]. Available: http://arxiv.org/abs/1910.10609.

[73] R. I. Epstein, M. I. Buchwald, B. C. Edwards, T. R. Gosnell, and C. E. Mungan, “Observation of laser-induced fluorescent cooling of a solid,” *Nature*, vol. 377, no. 6549, pp. 500–503, Oct. 1995.

[74] T. R. Gosnell, “Laser cooling of a solid by 65 K starting from room temperature,” *Opt. Lett.*, vol. 24, no. 15, p. 1041, Aug. 1999.

[75] C. W. Hoyt, M. Sheik-Bahae, R. I. Epstein, B. C. Edwards, and J. E. Anderson, “Observation of anti-Stokes fluorescence cooling in thulium-doped glass,” *Phys. Rev. Lett.*, vol. 85, no. 17, pp. 3600–3603, Oct. 2000.

[76] W.-J. Hwang, K.-S. Shin, J.-H. Roh, D.-S. Lee, and S.-H. Choa, “Development of micro-heaters with optimized temperature compensation design for gas sensors,” *Sensors*, vol. 11, no. 3, pp. 2580–2591, Mar. 2011.

[77] Y. Fan *et al.*, “Thermal effects in kilowatt all-fiber MOPA,” *Opt. Express*, vol. 19, no. 16, p. 15162, 2011.

[78] P.-C. Law, A. Croteau, and P. D. Dragic, “Acoustic coefficients of P_2O_5-doped silica fiber: The strain-optic and strain-acoustic coefficients,” *Opt. Mater. Express*, vol. 2, no. 4, p. 391, 2012.

[79] P. D. Dragic, J. Ballato, S. Morris, and T. Hawkins, “The Brillouin gain coefficient of Yb-doped aluminosilicate glass optical fibers,” *Opt. Mater. (Amst).*, vol. 35, no. 9, pp. 1627–1632, 2013.

[80] P. Yan, “Numerical analysis of temperature distributions in Yb-doped double-clad fiber lasers with consideration of radiative heat transfer,” *Opt. Eng.*, vol. 45, no. 12, p. 124201, 2006.

[81] R. Paschotta, J. Nilsson, P. R. Barber, J. E. Caplen, A. C. Tropper, and D. C. Hanna, “Lifetime quenching in Yb-doped fibres,” *Opt. Commun.*, vol. 136, no. 5–6, pp. 375–378, Apr. 1997.

[82] M.-J. Li *et al.*, “Al/Ge co-doped large mode area fiber with high SBS threshold,” *Opt. Express*, vol. 15, no. 13, p. 8290, 2007.

[83] C. C. Baker *et al.*, “Design solutions for increased thresholds of non-linear processes in silica fiber,” in *Advanced Solid State Lasers*, 2019, pp. JW2A-9, [Online]. Available: https://www.osapublishing.org/viewmedia.cfm?uri=ASSL-2019-JW2A.9&seq=0.

[84] P. Dragic, M. Cavillon, and J. Ballato, “The linear and nonlinear refractive index of amorphous Al_2O_3 deduced from aluminosilicate optical fibers,” *Int. J. Appl. Glas. Sci.*, vol. 9, no. 3, pp. 421–427, 2018.

[85] A. E. Mironov *et al.*, “All optical fiber thermal vacuum gauge,” *J. Phys. Photonics*, vol. 2, no. 1, p. 014006, Jan. 2020.

[86] N. Yu *et al.*, “All-optically-driven and all-optical-fiber vacuum gauge via Ytterbium-doped optical fiber microheater,” in *The International Conference on Optical Fibre Sensors*, 2021, p. 3375037.

APPENDIX A: Oscillator Stage Computer Code

Following is an example Mathematica code calculating slope efficiency for the 976.6 nm pumping case.

```
ClearAll[FiberLength];
l = 0;
Lambda1 = 976 * 10^-9;  (* Pumping Wavelength *)
Lambda2 = 985.6 * 10^-9;   (* Lasing Wavelength *)
Lambda3 = 1080 * 10^-9;    (* ASE Wavelength, ignore this for now *)
NA = Sqrt[(1.444 + 0.0415)^2 - 1.444^2];    (* Insert the delta-n for the fiber you are using *)
Dcore = 8.92 * 10^-6;     (* Core diameter, read from the table. *)
(* Fiber 'V' constants *)
V1 = Pi * Dcore * NA / Lambda1//N
V2 = Pi * Dcore * NA / Lambda2//N
V3 = Pi * Dcore * NA / Lambda3//N
(* Calculate the modes *)
Y1 = Sqrt[(V1)^2 - (X1)^2];
pumpa = (X1)BesselJ[1,X1]/BesselJ[0,X1];
pumpb = (Y1)BesselK[1,Y1]/BesselK[0,Y1];
Plot[{pumpa,pumpb},{X1,0,V1}];
Xpump=FindRoot[pumpa-pumpb==0,{X1,1.6}]
(* Seed modal structure next *)
Y2 = Sqrt[(V2)^2 - (X2)^2];
seeda = (X2)BesselJ[1,X2]/BesselJ[0,X2];
seedb = (Y2)BesselK[1,Y2]/BesselK[0,Y2];
Plot[{seeda,seedb},{X2,0,V2}];
Xseed=FindRoot[seeda-seedb==0,{X2,1.6}]

(* Setting up the LP(01) mode in the fiber and
   plots to find the modal wavenumbers *)
(* pump modal structure first *)
Y3 = Sqrt[(V3)^2 - (X3)^2];
asea = (X3)BesselJ[1,X3]/BesselJ[0,X3];
aseb = (Y3)BesselK[1,Y3]/BesselK[0,Y3];
Plot[{asea,aseb},{X3,0,V3}];
Xase=FindRoot[asea-aseb==0,{X3,2.3}]
(* Use the roots of the dispersion relation to
   define the modal wavenumbers. *)
IntersectX1 = X1/.Xpump;
IntersectX2 = X2/.Xseed;
IntersectX3 = X3/.Xase;
IntersectY1 = Sqrt[(V1)^2 - (IntersectX1)^2];
IntersectY2 = Sqrt[(V2)^2 - (IntersectX2)^2];
IntersectY3 = Sqrt[(V3)^2 - (IntersectX3)^2];
(* Modal Wavenumber given in inverse microns. *)
```

```
Kt1 = IntersectX1/(.5*Dcore)/10^6;
Kt2 = IntersectX2/(.5*Dcore)/10^6;
Kt3 = IntersectX3/(.5*Dcore)/10^6;
Gam1 = IntersectY1/(.5*Dcore)/10^6;
Gam2 = IntersectY2/(.5*Dcore)/10^6;
Gam3 = IntersectY3/(.5*Dcore)/10^6;
 (*  Fiber Mode Calculations and Plots *)
 (* Core mode structure *)
Mode1Core = Plot[(BesselJ[0, Kt1*r])^2, {r, 0, (10^6)*Dcore/2}];
(* Cladding mode structure with matched boundary condition *)
BoundaryCondition1 = BesselJ[0, Kt1*(10^6)*Dcore/2]/
                     BesselK[0, Gam1*(10^6)*Dcore/2];
Mode1Clad = Plot[(BoundaryCondition1)^2
                (BesselK[0, Gam1*r])^2, {r, (10^6)*Dcore/2, (10^6)*Dcore}];
(* Total pump mode picture *)
aaa = Show[Mode1Core, Mode1Clad, PlotRange -> All];
(* Electric field equations for future use *)
ClearAll[CoreMode1, CoreMode2];
CoreMode1 = BesselJ[0, Kt1*r];
CladMode1 = (BoundaryCondition1)*BesselK[0, Gam1*r];
(* Core mode structure *)
Mode2Core =
  Plot[(BesselJ[0, Kt2*r])^2, {r, 0, (10^6)*Dcore/2}, PlotRange -> All];
(* Cladding mode structure with matched boundary condition *)
BoundaryCondition2 =
  BesselJ[0, Kt2*(10^6)*Dcore/2]/BesselK[0, Gam2*(10^6)*Dcore/2];
Mode2Clad =
  Plot[(BoundaryCondition2)^2    (BesselK[0, Gam2*r])^2, {r, (10^6)*
    Dcore/2, (10^6)*Dcore}, PlotRange -> All];
(* Total seed mode picture *)
bbb = Show[Mode2Core, Mode2Clad, PlotRange -> All];
Show[aaa, bbb]
(* Electric field equations for future use *
CoreMode2 = BesselJ[0, Kt2*r];
CladMode2 = (BoundaryCondition2) BesselK[0, Gam2*r];
Mode3Core = Plot[(BesselJ[0, Kt3*r])^2, {r, 0, (10^6)*Dcore/2}];
(* Cladding mode structure with matched boundary condition *)
BoundaryCondition3 = BesselJ[0, Kt3*(10^6)*Dcore/2]/
                     BesselK[0, Gam3*(10^6)*Dcore/2];
Mode3Clad = Plot[(BoundaryCondition3)^2
                (BesselK[0, Gam3*r])^2, {r, (10^6)*Dcore/2, (10^6)*Dcore}];
(* Total pump mode picture *)
Show[Mode3Core, Mode3Clad, PlotRange -> All]
(* Electric field equations for future use *)
ClearAll[CoreMode3, CoreMode3];
CoreMode3 = BesselJ[0, Kt3*r];
```

```
CladMode3 = (BoundaryCondition3)*BesselK[0, Gam3*r];
 (* This section will detail some of the constants necessary
   for the power calculations to be performed later *)
(* Some constants in MKS *)
Plank = 6.6261 * 10^(-34);
SOL = 3 * 10^8;
(* Assume doping is uniform (a good approximation if Al co-doped fiber)
   or the peak resides at the given value with the Nd atoms pushed into the
   core due to the Germanium co-doping (if any).....*)
NdDensity =
  1.65 10^26;    (*  m^-3, concentration of Yb in m^-3.  Read from table.  *)

DopingRadius = Dcore/2;
CoreRadius = (Dcore/2)*10^6;
(* Overlap Integrals *)
DopingEffectiveArea = Pi DopingRadius^2 // N;
PumpArea = (2 Pi
      (NIntegrate[(10^-12) r*(CoreMode1)^2, {r, 0, CoreRadius}] +
        NIntegrate[(10^-12) r*(CladMode1)^2, {r, CoreRadius, Infinity}]));
SeedArea = (2 Pi
       (NIntegrate[(10^-12) r*(CoreMode2)^2, {r, 0, CoreRadius}] +
         NIntegrate[(10^-12) r*(CladMode2)^2, {r, CoreRadius, Infinity}]));
ASEArea = (2 Pi
      (NIntegrate[(10^-12) r*(CoreMode3)^2, {r, 0, CoreRadius}] +
        NIntegrate[(10^-12) r*(CladMode3)^2, {r, CoreRadius, Infinity}]));
PumpEffectiveArea = (2 Pi
       (NIntegrate[(10^-12) r*(CoreMode1)^2, {r, 0, CoreRadius}]));
SeedEffectiveArea = (2 Pi
       (NIntegrate[(10^-12) r*(CoreMode2)^2, {r, 0, CoreRadius}]));
ASEEffectiveArea = (2 Pi
       (NIntegrate[(10^-12) r*(CoreMode3)^2, {r, 0, CoreRadius}]));
PumpOverlap = (PumpEffectiveArea/PumpArea)
SeedOverlap = (SeedEffectiveArea/SeedArea)
ASEOverlap = (ASEEffectiveArea/ASEArea)

(* Effective Areas For Saturation Power Calculations *)
PumpEffectiveArea = (2 Pi  ((NIntegrate[(10^-12) r*(CoreMode1)^1, {r, 0,
        CoreRadius}]) + (NIntegrate[(10^-12) r*(CladMode1)^1, {r,
        CoreRadius,
        100 CoreRadius}]))^2)/((NIntegrate[(10^-12) r*(CoreMode1)^2, {r, 0,
      CoreRadius}]) + (NIntegrate[(10^-12) r*(CladMode1)^2, {r, CoreRadius,
      100 CoreRadius}]))
SeedEffectiveArea = (2 Pi  ((NIntegrate[(10^-12) r*(CoreMode2)^1, {r, 0,
        CoreRadius}]) + (NIntegrate[(10^-12) r*(CladMode2)^1, {r,
        CoreRadius,
        100 CoreRadius}]))^2)/((NIntegrate[(10^-12) r*(CoreMode2)^2, {r, 0,
```

```
      CoreRadius}]) + (NIntegrate[(10^-12) r*(CladMode2)^2, {r, CoreRadius,
      100 CoreRadius}]))
ASEEffectiveArea = (2 Pi  ((NIntegrate[(10^-12) r*(CoreMode3)^1, {r, 0,
        CoreRadius}]) + (NIntegrate[(10^-12) r*(CladMode3)^1, {r,
        CoreRadius,
        100 CoreRadius}]))^2)/((NIntegrate[(10^-12) r*(CoreMode3)^2, {r, 0,
      CoreRadius}]) + (NIntegrate[(10^-12) r*(CladMode3)^2, {r, CoreRadius,
      100 CoreRadius}]))
 (*Constants *)
FLifetime = 1270 * 10^-6;  (* Read this from the table *)
(* P is for pump, S is for lasing signal.  Read values from "CS \
calculations.xlsx" at the correct wavelengths.  You use the data from the \
gray and blue curves.  Do not use the data from the orange curve. *)

PAbsCrsSec =
  1.438* 10^(-24);   (* Use the gray curve for absorption cross section at \
the pump wavelength.  Interpolated between points if you don't have an \
exactly wavelength value available. *)
SAbsCrsSec =
  3.223* 10^(-25);    (* Use the gray curve for absorption cross section at \
the signal wavelength *)
PEmCrsSec =
  1.42* 10^(-24);     (* Use the blue curve for emission cross section at \
the pump wavelength *)
SEmCrsSec =
  4.2349* 10^(-25);    (* Use the blue curve for emission cross section at \
the signal wavelength *)
AAbsCrsSec = 0 * 10^(-25);  (* don't worry about A (ASE) *)
AEmCrsSec = 0.5 * 10^(-25);   (* don't worry about A (ASE) *)
(*Find the inversion threshold *)
ClearAll[PumpPin, Manji, Helicalization]
(* Attenuation constants in m^-1 *)
SAbsCoeff = (NdDensity)*(1)*(SAbsCrsSec);
PAbsCoeff = (NdDensity)*(1)*(PAbsCrsSec);
AAbsCoeff = (NdDensity)*(1)*(AAbsCrsSec);
(* These are photon densities normalized to
   P denotes Pump and S denotes seed. *)
PSSatPhot = (SeedEffectiveArea)/((1)*
            (FLifetime)*((SAbsCrsSec) + (SEmCrsSec)))/10^16;

PPSatPhot = (PumpEffectiveArea)/((1)*
           (FLifetime)*((PAbsCrsSec) + (PEmCrsSec)))/10^16;
AS atPhot = (ASEEffectiveArea)/((1)*
           (FLifetime)*((AAbsCrsSec) + (AEmCrsSec)))/10^16;
Delta = PSSatPhot/PPSatPhot;
GMAX = Exp[((PAbsCoeff/Delta)    -   SAbsCoeff) FiberLength];
```

```
(* These are saturation intensities in Watts *)
PSSatPow = 10^16 PSSatPhot Plank SOL/Lambda2;
PPSatPow = 10^16 PPSatPhot Plank SOL/Lambda1;
ASatPow = 10^16 A SatPhot Plank SOL/Lambda3;
(* Here we estimate the input powers
   for a forward pump direction (i.e. co-propagating beams) *)
ClearAll[A3, A1, A2, Fiberlength, SeedPinPhot, PumpPinPhot, ASEPinPhot];
(*Convert to photon flux for rate equations*)
SeedPinPhot[SeedPin_] := SeedPin Lambda2/(Plank SOL)/10^16;
ASEPinPhot[ASEPin_] := ASEPin Lambda3/(Plank SOL)/10^16;
(*PumpPinPhot[PumpPin_] := PumpPin Lambda1/(Plank SOL)/10^0;*)
PumpPinPhot = PumpPin Lambda1/(Plank SOL)/10^16;
PLaser = (1 - R2) Eps2 PRout;
R1 = 0.9902;     (* FBG #1 reflectivity *)
R2 =    0.3834;     (* FBG #2 reflectivity *)
R = Sqrt[R1 R2];
Eps1 = 1*1;  (* 0.9649*0.965 Background loss to make your data match the \
model result below. *)
Eps2 = 1;
Eps = Eps1 Eps2;
Teff = (1 - Eps2^2   R2) + (1 - Eps1^2  R1) Eps2^2  R2  *(1/(Eps R));
FiberLength = 0.116;     (* Length of Yb-doped fiber *)
LaserOutput = {};
PumpPower = {};
Do[
  PumpPin = i;
  LaserPhot =
   PROUT /. FindRoot[
     PSSatPhot  (SAbsCoeff FiberLength -
         Log[Eps R] + (Teff  PROUT)/PSSatPhot)  -
       PumpPinPhot (1 - ((GMAX Eps R)^(-Delta)) Exp[
           PROUT  Teff ((Delta/PSSatPhot) - (1/PPSatPhot))]) == 0, {PROUT,
      1000}];
  PowerOut = 10^16  (Plank  SOL/Lambda2)*LaserPhot;
  AppendTo[PumpPower, i];
  AppendTo[LaserOutput, (1 - R2) Eps2  PowerOut],
  {i, 0, 1.00, 0.001}];
aaaa = ListPlot[Transpose[{1000*PumpPower, 1000*LaserOutput}], Joined -> True,
   PlotStyle -> {Black, Thickness[0.001]},
  BaseStyle -> {FontColor -> Black, FontWeight -> "Bold",
    FontFamily -> "Times", FontSize -> 14}, Frame -> True,
  FrameLabel -> {"Pump Power (mW)", "Output Power (mW)"}]

Slope = (Lambda1/Lambda2)  Eps2 (1 - R2) (1/Teff) (PSSatPhot/
    PSSatPhot) (1 - (GMAX  Eps R)^(-Delta))
Eps2 (1 - R2) (1/Teff) (PSSatPhot/PSSatPhot) (1 - (GMAX  Eps R)^(-Delta));
```

APPENDIX B: Amplifier Stage Single-end Pumping Computer Code

Following is an example MATLAB code for the simulation of using a 20 um-core commercial double-clad fiber as the gain medium in an amplifier.

```
clc
clear all
%% First solve for signal
% input optical wavelength in um
lambda_for_signal=1.005;
% input the number of layer to simulate (include the cladding)
number_layer=3;
%input the order of Bessel function
nu=0;
%% Prepare for calculation, run this part separately to find a rough range
for beta and put into the next part
% calculate the cldding index (if it is silica)
n_clad=sqrt(1+(( 0.69616630*lambda_for_signal^2)./(lambda_for_signal^2-
0.068404300^2))...
+((0.40794260*lambda_for_signal^2)./(lambda_for_signal^2-0.11624140^2))...
+((0.89747940*lambda_for_signal^2)./(lambda_for_signal^2-9.8961610^2)));

% calculate the wavenumber
wavenumber=2*pi/(lambda_for_signal*1e-6);

%generate the radius matrix
data = xlsread('RIP1.xlsx');
%data2 = xlsread('RIP2.xlsx');
r=data(:,1)./6.126.*10;
r_core=max(r)*1e-6;
r_clad=62.5*1e-6;
R=data(:,2)*(sqrt(n_clad^2+0.08^2)-n_clad);
%r_original=data2(:,1);
%index_original=data2(:,2);
radi=zeros(numel(r)+9*(numel(r)-1),1);
RIP=zeros(numel(R)+9*(numel(R)-1),1);
for i=1:numel(radi)
    if rem(i,10)==1
        radi(i,1)=r(floor(i/10)+1,1);
    end
    if rem(i,10)>1
        Delta=(r(floor(i/10)+1,1)-r(floor(i/10)+2,1))/10;
        radi(i,1)=r(floor(i/10)+1,1)-(rem(i,10)-1)*Delta;
    end
    if rem(i,10)==0
        Delta=(r(floor(i/10),1)-r(floor(i/10)+1,1))/10;
        radi(i,1)=r(floor(i/10),1)-9*Delta;
    end
end
for i=1:numel(RIP)
    if rem(i,10)==1
        RIP(i,1)=R(floor(i/10)+1,1);
    end
    if rem(i,10)>1
        Delta=(R(floor(i/10)+1,1)-R(floor(i/10)+2,1))/10;
        RIP(i,1)=R(floor(i/10)+1,1)-(rem(i,10)-1)*Delta;
    end
```

```
    if rem(i,10)==0
        Delta=(R(floor(i/10),1)-R(floor(i/10)+1,1))/10;
        RIP(i,1)=R(floor(i/10),1)-9*Delta;
    end
end
figure ('Name','RIP')
% plot(r,R,'k*');
% hold on
plot(radi,RIP+n_clad,'b.')
hold on
% plot(-r,R,'k*');
% hold on
plot(-radi,RIP+n_clad,'b.')
x0=[max(r) 62.5];
y0=[n_clad n_clad];
plot(x0,y0,'b','Linewidth',1.5)
hold on
plot(-x0,y0,'b','Linewidth',1.5)
hold on
% plot(r_original,index_original+n_clad, 'r')
% hold on
xlabel('Position (um)')
ylabel('Index')
set(gca,'FontSize',18)
 xlim([-30 30]);

% generate the radius matri for calculation
number_of_point=int32(numel(radi)/(number_layer-1));
num=double(number_of_point);
radius=zeros(number_layer,1);
for i=2:number_layer-1
     radius(i,1)=radi((i-1)*number_of_point-1,1)*10^(-6);
end
radius(number_layer,1)=radi(numel(radi),1)*10^(-6);

% generate the index matrix for calculation
index=zeros(number_layer,1);
for i=1:number_layer-1
    if i==1
        for ii=1:number_of_point-1
    index(i,1)=index(i,1)+RIP(ii,1);
        end
     index(i,1)=index(i,1)/(num-1)+n_clad;
    end
    if i>1 & i<number_layer-1
        for ii=1:number_of_point
    index(i,1)=index(i,1)+RIP((i-1)*num-1+ii,1);
        end
        index(i,1)=index(i,1)/num+n_clad;
    end
    if i==number_layer-1
        for ii=1:(numel(radi)-(i-1)*num)+1
    index(i,1)=index(i,1)+RIP((i-1)*num-1+ii,1);
        end
        index(i,1)=index(i,1)/((numel(radi)-(i-1)*num)+1)+n_clad;
    end
end
index(number_layer,1)=n_clad;
```

```
 stairs(radius*10^(6),index,'m','LineWidth',1.5);
 hold on
 stairs(-radius*10^(6),index,'m','LineWidth',1.5);
% scan beta
beta_min=wavenumber*n_clad;
beta_max=wavenumber*max(index);
scan_number=5000;
beta=linspace(beta_min,beta_max,scan_number);

% Calculation
%generate u matrix
u=zeros(number_layer,scan_number);
for i=1:number_layer-1
    u(i,:)=sqrt(index(i,1)^2*wavenumber^2-beta.^2);
end
u(number_layer,:)=sqrt(-n_clad^2*wavenumber^2+beta.^2);

% generate the element matrix
matrix_plot=zeros(scan_number,1);
value=10^(-4);
for j=1:scan_number
matrix=zeros(2*(number_layer-1),2*(number_layer-1));
matrix(1,1)=value*besselj(nu,radius(2,1)*u(1,j));
matrix(2,1)=value*u(1,j)*(besselj(nu-1,radius(2,1)*u(1,j))-
nu*besselj(nu,radius(2,1)*u(1,j))/(radius(2,1)*u(1,j)));
matrix(2*(number_layer-1)-1,2*(number_layer-1))=-
value*besselk(nu,radius(number_layer,1)*u(number_layer,j));
matrix(2*(number_layer-1),2*(number_layer-
1))=value*u(number_layer,j)*(besselk(nu-
1,radius(number_layer,1)*u(number_layer,j))...
+nu*besselk(nu,radius(number_layer,1)*u(number_layer,j))/(radius(number_layer
,1)*u(number_layer,j)));
if number_layer==2
end
if number_layer>2
    matrix(1,2)=-value*besselj(nu,radius(2,1)*u(2,j));
    matrix(1,3)=-value*bessely(nu,radius(2,1)*u(2,j));
    matrix(2,2)=-value*u(2,j)*(besselj(nu-1,radius(2,1)*u(2,j))-
nu*besselj(nu,radius(2,1)*u(2,j))/(radius(2,1)*u(2,j)));
    matrix(2,3)=-value*u(2,j)*(bessely(nu-1,radius(2,1)*u(2,j))-
nu*bessely(nu,radius(2,1)*u(2,j))/(radius(2,1)*u(2,j)));
    matrix(2*(number_layer-1)-1,2*(number_layer-1)-
2)=value*besselj(nu,radius(number_layer,1)*u(number_layer-1,j));
    matrix(2*(number_layer-1)-1,2*(number_layer-1)-
1)=value*bessely(nu,radius(number_layer,1)*u(number_layer-1,j));
    matrix(2*(number_layer-1),2*(number_layer-1)-2)=value*u(number_layer-
1,j)*(besselj(nu-1,radius(number_layer,1)*u(number_layer-1,j))...
        -nu*besselj(nu,radius(number_layer,1)*u(number_layer-
1,j))/(radius(number_layer,1)*u(number_layer-1,j)));
    matrix(2*(number_layer-1),2*(number_layer-1)-1)=value*u(number_layer-
1,j)*(bessely(nu-1,radius(number_layer,1)*u(number_layer-1,j))...
        -nu*bessely(nu,radius(number_layer,1)*u(number_layer-
1,j))/(radius(number_layer,1)*u(number_layer-1,j)));
    if number_layer>3
        for ii=3:2*(number_layer-1)-2
            if rem(ii,2)==1
                ord=(ii+1)/2;
                matrix(ii,ii-1)=value*besselj(nu,radius(ord+1,1)*u(ord,j));
```

```
                matrix(ii,ii)=value*bessely(nu,radius(ord+1,1)*u(ord,j));
                matrix(ii,ii+1)=-
value*besselj(nu,radius(ord+1,1)*u(ord+1,j));
                matrix(ii,ii+2)=-
value*bessely(nu,radius(ord+1,1)*u(ord+1,j));
            end
            if rem(ii,2)==0
                ord=ii/2;
                matrix(ii,ii-2)=value*u(ord,j)*(besselj(nu-
1,radius(ord+1,1)*u(ord,j))-
nu*besselj(nu,radius(ord+1,1)*u(ord,j))/(radius(ord+1,1)*u(ord,j)));
                matrix(ii,ii-1)=value*u(ord,j)*(bessely(nu-
1,radius(ord+1,1)*u(ord,j))-
nu*bessely(nu,radius(ord+1,1)*u(ord,j))/(radius(ord+1,1)*u(ord,j)));
                matrix(ii,ii)=-value*u(ord+1,j)*(besselj(nu-
1,radius(ord+1,1)*u(ord+1,j))-
nu*besselj(nu,radius(ord+1,1)*u(ord+1,j))/(radius(ord+1,1)*u(ord+1,j)));
                matrix(ii,ii+1)=-value*u(ord+1,j)*(bessely(nu-
1,radius(ord+1,1)*u(ord+1,j))-
nu*bessely(nu,radius(ord+1,1)*u(ord+1,j))/(radius(ord+1,1)*u(ord+1,j)));
            end
        end
    end
end
matrix_plot(j,1)=det(matrix);
end
% plot det(matrix) vs beta
b=zeros(scan_number,1);
figure ('Name','Check')
%If not working change here for real and imag
plot (beta,real(matrix_plot));
hold on
plot (beta,b);
%axis([beta_min,beta_max,-1e2,1e2])
xlabel('Beta (Hz)')
ylabel('Det (matrix)')


%% search for beta
beta_min=9.078e6;
beta_max=9.08e6;

% generate the element matrix
matrix_plot=zeros(scan_number,1);

 for times=1:4
    scan_number=5000;
    beta=linspace(beta_min,beta_max,scan_number);
    u=zeros(number_layer,scan_number);
        for i=1:number_layer-1
            u(i,:)=sqrt(index(i,1)^2*wavenumber^2-beta.^2);
        end
        u(number_layer,:)=sqrt(-n_clad^2*wavenumber^2+beta.^2);
            for j=1:scan_number
            matrix=zeros(2*(number_layer-1),2*(number_layer-1));
            matrix(1,1)=value*besselj(nu,radius(2,1)*u(1,j));
```

```
            matrix(2,1)=value*u(1,j)*(besselj(nu-1,radius(2,1)*u(1,j))-
nu*besselj(nu,radius(2,1)*u(1,j))/(radius(2,1)*u(1,j)));
            matrix(2*(number_layer-1)-1,2*(number_layer-1))=-
value*besselk(nu,radius(number_layer,1)*u(number_layer,j));
            matrix(2*(number_layer-1),2*(number_layer-
1))=value*u(number_layer,j)*(besselk(nu-
1,radius(number_layer,1)*u(number_layer,j))...

+nu*besselk(nu,radius(number_layer,1)*u(number_layer,j))/(radius(number_layer
,1)*u(number_layer,j)));
                if number_layer==2
                end
                if number_layer>2
                    matrix(1,2)=-value*besselj(nu,radius(2,1)*u(2,j));
                    matrix(1,3)=-value*bessely(nu,radius(2,1)*u(2,j));
                    matrix(2,2)=-value*u(2,j)*(besselj(nu-
1,radius(2,1)*u(2,j))-
nu*besselj(nu,radius(2,1)*u(2,j))/(radius(2,1)*u(2,j)));
                    matrix(2,3)=-value*u(2,j)*(bessely(nu-
1,radius(2,1)*u(2,j))-
nu*bessely(nu,radius(2,1)*u(2,j))/(radius(2,1)*u(2,j)));
                    matrix(2*(number_layer-1)-1,2*(number_layer-1)-
2)=value*besselj(nu,radius(number_layer,1)*u(number_layer-1,j));
                    matrix(2*(number_layer-1)-1,2*(number_layer-1)-
1)=value*bessely(nu,radius(number_layer,1)*u(number_layer-1,j));
                    matrix(2*(number_layer-1),2*(number_layer-1)-
2)=value*u(number_layer-1,j)*(besselj(nu-
1,radius(number_layer,1)*u(number_layer-1,j))...
                        -nu*besselj(nu,radius(number_layer,1)*u(number_layer-
1,j))/(radius(number_layer,1)*u(number_layer-1,j)));
                    matrix(2*(number_layer-1),2*(number_layer-1)-
1)=value*u(number_layer-1,j)*(bessely(nu-
1,radius(number_layer,1)*u(number_layer-1,j))...
                        -nu*bessely(nu,radius(number_layer,1)*u(number_layer-
1,j))/(radius(number_layer,1)*u(number_layer-1,j)));
                    if number_layer>3
                        for ii=3:2*(number_layer-1)-2
                            if rem(ii,2)==1
                                ord=(ii+1)/2;
                                matrix(ii,ii-
1)=value*besselj(nu,radius(ord+1,1)*u(ord,j));

matrix(ii,ii)=value*bessely(nu,radius(ord+1,1)*u(ord,j));
                                matrix(ii,ii+1)=-
value*besselj(nu,radius(ord+1,1)*u(ord+1,j));
                                matrix(ii,ii+2)=-
value*bessely(nu,radius(ord+1,1)*u(ord+1,j));
                            end
                            if rem(ii,2)==0
                                ord=ii/2;
                                matrix(ii,ii-2)=value*u(ord,j)*(besselj(nu-
1,radius(ord+1,1)*u(ord,j))-
nu*besselj(nu,radius(ord+1,1)*u(ord,j))/(radius(ord+1,1)*u(ord,j)));
                                matrix(ii,ii-1)=value*u(ord,j)*(bessely(nu-
1,radius(ord+1,1)*u(ord,j))-
nu*bessely(nu,radius(ord+1,1)*u(ord,j))/(radius(ord+1,1)*u(ord,j)));
```

```
                                matrix(ii,ii)=-value*u(ord+1,j)*(besselj(nu-
1,radius(ord+1,1)*u(ord+1,j))-
nu*besselj(nu,radius(ord+1,1)*u(ord+1,j))/(radius(ord+1,1)*u(ord+1,j)));
                                matrix(ii,ii+1)=-
value*u(ord+1,j)*(bessely(nu-1,radius(ord+1,1)*u(ord+1,j))-
nu*bessely(nu,radius(ord+1,1)*u(ord+1,j))/(radius(ord+1,1)*u(ord+1,j)));
                            end
                        end
                    end
                end
                %If not working change here for real and imag
                matrix_plot(j,1)=real(det(matrix));
                    if j>1&& matrix_plot(j,1)*matrix_plot(j-1,1)<0
                        beta_min=beta(1,j-1);
                        beta_max=beta(1,j);
                        det_min=abs(matrix_plot(j-1,1));
                        det_max=abs(matrix_plot(j,1));
                    end
        end
 end

beta_solve= beta_min+(beta_max-beta_min)*det_min/(det_min+det_max);
modal_index=beta_solve*lambda_for_signal*10^(-6)/(2*pi);
digitsOld = digits(100);
vpa(beta_solve)
vpa(modal_index)
% figure ('Name','Check1')
% plot (beta,matrix_plot);
%% solve for constant
% generate u matrix again
u_solve=zeros(number_layer,1);
for i=1:number_layer-1
    u_solve(i,1)=sqrt(index(i,1)^2*wavenumber^2-beta_solve^2);
end
u_solve(number_layer,1)=sqrt(-n_clad^2*wavenumber^2+beta_solve^2);

% generate the matrix again
value=10^(-4);
matrix_solve=zeros(2*(number_layer-1),2*(number_layer-1));
matrix_solve(1,1)=value*besselj(nu,radius(2,1)*u_solve(1,1));
matrix_solve(2,1)=value*u_solve(1,1)*(besselj(nu-1,radius(2,1)*u_solve(1,1))-
nu*besselj(nu,radius(2,1)*u_solve(1,1))/(radius(2,1)*u_solve(1,1)));
matrix_solve(2*(number_layer-1)-1,2*(number_layer-1))=-
value*besselk(nu,radius(number_layer,1)*u_solve(number_layer,1));
matrix_solve(2*(number_layer-1),2*(number_layer-
1))=value*u_solve(number_layer,1)*(besselk(nu-
1,radius(number_layer,1)*u_solve(number_layer,1))...
+nu*besselk(nu,radius(number_layer,1)*u_solve(number_layer,1))/(radius(number
_layer,1)*u_solve(number_layer,1)));

if number_layer>2
    matrix_solve(1,2)=-value*besselj(nu,radius(2,1)*u_solve(2,1));
    matrix_solve(1,3)=-value*bessely(nu,radius(2,1)*u_solve(2,1));
    matrix_solve(2,2)=-value*u_solve(2,1)*(besselj(nu-
1,radius(2,1)*u_solve(2,1))-
nu*besselj(nu,radius(2,1)*u_solve(2,1))/(radius(2,1)*u_solve(2,1)));
```

```
    matrix_solve(2,3)=-value*u_solve(2,1)*(bessely(nu-
1,radius(2,1)*u_solve(2,1))-
nu*bessely(nu,radius(2,1)*u_solve(2,1))/(radius(2,1)*u_solve(2,1)));
    matrix_solve(2*(number_layer-1)-1,2*(number_layer-1)-
2)=value*besselj(nu,radius(number_layer,1)*u_solve(number_layer-1,1));
    matrix_solve(2*(number_layer-1)-1,2*(number_layer-1)-
1)=value*bessely(nu,radius(number_layer,1)*u_solve(number_layer-1,1));
    matrix_solve(2*(number_layer-1),2*(number_layer-1)-
2)=value*u_solve(number_layer-1,1)*(besselj(nu-
1,radius(number_layer,1)*u_solve(number_layer-1,1))...
        -nu*besselj(nu,radius(number_layer,1)*u_solve(number_layer-
1,1))/(radius(number_layer,1)*u_solve(number_layer-1,1)));
    matrix_solve(2*(number_layer-1),2*(number_layer-1)-
1)=value*u_solve(number_layer-1,1)*(bessely(nu-
1,radius(number_layer,1)*u_solve(number_layer-1,1))...
        -nu*bessely(nu,radius(number_layer,1)*u_solve(number_layer-
1,1))/(radius(number_layer,1)*u_solve(number_layer-1,1)));
    if number_layer>3
        for ii=3:2*(number_layer-1)-2
            if rem(ii,2)==1
                ord=(ii+1)/2;
                matrix_solve(ii,ii-
1)=value*besselj(nu,radius(ord+1,1)*u_solve(ord,1));

matrix_solve(ii,ii)=value*bessely(nu,radius(ord+1,1)*u_solve(ord,1));
                matrix_solve(ii,ii+1)=-
value*besselj(nu,radius(ord+1,1)*u_solve(ord+1,1));
                matrix_solve(ii,ii+2)=-
value*bessely(nu,radius(ord+1,1)*u_solve(ord+1,1));
            end
            if rem(ii,2)==0
                ord=ii/2;
                matrix_solve(ii,ii-2)=value*u_solve(ord,1)*(besselj(nu-
1,radius(ord+1,1)*u_solve(ord,1))-
nu*besselj(nu,radius(ord+1,1)*u_solve(ord,1))/(radius(ord+1,1)*u_solve(ord,1)
));
                matrix_solve(ii,ii-1)=value*u_solve(ord,1)*(bessely(nu-
1,radius(ord+1,1)*u_solve(ord,1))-
nu*bessely(nu,radius(ord+1,1)*u_solve(ord,1))/(radius(ord+1,1)*u_solve(ord,1)
));
                matrix_solve(ii,ii)=-value*u_solve(ord+1,1)*(besselj(nu-
1,radius(ord+1,1)*u_solve(ord+1,1))-
nu*besselj(nu,radius(ord+1,1)*u_solve(ord+1,1))/(radius(ord+1,1)*u_solve(ord+
1,1)));
                matrix_solve(ii,ii+1)=-value*u_solve(ord+1,1)*(bessely(nu-
1,radius(ord+1,1)*u_solve(ord+1,1))-
nu*bessely(nu,radius(ord+1,1)*u_solve(ord+1,1))/(radius(ord+1,1)*u_solve(ord+
1,1)));
            end
        end
    end
end

% solve for all the coefficients
answer=null(matrix_solve);
coeff=answer./answer(1,1);
% coeff=real(coeff)
%% Part III: plot the 2D electric mode
```

```
% type the radical range of simulation
r_plot_outbound=62.5;

% plot point density
times=1000;

 figure ('Name','2D Electric Mode')
for i=1:number_layer
    if i==1
    r_1=linspace(0,radius(2,1),times);
    mode_1_electric=real(coeff(1,1)*besselj(nu,u_solve(1,1).*r_1));
%     yyaxis left
    plot(r_1*10^(6),mode_1_electric,'r','LineWidth',2);
    hold on
%     yyaxis left
    plot(-r_1*10^(6),mode_1_electric,'r','LineWidth',2);
    hold on
    r_sum_electrical=0+r_1;
    mode_sum_electrical=0+mode_1_electric;
    end
    if i>1 & i<number_layer
      r=linspace(radius(i,1),radius(i+1,1),times);
      mode_electric=real(coeff(2*i-
2,1)*besselj(nu,u_solve(i,1).*r)+coeff(2*i-1,1)*bessely(nu,u_solve(i,1).*r));
%       yyaxis left
      plot(r*10^(6),mode_electric,'r','LineWidth',2);
      hold on
%       yyaxis left
      plot(-r*10^(6),mode_electric,'r','LineWidth',2);
      hold on
      r_sum_electrical=[r_sum_electrical r];
      mode_sum_electrical=[mode_sum_electrical mode_electric];

    end
    if i==number_layer
        r_2=linspace(radius(number_layer,1),r_plot_outbound*10^(-6),times);
        mode_clad_electric=real(coeff(2*(number_layer-
1),1)*besselk(nu,u_solve(number_layer,1).*r_2));
%         yyaxis left
        plot(r_2*10^(6),mode_clad_electric,'r','LineWidth',2);
        hold on
%         yyaxis left
        plot(-r_2*10^(6),mode_clad_electric,'r','LineWidth',2);
        hold on
        r_sum_electrical=[r_sum_electrical r_2];
       mode_sum_electrical=[mode_sum_electrical  mode_clad_electric];
    end

end



a=[-100,100];
b=[0,0];
plot (a,b,'b:','LineWidth',1.5)

axis([-r_plot_outbound,r_plot_outbound,-0.02,0.02]);
```

```
yyaxis right
ylim([-1*max(RIP) 1.2*max(RIP)]);
plot(radi,RIP,'k:','LineWidth',1.5);
hold on
plot(-radi,RIP,'k:','LineWidth',1.5);
hold on
stairs(radius*10^(6),index-n_clad,'m-','LineWidth',1);
hold on
stairs(-radius*10^(6),index-n_clad,'m-','LineWidth',1);
hold on
rr=[radius(number_layer,1)*10^(6),r_plot_outbound];
aaa=[0,0];
plot(rr,aaa,'k:','LineWidth',1.5);
hold on
plot(-rr,aaa,'k:','LineWidth',1.5);
hold on
plot(rr,aaa,'m-','LineWidth',1);
hold on
plot(-rr,aaa,'m-','LineWidth',1);

yyaxis left
ylim([0 1.2]);
title('Mode (Electric) and RIP')
xlabel('Position (um)')
ylabel('Normalized Amplitude')

yyaxis right
ylim([0, 2.5e-3]);
ylabel('Index Difference')
xlim([-30 30]);
set(gca,'FontSize',18)


%% Final results for signal

% mode
r_signal=r_sum_electrical;
mode_signal=mode_sum_electrical;
r_signal_sum=[-fliplr(r_signal) r_signal];
mode_signal_sum=[fliplr(mode_signal) mode_signal];

% Aeff and overlap integral

 %integral of (E)^2 from 0 to cladding
 E2=zeros(numel(r_signal)-1,1);
 for i=1:numel(r_signal)-1

E2(i,1)=(((mode_signal(1,i))+(mode_signal(1,i+1)))/2)^2*(r_signal(1,i+1)+r_si
gnal(1,i))/2*(r_signal(1,i+1)-r_signal(1,i));
 end
 inte_E2=sum(E2);

  %integral of (E)^2 from 0 to core
 E2_core=zeros(numel(r_signal)-times-1,1);
 for i=1:numel(r_signal)-1-times
```

```
E2_core(i,1)=(((mode_signal(1,i))+(mode_signal(1,i+1)))/2)^2*(r_signal(1,i+1)
+r_signal(1,i))/2*(r_signal(1,i+1)-r_signal(1,i));
 end
 inte_E2_core=sum(E2_core);


  %integral of (E)^4 from 0 to cladding
 E4=zeros(numel(r_signal)-1,1);
 for i=1:numel(r_signal)-1

E4(i,1)=(((mode_signal(1,i))+(mode_signal(1,i+1)))/2)^4*(r_signal(1,i+1)+r_si
gnal(1,i))/2*(r_signal(1,i+1)-r_signal(1,i));
 end
 inte_E4=sum(E4);

overlap_signal=inte_E2_core/inte_E2;
Aeff_signal=2*pi*inte_E2^2/inte_E4;
reff_signal=sqrt(Aeff_signal/pi);
overlap_ASE=overlap_signal;
Aeff_ASE=Aeff_signal;
reff_ASE=reff_signal;

%% Input constant for power simulation
data1 = xlsread('cross_section.xlsx');
% cross_emi=data1(:,9);
% cross_abs=data1(:,11);
 cross_emi=data1(:,3);
 cross_abs=data1(:,2);
lambda_ASE_all=1e-9.*transpose(linspace(1000,1090,10));
cross_emi_all=zeros(1,1);
cross_abs_all=zeros(1,1);
data2 = xlsread('signal_spec.xlsx');
lambsss=data2(1:1001,5);
out_ASE_spectra=data2(1:1001,6);
out_signal_spectra=data2(1:1001,7);
signal_ratio=sum(out_signal_spectra)/(sum(out_signal_spectra)+sum(out_ASE_spe
ctra))-0.025;
ASE_ratio=1-signal_ratio;
out_power=zeros(1,1);
for i=1:10
    cross_abs_all(i,1)=mean(cross_abs((i-1)*10+1:i*10,1));
    cross_emi_all(i,1)=mean(cross_emi((i-1)*10+1:i*10,1));
    out_power(i,1)=sum(out_ASE_spectra((i-1)*100+1:i*100,1));
end
nor_para=sum(out_power);
out_ASE_ratio=out_power./nor_para;
%
%speed of light
sol=299792458;
%plank constant
plank=6.62607004e-34;
% Yb density
rho=6e25;
%lifetime
tau=0.8e-3;
% wavelength
```

```
lambda_pump=975*1e-9;
lambda_signal=lambda_for_signal*1e-6;
lambda_ASE_1=lambda_ASE_all(1,1);
lambda_ASE_2=lambda_ASE_all(2,1);
lambda_ASE_3=lambda_ASE_all(3,1);
lambda_ASE_4=lambda_ASE_all(4,1);
lambda_ASE_5=lambda_ASE_all(5,1);
lambda_ASE_6=lambda_ASE_all(6,1);
lambda_ASE_7=lambda_ASE_all(7,1);
lambda_ASE_8=lambda_ASE_all(8,1);
lambda_ASE_9=lambda_ASE_all(9,1);
lambda_ASE_10=lambda_ASE_all(10,1);
% Absorption cross sections
Abs_cross_pump=2.5e-24;
Abs_cross_signal=1.02e-25;
Abs_cross_ASE_1=cross_abs_all(1,1);
Abs_cross_ASE_2=cross_abs_all(2,1);
Abs_cross_ASE_3=cross_abs_all(3,1);
Abs_cross_ASE_4=cross_abs_all(4,1);
Abs_cross_ASE_5=cross_abs_all(5,1);
Abs_cross_ASE_6=cross_abs_all(6,1);
Abs_cross_ASE_7=cross_abs_all(7,1);
Abs_cross_ASE_8=cross_abs_all(8,1);
Abs_cross_ASE_9=cross_abs_all(9,1);
Abs_cross_ASE_10=cross_abs_all(10,1);
% Emission cross sections
Emi_cross_pump=2.5e-24;
Emi_cross_signal=4.28e-25;
Emi_cross_ASE_1=cross_emi_all(1,1);
Emi_cross_ASE_2=cross_emi_all(2,1);
Emi_cross_ASE_3=cross_emi_all(3,1);
Emi_cross_ASE_4=cross_emi_all(4,1);
Emi_cross_ASE_5=cross_emi_all(5,1);
Emi_cross_ASE_6=cross_emi_all(6,1);
Emi_cross_ASE_7=cross_emi_all(7,1);
Emi_cross_ASE_8=cross_emi_all(8,1);
Emi_cross_ASE_9=cross_emi_all(9,1);
Emi_cross_ASE_10=cross_emi_all(10,1);
% pump overlap integral
overlap_pump=(r_core/r_clad)^2;
% Absorption coefficient
alpha_pump=rho*Abs_cross_pump*overlap_pump;
alpha_signal=rho*Abs_cross_signal*overlap_signal;
alpha_ASE_1=rho*Abs_cross_ASE_1*overlap_ASE;
alpha_ASE_2=rho*Abs_cross_ASE_2*overlap_ASE;
alpha_ASE_3=rho*Abs_cross_ASE_3*overlap_ASE;
alpha_ASE_4=rho*Abs_cross_ASE_4*overlap_ASE;
alpha_ASE_5=rho*Abs_cross_ASE_5*overlap_ASE;
alpha_ASE_6=rho*Abs_cross_ASE_6*overlap_ASE;
alpha_ASE_7=rho*Abs_cross_ASE_7*overlap_ASE;
alpha_ASE_8=rho*Abs_cross_ASE_8*overlap_ASE;
alpha_ASE_9=rho*Abs_cross_ASE_9*overlap_ASE;
alpha_ASE_10=rho*Abs_cross_ASE_10*overlap_ASE;
% background loss
alpha_background_pump=-log10(10^(-20/10*1e-3))*(1-overlap_pump);%20 dB/km of
background loss in cladding
alpha_background_signal=-log10(10^(-50/10*1e-3))*overlap_signal;%50 dB/km of
background loss for signal
```

```
alpha_background_ASE=alpha_background_signal;
% Saturation power
p_sat_pump=pi*r_core^2*plank*sol/(overlap_pump*tau*(Abs_cross_pump+Emi_cross_
pump)*lambda_pump);
p_sat_signal=Aeff_signal*plank*sol/(overlap_signal*tau*(Abs_cross_signal+Emi_
cross_signal)*lambda_signal);
p_sat_ASE_1=Aeff_ASE*plank*sol/(overlap_ASE*tau*(Abs_cross_ASE_1+Emi_cross_AS
E_1)*lambda_ASE_1);
p_sat_ASE_2=Aeff_ASE*plank*sol/(overlap_ASE*tau*(Abs_cross_ASE_2+Emi_cross_AS
E_2)*lambda_ASE_2);
p_sat_ASE_3=Aeff_ASE*plank*sol/(overlap_ASE*tau*(Abs_cross_ASE_3+Emi_cross_AS
E_3)*lambda_ASE_3);
p_sat_ASE_4=Aeff_ASE*plank*sol/(overlap_ASE*tau*(Abs_cross_ASE_4+Emi_cross_AS
E_4)*lambda_ASE_4);
p_sat_ASE_5=Aeff_ASE*plank*sol/(overlap_ASE*tau*(Abs_cross_ASE_5+Emi_cross_AS
E_5)*lambda_ASE_5);
p_sat_ASE_6=Aeff_ASE*plank*sol/(overlap_ASE*tau*(Abs_cross_ASE_6+Emi_cross_AS
E_6)*lambda_ASE_6);
p_sat_ASE_7=Aeff_ASE*plank*sol/(overlap_ASE*tau*(Abs_cross_ASE_7+Emi_cross_AS
E_7)*lambda_ASE_7);
p_sat_ASE_8=Aeff_ASE*plank*sol/(overlap_ASE*tau*(Abs_cross_ASE_8+Emi_cross_AS
E_8)*lambda_ASE_8);
p_sat_ASE_9=Aeff_ASE*plank*sol/(overlap_ASE*tau*(Abs_cross_ASE_9+Emi_cross_AS
E_9)*lambda_ASE_9);
p_sat_ASE_10=Aeff_ASE*plank*sol/(overlap_ASE*tau*(Abs_cross_ASE_10+Emi_cross_
ASE_10)*lambda_ASE_10);

%% First, find the optimized fiber length
% pump shaping factor (=1 if cladding is shaped)
shape=0.95;%0.47
%input parameter
L_simulation_max=5;
p_in_pump_max=20;
p_in_all=0.2;
p_in_signal=p_in_all*signal_ratio;
p_in_ASE_1=p_in_all*ASE_ratio*out_ASE_ratio(1,1);
p_in_ASE_2=p_in_all*ASE_ratio*out_ASE_ratio(2,1);
p_in_ASE_3=p_in_all*ASE_ratio*out_ASE_ratio(3,1);
p_in_ASE_4=p_in_all*ASE_ratio*out_ASE_ratio(4,1);
p_in_ASE_5=p_in_all*ASE_ratio*out_ASE_ratio(5,1);
p_in_ASE_6=p_in_all*ASE_ratio*out_ASE_ratio(6,1);
p_in_ASE_7=p_in_all*ASE_ratio*out_ASE_ratio(7,1);
p_in_ASE_8=p_in_all*ASE_ratio*out_ASE_ratio(8,1);
p_in_ASE_9=p_in_all*ASE_ratio*out_ASE_ratio(9,1);
p_in_ASE_10=p_in_all*ASE_ratio*out_ASE_ratio(10,1);
times=251;

L=linspace(0,L_simulation_max,times);
p_out_pump_L=zeros(1,times);
p_out_signal_L=zeros(1,times);
p_out_ASE_1_L=zeros(1,times);
p_out_ASE_2_L=zeros(1,times);
p_out_ASE_3_L=zeros(1,times);
p_out_ASE_4_L=zeros(1,times);
p_out_ASE_5_L=zeros(1,times);
p_out_ASE_6_L=zeros(1,times);
p_out_ASE_7_L=zeros(1,times);
p_out_ASE_8_L=zeros(1,times);
```

```
p_out_ASE_9_L=zeros(1,times);
p_out_ASE_10_L=zeros(1,times);
p_out_pump_L(1,1)=p_in_pump_max;
p_out_signal_L(1,1)=p_in_signal;
p_out_ASE_1_L(1,1)=p_in_ASE_1;
p_out_ASE_2_L(1,1)=p_in_ASE_2;
p_out_ASE_3_L(1,1)=p_in_ASE_3;
p_out_ASE_4_L(1,1)=p_in_ASE_4;
p_out_ASE_5_L(1,1)=p_in_ASE_5;
p_out_ASE_6_L(1,1)=p_in_ASE_6;
p_out_ASE_7_L(1,1)=p_in_ASE_7;
p_out_ASE_8_L(1,1)=p_in_ASE_8;
p_out_ASE_9_L(1,1)=p_in_ASE_9;
p_out_ASE_10_L(1,1)=p_in_ASE_10;

  for i=2:times

    syms p_p_out p_s_out p_ASE_out_1 p_ASE_out_2 p_ASE_out_3 p_ASE_out_4
p_ASE_out_5...
        p_ASE_out_6 p_ASE_out_7 p_ASE_out_8 p_ASE_out_9 p_ASE_out_10
        eq1=p_p_out-p_in_pump_max.*shape.*exp(-alpha_pump.*L(1,i)-
alpha_background_pump.*L(1,i)+...
            (p_in_pump_max.*shape+p_in_signal+p_in_all*ASE_ratio-p_p_out-
p_s_out-p_ASE_out_1-p_ASE_out_2-p_ASE_out_3...
            -p_ASE_out_4-p_ASE_out_5-p_ASE_out_6-p_ASE_out_7-p_ASE_out_8-
p_ASE_out_9...
            -p_ASE_out_10)./(p_sat_pump));

        eq2=p_s_out-p_in_signal.*exp(-alpha_signal.*L(1,i)-
alpha_background_signal.*L(1,i)+...
            (p_in_pump_max.*shape+p_in_signal+p_in_all*ASE_ratio-p_p_out-
p_s_out-p_ASE_out_1-p_ASE_out_2-p_ASE_out_3...
            -p_ASE_out_4-p_ASE_out_5-p_ASE_out_6-p_ASE_out_7-p_ASE_out_8-
p_ASE_out_9...
            -p_ASE_out_10)./(p_sat_signal));

        eq3=p_ASE_out_1-p_in_ASE_1.*exp(-alpha_ASE_1.*L(1,i)-
alpha_background_ASE.*L(1,i)+...
            (p_in_pump_max.*shape+p_in_signal+p_in_all*ASE_ratio-p_p_out-
p_s_out-p_ASE_out_1-p_ASE_out_2-p_ASE_out_3...
            -p_ASE_out_4-p_ASE_out_5-p_ASE_out_6-p_ASE_out_7-p_ASE_out_8-
p_ASE_out_9...
            -p_ASE_out_10)./(p_sat_ASE_1));
        eq4=p_ASE_out_2-p_in_ASE_2.*exp(-alpha_ASE_2.*L(1,i)-
alpha_background_ASE.*L(1,i)+...
            (p_in_pump_max.*shape+p_in_signal+p_in_all*ASE_ratio-p_p_out-
p_s_out-p_ASE_out_1-p_ASE_out_2-p_ASE_out_3...
            -p_ASE_out_4-p_ASE_out_5-p_ASE_out_6-p_ASE_out_7-p_ASE_out_8-
p_ASE_out_9...
            -p_ASE_out_10)./(p_sat_ASE_2));
        eq5=p_ASE_out_3-p_in_ASE_3.*exp(-alpha_ASE_3.*L(1,i)-
alpha_background_ASE.*L(1,i)+...
            (p_in_pump_max.*shape+p_in_signal+p_in_all*ASE_ratio-p_p_out-
p_s_out-p_ASE_out_1-p_ASE_out_2-p_ASE_out_3...
            -p_ASE_out_4-p_ASE_out_5-p_ASE_out_6-p_ASE_out_7-p_ASE_out_8-
p_ASE_out_9...
            -p_ASE_out_10)./(p_sat_ASE_3));
```

```
        eq6=p_ASE_out_4-p_in_ASE_4.*exp(-alpha_ASE_4.*L(1,i)-
alpha_background_ASE.*L(1,i)+...
            (p_in_pump_max.*shape+p_in_signal+p_in_all*ASE_ratio-p_p_out-
p_s_out-p_ASE_out_1-p_ASE_out_2-p_ASE_out_3...
            -p_ASE_out_4-p_ASE_out_5-p_ASE_out_6-p_ASE_out_7-p_ASE_out_8-
p_ASE_out_9...
            -p_ASE_out_10)./(p_sat_ASE_4));
        eq7=p_ASE_out_5-p_in_ASE_5.*exp(-alpha_ASE_5.*L(1,i)-
alpha_background_ASE.*L(1,i)+...
            (p_in_pump_max.*shape+p_in_signal+p_in_all*ASE_ratio-p_p_out-
p_s_out-p_ASE_out_1-p_ASE_out_2-p_ASE_out_3...
            -p_ASE_out_4-p_ASE_out_5-p_ASE_out_6-p_ASE_out_7-p_ASE_out_8-
p_ASE_out_9...
            -p_ASE_out_10)./(p_sat_ASE_5));
        eq8=p_ASE_out_6-p_in_ASE_6.*exp(-alpha_ASE_6.*L(1,i)-
alpha_background_ASE.*L(1,i)+...
            (p_in_pump_max.*shape+p_in_signal+p_in_all*ASE_ratio-p_p_out-
p_s_out-p_ASE_out_1-p_ASE_out_2-p_ASE_out_3...
            -p_ASE_out_4-p_ASE_out_5-p_ASE_out_6-p_ASE_out_7-p_ASE_out_8-
p_ASE_out_9...
            -p_ASE_out_10)./(p_sat_ASE_6));
        eq9=p_ASE_out_7-p_in_ASE_7.*exp(-alpha_ASE_7.*L(1,i)-
alpha_background_ASE.*L(1,i)+...
            (p_in_pump_max.*shape+p_in_signal+p_in_all*ASE_ratio-p_p_out-
p_s_out-p_ASE_out_1-p_ASE_out_2-p_ASE_out_3...
            -p_ASE_out_4-p_ASE_out_5-p_ASE_out_6-p_ASE_out_7-p_ASE_out_8-
p_ASE_out_9...
            -p_ASE_out_10)./(p_sat_ASE_7));
        eq10=p_ASE_out_8-p_in_ASE_8.*exp(-alpha_ASE_8.*L(1,i)-
alpha_background_ASE.*L(1,i)+...
            (p_in_pump_max.*shape+p_in_signal+p_in_all*ASE_ratio-p_p_out-
p_s_out-p_ASE_out_1-p_ASE_out_2-p_ASE_out_3...
            -p_ASE_out_4-p_ASE_out_5-p_ASE_out_6-p_ASE_out_7-p_ASE_out_8-
p_ASE_out_9...
            -p_ASE_out_10)./(p_sat_ASE_8));
        eq11=p_ASE_out_9-p_in_ASE_9.*exp(-alpha_ASE_9.*L(1,i)-
alpha_background_ASE.*L(1,i)+...
            (p_in_pump_max.*shape+p_in_signal+p_in_all*ASE_ratio-p_p_out-
p_s_out-p_ASE_out_1-p_ASE_out_2-p_ASE_out_3...
            -p_ASE_out_4-p_ASE_out_5-p_ASE_out_6-p_ASE_out_7-p_ASE_out_8-
p_ASE_out_9...
            -p_ASE_out_10)./(p_sat_ASE_9));
        eq12=p_ASE_out_10-p_in_ASE_10.*exp(-alpha_ASE_10.*L(1,i)-
alpha_background_ASE.*L(1,i)+...
            (p_in_pump_max.*shape+p_in_signal+p_in_all*ASE_ratio-p_p_out-
p_s_out-p_ASE_out_1-p_ASE_out_2-p_ASE_out_3...
            -p_ASE_out_4-p_ASE_out_5-p_ASE_out_6-p_ASE_out_7-p_ASE_out_8-
p_ASE_out_9...
            -p_ASE_out_10)./(p_sat_ASE_10));

        eqs = [eq1, eq2, eq3, eq4, eq5, eq6, eq7, eq8, eq9, eq10, eq11,
eq12];

[p_p_out,p_s_out,p_ASE_out_1,p_ASE_out_2,p_ASE_out_3,p_ASE_out_4,p_ASE_out_5.
..
            ,p_ASE_out_6,p_ASE_out_7,p_ASE_out_8,p_ASE_out_9,p_ASE_out_10]...
```

```
=vpasolve(eqs,[p_p_out,p_s_out,p_ASE_out_1,p_ASE_out_2,p_ASE_out_3,p_ASE_out_
4,p_ASE_out_5...
            ,p_ASE_out_6,p_ASE_out_7,p_ASE_out_8,p_ASE_out_9,p_ASE_out_10],..
.
            [p_out_pump_L(1,i-1),p_out_signal_L(1,i-1),p_out_ASE_1_L(1,i-
1),p_out_ASE_2_L(1,i-1),p_out_ASE_3_L(1,i-1)...
            ,p_out_ASE_4_L(1,i-1),p_out_ASE_5_L(1,i-1),p_out_ASE_6_L(1,i-
1),p_out_ASE_7_L(1,i-1)...
            ,p_out_ASE_8_L(1,i-1),p_out_ASE_9_L(1,i-1),p_out_ASE_10_L(1,i-
1)]);


answer=double([p_p_out,p_s_out,p_ASE_out_1,p_ASE_out_2,p_ASE_out_3,p_ASE_out_
4...
            ,p_ASE_out_5,p_ASE_out_6,p_ASE_out_7,p_ASE_out_8,p_ASE_out_9,p_AS
E_out_10]);
        p_out_pump_L(1,i)=answer(1,1)+p_in_pump_max*(1-shape);
        p_out_signal_L(1,i)=answer(1,2);
        p_out_ASE_1_L(1,i)=answer(1,3);
        p_out_ASE_2_L(1,i)=answer(1,4);
        p_out_ASE_3_L(1,i)=answer(1,5);
        p_out_ASE_4_L(1,i)=answer(1,6);
        p_out_ASE_5_L(1,i)=answer(1,7);
        p_out_ASE_6_L(1,i)=answer(1,8);
        p_out_ASE_7_L(1,i)=answer(1,9);
        p_out_ASE_8_L(1,i)=answer(1,10);
        p_out_ASE_9_L(1,i)=answer(1,11);
        p_out_ASE_10_L(1,i)=answer(1,12);

   end

 plot(L,p_out_pump_L,'b','Linewidth',1.5);
 hold on
 plot(L,p_out_signal_L,'r','Linewidth',1.5);
 hold on

plot(L,p_out_ASE_1_L+p_out_ASE_2_L+p_out_ASE_3_L+p_out_ASE_4_L+p_out_ASE_5_L+
p_out_ASE_6_L...

+p_out_ASE_7_L+p_out_ASE_8_L+p_out_ASE_9_L+p_out_ASE_10_L,'g','Linewidth',1.5
);
 legend('Pump','Signal','ASE','Location','best')
 xlabel('Fiber Length (m)')
 ylabel('Power (W)')
 set(gca,'Fontsize',18)


a3_out=[transpose(L),transpose(p_out_pump_L),transpose(p_out_signal_L),transp
ose(p_out_ASE_1_L+p_out_ASE_2_L+p_out_ASE_3_L...
     +p_out_ASE_4_L+p_out_ASE_5_L+p_out_ASE_6_L...
     +p_out_ASE_7_L+p_out_ASE_8_L+p_out_ASE_9_L+p_out_ASE_10_L)];


a4_out=[lambda_ASE_all.*1e9,[p_out_ASE_1_L(1,times);p_out_ASE_2_L(1,times);p_
out_ASE_3_L(1,times);p_out_ASE_4_L(1,times);...
```

```
p_out_ASE_5_L(1,times);p_out_ASE_6_L(1,times);p_out_ASE_7_L(1,times);p_out_AS
E_8_L(1,times);p_out_ASE_9_L(1,times);p_out_ASE_10_L(1,times);]];


  aa_length_output=[transpose(p_out_pump_L) transpose(p_out_signal_L)
transpose(p_out_ASE_1_L+p_out_ASE_2_L+p_out_ASE_3_L+p_out_ASE_4_L+p_out_ASE_5
_L+p_out_ASE_6_L...
     +p_out_ASE_7_L+p_out_ASE_8_L+p_out_ASE_9_L+p_out_ASE_10_L)];
```

APPENDIX C: Amplifier Stage Double-end Pumping Computer Code

Following is an example MATLAB code for the simulation of using a 25 um-core phosphosilicate double-clad fiber as the gain medium in an amplifier.

```
clc
clear all
%% First solve for signal
% input optical wavelength in um
lambda_for_signal=1.005;
% input the number of layer to simulate (include the cladding)
number_layer=21;
%input the order of Bessel function
nu=0;
%% Prepare for calculation, run this part separately to find a rough range
for beta and put into the next part
% calculate the cldding index (if it is silica)
n_clad=sqrt(1+(( 0.69616630*lambda_for_signal^2)./(lambda_for_signal^2-
0.068404300^2))...
+((0.40794260*lambda_for_signal^2)./(lambda_for_signal^2-0.11624140^2))...
+((0.89747940*lambda_for_signal^2)./(lambda_for_signal^2-9.8961610^2)));

% calculate the wavenumber
wavenumber=2*pi/(lambda_for_signal*1e-6);

%generate the radius matrix
data = xlsread('RIP1.xlsx');
%data2 = xlsread('RIP2.xlsx');
r=data(:,1)./6.156.*12.5;
r_core=max(r)*1e-6;
r_clad=62.5*1e-6;
R=data(:,2);
%r_original=data2(:,1);
%index_original=data2(:,2);
radi=zeros(numel(r)+9*(numel(r)-1),1);
RIP=zeros(numel(R)+9*(numel(R)-1),1);
for i=1:numel(radi)
    if rem(i,10)==1
        radi(i,1)=r(floor(i/10)+1,1);
    end
    if rem(i,10)>1
        Delta=(r(floor(i/10)+1,1)-r(floor(i/10)+2,1))/10;
        radi(i,1)=r(floor(i/10)+1,1)-(rem(i,10)-1)*Delta;
    end
    if rem(i,10)==0
        Delta=(r(floor(i/10),1)-r(floor(i/10)+1,1))/10;
        radi(i,1)=r(floor(i/10),1)-9*Delta;
    end
end
for i=1:numel(RIP)
    if rem(i,10)==1
        RIP(i,1)=R(floor(i/10)+1,1);
    end
    if rem(i,10)>1
```

```
        Delta=(R(floor(i/10)+1,1)-R(floor(i/10)+2,1))/10;
        RIP(i,1)=R(floor(i/10)+1,1)-(rem(i,10)-1)*Delta;
    end
    if rem(i,10)==0
        Delta=(R(floor(i/10),1)-R(floor(i/10)+1,1))/10;
        RIP(i,1)=R(floor(i/10),1)-9*Delta;
    end
end
figure ('Name','RIP')
% plot(r,R,'k*');
% hold on
plot(radi,RIP+n_clad,'b.')
hold on
% plot(-r,R,'k*');
% hold on
plot(-radi,RIP+n_clad,'b.')
x0=[max(r) 62.5];
y0=[n_clad n_clad];
plot(x0,y0,'b','Linewidth',1.5)
hold on
plot(-x0,y0,'b','Linewidth',1.5)
hold on
% plot(r_original,index_original+n_clad, 'r')
% hold on
xlabel('Position (um)')
ylabel('Index')
set(gca,'FontSize',18)
 xlim([-30 30]);

% generate the radius matri for calculation
number_of_point=int32(numel(radi)/(number_layer-1));
num=double(number_of_point);
radius=zeros(number_layer,1);
for i=2:number_layer-1
     radius(i,1)=radi((i-1)*number_of_point-1,1)*10^(-6);
end
radius(number_layer,1)=radi(numel(radi),1)*10^(-6);

% generate the index matrix for calculation
index=zeros(number_layer,1);
for i=1:number_layer-1
    if i==1
        for ii=1:number_of_point-1
    index(i,1)=index(i,1)+RIP(ii,1);
        end
     index(i,1)=index(i,1)/(num-1)+n_clad;
    end
    if i>1 & i<number_layer-1
        for ii=1:number_of_point
    index(i,1)=index(i,1)+RIP((i-1)*num-1+ii,1);
        end
        index(i,1)=index(i,1)/num+n_clad;
    end
    if i==number_layer-1
        for ii=1:(numel(radi)-(i-1)*num)+1
    index(i,1)=index(i,1)+RIP((i-1)*num-1+ii,1);
        end
        index(i,1)=index(i,1)/((numel(radi)-(i-1)*num)+1)+n_clad;
```

```
    end
end
index(number_layer,1)=n_clad;
 stairs(radius*10^(6),index,'m','LineWidth',1.5);
 hold on
 stairs(-radius*10^(6),index,'m','LineWidth',1.5);
% scan beta
beta_min=wavenumber*n_clad;
beta_max=wavenumber*max(index);
scan_number=5000;
beta=linspace(beta_min,beta_max,scan_number);

% Calculation
%generate u matrix
u=zeros(number_layer,scan_number);
for i=1:number_layer-1
    u(i,:)=sqrt(index(i,1)^2*wavenumber^2-beta.^2);
end
u(number_layer,:)=sqrt(-n_clad^2*wavenumber^2+beta.^2);

% generate the element matrix
matrix_plot=zeros(scan_number,1);
value=10^(-4);
for j=1:scan_number
matrix=zeros(2*(number_layer-1),2*(number_layer-1));
matrix(1,1)=value*besselj(nu,radius(2,1)*u(1,j));
matrix(2,1)=value*u(1,j)*(besselj(nu-1,radius(2,1)*u(1,j))-
nu*besselj(nu,radius(2,1)*u(1,j))/(radius(2,1)*u(1,j)));
matrix(2*(number_layer-1)-1,2*(number_layer-1))=-
value*besselk(nu,radius(number_layer,1)*u(number_layer,j));
matrix(2*(number_layer-1),2*(number_layer-
1))=value*u(number_layer,j)*(besselk(nu-
1,radius(number_layer,1)*u(number_layer,j))...
+nu*besselk(nu,radius(number_layer,1)*u(number_layer,j))/(radius(number_layer
,1)*u(number_layer,j)));
if number_layer==2
end
if number_layer>2
    matrix(1,2)=-value*besselj(nu,radius(2,1)*u(2,j));
    matrix(1,3)=-value*bessely(nu,radius(2,1)*u(2,j));
    matrix(2,2)=-value*u(2,j)*(besselj(nu-1,radius(2,1)*u(2,j))-
nu*besselj(nu,radius(2,1)*u(2,j))/(radius(2,1)*u(2,j)));
    matrix(2,3)=-value*u(2,j)*(bessely(nu-1,radius(2,1)*u(2,j))-
nu*bessely(nu,radius(2,1)*u(2,j))/(radius(2,1)*u(2,j)));
    matrix(2*(number_layer-1)-1,2*(number_layer-1)-
2)=value*besselj(nu,radius(number_layer,1)*u(number_layer-1,j));
    matrix(2*(number_layer-1)-1,2*(number_layer-1)-
1)=value*bessely(nu,radius(number_layer,1)*u(number_layer-1,j));
    matrix(2*(number_layer-1),2*(number_layer-1)-2)=value*u(number_layer-
1,j)*(besselj(nu-1,radius(number_layer,1)*u(number_layer-1,j))...
        -nu*besselj(nu,radius(number_layer,1)*u(number_layer-
1,j))/(radius(number_layer,1)*u(number_layer-1,j)));
    matrix(2*(number_layer-1),2*(number_layer-1)-1)=value*u(number_layer-
1,j)*(bessely(nu-1,radius(number_layer,1)*u(number_layer-1,j))...
        -nu*bessely(nu,radius(number_layer,1)*u(number_layer-
1,j))/(radius(number_layer,1)*u(number_layer-1,j)));
    if number_layer>3
        for ii=3:2*(number_layer-1)-2
```

```
            if rem(ii,2)==1
                ord=(ii+1)/2;
                matrix(ii,ii-1)=value*besselj(nu,radius(ord+1,1)*u(ord,j));
                matrix(ii,ii)=value*bessely(nu,radius(ord+1,1)*u(ord,j));
                matrix(ii,ii+1)=-
value*besselj(nu,radius(ord+1,1)*u(ord+1,j));
                matrix(ii,ii+2)=-
value*bessely(nu,radius(ord+1,1)*u(ord+1,j));
            end
            if rem(ii,2)==0
                ord=ii/2;
                matrix(ii,ii-2)=value*u(ord,j)*(besselj(nu-
1,radius(ord+1,1)*u(ord,j))-
nu*besselj(nu,radius(ord+1,1)*u(ord,j))/(radius(ord+1,1)*u(ord,j)));
                matrix(ii,ii-1)=value*u(ord,j)*(bessely(nu-
1,radius(ord+1,1)*u(ord,j))-
nu*bessely(nu,radius(ord+1,1)*u(ord,j))/(radius(ord+1,1)*u(ord,j)));
                matrix(ii,ii)=-value*u(ord+1,j)*(besselj(nu-
1,radius(ord+1,1)*u(ord+1,j))-
nu*besselj(nu,radius(ord+1,1)*u(ord+1,j))/(radius(ord+1,1)*u(ord+1,j)));
                matrix(ii,ii+1)=-value*u(ord+1,j)*(bessely(nu-
1,radius(ord+1,1)*u(ord+1,j))-
nu*bessely(nu,radius(ord+1,1)*u(ord+1,j))/(radius(ord+1,1)*u(ord+1,j)));
            end
        end
    end
end
matrix_plot(j,1)=det(matrix);
end
% plot det(matrix) vs beta
b=zeros(scan_number,1);
figure ('Name','Check')
%If not working change here for real and imag
plot (beta,real(matrix_plot));
hold on
plot (beta,b);
%axis([beta_min,beta_max,-1e2,1e2])
xlabel('Beta (Hz)')
ylabel('Det (matrix)')


%% search for beta
beta_min=9.0775e6;
beta_max=9.0776e6;


% generate the element matrix
matrix_plot=zeros(scan_number,1);

 for times=1:4
    scan_number=5000;
    beta=linspace(beta_min,beta_max,scan_number);
    u=zeros(number_layer,scan_number);
        for i=1:number_layer-1
            u(i,:)=sqrt(index(i,1)^2*wavenumber^2-beta.^2);
        end
        u(number_layer,:)=sqrt(-n_clad^2*wavenumber^2+beta.^2);
```

```
            for j=1:scan_number
            matrix=zeros(2*(number_layer-1),2*(number_layer-1));
            matrix(1,1)=value*besselj(nu,radius(2,1)*u(1,j));
            matrix(2,1)=value*u(1,j)*(besselj(nu-1,radius(2,1)*u(1,j))-
nu*besselj(nu,radius(2,1)*u(1,j))/(radius(2,1)*u(1,j)));
            matrix(2*(number_layer-1)-1,2*(number_layer-1))=-
value*besselk(nu,radius(number_layer,1)*u(number_layer,j));
            matrix(2*(number_layer-1),2*(number_layer-
1))=value*u(number_layer,j)*(besselk(nu-
1,radius(number_layer,1)*u(number_layer,j))...

+nu*besselk(nu,radius(number_layer,1)*u(number_layer,j))/(radius(number_layer
,1)*u(number_layer,j)));
                if number_layer==2
                end
                if number_layer>2
                    matrix(1,2)=-value*besselj(nu,radius(2,1)*u(2,j));
                    matrix(1,3)=-value*bessely(nu,radius(2,1)*u(2,j));
                    matrix(2,2)=-value*u(2,j)*(besselj(nu-
1,radius(2,1)*u(2,j))-
nu*besselj(nu,radius(2,1)*u(2,j))/(radius(2,1)*u(2,j)));
                    matrix(2,3)=-value*u(2,j)*(bessely(nu-
1,radius(2,1)*u(2,j))-
nu*bessely(nu,radius(2,1)*u(2,j))/(radius(2,1)*u(2,j)));
                    matrix(2*(number_layer-1)-1,2*(number_layer-1)-
2)=value*besselj(nu,radius(number_layer,1)*u(number_layer-1,j));
                    matrix(2*(number_layer-1)-1,2*(number_layer-1)-
1)=value*bessely(nu,radius(number_layer,1)*u(number_layer-1,j));
                    matrix(2*(number_layer-1),2*(number_layer-1)-
2)=value*u(number_layer-1,j)*(besselj(nu-
1,radius(number_layer,1)*u(number_layer-1,j))...
                        -nu*besselj(nu,radius(number_layer,1)*u(number_layer-
1,j))/(radius(number_layer,1)*u(number_layer-1,j)));
                    matrix(2*(number_layer-1),2*(number_layer-1)-
1)=value*u(number_layer-1,j)*(bessely(nu-
1,radius(number_layer,1)*u(number_layer-1,j))...
                        -nu*bessely(nu,radius(number_layer,1)*u(number_layer-
1,j))/(radius(number_layer,1)*u(number_layer-1,j)));
                    if number_layer>3
                        for ii=3:2*(number_layer-1)-2
                            if rem(ii,2)==1
                                ord=(ii+1)/2;
                                matrix(ii,ii-
1)=value*besselj(nu,radius(ord+1,1)*u(ord,j));

matrix(ii,ii)=value*bessely(nu,radius(ord+1,1)*u(ord,j));
                                matrix(ii,ii+1)=-
value*besselj(nu,radius(ord+1,1)*u(ord+1,j));
                                matrix(ii,ii+2)=-
value*bessely(nu,radius(ord+1,1)*u(ord+1,j));
                            end
                            if rem(ii,2)==0
                                ord=ii/2;
                                matrix(ii,ii-2)=value*u(ord,j)*(besselj(nu-
1,radius(ord+1,1)*u(ord,j))-
nu*besselj(nu,radius(ord+1,1)*u(ord,j))/(radius(ord+1,1)*u(ord,j)));
```

```
                                matrix(ii,ii-1)=value*u(ord,j)*(bessely(nu-
1,radius(ord+1,1)*u(ord,j))-
nu*bessely(nu,radius(ord+1,1)*u(ord,j))/(radius(ord+1,1)*u(ord,j)));
                                matrix(ii,ii)=-value*u(ord+1,j)*(besselj(nu-
1,radius(ord+1,1)*u(ord+1,j))-
nu*besselj(nu,radius(ord+1,1)*u(ord+1,j))/(radius(ord+1,1)*u(ord+1,j)));
                                matrix(ii,ii+1)=-
value*u(ord+1,j)*(bessely(nu-1,radius(ord+1,1)*u(ord+1,j))-
nu*bessely(nu,radius(ord+1,1)*u(ord+1,j))/(radius(ord+1,1)*u(ord+1,j)));
                            end
                        end
                    end
                end
                %If not working change here for real and imag
                matrix_plot(j,1)=real(det(matrix));
                    if j>1&& matrix_plot(j,1)*matrix_plot(j-1,1)<0
                        beta_min=beta(1,j-1);
                        beta_max=beta(1,j);
                        det_min=abs(matrix_plot(j-1,1));
                        det_max=abs(matrix_plot(j,1));
                    end
        end
 end

beta_solve= beta_min+(beta_max-beta_min)*det_min/(det_min+det_max);
modal_index=beta_solve*lambda_for_signal*10^(-6)/(2*pi);
digitsOld = digits(100);
vpa(beta_solve)
vpa(modal_index)
% figure ('Name','Check1')
% plot (beta,matrix_plot);
%% solve for constant
% generate u matrix again
u_solve=zeros(number_layer,1);
for i=1:number_layer-1
    u_solve(i,1)=sqrt(index(i,1)^2*wavenumber^2-beta_solve^2);
end
u_solve(number_layer,1)=sqrt(-n_clad^2*wavenumber^2+beta_solve^2);

% generate the matrix again
value=10^(-4);
matrix_solve=zeros(2*(number_layer-1),2*(number_layer-1));
matrix_solve(1,1)=value*besselj(nu,radius(2,1)*u_solve(1,1));
matrix_solve(2,1)=value*u_solve(1,1)*(besselj(nu-1,radius(2,1)*u_solve(1,1))-
nu*besselj(nu,radius(2,1)*u_solve(1,1))/(radius(2,1)*u_solve(1,1)));
matrix_solve(2*(number_layer-1)-1,2*(number_layer-1))=-
value*besselk(nu,radius(number_layer,1)*u_solve(number_layer,1));
matrix_solve(2*(number_layer-1),2*(number_layer-
1))=value*u_solve(number_layer,1)*(besselk(nu-
1,radius(number_layer,1)*u_solve(number_layer,1))...
+nu*besselk(nu,radius(number_layer,1)*u_solve(number_layer,1))/(radius(number
_layer,1)*u_solve(number_layer,1)));

if number_layer>2
    matrix_solve(1,2)=-value*besselj(nu,radius(2,1)*u_solve(2,1));
    matrix_solve(1,3)=-value*bessely(nu,radius(2,1)*u_solve(2,1));
```

```
    matrix_solve(2,2)=-value*u_solve(2,1)*(besselj(nu-
1,radius(2,1)*u_solve(2,1))-
nu*besselj(nu,radius(2,1)*u_solve(2,1))/(radius(2,1)*u_solve(2,1)));
    matrix_solve(2,3)=-value*u_solve(2,1)*(bessely(nu-
1,radius(2,1)*u_solve(2,1))-
nu*bessely(nu,radius(2,1)*u_solve(2,1))/(radius(2,1)*u_solve(2,1)));
    matrix_solve(2*(number_layer-1)-1,2*(number_layer-1)-
2)=value*besselj(nu,radius(number_layer,1)*u_solve(number_layer-1,1));
    matrix_solve(2*(number_layer-1)-1,2*(number_layer-1)-
1)=value*bessely(nu,radius(number_layer,1)*u_solve(number_layer-1,1));
    matrix_solve(2*(number_layer-1),2*(number_layer-1)-
2)=value*u_solve(number_layer-1,1)*(besselj(nu-
1,radius(number_layer,1)*u_solve(number_layer-1,1))...
        -nu*besselj(nu,radius(number_layer,1)*u_solve(number_layer-
1,1))/(radius(number_layer,1)*u_solve(number_layer-1,1)));
    matrix_solve(2*(number_layer-1),2*(number_layer-1)-
1)=value*u_solve(number_layer-1,1)*(bessely(nu-
1,radius(number_layer,1)*u_solve(number_layer-1,1))...
        -nu*bessely(nu,radius(number_layer,1)*u_solve(number_layer-
1,1))/(radius(number_layer,1)*u_solve(number_layer-1,1)));
    if number_layer>3
        for ii=3:2*(number_layer-1)-2
            if rem(ii,2)==1
                ord=(ii+1)/2;
                matrix_solve(ii,ii-
1)=value*besselj(nu,radius(ord+1,1)*u_solve(ord,1));

matrix_solve(ii,ii)=value*bessely(nu,radius(ord+1,1)*u_solve(ord,1));
                matrix_solve(ii,ii+1)=-
value*besselj(nu,radius(ord+1,1)*u_solve(ord+1,1));
                matrix_solve(ii,ii+2)=-
value*bessely(nu,radius(ord+1,1)*u_solve(ord+1,1));
            end
            if rem(ii,2)==0
                ord=ii/2;
                matrix_solve(ii,ii-2)=value*u_solve(ord,1)*(besselj(nu-
1,radius(ord+1,1)*u_solve(ord,1))-
nu*besselj(nu,radius(ord+1,1)*u_solve(ord,1))/(radius(ord+1,1)*u_solve(ord,1)
));
                matrix_solve(ii,ii-1)=value*u_solve(ord,1)*(bessely(nu-
1,radius(ord+1,1)*u_solve(ord,1))-
nu*bessely(nu,radius(ord+1,1)*u_solve(ord,1))/(radius(ord+1,1)*u_solve(ord,1)
));
                matrix_solve(ii,ii)=-value*u_solve(ord+1,1)*(besselj(nu-
1,radius(ord+1,1)*u_solve(ord+1,1))-
nu*besselj(nu,radius(ord+1,1)*u_solve(ord+1,1))/(radius(ord+1,1)*u_solve(ord+
1,1)));
                matrix_solve(ii,ii+1)=-value*u_solve(ord+1,1)*(bessely(nu-
1,radius(ord+1,1)*u_solve(ord+1,1))-
nu*bessely(nu,radius(ord+1,1)*u_solve(ord+1,1))/(radius(ord+1,1)*u_solve(ord+
1,1)));
            end
        end
    end
end

% solve for all the coefficients
answer=null(matrix_solve);
```

```
coeff=answer./answer(1,1);
% coeff=real(coeff)
%% Part III: plot the 2D electric mode
% type the radical range of simulation
r_plot_outbound=62.5;

% plot point density
times=1000;

 figure ('Name','2D Electric Mode')
for i=1:number_layer
    if i==1
    r_1=linspace(0,radius(2,1),times);
    mode_1_electric=real(coeff(1,1)*besselj(nu,u_solve(1,1).*r_1));
%     yyaxis left
    plot(r_1*10^(6),mode_1_electric,'r','LineWidth',2);
    hold on
%     yyaxis left
    plot(-r_1*10^(6),mode_1_electric,'r','LineWidth',2);
    hold on
    r_sum_electrical=0+r_1;
    mode_sum_electrical=0+mode_1_electric;
    end
    if i>1 & i<number_layer
      r=linspace(radius(i,1),radius(i+1,1),times);
      mode_electric=real(coeff(2*i-
2,1)*besselj(nu,u_solve(i,1).*r)+coeff(2*i-1,1)*bessely(nu,u_solve(i,1).*r));
%       yyaxis left
      plot(r*10^(6),mode_electric,'r','LineWidth',2);
      hold on
%       yyaxis left
      plot(-r*10^(6),mode_electric,'r','LineWidth',2);
      hold on
      r_sum_electrical=[r_sum_electrical r];
      mode_sum_electrical=[mode_sum_electrical mode_electric];

    end
    if i==number_layer
        r_2=linspace(radius(number_layer,1),r_plot_outbound*10^(-6),times);
        mode_clad_electric=real(coeff(2*(number_layer-
1),1)*besselk(nu,u_solve(number_layer,1).*r_2));
%         yyaxis left
        plot(r_2*10^(6),mode_clad_electric,'r','LineWidth',2);
        hold on
%         yyaxis left
        plot(-r_2*10^(6),mode_clad_electric,'r','LineWidth',2);
        hold on
        r_sum_electrical=[r_sum_electrical r_2];
       mode_sum_electrical=[mode_sum_electrical  mode_clad_electric];
    end

end



a=[-100,100];
b=[0,0];
```

```
plot (a,b,'b:','LineWidth',1.5)

axis([-r_plot_outbound,r_plot_outbound,-0.02,0.02]);

yyaxis right
ylim([-1*max(RIP) 1.2*max(RIP)]);
plot(radi,RIP,'k:','LineWidth',1.5);
hold on
plot(-radi,RIP,'k:','LineWidth',1.5);
hold on
stairs(radius*10^(6),index-n_clad,'m-','LineWidth',1);
hold on
stairs(-radius*10^(6),index-n_clad,'m-','LineWidth',1);
hold on
rr=[radius(number_layer,1)*10^(6),r_plot_outbound];
aaa=[0,0];
plot(rr,aaa,'k:','LineWidth',1.5);
hold on
plot(-rr,aaa,'k:','LineWidth',1.5);
hold on
plot(rr,aaa,'m-','LineWidth',1);
hold on
plot(-rr,aaa,'m-','LineWidth',1);

yyaxis left
ylim([0 1.2]);
title('Mode (Electric) and RIP')
xlabel('Position (um)')
ylabel('Normalized Amplitude')

yyaxis right
ylim([0, 2.5e-3]);
ylabel('Index Difference')
xlim([-30 30]);
set(gca,'FontSize',18)


%% Final results for signal

% mode
r_signal=r_sum_electrical;
mode_signal=mode_sum_electrical;
r_signal_sum=[-fliplr(r_signal) r_signal];
mode_signal_sum=[fliplr(mode_signal) mode_signal];

% Aeff and overlap integral

 %integral of (E)^2 from 0 to cladding
 E2=zeros(numel(r_signal)-1,1);
 for i=1:numel(r_signal)-1

E2(i,1)=(((mode_signal(1,i))+(mode_signal(1,i+1)))/2)^2*(r_signal(1,i+1)+r_si
gnal(1,i))/2*(r_signal(1,i+1)-r_signal(1,i));
 end
 inte_E2=sum(E2);
```

```
  %integral of (E)^2 from 0 to core
 E2_core=zeros(numel(r_signal)-times-1,1);
 for i=1:numel(r_signal)-1-times

E2_core(i,1)=(((mode_signal(1,i))+(mode_signal(1,i+1)))/2)^2*(r_signal(1,i+1)
+r_signal(1,i))/2*(r_signal(1,i+1)-r_signal(1,i));
 end
 inte_E2_core=sum(E2_core);


  %integral of (E)^4 from 0 to cladding
 E4=zeros(numel(r_signal)-1,1);
 for i=1:numel(r_signal)-1

E4(i,1)=(((mode_signal(1,i))+(mode_signal(1,i+1)))/2)^4*(r_signal(1,i+1)+r_si
gnal(1,i))/2*(r_signal(1,i+1)-r_signal(1,i));
 end
 inte_E4=sum(E4);

overlap_signal=inte_E2_core/inte_E2;
Aeff_signal=2*pi*inte_E2^2/inte_E4;
reff_signal=sqrt(Aeff_signal/pi);
overlap_ASE=overlap_signal;
Aeff_ASE=Aeff_signal;
reff_ASE=reff_signal;

%% Input constant for power simulation
data1 = xlsread('cross_section.xlsx');
% cross_emi=data1(:,9);
% cross_abs=data1(:,11);
 cross_emi=data1(:,14);
 cross_abs=data1(:,16);
lambda_ASE_all=1e-9.*transpose(linspace(1000,1090,10));
cross_emi_all=zeros(1,1);
cross_abs_all=zeros(1,1);
data2 = xlsread('signal_spec.xlsx');
lambsss=data2(1:1001,5);
out_ASE_spectra=data2(1:1001,6);
out_signal_spectra=data2(1:1001,7);
signal_ratio=sum(out_signal_spectra)/(sum(out_signal_spectra)+sum(out_ASE_spe
ctra))-0.025;
ASE_ratio=1-signal_ratio;
out_power=zeros(1,1);
for i=1:10
    cross_abs_all(i,1)=mean(cross_abs((i-1)*50+1:i*50,1));
    cross_emi_all(i,1)=mean(cross_emi((i-1)*50+1:i*50,1));
    out_power(i,1)=sum(out_ASE_spectra((i-1)*100+1:i*100,1));
end
nor_para=sum(out_power);
out_ASE_ratio=out_power./nor_para;
%
%speed of light
sol=299792458;
%plank constant
plank=6.62607004e-34;
% Yb density
rho=7.2e25;
```

```
%lifetime
tau=1.48e-3;
% wavelength
lambda_pump=975*1e-9;
lambda_signal=lambda_for_signal*1e-6;
lambda_ASE_1=lambda_ASE_all(1,1);
lambda_ASE_2=lambda_ASE_all(2,1);
lambda_ASE_3=lambda_ASE_all(3,1);
lambda_ASE_4=lambda_ASE_all(4,1);
lambda_ASE_5=lambda_ASE_all(5,1);
lambda_ASE_6=lambda_ASE_all(6,1);
lambda_ASE_7=lambda_ASE_all(7,1);
lambda_ASE_8=lambda_ASE_all(8,1);
lambda_ASE_9=lambda_ASE_all(9,1);
lambda_ASE_10=lambda_ASE_all(10,1);
% Absorption cross sections
Abs_cross_pump=1.72e-24;
Abs_cross_signal=8.64e-26;
Abs_cross_ASE_1=cross_abs_all(1,1);
Abs_cross_ASE_2=cross_abs_all(2,1);
Abs_cross_ASE_3=cross_abs_all(3,1);
Abs_cross_ASE_4=cross_abs_all(4,1);
Abs_cross_ASE_5=cross_abs_all(5,1);
Abs_cross_ASE_6=cross_abs_all(6,1);
Abs_cross_ASE_7=cross_abs_all(7,1);
Abs_cross_ASE_8=cross_abs_all(8,1);
Abs_cross_ASE_9=cross_abs_all(9,1);
Abs_cross_ASE_10=cross_abs_all(10,1);
% Emission cross sections
Emi_cross_pump=1.72e-24;
Emi_cross_signal=4.32e-25;
Emi_cross_ASE_1=cross_emi_all(1,1);
Emi_cross_ASE_2=cross_emi_all(2,1);
Emi_cross_ASE_3=cross_emi_all(3,1);
Emi_cross_ASE_4=cross_emi_all(4,1);
Emi_cross_ASE_5=cross_emi_all(5,1);
Emi_cross_ASE_6=cross_emi_all(6,1);
Emi_cross_ASE_7=cross_emi_all(7,1);
Emi_cross_ASE_8=cross_emi_all(8,1);
Emi_cross_ASE_9=cross_emi_all(9,1);
Emi_cross_ASE_10=cross_emi_all(10,1);
% pump overlap integral
overlap_pump=(r_core/r_clad)^2;
% Absorption coefficient
alpha_pump=rho*Abs_cross_pump*overlap_pump;
alpha_signal=rho*Abs_cross_signal*overlap_signal;
alpha_ASE_1=rho*Abs_cross_ASE_1*overlap_ASE;
alpha_ASE_2=rho*Abs_cross_ASE_2*overlap_ASE;
alpha_ASE_3=rho*Abs_cross_ASE_3*overlap_ASE;
alpha_ASE_4=rho*Abs_cross_ASE_4*overlap_ASE;
alpha_ASE_5=rho*Abs_cross_ASE_5*overlap_ASE;
alpha_ASE_6=rho*Abs_cross_ASE_6*overlap_ASE;
alpha_ASE_7=rho*Abs_cross_ASE_7*overlap_ASE;
alpha_ASE_8=rho*Abs_cross_ASE_8*overlap_ASE;
alpha_ASE_9=rho*Abs_cross_ASE_9*overlap_ASE;
alpha_ASE_10=rho*Abs_cross_ASE_10*overlap_ASE;
% background loss
```

```
alpha_background_pump=-log10(10^(-20/10*1e-3))*(1-overlap_pump);%20 dB/km of
background loss in cladding
alpha_background_signal=-log10(10^(-50/10*1e-3))*overlap_signal;%50 dB/km of
background loss for signal
alpha_background_ASE=alpha_background_signal;
% Saturation power
p_sat_pump=pi*r_core^2*plank*sol/(overlap_pump*tau*(Abs_cross_pump+Emi_cross_
pump)*lambda_pump);
p_sat_signal=Aeff_signal*plank*sol/(overlap_signal*tau*(Abs_cross_signal+Emi_
cross_signal)*lambda_signal);
p_sat_ASE_1=Aeff_ASE*plank*sol/(overlap_ASE*tau*(Abs_cross_ASE_1+Emi_cross_AS
E_1)*lambda_ASE_1);
p_sat_ASE_2=Aeff_ASE*plank*sol/(overlap_ASE*tau*(Abs_cross_ASE_2+Emi_cross_AS
E_2)*lambda_ASE_2);
p_sat_ASE_3=Aeff_ASE*plank*sol/(overlap_ASE*tau*(Abs_cross_ASE_3+Emi_cross_AS
E_3)*lambda_ASE_3);
p_sat_ASE_4=Aeff_ASE*plank*sol/(overlap_ASE*tau*(Abs_cross_ASE_4+Emi_cross_AS
E_4)*lambda_ASE_4);
p_sat_ASE_5=Aeff_ASE*plank*sol/(overlap_ASE*tau*(Abs_cross_ASE_5+Emi_cross_AS
E_5)*lambda_ASE_5);
p_sat_ASE_6=Aeff_ASE*plank*sol/(overlap_ASE*tau*(Abs_cross_ASE_6+Emi_cross_AS
E_6)*lambda_ASE_6);
p_sat_ASE_7=Aeff_ASE*plank*sol/(overlap_ASE*tau*(Abs_cross_ASE_7+Emi_cross_AS
E_7)*lambda_ASE_7);
p_sat_ASE_8=Aeff_ASE*plank*sol/(overlap_ASE*tau*(Abs_cross_ASE_8+Emi_cross_AS
E_8)*lambda_ASE_8);
p_sat_ASE_9=Aeff_ASE*plank*sol/(overlap_ASE*tau*(Abs_cross_ASE_9+Emi_cross_AS
E_9)*lambda_ASE_9);
p_sat_ASE_10=Aeff_ASE*plank*sol/(overlap_ASE*tau*(Abs_cross_ASE_10+Emi_cross_
ASE_10)*lambda_ASE_10);

%% Simulate length vs power

% pump shaping factor (=1 if cladding is shaped)
shape=0.95;
%input parameter
L_simulation_max=0.25;
p_in_pump_max_left=10;
p_in_all=0.2;
p_in_pump_max_right=10;
times=int16(1+L_simulation_max*50);

p_in_signal=p_in_all*signal_ratio;
p_in_ASE_1=p_in_all*ASE_ratio*out_ASE_ratio(1,1);
p_in_ASE_2=p_in_all*ASE_ratio*out_ASE_ratio(2,1);
p_in_ASE_3=p_in_all*ASE_ratio*out_ASE_ratio(3,1);
p_in_ASE_4=p_in_all*ASE_ratio*out_ASE_ratio(4,1);
p_in_ASE_5=p_in_all*ASE_ratio*out_ASE_ratio(5,1);
p_in_ASE_6=p_in_all*ASE_ratio*out_ASE_ratio(6,1);
p_in_ASE_7=p_in_all*ASE_ratio*out_ASE_ratio(7,1);
p_in_ASE_8=p_in_all*ASE_ratio*out_ASE_ratio(8,1);
p_in_ASE_9=p_in_all*ASE_ratio*out_ASE_ratio(9,1);
p_in_ASE_10=p_in_all*ASE_ratio*out_ASE_ratio(10,1);

L=linspace(0,L_simulation_max,times);
p_out_pump_L_left=zeros(1,times);
p_out_signal_L=zeros(1,times);
```

```
p_out_ASE_1_L=zeros(1,times);
p_out_ASE_2_L=zeros(1,times);
p_out_ASE_3_L=zeros(1,times);
p_out_ASE_4_L=zeros(1,times);
p_out_ASE_5_L=zeros(1,times);
p_out_ASE_6_L=zeros(1,times);
p_out_ASE_7_L=zeros(1,times);
p_out_ASE_8_L=zeros(1,times);
p_out_ASE_9_L=zeros(1,times);
p_out_ASE_10_L=zeros(1,times);
p_out_pump_L_right=zeros(1,times);

p_out_pump_L_left(1,1)=p_in_pump_max_left;
p_out_signal_L(1,1)=p_in_signal;
p_out_ASE_1_L(1,1)=p_in_ASE_1;
p_out_ASE_2_L(1,1)=p_in_ASE_2;
p_out_ASE_3_L(1,1)=p_in_ASE_3;
p_out_ASE_4_L(1,1)=p_in_ASE_4;
p_out_ASE_5_L(1,1)=p_in_ASE_5;
p_out_ASE_6_L(1,1)=p_in_ASE_6;
p_out_ASE_7_L(1,1)=p_in_ASE_7;
p_out_ASE_8_L(1,1)=p_in_ASE_8;
p_out_ASE_9_L(1,1)=p_in_ASE_9;
p_out_ASE_10_L(1,1)=p_in_ASE_10;
p_out_pump_L_right(1,times)=p_in_pump_max_right;
%
syms p_p_out_left p_s_out p_ASE_out_1 p_ASE_out_2 p_ASE_out_3 p_ASE_out_4
p_ASE_out_5...
        p_ASE_out_6 p_ASE_out_7 p_ASE_out_8 p_ASE_out_9 p_ASE_out_10
p_p_out_right

eq1=p_p_out_left-p_in_pump_max_left.*shape.*exp(-
alpha_pump.*L_simulation_max-alpha_background_pump.*L_simulation_max+...

(p_in_pump_max_left.*shape+p_in_signal+p_in_all*ASE_ratio+p_in_pump_max_right
.*shape-p_p_out_left-p_s_out-...
            p_ASE_out_1-p_ASE_out_2-p_ASE_out_3-p_ASE_out_4-p_ASE_out_5-
p_ASE_out_6-p_ASE_out_7-p_ASE_out_8-p_ASE_out_9...
            -p_ASE_out_10-p_p_out_right)./(p_sat_pump));
eq2=p_s_out-p_in_signal.*exp(-alpha_signal.*L_simulation_max-
alpha_background_signal.*L_simulation_max+...

(p_in_pump_max_left.*shape+p_in_signal+p_in_all*ASE_ratio+p_in_pump_max_right
.*shape-p_p_out_left-p_s_out-...
            p_ASE_out_1-p_ASE_out_2-p_ASE_out_3-p_ASE_out_4-p_ASE_out_5-
p_ASE_out_6-p_ASE_out_7-p_ASE_out_8-p_ASE_out_9...
            -p_ASE_out_10-p_p_out_right)./(p_sat_signal));
eq3=p_ASE_out_1-p_in_ASE_1.*exp(-alpha_ASE_1.*L_simulation_max-
alpha_background_ASE.*L_simulation_max+...

(p_in_pump_max_left.*shape+p_in_signal+p_in_all*ASE_ratio+p_in_pump_max_right
.*shape-p_p_out_left-p_s_out-...
            p_ASE_out_1-p_ASE_out_2-p_ASE_out_3-p_ASE_out_4-p_ASE_out_5-
p_ASE_out_6-p_ASE_out_7-p_ASE_out_8-p_ASE_out_9...
            -p_ASE_out_10-p_p_out_right)./(p_sat_ASE_1));
eq4=p_ASE_out_2-p_in_ASE_2.*exp(-alpha_ASE_2.*L_simulation_max-
alpha_background_ASE.*L_simulation_max+...
```

```
(p_in_pump_max_left.*shape+p_in_signal+p_in_all*ASE_ratio+p_in_pump_max_right
.*shape-p_p_out_left-p_s_out-...
            p_ASE_out_1-p_ASE_out_2-p_ASE_out_3-p_ASE_out_4-p_ASE_out_5-
p_ASE_out_6-p_ASE_out_7-p_ASE_out_8-p_ASE_out_9...
            -p_ASE_out_10-p_p_out_right)./(p_sat_ASE_2));
eq5=p_ASE_out_3-p_in_ASE_3.*exp(-alpha_ASE_3.*L_simulation_max-
alpha_background_ASE.*L_simulation_max+...

(p_in_pump_max_left.*shape+p_in_signal+p_in_all*ASE_ratio+p_in_pump_max_right
.*shape-p_p_out_left-p_s_out-...
            p_ASE_out_1-p_ASE_out_2-p_ASE_out_3-p_ASE_out_4-p_ASE_out_5-
p_ASE_out_6-p_ASE_out_7-p_ASE_out_8-p_ASE_out_9...
            -p_ASE_out_10-p_p_out_right)./(p_sat_ASE_3));
eq6=p_ASE_out_4-p_in_ASE_4.*exp(-alpha_ASE_4.*L_simulation_max-
alpha_background_ASE.*L_simulation_max+...

(p_in_pump_max_left.*shape+p_in_signal+p_in_all*ASE_ratio+p_in_pump_max_right
.*shape-p_p_out_left-p_s_out-...
            p_ASE_out_1-p_ASE_out_2-p_ASE_out_3-p_ASE_out_4-p_ASE_out_5-
p_ASE_out_6-p_ASE_out_7-p_ASE_out_8-p_ASE_out_9...
            -p_ASE_out_10-p_p_out_right)./(p_sat_ASE_4));
eq7=p_ASE_out_5-p_in_ASE_5.*exp(-alpha_ASE_5.*L_simulation_max-
alpha_background_ASE.*L_simulation_max+...

(p_in_pump_max_left.*shape+p_in_signal+p_in_all*ASE_ratio+p_in_pump_max_right
.*shape-p_p_out_left-p_s_out-...
            p_ASE_out_1-p_ASE_out_2-p_ASE_out_3-p_ASE_out_4-p_ASE_out_5-
p_ASE_out_6-p_ASE_out_7-p_ASE_out_8-p_ASE_out_9...
            -p_ASE_out_10-p_p_out_right)./(p_sat_ASE_5));
 eq8=p_ASE_out_6-p_in_ASE_6.*exp(-alpha_ASE_6.*L_simulation_max-
alpha_background_ASE.*L_simulation_max+...

(p_in_pump_max_left.*shape+p_in_signal+p_in_all*ASE_ratio+p_in_pump_max_right
.*shape-p_p_out_left-p_s_out-...
            p_ASE_out_1-p_ASE_out_2-p_ASE_out_3-p_ASE_out_4-p_ASE_out_5-
p_ASE_out_6-p_ASE_out_7-p_ASE_out_8-p_ASE_out_9...
            -p_ASE_out_10-p_p_out_right)./(p_sat_ASE_6));
 eq9=p_ASE_out_7-p_in_ASE_7.*exp(-alpha_ASE_7.*L_simulation_max-
alpha_background_ASE.*L_simulation_max+...

(p_in_pump_max_left.*shape+p_in_signal+p_in_all*ASE_ratio+p_in_pump_max_right
.*shape-p_p_out_left-p_s_out-...
            p_ASE_out_1-p_ASE_out_2-p_ASE_out_3-p_ASE_out_4-p_ASE_out_5-
p_ASE_out_6-p_ASE_out_7-p_ASE_out_8-p_ASE_out_9...
            -p_ASE_out_10-p_p_out_right)./(p_sat_ASE_7));
 eq10=p_ASE_out_8-p_in_ASE_8.*exp(-alpha_ASE_8.*L_simulation_max-
alpha_background_ASE.*L_simulation_max+...

(p_in_pump_max_left.*shape+p_in_signal+p_in_all*ASE_ratio+p_in_pump_max_right
.*shape-p_p_out_left-p_s_out-...
            p_ASE_out_1-p_ASE_out_2-p_ASE_out_3-p_ASE_out_4-p_ASE_out_5-
p_ASE_out_6-p_ASE_out_7-p_ASE_out_8-p_ASE_out_9...
            -p_ASE_out_10-p_p_out_right)./(p_sat_ASE_8));
 eq11=p_ASE_out_9-p_in_ASE_9.*exp(-alpha_ASE_9.*L_simulation_max-
alpha_background_ASE.*L_simulation_max+...
```

```
(p_in_pump_max_left.*shape+p_in_signal+p_in_all*ASE_ratio+p_in_pump_max_right
.*shape-p_p_out_left-p_s_out-...
            p_ASE_out_1-p_ASE_out_2-p_ASE_out_3-p_ASE_out_4-p_ASE_out_5-
p_ASE_out_6-p_ASE_out_7-p_ASE_out_8-p_ASE_out_9...
            -p_ASE_out_10-p_p_out_right)./(p_sat_ASE_9));
 eq12=p_ASE_out_10-p_in_ASE_10.*exp(-alpha_ASE_10.*L_simulation_max-
alpha_background_ASE.*L_simulation_max+...

(p_in_pump_max_left.*shape+p_in_signal+p_in_all*ASE_ratio+p_in_pump_max_right
.*shape-p_p_out_left-p_s_out-...
            p_ASE_out_1-p_ASE_out_2-p_ASE_out_3-p_ASE_out_4-p_ASE_out_5-
p_ASE_out_6-p_ASE_out_7-p_ASE_out_8-p_ASE_out_9...
            -p_ASE_out_10-p_p_out_right)./(p_sat_ASE_10));
  eq13=p_p_out_right-p_in_pump_max_right.*shape.*exp(-
alpha_pump.*L_simulation_max-alpha_background_pump.*L_simulation_max+...

(p_in_pump_max_left.*shape+p_in_signal+p_in_all*ASE_ratio+p_in_pump_max_right
.*shape-p_p_out_left-p_s_out-...
            p_ASE_out_1-p_ASE_out_2-p_ASE_out_3-p_ASE_out_4-p_ASE_out_5-
p_ASE_out_6-p_ASE_out_7-p_ASE_out_8-p_ASE_out_9...
            -p_ASE_out_10-p_p_out_right)./(p_sat_pump));
  eqs = [eq1, eq2, eq3, eq4, eq5, eq6, eq7, eq8, eq9, eq10, eq11, eq12,
eq13];

[p_p_out_left,p_s_out,p_ASE_out_1,p_ASE_out_2,p_ASE_out_3,p_ASE_out_4,p_ASE_o
ut_5...
            ,p_ASE_out_6,p_ASE_out_7,p_ASE_out_8,p_ASE_out_9,p_ASE_out_10,p_p
_out_right]...

=vpasolve(eqs,[p_p_out_left,p_s_out,p_ASE_out_1,p_ASE_out_2,p_ASE_out_3,p_ASE
_out_4,p_ASE_out_5...
            ,p_ASE_out_6,p_ASE_out_7,p_ASE_out_8,p_ASE_out_9,p_ASE_out_10,p_p
_out_right],...
            [0,20,20,20,20,20,20,20,20,20,20,20,0]);

answer=double([p_p_out_left,p_s_out,p_ASE_out_1,p_ASE_out_2,p_ASE_out_3,p_ASE
_out_4...
            ,p_ASE_out_5,p_ASE_out_6,p_ASE_out_7,p_ASE_out_8,p_ASE_out_9,p_AS
E_out_10,p_p_out_right]);
        p_out_pump_L_left(1,times)=answer(1,1)+p_in_pump_max_left*(1-shape);
        p_out_signal_L(1,times)=answer(1,2);
        p_out_ASE_1_L(1,times)=answer(1,3);
        p_out_ASE_2_L(1,times)=answer(1,4);
        p_out_ASE_3_L(1,times)=answer(1,5);
        p_out_ASE_4_L(1,times)=answer(1,6);
        p_out_ASE_5_L(1,times)=answer(1,7);
        p_out_ASE_6_L(1,times)=answer(1,8);
        p_out_ASE_7_L(1,times)=answer(1,9);
        p_out_ASE_8_L(1,times)=answer(1,10);
        p_out_ASE_9_L(1,times)=answer(1,11);
        p_out_ASE_10_L(1,times)=answer(1,12);
        p_out_pump_L_right(1,1)=answer(1,13)+p_in_pump_max_right*(1-shape);

%
  for i=2:times
```

```
    syms p_p_out_left p_s_out p_ASE_out_1 p_ASE_out_2 p_ASE_out_3 p_ASE_out_4
p_ASE_out_5...
        p_ASE_out_6 p_ASE_out_7 p_ASE_out_8 p_ASE_out_9 p_ASE_out_10
p_p_out_right

        eq1=p_p_out_left-p_in_pump_max_left.*shape.*exp(-alpha_pump.*L(1,i)-
alpha_background_pump.*L(1,i)+...

(p_in_pump_max_left.*shape+p_in_signal+p_in_all*ASE_ratio+p_p_out_right-
p_p_out_left-p_s_out-...
            p_ASE_out_1-p_ASE_out_2-p_ASE_out_3-p_ASE_out_4-p_ASE_out_5-
p_ASE_out_6-p_ASE_out_7-p_ASE_out_8-p_ASE_out_9...
            -p_ASE_out_10-p_out_pump_L_right(1,1))./(p_sat_pump));

        eq2=p_s_out-p_in_signal.*exp(-alpha_signal.*L(1,i)-
alpha_background_signal.*L(1,i)+...

(p_in_pump_max_left.*shape+p_in_signal+p_in_all*ASE_ratio+p_p_out_right-
p_p_out_left-p_s_out-...
            p_ASE_out_1-p_ASE_out_2-p_ASE_out_3-p_ASE_out_4-p_ASE_out_5-
p_ASE_out_6-p_ASE_out_7-p_ASE_out_8-p_ASE_out_9...
            -p_ASE_out_10-p_out_pump_L_right(1,1))./(p_sat_signal));

        eq3=p_ASE_out_1-p_in_ASE_1.*exp(-alpha_ASE_1.*L(1,i)-
alpha_background_ASE.*L(1,i)+...

(p_in_pump_max_left.*shape+p_in_signal+p_in_all*ASE_ratio+p_p_out_right-
p_p_out_left-p_s_out-...
            p_ASE_out_1-p_ASE_out_2-p_ASE_out_3-p_ASE_out_4-p_ASE_out_5-
p_ASE_out_6-p_ASE_out_7-p_ASE_out_8-p_ASE_out_9...
            -p_ASE_out_10-p_out_pump_L_right(1,1))./(p_sat_ASE_1));

        eq4=p_ASE_out_2-p_in_ASE_2.*exp(-alpha_ASE_2.*L(1,i)-
alpha_background_ASE.*L(1,i)+...

(p_in_pump_max_left.*shape+p_in_signal+p_in_all*ASE_ratio+p_p_out_right-
p_p_out_left-p_s_out-...
            p_ASE_out_1-p_ASE_out_2-p_ASE_out_3-p_ASE_out_4-p_ASE_out_5-
p_ASE_out_6-p_ASE_out_7-p_ASE_out_8-p_ASE_out_9...
            -p_ASE_out_10-p_out_pump_L_right(1,1))./(p_sat_ASE_2));

        eq5=p_ASE_out_3-p_in_ASE_3.*exp(-alpha_ASE_3.*L(1,i)-
alpha_background_ASE.*L(1,i)+...

(p_in_pump_max_left.*shape+p_in_signal+p_in_all*ASE_ratio+p_p_out_right-
p_p_out_left-p_s_out-...
            p_ASE_out_1-p_ASE_out_2-p_ASE_out_3-p_ASE_out_4-p_ASE_out_5-
p_ASE_out_6-p_ASE_out_7-p_ASE_out_8-p_ASE_out_9...
            -p_ASE_out_10-p_out_pump_L_right(1,1))./(p_sat_ASE_3));

        eq6=p_ASE_out_4-p_in_ASE_4.*exp(-alpha_ASE_4.*L(1,i)-
alpha_background_ASE.*L(1,i)+...

(p_in_pump_max_left.*shape+p_in_signal+p_in_all*ASE_ratio+p_p_out_right-
p_p_out_left-p_s_out-...
            p_ASE_out_1-p_ASE_out_2-p_ASE_out_3-p_ASE_out_4-p_ASE_out_5-
p_ASE_out_6-p_ASE_out_7-p_ASE_out_8-p_ASE_out_9...
```

```
            -p_ASE_out_10-p_out_pump_L_right(1,1))./(p_sat_ASE_4));

        eq7=p_ASE_out_5-p_in_ASE_5.*exp(-alpha_ASE_5.*L(1,i)-
alpha_background_ASE.*L(1,i)+...

(p_in_pump_max_left.*shape+p_in_signal+p_in_all*ASE_ratio+p_p_out_right-
p_p_out_left-p_s_out-...
            p_ASE_out_1-p_ASE_out_2-p_ASE_out_3-p_ASE_out_4-p_ASE_out_5-
p_ASE_out_6-p_ASE_out_7-p_ASE_out_8-p_ASE_out_9...
            -p_ASE_out_10-p_out_pump_L_right(1,1))./(p_sat_ASE_5));

        eq8=p_ASE_out_6-p_in_ASE_6.*exp(-alpha_ASE_6.*L(1,i)-
alpha_background_ASE.*L(1,i)+...

(p_in_pump_max_left.*shape+p_in_signal+p_in_all*ASE_ratio+p_p_out_right-
p_p_out_left-p_s_out-...
            p_ASE_out_1-p_ASE_out_2-p_ASE_out_3-p_ASE_out_4-p_ASE_out_5-
p_ASE_out_6-p_ASE_out_7-p_ASE_out_8-p_ASE_out_9...
            -p_ASE_out_10-p_out_pump_L_right(1,1))./(p_sat_ASE_6));

        eq9=p_ASE_out_7-p_in_ASE_7.*exp(-alpha_ASE_7.*L(1,i)-
alpha_background_ASE.*L(1,i)+...

(p_in_pump_max_left.*shape+p_in_signal+p_in_all*ASE_ratio+p_p_out_right-
p_p_out_left-p_s_out-...
            p_ASE_out_1-p_ASE_out_2-p_ASE_out_3-p_ASE_out_4-p_ASE_out_5-
p_ASE_out_6-p_ASE_out_7-p_ASE_out_8-p_ASE_out_9...
            -p_ASE_out_10-p_out_pump_L_right(1,1))./(p_sat_ASE_7));

        eq10=p_ASE_out_8-p_in_ASE_8.*exp(-alpha_ASE_8.*L(1,i)-
alpha_background_ASE.*L(1,i)+...

(p_in_pump_max_left.*shape+p_in_signal+p_in_all*ASE_ratio+p_p_out_right-
p_p_out_left-p_s_out-...
            p_ASE_out_1-p_ASE_out_2-p_ASE_out_3-p_ASE_out_4-p_ASE_out_5-
p_ASE_out_6-p_ASE_out_7-p_ASE_out_8-p_ASE_out_9...
            -p_ASE_out_10-p_out_pump_L_right(1,1))./(p_sat_ASE_8));

        eq11=p_ASE_out_9-p_in_ASE_9.*exp(-alpha_ASE_9.*L(1,i)-
alpha_background_ASE.*L(1,i)+...

(p_in_pump_max_left.*shape+p_in_signal+p_in_all*ASE_ratio+p_p_out_right-
p_p_out_left-p_s_out-...
            p_ASE_out_1-p_ASE_out_2-p_ASE_out_3-p_ASE_out_4-p_ASE_out_5-
p_ASE_out_6-p_ASE_out_7-p_ASE_out_8-p_ASE_out_9...
            -p_ASE_out_10-p_out_pump_L_right(1,1))./(p_sat_ASE_9));

        eq12=p_ASE_out_10-p_in_ASE_10.*exp(-alpha_ASE_10.*L(1,i)-
alpha_background_ASE.*L(1,i)+...

(p_in_pump_max_left.*shape+p_in_signal+p_in_all*ASE_ratio+p_p_out_right-
p_p_out_left-p_s_out-...
            p_ASE_out_1-p_ASE_out_2-p_ASE_out_3-p_ASE_out_4-p_ASE_out_5-
p_ASE_out_6-p_ASE_out_7-p_ASE_out_8-p_ASE_out_9...
            -p_ASE_out_10-p_out_pump_L_right(1,1))./(p_sat_ASE_10));
```

```
        not_absorb=p_in_pump_max_right*(1-shape);
         eq13=(p_out_pump_L_right(1,1)-not_absorb)-(p_p_out_right-
not_absorb).*exp(-alpha_pump.*L(1,i)-alpha_background_pump.*L(1,i)+...

(p_in_pump_max_left.*shape+p_in_signal+p_in_all*ASE_ratio+p_p_out_right-
p_p_out_left-p_s_out-...
            p_ASE_out_1-p_ASE_out_2-p_ASE_out_3-p_ASE_out_4-p_ASE_out_5-
p_ASE_out_6-p_ASE_out_7-p_ASE_out_8-p_ASE_out_9...
            -p_ASE_out_10-p_out_pump_L_right(1,1))./(p_sat_pump));



        eqs = [eq1, eq2, eq3, eq4, eq5, eq6, eq7, eq8, eq9, eq10, eq11,
eq12,eq13];

[p_p_out_left,p_s_out,p_ASE_out_1,p_ASE_out_2,p_ASE_out_3,p_ASE_out_4,p_ASE_o
ut_5...
            ,p_ASE_out_6,p_ASE_out_7,p_ASE_out_8,p_ASE_out_9,p_ASE_out_10,p_p
_out_right]...

=vpasolve(eqs,[p_p_out_left,p_s_out,p_ASE_out_1,p_ASE_out_2,p_ASE_out_3,p_ASE
_out_4,p_ASE_out_5...
            ,p_ASE_out_6,p_ASE_out_7,p_ASE_out_8,p_ASE_out_9,p_ASE_out_10,p_p
_out_right],...
            [p_out_pump_L_left(1,i-1),p_out_signal_L(1,i-
1),p_out_ASE_1_L(1,i-1),p_out_ASE_2_L(1,i-1),p_out_ASE_3_L(1,i-1)...
            ,p_out_ASE_4_L(1,i-1),p_out_ASE_5_L(1,i-1),p_out_ASE_6_L(1,i-
1),p_out_ASE_7_L(1,i-1)...
            ,p_out_ASE_8_L(1,i-1),p_out_ASE_9_L(1,i-1),p_out_ASE_10_L(1,i-
1),p_out_pump_L_right(1,i-1)]);


answer=double([p_p_out_left,p_s_out,p_ASE_out_1,p_ASE_out_2,p_ASE_out_3,p_ASE
_out_4...
            ,p_ASE_out_5,p_ASE_out_6,p_ASE_out_7,p_ASE_out_8,p_ASE_out_9,p_AS
E_out_10,p_p_out_right]);
        p_out_pump_L_left(1,i)=answer(1,1)+p_in_pump_max_left*(1-shape);
        p_out_signal_L(1,i)=answer(1,2);
        p_out_ASE_1_L(1,i)=answer(1,3);
        p_out_ASE_2_L(1,i)=answer(1,4);
        p_out_ASE_3_L(1,i)=answer(1,5);
        p_out_ASE_4_L(1,i)=answer(1,6);
        p_out_ASE_5_L(1,i)=answer(1,7);
        p_out_ASE_6_L(1,i)=answer(1,8);
        p_out_ASE_7_L(1,i)=answer(1,9);
        p_out_ASE_8_L(1,i)=answer(1,10);
        p_out_ASE_9_L(1,i)=answer(1,11);
        p_out_ASE_10_L(1,i)=answer(1,12);
        p_out_pump_L_right(1,i)=answer(1,13);

   end

 plot(L,p_out_pump_L_left,'r','Linewidth',1.5);
 hold on
 plot(L,p_out_signal_L,'g','Linewidth',1.5);
 hold on
```

```
plot(L,p_out_ASE_1_L+p_out_ASE_2_L+p_out_ASE_3_L+p_out_ASE_4_L+p_out_ASE_5_L+
p_out_ASE_6_L...

+p_out_ASE_7_L+p_out_ASE_8_L+p_out_ASE_9_L+p_out_ASE_10_L,'b','Linewidth',1.5
);
 hold on
 plot(L,p_out_pump_L_right,'r--','Linewidth',1.5);
  legend('Left Pump','Signal','ASE','Right Pump','Location','best')
 xlabel('Fiber Length (m)')
 ylabel('Power (W)')
 set(gca,'Fontsize',18)

a1_out=[transpose(L),transpose(p_out_pump_L_left),transpose(p_out_signal_L),t
ranspose(p_out_ASE_1_L+p_out_ASE_2_L+p_out_ASE_3_L...
     +p_out_ASE_4_L+p_out_ASE_5_L+p_out_ASE_6_L...

+p_out_ASE_7_L+p_out_ASE_8_L+p_out_ASE_9_L+p_out_ASE_10_L),transpose(p_out_pu
mp_L_right)];


a2_out=[lambda_ASE_all.*1e9,[p_out_ASE_1_L(1,times);p_out_ASE_2_L(1,times);p_
out_ASE_3_L(1,times);p_out_ASE_4_L(1,times);...

p_out_ASE_5_L(1,times);p_out_ASE_6_L(1,times);p_out_ASE_7_L(1,times);p_out_AS
E_8_L(1,times);p_out_ASE_9_L(1,times);p_out_ASE_10_L(1,times);]];

  aa_length_output=[transpose(p_out_pump_L_left) transpose(p_out_signal_L)
transpose(p_out_ASE_1_L+p_out_ASE_2_L+p_out_ASE_3_L+p_out_ASE_4_L+p_out_ASE_5
_L+p_out_ASE_6_L...
     +p_out_ASE_7_L+p_out_ASE_8_L+p_out_ASE_9_L+p_out_ASE_10_L)];
```

APPENDIX D: FDTD Code for Excitation-Balanced Pulse Amplifier

This appendix is an example code for the simulation of excitation-balanced pulse amplifier.

```
clc
clear all

%
%input
rep_rate=10;
P_p_ASP_input=500;
P_p_SP_input=500;

p_s_SIGNAL_input=1000;

%Gaussian
pulsewidth_signal=10e-9/2.2e-4;% 10 ns pulse width

pulse_width=2e-2; %unit:ms
ASP_SP_ratio=2;% The ratio of the ASP pulse and the SP pulse
time_ratio=2;%the ratio of the delay and the SP pulse
delay=time_ratio*pulse_width;%unit:ms
r_eff=1.283392852186876e-05;
A_eff=pi*r_eff^2;
r_core_ini=15e-6;
r_cladd_ini=62.5e-6;
gamma_signal=0.965; %overlap integral
gamma_pump=(r_core_ini/r_cladd_ini)^2; %overlap integral
gamma_pump_adjust=A_eff/(pi*r_core_ini^2);
simulation_fiber_length=5;
loss_background=0.01*log(10)/10;%10dB/km background loss


% mesh
div=101;
z=linspace(0,simulation_fiber_length,div);%%
t_1=linspace(0,delay*1e-3,(div-1)*time_ratio+1);
t_2=linspace(delay*1e-3,pulse_width*ASP_SP_ratio*1e-3,ASP_SP_ratio*(div-1)-
(div-1)*time_ratio+1);
t_3=linspace(pulse_width*ASP_SP_ratio*1e-3,(pulse_width+delay)*1e-3,div-
(ASP_SP_ratio*(div-1)-(div-1)*time_ratio));
t4=(pulse_width+delay)*1e-3;
t_4=linspace((pulse_width+delay)*1e-3,(pulse_width+delay)*1e-
3+1.5*pulsewidth_signal*1e-3,5*div);
t_5=linspace((pulse_width+delay)*1e-3+pulsewidth_signal*1e-3,1/rep_rate,div);
dt1=pulse_width*1e-3/(div-1);
dt2=pulsewidth_signal*1e-3/(5*div-1);
dz=simulation_fiber_length/(div-1);%%

N1_1=zeros((div-1)*time_ratio+1,div);
N1_2=zeros(ASP_SP_ratio*(div-1)-(div-1)*time_ratio+1,div);
N1_3=zeros(div-(ASP_SP_ratio*(div-1)-(div-1)*time_ratio),div);
N1_4=zeros(5*div,div);
N1_5=zeros(div,div);

P_p_990=zeros((div-1)*time_ratio+1,div);
```

```
P_p_990_loss=zeros((div-1)*time_ratio+1,div);

P_p_overlap_990=zeros(ASP_SP_ratio*(div-1)-(div-1)*time_ratio+1,div);
P_p_overlap_990_loss=zeros(ASP_SP_ratio*(div-1)-(div-1)*time_ratio+1,div);

P_p_overlap_976=zeros(ASP_SP_ratio*(div-1)-(div-1)*time_ratio+1,div);
P_p_overlap_976_loss=zeros(ASP_SP_ratio*(div-1)-(div-1)*time_ratio+1,div);

P_p_976=zeros(div-(ASP_SP_ratio*(div-1)-(div-1)*time_ratio),div);
P_p_976_loss=zeros(div-(ASP_SP_ratio*(div-1)-(div-1)*time_ratio),div);

P_s_985=zeros(5*div,div);
P_s_985_loss=zeros(5*div,div);

P_p_990(:,1)=P_p_ASP_input;
P_p_overlap_990(:,1)=P_p_ASP_input;
P_p_overlap_976(:,1)=P_p_SP_input;
P_p_976(:,1)=P_p_SP_input;
tttt=10;

%rectangular
% P_s_985(:,1)=p_s_985_input;

% Gaussian
pulse_actual=4.4*pulsewidth_signal*1e3/tttt/2 %us
% P_s_985(:,1)=p_s_SIGNAL_input.*exp(-(t_4-(pulse_width+delay)*1e-3-
pulsewidth_signal/2*1e-3).^2./(2*((pulsewidth_signal*1e-3)/tttt)^2))...
%     -p_s_SIGNAL_input.*exp(-(t4-(pulse_width+delay)*1e-3-
pulsewidth_signal/2*1e-3).^2./(2*((pulsewidth_signal*1e-3)/tttt)^2));
% P_s_985(:,1)=exp(-(t_4-(pulse_width+delay)*1e-3-pulsewidth_signal/1.5*1e-
3).^2./(2*((pulsewidth_signal*1e-3)/tttt)^2));
% plot(t_4*1e6,P_s_985(:,1))
% hold on
% P_s_985(:,1)=(1./(exp((t_4-(pulse_width+delay)*1e-3-
pulsewidth_signal/1.5*1e-3)./5e-9)+1));
% plot(t_4*1e6,P_s_985(:,1))
% hold on
% P_s_985(:,1)=exp(-(t_4-(pulse_width+delay)*1e-3-pulsewidth_signal/1.5*1e-
3).^2./(2*((pulsewidth_signal*1e-3)/tttt)^2))...
%     .*(1./(exp((t_4-(pulse_width+delay)*1e-3-pulsewidth_signal/1.5*1e-
3)./1e-9)+1));
% plot(t_4*1e6,P_s_985(:,1))
dt_Gaussian_peak=pulsewidth_signal*2.2e-4*3;
P_s_985(:,1)=p_s_SIGNAL_input.*exp(-(t_4-(pulse_width+delay)*1e-3-
dt_Gaussian_peak).^2./(2*((pulsewidth_signal*1e-3)/tttt)^2));
% P_s_985(:,1)=p_s_SIGNAL_input.*exp(-(t_4-(pulse_width+delay)*1e-3-
pulsewidth_signal/1.5*1e-3).^2./(2*((pulsewidth_signal*1e-3)/tttt)^2))...
%     .*(1./(exp((t_4-(pulse_width+delay)*1e-3-pulsewidth_signal/1.5*1e-
3)./1e-9)+1));
plot(t_4*1e6,P_s_985(:,1))
hold on
% for i=1:5*div
%     if P_s_985(i,1)<0
%         P_s_985(i,1)=0;
%     end
% end
% plot(t_4*1e6,P_s_985(:,1))
```

```
%

%constants
A_10=1/(850*1e-6);
h=6.62607015e-34;
c=299792458;
rho=2e26;

%spontaneous emission
f_spon=c/(1010e-9);

% ASP
f_ASP=c/(1035e-9);
cross_abs_ASP=3.34E-26;
cross_emi_ASP=5.86E-25;
S1_ASP=gamma_pump*gamma_pump_adjust*(cross_abs_ASP+cross_emi_ASP)/(A_eff*h*f_
ASP);
S2_ASP=gamma_pump*gamma_pump_adjust*cross_abs_ASP*rho/(A_eff*h*f_ASP);
transparency_ASP=rho/(1+cross_emi_ASP/cross_abs_ASP)

% SP nm
f_SP=c/(1010e-9);
cross_abs_SP=9.68e-26;
cross_emi_SP=5.14e-25;
S1_SP=gamma_pump*gamma_pump_adjust*(cross_abs_SP+cross_emi_SP)/(A_eff*h*f_SP)
;
S2_SP=gamma_pump*gamma_pump_adjust*cross_abs_SP*rho/(A_eff*h*f_SP);
transparency_SP=rho/(1+cross_emi_SP/cross_abs_SP)

% signal
f_signal=c/(1020e-9);
cross_abs_signal=7.77E-26;
cross_emi_signal=6.66E-25;
S1_signal=(cross_abs_signal+cross_emi_signal)/(A_eff*h*f_signal);
S2_signal=cross_abs_signal*rho/(A_eff*h*f_signal);
transparency_signal=rho/(1+cross_emi_signal/cross_abs_signal)

P_lim=((transparency_signal-
transparency_SP)/dt2+A_10*transparency_SP)/(S2_signal-
S1_signal*transparency_SP)
E_saturation=h*f_signal*A_eff/(cross_abs_signal+cross_emi_signal)*1e3


%% calculation start

 for iii=1:2

N1_1(1,:)=N1_5(div,:);

% First let's calculate the 0-delay part
% first column
for k=2:(div-1)*time_ratio+1
    N1_1(k,1)=N1_1(k-1,1)+dt1*(-A_10*N1_1(k-1,1)-S1_ASP*P_p_990(k-
1,1)*N1_1(k-1,1)+S2_ASP*P_p_990(k-1,1));
end
```

```
% then remaining part
for j=2:div
for i=1:(div-1)*time_ratio+1
    %P_p_990(i,j)=P_p_990(i,j-1)*exp(gamma_pump*(N1_1(i,j-1).*cross_emi_ASP-
(rho-N1_1(i,j-1))*cross_abs_ASP-loss_background)*dz);
    P_p_990(i,j)=P_p_990(i,j-1)*exp(gamma_pump*(N1_1(i,j-1).*cross_emi_ASP-
(rho-N1_1(i,j-1))*cross_abs_ASP)*dz)*exp(-loss_background*dz);
    P_p_990_loss(i,j)=P_p_990(i,j-1)*exp(gamma_pump*(N1_1(i,j-
1).*cross_emi_ASP-(rho-N1_1(i,j-1))*cross_abs_ASP)*dz)-P_p_990(i,j-
1)*exp(gamma_pump*(N1_1(i,j-1).*cross_emi_ASP-(rho-N1_1(i,j-
1))*cross_abs_ASP)*dz)*exp(-loss_background*dz);
    if i<(div-1)*time_ratio+1
    N1_1(i+1,j)=N1_1(i,j)+dt1*(-A_10*N1_1(i,j)-
S1_ASP*P_p_990(i,j)*N1_1(i,j)+S2_ASP*P_p_990(i,j));
    end
end
end


%then let's calculate the delay-1 ms part
% first row of N is already calculated in previous section
N1_2(1,:)=N1_1((div-1)*time_ratio+1,:);

% first column
for kok=2:ASP_SP_ratio*(div-1)-(div-1)*time_ratio+1
    N1_2(kok,1)=N1_2(kok-1,1)+dt1*(-A_10*N1_2(kok-1,1)-
S1_ASP*P_p_overlap_990(kok-1,1)*N1_2(kok-1,1)+S2_ASP*P_p_overlap_990(kok-
1,1)-S1_SP*P_p_overlap_976(kok-1,1)*N1_2(kok-1,1)+S2_SP*P_p_overlap_976(kok-
1,1));
end

% remaining part
for joj=2:div
    for ioi=1:ASP_SP_ratio*(div-1)-(div-1)*time_ratio+1
        P_p_overlap_990(ioi,joj)=P_p_overlap_990(ioi,joj-
1)*exp(gamma_pump*(N1_2(ioi,joj).*cross_emi_ASP-(rho-
N1_2(ioi,joj))*cross_abs_ASP)*dz)*exp(-loss_background*dz);
        P_p_overlap_990_loss(ioi,joj)=P_p_overlap_990(ioi,joj-
1)*exp(gamma_pump*(N1_2(ioi,joj).*cross_emi_ASP-(rho-
N1_2(ioi,joj))*cross_abs_ASP)*dz)-P_p_overlap_990(ioi,joj-
1)*exp(gamma_pump*(N1_2(ioi,joj).*cross_emi_ASP-(rho-
N1_2(ioi,joj))*cross_abs_ASP)*dz)*exp(-loss_background*dz);
        P_p_overlap_976(ioi,joj)=P_p_overlap_976(ioi,joj-
1)*exp(gamma_pump*(N1_2(ioi,joj).*cross_emi_SP-(rho-
N1_2(ioi,joj))*cross_abs_SP)*dz)*exp(-loss_background*dz);
        P_p_overlap_976_loss(ioi,joj)=P_p_overlap_976(ioi,joj-
1)*exp(gamma_pump*(N1_2(ioi,joj).*cross_emi_SP-(rho-
N1_2(ioi,joj))*cross_abs_SP)*dz)-P_p_overlap_976(ioi,joj-
1)*exp(gamma_pump*(N1_2(ioi,joj).*cross_emi_SP-(rho-
N1_2(ioi,joj))*cross_abs_SP)*dz)*exp(-loss_background*dz);
            if ioi<ASP_SP_ratio*(div-1)-(div-1)*time_ratio+1
                N1_2(ioi+1,joj)=N1_2(ioi,joj)+dt1*(-A_10*N1_2(ioi,joj)-
S1_ASP*P_p_overlap_990(ioi,joj)*N1_2(ioi,joj)+S2_ASP*P_p_overlap_990(ioi,joj)
-
S1_SP*P_p_overlap_976(ioi,joj)*N1_2(ioi,joj)+S2_SP*P_p_overlap_976(ioi,joj));
            end
```

```
    end
end

% then let's calculate 1-1+delay part
% again, first row of N is already calculated in previous section
N1_3(1,:)=N1_2(ASP_SP_ratio*(div-1)-(div-1)*time_ratio+1,:);

% first column
for kk=2:div-(ASP_SP_ratio*(div-1)-(div-1)*time_ratio)
    N1_3(kk,1)=N1_3(kk-1,1)+dt1*(-A_10*N1_3(kk-1,1)-S1_SP*P_p_976(kk-
1,1)*N1_3(kk-1,1)+S2_SP*P_p_976(kk-1,1));
end

for jj=2:div
    for ii=1:div-(ASP_SP_ratio*(div-1)-(div-1)*time_ratio)
     P_p_976(ii,jj)=P_p_976(ii,jj-
1)*exp(gamma_pump*(N1_3(ii,jj).*cross_emi_SP-(rho-
N1_3(ii,jj))*cross_abs_SP)*dz)*exp(-loss_background*dz);
     P_p_976_loss(ii,jj)=P_p_976(ii,jj-
1)*exp(gamma_pump*(N1_3(ii,jj).*cross_emi_SP-(rho-
N1_3(ii,jj))*cross_abs_SP)*dz)-P_p_976(ii,jj-
1)*exp(gamma_pump*(N1_3(ii,jj).*cross_emi_SP-(rho-
N1_3(ii,jj))*cross_abs_SP)*dz)*exp(-loss_background*dz);
        if ii<div-(ASP_SP_ratio*(div-1)-(div-1)*time_ratio)
            N1_3(ii+1,jj)=N1_3(ii,jj)+dt1*(-A_10*N1_3(ii,jj)-
S1_SP*P_p_976(ii,jj)*N1_3(ii,jj)+S2_SP*P_p_976(ii,jj));
        end
    end
end



% then let's calculate signal pulse part
% again, first row of N is already calculated in previous section
N1_4(1,:)=N1_3(div-(ASP_SP_ratio*(div-1)-(div-1)*time_ratio),:);

% first column
for kook=2:5*div
    N1_4(kook,1)=N1_4(kook-1,1)+dt2*(-A_10*N1_4(kook-1,1)-
S1_signal*P_s_985(kook-1,1)*N1_4(kook-1,1)+S2_signal*P_s_985(kook-1,1));
end

for jj=2:div
    for ii=1:5*div
     P_s_985(ii,jj)=P_s_985(ii,jj-
1)*exp(gamma_signal*(N1_4(ii,jj).*cross_emi_signal-(rho-
N1_4(ii,jj))*cross_abs_signal-loss_background)*dz);
     P_s_985_loss(ii,jj)=P_s_985(ii,jj-
1)*exp(gamma_signal*(N1_4(ii,jj).*cross_emi_signal-(rho-
N1_4(ii,jj))*cross_abs_signal)*dz)-P_s_985(ii,jj-
1)*exp(gamma_signal*(N1_4(ii,jj).*cross_emi_signal-(rho-
N1_4(ii,jj))*cross_abs_signal-loss_background)*dz);
        if ii<5*div
            N1_4(ii+1,jj)=N1_4(ii,jj)+dt2*(-A_10*N1_4(ii,jj)-
S1_signal*P_s_985(ii,jj)*N1_4(ii,jj)+S2_signal*P_s_985(ii,jj));
        end
    end
end
```

```
%Finally for the decay
N1_5(1,:)=N1_4(5*div,:);


for m=1:div
    N1_5(:,m)=N1_5(1,m).*exp(-A_10.*(t_5-
(delay+pulse_width+pulsewidth_signal)*1e-3));
end

 end


figure
plot(z*1e2,N1_1(1,:),'Linewidth',1.5)
hold on
plot(z*1e2,N1_5(div,:),'Linewidth',1.5)
hold on
xlabel('Position (cm)')
ylabel('N_{1} (m^{-3})')
legend('Initial N_{1}','N_{1} after one period')
set(gca,'FontSize',18)

% % calculate gain as a function of time and position
 N1=[N1_1(1:(div-1)*time_ratio,:);N1_2(1:ASP_SP_ratio*(div-1)-(div-
1)*time_ratio,:);N1_3(1:div-(ASP_SP_ratio*(div-1)-(div-1)*time_ratio)-
1,:);N1_4(1:5*div-1,:);N1_5];
% Gain_local=zeros(2*div+(div-1)*time_ratio-1,div);
% Gain_local=gamma.*(N1.*cross_emi_985-(rho-N1).*cross_abs_985);% local gain,
m^-1
% Gain_local_dB=Gain_local*10/log(10);% local gain, dB/m
% Gain_inte=zeros(2*div+(div-1)*time_ratio-1,div);
% for i=1:2*div+(div-1)*time_ratio-1
%     for j=1:div
%         Gain_inte(i,j)=sum(Gain_local_dB(i,1:j))*dz;
%     end
% end

 %ylim([0,2e26]);
%%
% plot N1(z,t)
%  figure
t1=[t_1(:,1:(div-1)*time_ratio),t_2(:,1:ASP_SP_ratio*(div-1)-(div-
1)*time_ratio),t_3(:,1:div-(ASP_SP_ratio*(div-1)-(div-1)*time_ratio)-
1),t_4(:,1:5*div-1),t_5];
% [Z1,T1]=meshgrid(z,t1);
%  pcolor(Z1*1e2,T1*1e3,N1)
% shading interp
% colorbar
% xlabel('Position (cm)')
% ylabel('Time (ms)')
% title('N_{1} (m^{-3})')
% set(gca,'FontSize',18)
% aa_out=[transpose(t1),N1];
% aa_N1=[0,z;aa_out];
% check=[T1(:,1)*1e6,N1];
```

```
figure
for i=1:div
    out_energy(1,i)=sum(P_s_985(1:5*div-1,i))*dt2*1000*1000;
end
plot(z,out_energy/1e3)
xlabel('Fiber Length (m)')
ylabel('Output Pulse Energy (mJ)')
set(gca,'FontSize',18)

[a,b]=max(out_energy);
optimize_length=z(1,b);


% plot N1 at a position
figure
  plot(t1*1e6,N1(:,b),'Linewidth',1.5)
xlabel('Time (ms)')
ylabel('N1 (m^-3)')
set(gca,'FontSize',18)
xlim([0,(delay+pulse_width+2*pulsewidth_signal)*1e3])
%ylim([0,transparency_SP]);


%plot N1 when SP pulse ends
t_ASP_end=((div-1)*time_ratio)+(ASP_SP_ratio*(div-1)-(div-1)*time_ratio);
t_SP_end=((div-1)*time_ratio)+(ASP_SP_ratio*(div-1)-(div-1)*time_ratio)+(div-
(ASP_SP_ratio*(div-1)-(div-1)*time_ratio)-1);
t_signal_end=t_SP_end+5*div-1;
plot(z,N1(t_ASP_end,:),'Linewidth',1.5)
hold on
plot(z,N1(t_SP_end,:),'Linewidth',1.5)
plot(z,N1(t_signal_end,:),'Linewidth',1.5)
a3_out=[transpose(z),transpose(N1(t_ASP_end,:)),transpose(N1(t_SP_end,:)),tra
nspose(N1(t_signal_end,:))];

% no overlap
figure
plot([t_1,t_3,t_4,t_5].*1e6,[P_p_990(1:(div-
1)*time_ratio+1,1);P_p_976(1:div,1);P_s_985(1:5*div,1);zeros(div,1)],'r','Lin
ewidth',1.5)
hold on
plot([t_1,t_3,t_4,t_5].*1e6,[P_p_990(1:(div-
1)*time_ratio+1,b);P_p_976(1:div,b);P_s_985(1:5*div,b);zeros(div,1)],'b','Lin
ewidth',1.5)
xlim([0,(delay+pulse_width+2*pulsewidth_signal)*1e3])

out1=[transpose([t_1(:,1:(div-1)*time_ratio),t_3(:,1:div-(ASP_SP_ratio*(div-
1)-(div-1)*time_ratio)-1),t_4(:,1:5*div),t_5].*1e6),...
    [P_p_990(1:(div-1)*time_ratio,1);P_p_976(1:div-(ASP_SP_ratio*(div-1)-
(div-1)*time_ratio)-1,1);P_s_985(1:5*div,1);zeros(div,1)],...
    [P_p_990(1:(div-1)*time_ratio,b);P_p_976(1:div-(ASP_SP_ratio*(div-1)-
(div-1)*time_ratio)-1,b);P_s_985(1:5*div,b);zeros(div,1)]];
 out2=[transpose([t_1(:,1:(div-1)*time_ratio),t_3(:,1:div-(ASP_SP_ratio*(div-
1)-(div-1)*time_ratio)-1),t_4(:,1:5*div),t_5].*1e6),...
     [N1(1:((div-1)*time_ratio)+(div-(ASP_SP_ratio*(div-1)-(div-
1)*time_ratio)-1)+(5*div-1),b);...
```

```
     N1(((div-1)*time_ratio)+(div-(ASP_SP_ratio*(div-1)-(div-1)*time_ratio)-
1)+(5*div-1)+1,b);...
     N1(((div-1)*time_ratio)+(div-(ASP_SP_ratio*(div-1)-(div-1)*time_ratio)-
1)+(5*div-1)+1:((div-1)*time_ratio)+(div-(ASP_SP_ratio*(div-1)-(div-
1)*time_ratio)-1)+(5*div-1)+div,b)]];

  signal_peak_power=max(P_s_985(1:5*div,b));
% pulse shape change
figure
plot(t_4.*1e6,[P_s_985(1:5*div,b)]./max(P_s_985(1:5*div,b)),'b','Linewidth',1
.5)
hold on
plot(t_4.*1e6,[P_s_985(1:5*div,1)]./max(P_s_985(1:5*div,1)),'r','Linewidth',1
.5)



shape_in=[P_s_985(1:5*div,1)]./max(P_s_985(1:5*div,1));
factor_in=sum(shape_in)*dt2;
shape_in_final=shape_in./(factor_in);
shape_out=[P_s_985(1:5*div,b)]./max(P_s_985(1:5*div,b));
factor_out=sum(shape_out)*dt2;
shape_out_final=shape_out./(factor_out);
shape_cross=shape_in_final.*shape_out_final;
shape_auto=shape_in_final.*shape_in_final;
cross=sum(shape_cross)/sum(shape_auto);

a2_out=[transpose((t_4*1e3-pulse_width*(1+ASP_SP_ratio))*1e6),shape_out];
[c,d]=max(shape_out);
peak_time=(t_4(1,d)*1e3-pulse_width*(1+ASP_SP_ratio))*1e6;

% out1=[transpose([t_1,t_3].*1e6),[P_p_990(1:(div-
1)*time_ratio+1,1);P_p_976(1:div,1)],...
%     30+10.*log10([P_p_990(1:(div-1)*time_ratio+1,1);P_p_976(1:div,1)]),...
%     [P_p_990(1:(div-1)*time_ratio+1,b);P_p_976(1:div,b)],...
%      30+10.*log10([P_p_990(1:(div-1)*time_ratio+1,b);P_p_976(1:div,b)])];
% a1_out=[[-5 1e-30 -30 1e-30 -30];[-1e-10 1e-30 -30 1e-30 -
30];out1;[(pulse_width+delay)*1000+1e-10 1e-30 -30 1e-30 -
30];[(pulse_width+delay)*1000+5 1e-30 -30 1e-30 -30]];
%
% out2=[transpose(t_4.*1e6),P_s_985(1:5*div,1),...
%     30+10.*log10(P_s_985(1:5*div,1)),...
%     P_s_985(1:5*div,b),...
%     30+10.*log10(P_s_985(1:5*div,b))];
% a2_out=[[(pulse_width+delay)*1000-0.5 1e-30 -30 1e-30 -
30];[(pulse_width+delay)*1000-1e-10 1e-30 -30 1e-30 -
30];out2;[(pulse_width+delay+pulsewidth_signal)*1000+1e-10 1e-30 -30 1e-30 -
30];[(pulse_width+delay+pulsewidth_signal)*1000+0.5 1e-30 -30 1e-30 -30]];

%energies in unit mJ
input_ASP_pump_energy=(sum(P_p_990(1:(div-1)*time_ratio,1)))*dt1*1000;
input_SP_pump_energy=(sum(P_p_976(1:div-1,1)))*dt1*1000;
out_ASP_pump_energy=(sum(P_p_990(1:(div-1)*time_ratio,b)))*dt1*1000;
out_SP_pump_energy=(sum(P_p_976(1:div-1,b)))*dt1*1000;
abs_ASP_energy=input_ASP_pump_energy-out_ASP_pump_energy;
abs_SP_energy=input_SP_pump_energy-out_SP_pump_energy;
input_signal_energy=sum(P_s_985(1:5*div-1,1))*dt2*1000;
```

```
output_signal_energy=sum(P_s_985(1:5*div-1,b))*dt2*1000
pulse_amp=10*log10(output_signal_energy/input_signal_energy);

N_SP=abs_SP_energy/(h*f_SP)/1000;
N_ASP=abs_ASP_energy/(h*f_SP)/1000;
N_sig=(output_signal_energy-input_signal_energy)/(h*f_signal)/1000;
N_loss_SP=sum(P_p_990_loss(:,b))*dt1/(h*f_SP);
N_loss_ASP=sum(P_p_976_loss(:,b))*dt1/(h*f_ASP);
N_loss_signal=sum(P_s_985_loss(:,b))*dt2/(h*f_ASP);
N_spon=N_SP+N_ASP-N_sig-N_loss_SP-N_loss_ASP-N_loss_signal;
N_spon_noloss=N_SP+N_ASP-N_sig;
N_sig_SP=N_sig*(N_SP/(N_SP+N_ASP));
N_sig_ASP=N_sig*(N_ASP/(N_SP+N_ASP));
thermal_energy_generated_mJ_by_pulse=(N_sig_SP*h*(f_SP-
f_signal)+N_sig_ASP*h*(f_ASP-f_signal)+N_loss_signal*h*f_signal)*1000


E_SP=abs_SP_energy*1e-3;
E_ASP=abs_ASP_energy*1e-3;
E_sig=h*f_signal*N_sig;
E_spon=h*f_spon*N_spon;
E_spon_noloss=h*f_spon*N_spon_noloss;
EQD=1-(E_sig+E_spon)/(E_SP+E_ASP)
EQD_noloss=1-(E_sig+E_spon_noloss)/(E_SP+E_ASP);
a1_out=[div;rep_rate;pulse_width*ASP_SP_ratio*1000;pulse_width*1000;pulse_act
ual*1000;P_p_ASP_input;P_p_SP_input;p_s_SIGNAL_input;...
    input_ASP_pump_energy;out_ASP_pump_energy;input_ASP_pump_energy-
out_ASP_pump_energy;input_SP_pump_energy;out_SP_pump_energy;input_SP_pump_ene
rgy-out_SP_pump_energy;input_signal_energy*1000;output_signal_energy;...
    100*(output_signal_energy-input_signal_energy)/(input_ASP_pump_energy-
out_ASP_pump_energy+input_SP_pump_energy-out_SP_pump_energy);...
    100*(output_signal_energy-
input_signal_energy)/(input_ASP_pump_energy+input_SP_pump_energy);...

EQD*100;z(1,b);pulse_amp;thermal_energy_generated_mJ_by_pulse*1000;peak_time]
;
sound(sin(1:10000));

%%
filename = 'Example.mat';
save(filename,'N1','P_p_990','P_p_976','P_s_985')
sound(sin(1:10000));
```